

Design, Fabrication and Characterization of Novel Directional Thermoelectric IR Sensors

by
Siamack V. Grayli

M.Sc., Simon Fraser University, 2012
B.Sc. Aachen University of Applied Sciences 2007

Thesis Submitted in Partial Fulfillment of the
Requirements for the Degree of
Doctor of Philosophy

in the
Department of Mechatronics Systems Engineering
Faculty of Applied Sciences

© Siamack V. Grayli 2019
SIMON FRASER UNIVERSITY
Fall 2019

Copyright in this work rests with the author. Please ensure that any reproduction or re-use is done in accordance with the relevant national copyright legislation.

Approval

Name: Siamack V. Grayli

Degree: Doctor of Philosophy (Mechatronics Systems Engineering)

Title: Design, Fabrication and Characterization of Novel Directional Thermo-Electric IR Sensors

Examining Committee:

Chair: Michael Sjoerdsma
Senior Lecturer

Behraad Bahreyni
Senior Supervisor
Associate Professor

Gary W. Leach
Supervisor
Associate Professor

Glenn Chapman
Supervisor
Professor

Woo Soo Kim
Supervisor
Associate Professor

Carlo Menon
Internal Examiner
Professor

Roger Zemp
External Examiner
Professor
Electrical and Computer Engineering
University of Alberta

Date Defended/Approved: October 24th 2019

Abstract

This thesis project reports on implementation of the thermoelectric effect in conjunction with 3D microfabricated silicon structures to create a novel pixel detector that is capable of directional sensing in the infrared (IR) regime. Here, the effect is used in conjunction with a 3D design to not only sense the presence of an IR target, but also to recalculate its incidence angle using known trigonometric relationships that arise from the silicon micromachining process. Room temperature (RT) IR sensing applications use thermoelectric (thermoelectric) material such as transition metal oxides (TMOs) which depict an inverse relationship between the materials temperature and its electrical resistance. The incident IR radiation is detected via measuring the induced change in the material's electrical resistance as a result of materials temperature change due to IR radiation absorption. Depending on the distance to the target and the magnitude of the induced change (indicated by the material's temperature coefficient of resistance (TCR)), the detector creates an image of the IR radiative source. There has been no prior report on use of such effect in tracking an IR target's angular path as it traverses a pixel detector hence recalculate the incidence angle of an IR target using thermoelectric effect. In this work, standard silicon micromachining techniques were employed to create 3D micro pixels that were further coated with vanadium pentoxide via dip coating. The desired sense regions were then created via patterning of the deposited vanadium pentoxide thin film through an innovative process flow that allowed for selective removal of the material from across the surface of the fabricated device die. Prior to deposition, the material underwent extensive synthesis and characterization routines in order to achieve an optimum recipe that produces the maximum TCR and least possible sheet resistance. Electrodes were put in place across the inclined (111) facets of the micromachined pixels through photoresist spray coating and photolithography and lift off process. The device responses were measured using a test setup comprised of an automated NI LabView® data capture interface, Keithley digital source meters, IR source and calcium fluoride lenses to illuminate the devices in an angular fashion. Two generation of the devices were designed prototyped in order to investigate the effects of optical and thermal noise and parasitic factors on the proposed functionality of the device. The results show an improvement in the capability of the devices to measure the angle of incidence of an IR source using thermal IR sensing at room temperature.

Keywords: Room Temperature IR Sensing, Silicon Micromachining, Vanadium Pentoxide, Directional IR Sensors

Dedication

To my kin and source of blood, my mother Zahra, my father Hossein, my sister Firoozeh and my brother Sasan at first, for every man's first and foremost source of comfort comes from where his blood first forms.

To my teachers, Drs Gary Leach and Behraad Bahreyni at second, for a path without the guidance of a teacher is no path to recognize and to endeavour.

To myself as an entity at third, whom I must satisfy through the years of my learning to come, to know how near my goal I reside and how far off my purpose I stand.

Acknowledgements

I would like to express my deepest degrees of respect and gratitude towards my senior supervisors Drs. B. Bahreyni and G. W. Leach for putting trust and confidence in my aptitude as a graduate researcher and guiding me through my graduate career. Given the interdisciplinary nature of the project at hand, I had the privilege of receiving mentorship under two of the most outstanding principal investigators from the two respective departments of mechatronics systems engineering and chemistry, which brought me about a wealth of knowledge otherwise inaccessible through non-academic routes. As a result, I sincerely state my acknowledgement of the assumed opportunity and dedicate an everlasting notion of gratitude to both of these gentlemen for the rest of my academic career.

I would like to thank Dr. Dimitri Starr, a fellow associate researcher with Dr. Leach's group, an avid optics and photonics specialist who assisted my research greatly and from whom I gained invaluable insight into optics and photonics principles.

I would like to thank Dr. Xin Zhang, a fellow staff researcher at the 4D Labs Nano-Imaging and Characterization facility at Simon Fraser University for his enabling input and teaching which elevated the quality and the capacity of the scientific work underway in the course of my thesis.

I would like to thank the Simon Fraser University's electronic shop staff, for the constant technical support and insightful assistance during the construction of several test setups necessary to the thesis work's data acquisition.

I would like to thank Dr. Sasan Grayli, my dear brother and research cohort for his scientific and moral support during the course of this PhD work.

I would like to thank 4D Labs staff for the enabling training and research services provided to me during the course of my degree.

I would like to thank National Research Council of Canada for providing the financial support of my research project.

Table of Contents

Approval.....	ii
Abstract.....	iii
Dedication.....	v
Acknowledgements.....	vi
Table of Contents.....	vii
List of Tables.....	x
List of Figures.....	xi
List of Acronyms.....	xix
List of Symbols.....	xx
CMC-MNT Competition Winning Scanning Electron Micrographs.....	xxii
Chapter 1. Introduction.....	1
1.1. IR Sensing Applications.....	1
1.1.1. Examples of Currently Used IR Sensors in Robotic Application.....	2
1.1.2. Different IR Sensing Mechanisms.....	3
1.2. Motivation and Objectives.....	4
1.2.1. Thesis Outline.....	6
Chapter 2. Infrared sensing: Theory and Background.....	8
2.1. Electromagnetic Radiation Interaction with Materials.....	8
2.2. Black Body Radiation and Radiometric Models.....	10
2.3. Infrared sensing.....	11
2.3.1. Types of Infrared Detectors.....	12
Photon Detectors.....	12
Thermal Detectors.....	14
Tunneling Thermal Infrared Detectors.....	17
Micro-resonating Thermal IR Detectors.....	18
Thermoelectric Detectors.....	19
2.3.2. Thermal Infrared Detectors.....	19
2.3.3. Pyroelectric versus Bolometric Detectors.....	21
2.4. Transition Metal Oxides in Infrared Sensing.....	25
2.4.1. Vanadium Oxide properties.....	26
2.4.2. Vanadium Oxide Thin Films for Room Temperature IR Sensing.....	27
2.4.3. Vanadium Oxide Deposition techniques.....	29
Chapter 3. IR Vector Light Sensor.....	31
3.1. Device's Design and Principles of Operation.....	31
3.1.1. Mathematical Model for the IR Source and Sense Material.....	31
3.1.2. Device Design and Principles of Operation.....	34
3.2. Thermoelectric Signal Modeling.....	37
3.2.1. Device's Thermal Conduction Equation.....	37
3.2.2. Device's Readout Voltage Equation.....	38

3.2.3.	Device's Readout Noise Equation and Parasitic Sources	39
3.3.	Device Heat Conduction Modeling.....	41
3.3.1.	Thermal Transfer Simulation Results.....	43
	100 μm wide silicon structure	44
	4500 μm wide silicon structure	46
	2D Simulation using COMSOL Multiphysics Software.....	47
Chapter 4.	Device's Sense Material Preparation	50
4.1.	Sense Material Preparation	50
4.1.1.	Room Temperature Methods for Sense Layer Deposition.....	50
4.1.2.	Sol Gel Synthesis of the Sense Layer Material	51
4.2.	Sense Material Deposition.....	54
4.3.	Sense Material Characterization	56
4.3.1.	Surface Roughness Analysis	56
4.3.2.	Structural Characterization	58
4.3.3.	Thermoelectric Characterization	61
	TCR Calculation and Sense Layer Fabrication Recipe.....	63
4.3.4.	Opto-Electronic Characterization	66
Chapter 5.	Vector Light Detector's Fabrication and Processes.....	68
5.1.	Vector Light Sensor Fabrication Mask Design	68
5.2.	Silicon micromachining and basic structure Fabrication.....	72
5.3.	Photoresist Spray Coating on 3D Structures.....	75
5.4.	Vanadium Pentoxide Preparation and Deposition.....	78
5.5.	3D Lithography and Electrical Contact Deposition	81
5.5.1.	Process 01: Gold (Au)-Over- V_2O_5 Lift-off	81
5.5.2.	Process 02: Gold (Au)-Over- V_2O_5 Lift-off-Chromium-Mask.....	82
5.5.3.	Process 03: (Gold)-Under- V_2O_5 Lift-off-Small-Pads	84
Chapter 6.	Experimental Results and Discussion.....	87
6.1.	Device Level Characterization	87
6.1.1.	Raised (Mesa) Device IV Characteristics.....	87
6.1.2.	Inverted Device IV Characteristics	90
6.2.	Device Level (1 st Design Generation) IR Response	92
6.2.1.	Device Level (1 st Design Generation) Signal Acquisition and IR Response (Pre-FIB).....	92
6.2.2.	Device (1st Design Generation) IR Incidence Measurement (Pre FIB)	97
	Approximation of Parasitic Resistive Regions Contribution to the Device's Performance	101
6.2.3.	Device (1 st Design Generation) IR Incidence Angle Recalculation (Pre FIB) 107	
6.2.4.	Device (1st Design Generation) Signal Acquisition and IR Response (Post FIB) 109	
6.2.5.	Device (1 st Design Generation) IR Incidence Measurement and Incidence Angle Recalculation (Post FIB)	110
6.3.	Device Level (2 nd Design Generation) IR Response	116

6.3.1.	Device (2 nd Design Generation) Signal Acquisition and Conditioning	116
6.3.2.	Device (2 nd Design Generation) Inter-Facet Thermal Insulation Control Experiment	119
6.3.3.	Device (2 nd Design Generation) Incidence IR Measurement and Recalculation	122
6.3.4.	Device (2 nd Design Generation) Model Refinement to Account for Optical Power Losses	125
6.3.5.	Device (2 nd Design Generation) Angular Response Control Experiment	130
6.3.6.	Device (2 nd Design Generation) Incidence Angle Recalculation Considerations.....	133
Chapter 7. Conclusion and Future Work		134
7.1.	Conclusion.....	134
7.1.1.	Contributions	135
7.1.2.	Future Work.....	136
	Device Field of View Limitation Improvement	136
	Device Thermal Conduction Improvement	138
	Device Thermal Response Selectivity Improvement.....	138
References.....		141
Appendix A. Derivation of the Parasitic Parameter N		147
Appendix B. Derivation of Exponential Valued TCR		150
Appendix C. Effect of Background Radiation on The Detector's Angular Recalculation		151
Appendix D. Statistical Relevance and Goodness of the Fitted Models		155

List of Tables

Table 5- 1 Optimum spray coating parameters for conformal photoresist deposition	76
Table 5- 2 The synthesis and annealing parameters of the deposited V_2O_5 layers	80
Table 5- 3 The post resist development and lift-off process results for different exposure times using the process flow from figure 47. The yellow arrows mark the isotropic removal of the underlying V_2O_5 layer as a result of interaction with the photoresist developer.....	82

List of Figures

Figure 1- 1 IR sensing in robotic applications2

Figure 1- 2 Micro-machined IR bolometer structure (Honeywell Design 1985)4

Figure 1- 3 Left) 3D depiction and Right) cross-sectional view of the proposed single pixel IR detector5

Figure 1- 4 IR Source detection for industrial robotic are as a potential application for the proposed detector6

Figure 2- 1 Electromagnetic field decay as a result of wave-matter interaction.....9

Figure 2- 2 Planck's Spectral Power Distribution of a Black Body Radiator for bodies 100, 150, 200, 250 and 300 K. The red dashed line signifies the peak wavelength occurrence according to Wien's displacement law..... 11

Figure 2- 3 Transmitted thermal IR spectral bands of the atmospheric window and the corresponding absorbing atmospheric molecules in the far infrared region of the EM spectrum 12

Figure 2- 4 Principle of operation of a photon detector where the incident photon induces a) intrinsic absorption b) extrinsic absorption and c) free carrier absorption 14

Figure 2- 5 Principle of operation of a thermal IR detector and its equivalent circuit (simplified)..... 15

Figure 2- 6 Schematic of a thermopile comprised of thermocouple elements in series . 17

Figure 2- 7 Schematic depiction of a) micro-resonator IR detector whereby b) the resonant frequency of the micro-resonator undergoes a shift as a result of heating of resonating structure due to IR absorption 19

Figure 2- 8 Pyroelectric heat detection: a) No change in total dipole moment hence no current flows through the circuit b) a positive change in the temperature rearranges the surface-bound charges and an electric current flows.....21

Figure 2- 9 Least to most probable conduction pathways in a vanadium pentoxide unit cell for an arbitrary initiation site.28

Figure 3- 1 Differential left) source emission solid angle and right) detector's perceived irradiance32

Figure 3- 2 Schematic of the incidence source and the detector's material undergoing a change in the electrical resistance as a result of interacting with the incoming radiative power.....33

Figure 3- 3 Depiction of the radiative IR source as a point source whereby its emitted wave fronts can be approximated as plane waves at distance $d \gg$ Detector's Dimensions.34

Figure 3- 4 Theoretical device's angular field of view and angular modulation of the sense facets' output as a result of changes in the angle of incidence of the incoming radiative power.....35

Figure 3- 5 System of two IR VLS detectors to triangulate the distance to radiation source	37
Figure 3- 6 Equivalent noise voltage sources' contribution to the output signal of the device	40
Figure 3- 7 Heat contamination of the device's output voltage (signal) as a result of inter-facet thermal conduction	42
Figure 3- 8 The initial and boundary conditions of the 1D heat transfer simulation using forwarding boundary conditions at the boundaries as shown above such that the material constants before and after the boundary were those of the preceding and proceeding media.	43
Figure 3- 9 The transient heat conduction solution as a function of distance in a 100 μm wide structure for a) 0.5 μm thick, b) 2.0 μm thick and c) 4.0 μm thick silicon dioxide as thermal insulation layer (referenced to figure 11 for the device geometry).....	44
Figure 3- 10 The transient heat conduction solution as a function of time in a 100 μm wide structure for a) 0.5 μm thick, b) 2.0 μm thick and c) 4.0 μm thick silicon dioxide as thermal insulation layer (referenced to figure 11 for the device geometry).....	45
Figure 3- 11 a) Transient solution as a function of distance and b) as a function of time for 4500 μm wide silicon structure	47
Figure 3- 12 2D heat transfer simulation of a 100 μm raised pyramid with 2 μm of oxide at a) 0.1 ms, b) 1 ms, c) 10 ms and d) 100 ms into the simulation.....	48
Figure 4- 1 a) 2D view of the orthorhombic $\alpha\text{-V}_2\text{O}_5$ crystal lattice along the (001) direction where line AB depicts the crystal packing in the (010) direction	54
Figure 4- 2 a) Landau model of a rising planar substrate from a Newtonian fluid depicting three regions for the fluid film thickness as a function of distance from the fluid bath-fluid film interface b) The numerical evaluation for vanadium pentoxide sol (fluid parameters extracted from literature) and capillary constant C_N approximated for Newtonian fluids.....	55
Figure 4- 3 Film thickness (derived from the average profile height in profilometry data) versus the annealing temperature of the samples.	57
Figure 4- 4 The SEM images of a-(i-v) Low concentration samples and b-(i-v) High concentration samples, annealed at 300°C, 400°C, 500°C and 650°C, respectively The blown-up sections in either group depict the sheet structural differences between the low and high concentration.....	58
Figure 4- 5 ai-iii) The comparison between the XRD traces of low and high concentration samples (a-i and a-ii, respectively) annealed at different temperatures against powder reference of $\alpha\text{-V}_2\text{O}_5$ (a-iii).; b) the layered structure of $\alpha\text{-V}_2\text{O}_5$	59
Figure 4- 6 Raman spectra of a) low-concentration and b) high-concentration samples show identical characteristics with a nearly three-fold increase in the peak amplitudes associated with $\alpha\text{-V}_2\text{O}_5$ of the high-concentration group compared to the low-concentration ones.....	61

Figure 4- 7 a) 650 ° C annealed and b) as-deposited high concentration V ₂ O ₅ samples undergone thermoelectric characterization	62
Figure 4- 8 The schematic of the measurement setup that was used to characterize the electrical resistance of the samples as a function of temperature	62
Figure 4- 9 Sheet resistance of low concentration and high concentration samples at 320 K as a function of the annealing temperature. The high concentration samples follow a general increasing trend whereas the low concentration samples electrical resistance drops as a function of the annealing temperature. Room temperature (RT=295K) values are included for reference.....	63
Figure 4- 10 Exponential fit to the measured temperature dependent resistance for low concentration samples a) as-deposited, and annealed at b) 300 °C, c) 400 °C and d) 500 °C.....	65
Figure 4- 11 The TCR of the low-concentration and high-concentration samples at 37 °C as a function of the sample's annealing temperature. The inset shows the exponential fit to the measurements for one of the low concentration samples annealed at 500°C.The uncertainty is calculated from the fluctuations of the electrical resistance across the measurement time at a given temperature.	65
Figure 4- 12 Radar chart for the average sheet resistance and TCR as function of annealing temperature for the characterized samples	66
Figure 4- 13 Fourier-Transform Infrared (FTIR) spectra of V ₂ O ₅ samples annealed at various temperatures showing all the samples begin absorption in longer portion of the infrared spectrum where the peak absorption occurring at around 10 μm (~1000 cm ⁻¹).....	67
Figure 5- 1 The device floor plan including substrate and metallization masks with dimensions.....	69
Figure 5- 2 Substrate mask design and corner compensation design with dimensions..	70
Figure 5- 3 An example of emergence of high index fast etching crystalline planes at a) short, b) moderate and c) long exposures of the bulk silicon to an isotropic etchant	71
Figure 5- 4 The design guidelines for the corner compensation structures with a) surface lengths and b) etch depth.....	71
Figure 5- 5 a) 2D and b) 3D rendering of the device floor plan with both upright (mesa) and inverted pyramids in the final form.....	72
Figure 5- 6 a)-i) The device fabrication process flow with d-i) to i-i) depicting the mesa and d-ii) to i-ii) the inverted structures	74
Figure 5- 7 a) Silicon etching in TMAH. The wafer was oriented perpendicular to the etching direction to achieve optimum surface uniformity, b-i) the inverted pyramid structure and b-ii) the mesa pyramid structure.	75
Figure 5- 8 Different parameters affecting the spray coating process on a 3D surface. The process optimization is designed to avoid a) cavity planarization as a result of excess resist deposition and c) granulated resist formation due to overly powdered resist flow as a result of high sonication power. The uniform layer	

is achieved in middle ground between the two extremes with high enough sonication power and low enough speed as depicted in b). 77

Figure 5- 9 The automated dip coating setup used to deposit vanadium pentoxide sol onto the samples. The figures a) through d) depict a full dipping cycle whereby the sample is completely submerged into the solution to avoid non-uniformities induced by dip lines as a result of multiple coatings 78

Figure 5- 10 The V_2O_5 dip coating routines one mesa and three inverted sample structures with a-i) – d-i) depicting the bare, a-ii) – d-ii) the pre-annealed and a-iii – d-iii) the post annealed samples for 4, 6, 8 and 12 coated layers. 79

Figure 5- 11 The pre deposition, post deposition and post annealing profiles of one mesa and two inverted structures undergone V_2O_5 dip coating for a-i) to a-iii, b-i) to b-iii 6 and c-i) to c-iii 8 coatings using the synthesis parameters presented in table 2 and dipping and pulling rate of 50 mm/min 80

Figure 5- 12 The variation to intended process flow whereby the lift-off process happens through a layer of chromium aimed to protect the underlying vanadium pentoxide from direct interaction with photoresist developer..... 83

Figure 5- 13 The inverted structure undergone the trial lift-off process depicted at a) post chromium deposition, b) post PR deposition and patterning and c) post chromium etching. The result of this trial rendered the proposed process obsolete due to the removal of the underlying V_2O_5 layer due to the chromium etchant CEP 200..... 83

Figure 5- 14 The third and final process flow resulting in a successful deposition and lift-off of the designated electrode pattern underneath the sense material... 84

Figure 5- 15 a) 3D rendering of the device using the "Au-under- V_2O_5 -SmallPad" process flow; b) a 2D cross-section of the mechanism by means of which the electrode pads were accessed through the sense material. 85

Figure 5- 16 A collage of the actual a) mesa and b) inverted pyramid structures fabricated with the final process flow. The figures show the electrode configuration on the device body as well as the contact openings providing access to the Au electrode pads through the dip coated V_2O_5 layer. 86

Figure 6- 1 The schematic of the experimental setup used to measure the sheet resistance of the sense material across the sample devices 88

Figure 6- 2 Approximaton approach in order to evaluatre the sheet resistance of the sense layer using the comb electrode structures which resulted in 98 $k\Omega/\square$ for mesa and 91 $k\Omega/\square$ for the inverted device sample..... 89

Figure 6- 3 I-V traces measured across the large and medium sized comb structures. . 89

Figure 6- 4 I-V curves measured across the output terminals of different regions of the raised (mesa) device as labeled in figure 1; the slight differences in the slope of the traces from each of the regions points out the potential material thickness and/or area mismatches. 90

Figure 6- 5 I-V responses of the inverted device sample recorded from large and medium size comb electrodes; The traces from each size scale corrected for difference in structure dimensions show similar slopes. 91

Figure 6- 6 IV curves measured across the output terminals of different regions of the inverted device as labeled in Figure 6-1; the slight differences in the slope of the traces from each of the regions points out a larger degree of potential material thickness mismatch and or area across different sense regions.91

Figure 6- 7 Output routing of the sample test device wire-bonded to a prototyping board using silver epoxy resin92

Figure 6- 8 Device’s output terminal mapping as prepared for testing device’s electrical resistance across each sense region. The difference in room temperature resistances across the two terminals could be a result of different surface area and/or material thickness variations on the two sides.93

Figure 6- 9 a) Schematic of the optical test setup used for IR measurements; The calcium-fluoride (CaF₂) lenses were used to allow for focusing of the incident IR radiation onto the designated test area. b) The spotsize of the focused IR onto the DUT sense area94

Figure 6- 10 The IR induced change in the electrical resistance of the DUT. The exposure time was set long enough for the signal to stabilize as a result of the incident radiation95

Figure 6- 11 a) out of plane and b) in plane schematic depiction of the human hand induced IR response test setup96

Figure 6- 12 Changes in the electrical resistance of east (top) and west (bottom) side of the device as a result of human hand exposure at 75 cm. The markers indicate slight opposing changes in the resistance as a result of in-plane angular hand motion96

Figure 6- 13 a) 3D and b) 2D depiction of the IR source position with respect to the detector. The arc between the facet normals depicts angular path of the source to generate different incidence angles97

Figure 6- 14 Device’s output response to fractioned incident optical power using optical neutral density filters. The mismatch in the slope of the linear fits indicates different responsivity of the two sides and the uncertainty arises from the electrical resistance fluctuations of the device prior to exposure to IR source for each fraction of the incident power.98

Figure 6- 15 Schematic of the optical test setup used for measuring the DUT’s IR angular response99

Figure 6- 16 DUT’s angular $\Delta R/R$ response along with the theoretical or expected trends for a) ideal case (no parasitic resistance region contribution) and b) recalculated theoretical trends with 90% parasitic contribution to the east side and 80% parasitic contribution to the west side. The measurement uncertainty is calculated as the temperature induced fluctuations of the electrical resistance experienced over the entire duration of experiment. Statistical inference of the fitted model is provided in Appendix D. 100

Figure 6- 17 The effect of a) 0%, b) 30%, c) 50%, d) 70%, e) 80% and f) 90% parasitic resistive contribution to the theoretical $\Delta R/R$ trends as a result of exposure to IR. 101

Figure 6- 18 a) 3D depiction and b) cross-sectional depiction of incoming radiation angular interaction with sense and parasitic regions on the device 102

Figure 6- 19 a) Sense and parasitic regions in a single device using a symmetrical electrode design and b) division of the sense and parasitic regions along the structure symmetry line to generate rectangular and trapezoidal resistive regions	103
Figure 6- 20 Coordinate system used to calculate the integral resistance of an arbitrary half trapezoidal resistive region	104
Figure 6- 21 Device's equivalent circuit a) without the parasitic resistive elements and b) with the parasitic resistive elements	106
Figure 6- 22 The effect of the percentage parasitic contribution on the accuracy of the recalculated angle by the device.	107
Figure 6- 23 The predicted angular recalculation using a device output with 90% parasitic contribution compared to a) ideal device and b) recalculated angles from the measured device responses. The error bars reflect the uncertainty in the room temperature resistance of the device under test across the duration of the measurement. Statistical inference of the fitted trend lines are provided in appendix D.....	108
Figure 6- 24 The device die after partial removal of the sense material in order to reduce the effects of the parasitic resistance via focused ion beam milling. a) and b) depict the top of the DUT pixel before and after FIB, c), d) and e) are electron micrograms of FIB tracks across regions C, A and B.	109
Figure 6- 25 Device responsivity test at the two opposing side after FIB process	110
Figure 6- 26 DUT's angular $\Delta R/R$ response along with the theoretical or expected trends for a)ideal case (no parasitic region contribution) and b) recalculated theoretical trends with 80% parasitic contribution to the east side and 70% parasitic contribution to the west side. Statistical inference of the fitted model is provided in Appendix D.....	111
Figure 6- 27 The predicted angular recalculation using a device output with 80% parasitic contribution compared to a) ideal device and b) recalculated angles from the measured device responses post FIB milling. Statistical inference of the fitted trend lines are provided in appendix D.....	112
Figure 6- 28 The $\Delta R/R$ ratio for east and west side for top) ideal device, b) device with 90% and 100% parasitic contribution and bottom) device with 90% and 100% parasitic contribution corrected via multiplying the ratio with N at each incidence angle.....	114
Figure 6- 29 Theoretical curves for a) devices with 90% and 100% parasitic contribution and b) corrections thereof using N	114
Figure 6- 30 Recalculated angles through use of N from the measured $\Delta R/R$ for a) 1 st design generation device before FIB milling and b) after FIB milling process. As predicted by the theoretical trends in figure 6-30 the range of the recalculated angles improves drastically when compensated for the effects of the parasitic. Statistical inference of the fitted trend lines are provided in appendix D.....	115
Figure 6- 31 a) 2D and b) 3D rendering of the 2 nd generation device design focusing on reducing the effects of the parasitic resistive regions.....	116
Figure 6- 32 a) Upright and b) lateral sense region patterns employed in the 2 nd generation device design whereby the resistive sense regions are confined to the inclined facets of the (111) silicon.....	117

Figure 6- 33 Gen 02 device responsivity to IR radiation on the opposing east and west side 118

Figure 6- 34 Responsivity fits on the two sides of the 2nd device design obtained by their incident power dependence. The similar slopes of the fit lines indicate less mismatch between the sense regions on either side as result of of IR radiation. The observed offset is an indicator material induced change in room temperature resistivity which is used to normalise each side's response to the other. 119

Figure 6- 35 a) Schematic of the inter-facet heat diffusion control experiment setup whereby the diode laser's spot-size on the DUT sense region was visually monitored by means of a CCD camera and a solid state LED. b) The 670 nm photons generated by the diode laser bypassing the V₂O₅ and SiO₂ layers depositing energy into the underlying silicon substrate. 120

Figure 6- 36 a) The modulated device response at the exposed side (west side) in opposed to the non-exposed side's gradual drop (east side) at optical chopping frequency of 4 Hz. b)The blowup of the marked region depicting the amount of induced ΔR across one optical 122

Figure 6- 37 Angular $\Delta R/R$ responses of gen 02 devices in 15 ° increments to IR radiation fitted with a) 0% parasitic and b) 30% parasitic contribution. Errorbars were calculated from the uncertainties in the room temperature resistance across the duration of the measurements. Statistical inference of the fitted model is provided in Appendix D. 123

Figure 6- 38 The predicted angular recalculation using a device output with 30% parasitic contribution compared to a) ideal device and b) recalculated angles from the measured angular $\Delta R/R$ trends for 2nd design generation device. Statistical inference of the fitted trend lines are provided in appendix D. 124

Figure 6- 39 Schematic depiction of a) S and b) P polarized photons. The graph in c) shows the fraction of the transmitted optical power as a function of the incidence angle from normal to the surface and refractive indices of air and V₂O₅. 126

Figure 6- 40 Device output on the east and west side for 10 ° increment angular exposure being fitted to theoretical model with 30% parasitic contribution with and without accounting for the reflective losses for a) east side and b) west side of the 2nd design generation device. Statistical inference of the fitted model is provided in Appendix D..... 128

Figure 6- 41 The predicted angular recalculation using a device model output with 30% parasitic contribution and reflection induced optical power losses compared to a) ideal device and b) recalculated angles from the measured angular $\Delta R/R$ trends for 2nd design generation with linear trend lines fitted to the expected and measured data. c) Incorporation of parasitic parameter N does not improve the recalculated trends from measured data. Statistical inference of the fitted trend lines are provided in appendix D. 129

Figure 6- 42 a) A 2nd design generation device mounted on the prototyping board, b) The optical test setup used for inter-facet heat contamination; the dotted line shows the laser beam's path from the laser cavity all the way to DUT sense region, c) CCD image of the sense region; the red square shows the

surface area the beam was focused onto and d) the angular path through which the DUT was exposed by the diode laser	131
Figure 6- 43 a) The $\Delta R/R$ trends measured on the east and west sides of the 2 nd generation device using the optical test setup described in Figure 6-42-a; b) the recalculated incidence angle using the ratio of the east and west side's $\Delta R/R$ trends in a). The recalculated angles show a dramatic improvement in both range and accuracy of the outputted values relative to the ideal case.	132
Figure 7- 1 2D Schematic of different micromachined silicon facets with the inclined surface to be on a) (111) facet and b) (110) facet of the silicon substrate and their effects on the device FOV. c) 3D depiction of such structures on a 001 wafer	137
Figure 7- 2 Schematic of a device design with reference sense region on the top surface	137
Figure 7- 3 Device thermal contamination reduction for a) reducing the bulk silicon heat sink effect and b)2D and c) 3D depiction of air gap introduction between the device sense facets to reduce inter facet heat transfer	138
Figure 7- 4 a) Radiation spectra of blackbodies emitting at (from lowest intensity to the highest intensity) at 15 °C, 25 °C and 37 °C. b) the difference between the peak emission spectra of a target at 37 °C and room temperature object at 25 °C.....	139
Figure 7- 5 Schematic of spectrally selective devices vs current design for a) incidence of a photon at the desired wavelength (λ_1) and b) undesired wavelength (λ_2). The heat symbol's size indicates the magnitude of the thermal response due to absorbed photon.	140

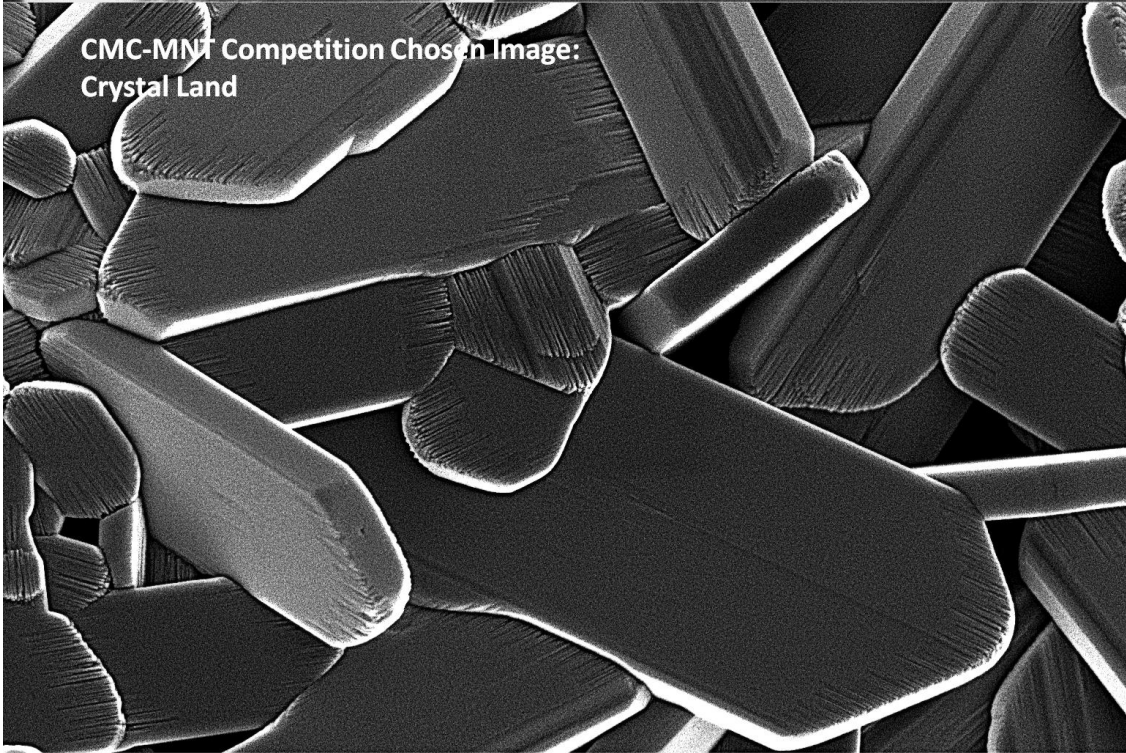
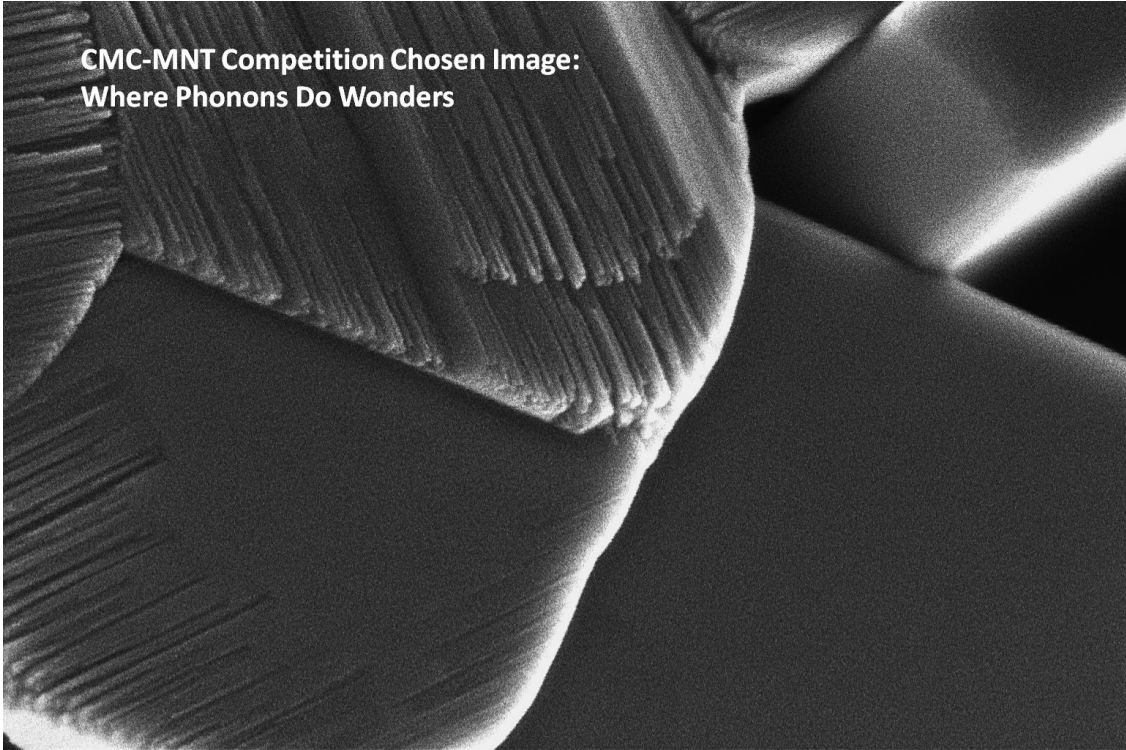
List of Acronyms

CdHgTe	Cadmium Mercury Telluride
CMOS	Complementary Metal Oxide Semiconductor
DOA	Direction of Arrival
EM	Electromagnetic
InSb	Indium Antimonide
IoT	Internet of Things
IR	Infrared Radiation
LWIR	Long Wavelength Infrared Radiation
MEMS	Micro-Electro Mechanical Systems
MIT	Metal to Insulator Transition
NEP	Noise Equivalent Power
NETD	Noise Equivalent Temperature Difference
RF	Radio Frequency
SiO ₂	Silicon Dioxide
TCR	Temperature Coefficient of Resistance
TMO	Transition Metal Oxide
V ₂ O ₅	Vanadium Pentoxide
VLS	Vector Light Sensor

List of Symbols

Φ_s	Radiant Flux
C_N	Newtonian Fluid Constant
C_P	Material Specific Heat
C_{th}	Thermal Capacitance
D^*	Detectivity
\tilde{E}	Electric Field Phasor Transform
E_a	Bandgap
E_s	Irradiance
I_{in}	Incoming Radiative Power
I_s	Radiant Power
K_0	Real valued Propagation Constant
M_P	Material Mass
$P_{L,R}$	Power (Left, Right)
R_{LR}	Power Ratio (Left to Right)
R_0	Room Temperature Electrical Resistance
T_0	Initial Temperature
U_w	Pulling Speed
V_N	Noise Voltage
V_b	Bias Voltage
k_B	Boltzmann Constant
m_e	Effective Mass of Electron
α_d	Thermal Diffusivity
β_m	Material Specific Temperature Constant
δ_R	Temperature Coefficient of Resistance
ρ_{sense}	Sense Area Resistivity
τ_c	Mean Time between Collision
$\psi_{L,R}$	Angular Deviation From Normal to Surface (Left, Right)
ϵ_c	Complex Permittivity
h	Planck's Constant
\hbar	Reduced Planck's Constant
Δf	Equivalent Noise Measurement Frequency Bandwidth
A	Material's Absorbance

B	Measurement Bandwidth
C	Speed of Light In Vacuum
E	Electric Field
F	Focal Ratio
G	Thermal Conductance
K	Degree Kelvin
R	Electrical Resistance
S	Seebeck Coefficient
T	Temperature
a	Attenuation Constant
b	Propagation Constant
e	Electron Charge
g	Gravitational Acceleration
j	Imaginary Unit
t	Time
α	Silicon (111) Facet Angle
β	Incidence Angle
ε	Emissivity
η	Absorption Coefficient
λ	Wavelength
ν	Photon Frequency
σ	Medium's Conductivity
τ	Transmittance
ω	Angular Frequency
ρ	Reflectance



Chapter 1. Introduction

1.1. IR Sensing Applications

There has been rapid development and an increasing interest in the micro electromechanical sensor devices in the past few decades. These developments have paved the way for the introduction of MEMS based detectors that can perform complex tasks [1], [2]. Using both the standard existing and/or novel process flows, MEMS based detectors have become integrated in a wide variety of intelligent sensing applications relevant to today's automated work environment and other areas of technology such as the internet of things (IoT) [3], [4]. Many of such intelligent sensing applications rely on the available high processing power to combine multiple detectable quantities such as temperature, motion and optical signature with environmental parameters to enable autonomous machinery to interact with their surroundings safely [1], [5]. As a result, infrared sensing has become a centre piece of such research and development due to the merits it brings about in enabling safe human-machine interactions through acknowledgment of a robotic system towards human presence [6]–[8]. Given that the human body has an IR signature in the long wavelength infrared (LWIR) regime, the associated sensing techniques, focus on both the design of the detector as well as the solid state properties of the IR sensitive material that allow for human IR signature detection. Depending on the intent, there are different IR sensing applications, each targeting a specific method of detection. A wide range of security applications, make use of passive (non-emitting) IR sensitive components to detect the IR-emitting target's motion or to track it's position within a designated range [9], [10]. Other security systems make use of thermal imagers to verify human presence in designated areas as a means to prevent intrusion [11]–[13]. In contrast, many factories and other large industrial work environments tend to apply IR based detection systems in order to identify human presence for the sake of safety and protection of the human workforce from undesirable collision with the machinery [14]–[16]. In the course of past research, the main focus has been on the improvement of the existing detectors in areas such as fabrication price, imaging quality and detection bandwidth [16].

1.1.1. Examples of Currently Used IR Sensors in Robotic Application

One of the main areas of application of IR sensing is its use in robotics. Although somewhat varied, its applications include vision assisted object manipulation, autonomous robotic navigation and line-of-sight position sensitive distance measurement [8], [9], [11], [17]. All three of the aforementioned applications fall under the umbrella of machine vision and robotic sensory interfaces. For vision assisted object manipulation, the implementation of complex object control systems relies on the use of IR proximity sensors [17]. In this case, proximity sensor arrays are positioned on the grip extremities of the robot, where, in combination with other sensors such as force and traction sensors, they provide feedback for the motor control unit to establish proper grip points [17]. Autonomous robotic navigation systems [18] similarly act as short range distance measurement units that can warn the robot about surrounding obstacles and hence guide the central controller to change course accordingly. Finally, position sensitive distance measurement systems represent more active detection in which an IR emitting component sends pulsed infrared signals towards an obstacle and records the reflected emission from the obstacle by the IR sensitive array [19], [20]. Changes in the reflected IR signals detected by the IR sensitive arrays provide information about object motion. All of the above mentioned technologies rely solely on the intensity of the received infrared radiation as a function of the distance between the reflected or emitted infrared pulse and the detector unit.



Figure 1- 1 IR sensing in robotic applications

1.1.2. Different IR Sensing Mechanisms

Infrared detectors are distinguished on the basis of their detection mechanisms and generally fall into two main categories: 1) Photonic detectors and 2) Thermal detectors. Photonic detectors rely on an intrinsic or extrinsic electronic excitation as a result of an IR photon's interaction with the detector to form a photovoltaic or photoconductive response. In contrast, thermal detectors respond to IR radiation with thermally-induced changes of the sensing material's physical properties. The most common signal generation mechanisms employed by thermal detectors are thermo-electric effects (temperature dependent changes in the electrical resistance) or the pyro-electric effect (an alteration in the material's electrical dipole orientation as a result of the absorbed IR radiation). Thermal IR detectors have gained wide acceptance in a range of applications due to their large spectral response, room temperature operation, material stability and lower fabrication costs compared to photonic devices [11], [13], [14]. Of the two common thermal IR detectors thermoelectric and pyroelectric, thermoelectric detectors offer simpler sensing mechanism that allow for the detection of non-modulated infrared radiation from the background with low voltage noise. The device response however, is not stabilized and at low biasing voltage the responsivity is limited [13], [14]. Pyro-electric sensors on the other hand offer much wider range of spectral responsivity as well as sensitivity to modulated sources due to the time-differentiable electronic charge shift as the device output response. However, pyro-electric detectors are more complex to make and are prone to vibrational noise. As a result, thermo-electric detectors are the more popular choice among thermal IR detectors for DC IR sensing applications [13], [14], [21]. Given that all different forms of thermal detectors rely on the conversion of the incident IR radiation to heat, the fundamental governing principle of a thermal detector is modelled with heat flow equations to describe the temperature increase as a result of the incident radiation [13]. Although there are three main mechanisms by which the induced heat can flow across the target material, conduction is the main design consideration made in the structure of a thermoelectric IR detector [13], [14]. Since the flow of heat from the sensitive area to the surrounding thermal elements can reduce the degree of the induced change in the sensor, IR sensitive structures are designed in a way to minimize the conduction pathways for the generated heat away from the surface of the IR sensitive material. Thermal insulation for the IR sensitive area occurs through incorporation of thick insulating layers underneath the sensitive area and/or minimizing the area of material contact that joins the IR sensitive

area to the rest of the structure [11], [13], [14]. Other measures in lowering the thermal conductance of the sense structures are taken through creating an air gap between the sense region and the rest of the structure via suspending the sense area (see Figure 1-2). The latter approach, however, adds significantly to the fabrication challenges [22]–[25].

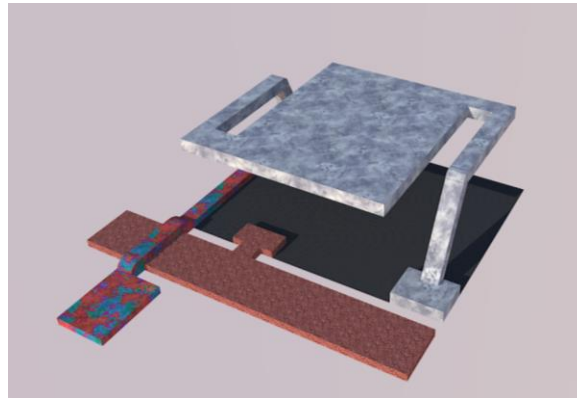


Figure 1-2 Micro-machined IR bolometer structure (Honeywell Design 1985)

1.2. Motivation and Objectives

In the majority of the previous research, near IR detectors or LWIR thermal imagers have reported on improving figures of merit such as thermal image quality and the detection range [18], [26]. An example of integration of such IR imaging systems into industrial robotics has been to provide visual feedback to ensure safe collaboration between the human and an autonomous robotic work force [7], [17], [20]. However there has not yet been any reports of IR detectors that aside from the IR source identification, could detect the angle at which the IR source is located. In this work, we have researched the advantages of a design that not only can detect the source of the incoming infrared radiation but also has the potential to determine the angle of incidence and the direction of the source relative to the detector. Due to their previously mentioned advantages, we have selected the thermal IR detection mechanism as our detection method and have investigated a low-cost non-vacuum-based synthesis route to fabricate the thermoelectric material of choice. Associated with IR sensors are classes of noise that in case of under-developed manufacturing and/or poor design parameters can distort and compromise the device's readout signal entirely [13], [14], [21]. Therefore the majority of the technologies in which thermal IR detection is implemented, endure higher costs in the process of fabricating sensing materials suitable for practical applications. Scientists and engineers

have implemented complex fabrication methods, often based on cleanroom processes, to both enhance the material's response to IR radiation and reduce the effect of associated noise during signal acquisition [8], [9], [13], [21]. Therefore the current work has also focused on a full set of characterisation experiments that were designed to evaluate both the morphological and thermoelectrical figures of merit of the sol-gel synthesis methodology used to synthesize the thermal IR sensing material. This work is using a novel approach towards human-emitted IR detection through employment of a 3D design micro pixel by which not only the IR target is being detected in the desired range (1-3 m) but also using trigonometric calculations, the direction of the perceived IR radiation is recalculated. The schematic below (Figure 1-3) shows both the 2D and 3D depiction of the proposed detector and its interaction with the incident IR.

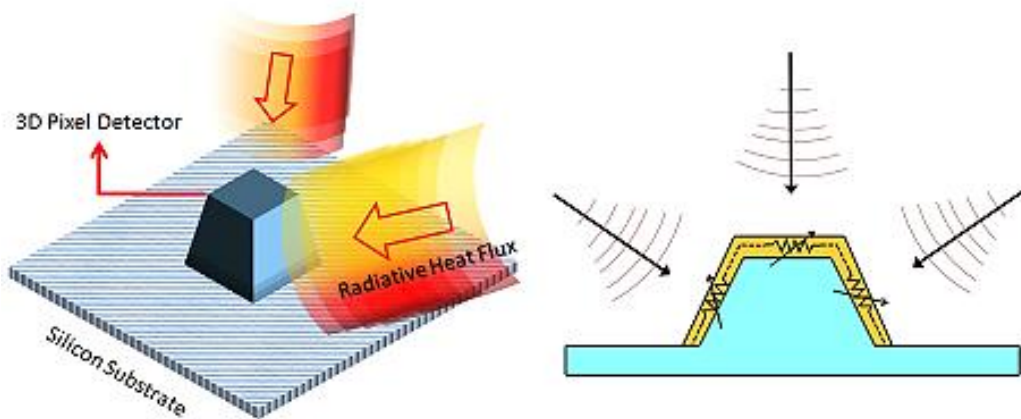


Figure 1- 3 Left) 3D depiction and Right) cross-sectional view of the proposed single pixel IR detector

Unlike radio frequency based directional detectors, thermal IR sensors have no means of detecting the phase of the incoming radiative heat to calculate the direction of arrival (DOA). The proposed three-dimensional pixel structure allows for a multi-faceted detection surface where each surface creates a fixed angle with the incoming radiation depending on the incidence angle, as depicted in Figure 1-3-right above. As a result of the interaction between the incident IR photon and the sensing surface at an angle with respect to the direction of propagation of the photon, only a portion of the photon's energy is absorbed by the thermally active material. Incidence angle (or the direction) of the incoming radiation is therefore calculated using the ratio of the perceived radiation on two opposing surfaces on a single device. Integration of such angular detection into an autonomous device can give the robot an analog field of view (FOV) and therefore ensure the robot's safe

interaction with its surroundings when co-occupied by a human workforce. Figure 1-4 depicts the device's detection mechanism in a real-life working environment.

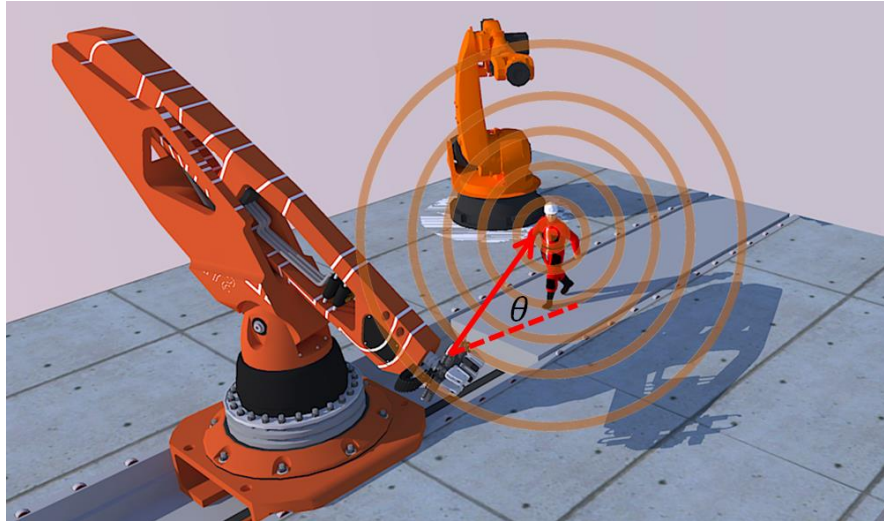


Figure 1- 4 IR Source detection for industrial robotic are as a potential application for the proposed detector

Previously angle sensitivity has been reported using optical arrays and plasmonically enhanced diodic detectors [27]–[30]. Alternatively, use of angle sensitive pixels have led to the development of light field cameras wherein the recorded variation in the intensity of the incoming light allows for plenoptical (multi-focused) imaging [31]–[34]. The majority of the angle sensitive designs in previous works, have focused on use of detector arrays in conjunction with an aperture to limit the stray light exposure [35]–[39]. Use of aperture arrays and waveguides with a single detector was also shown to lead into angle dependent optical response and directional sensing [40]. Although effective, these techniques are only capable of approximating the direction of an optical source in the visible portion of the spectrum without giving any measures of the angle at which the source is located. Moreover, array-based angle sensitive designs become more accurate by increasing the grid size or miniaturizing the pixels, both of which can add to the fabrication and assembly costs of the device. The proposed device avoids the design and structural complexities of the previously reported angle sensitive sensors while quantifying the changes in the perceived incidence angle of a photon in the LWIR regime.

1.2.1. Thesis Outline

Below is a brief introduction to each of the chapters comprising the thesis work as well as a summary of each chapter's contribution to the work.

Chapter 1 provides the introductory and background information necessary for the reader to better understand and appreciate the motivation behind the project. It also includes the state of the art techniques for infrared sensing and the underlying working principles of an infrared detector.

Chapter 2 provides the theoretical and background information necessary for the reader to better understand the scientific principles exploited in the course of the project as well as a brief review of the transition metal oxides and their characteristics along with grounds for the material of choice.

Chapter 3 discusses the design characteristics and principles of operation of the proposed device as well as the estimated noise and parasitic processes that could impede the device's functionality. Thermal energy transfer models are also included in the chapter to justify the design parameters proposed for the device fabrication.

Chapter 4 describes the synthesis and deposition methodologies used to fabricate an IR sensitive thermal sensing thin film. A full review of the sense material's structural, morphological and electronic properties are also included in the chapter.

Chapter 5 describes the fabrication process flow of the proposed device along with a brief review of the micro-fabrication techniques necessary to elaborate the work presented.

Chapter 6 presents full characterization of the fabricated devices regarding the thermal IR response and angular detection.

Chapter 7 concludes with a discussion of future enhancements to the proposed design of the device to enable higher degree of sensitivity and functionality.

Chapter 2. Infrared sensing: Theory and Background

This chapter provides a brief discussion of the general physical principles of an IR sensor including wave-matter interaction and black body radiation.

2.1. Electromagnetic Radiation Interaction with Materials

At steady state, an electromagnetic (EM) wave can be described in terms of its electric field components as in the following form:

$$\frac{\partial^2}{\partial x^2} \tilde{E} + \frac{\partial^2}{\partial y^2} \tilde{E} + \frac{\partial^2}{\partial z^2} \tilde{E} = -K_0^2 \tilde{E} \quad (1)$$

Where \tilde{E} is the phasor transform of the electric field and K_0 is the real valued propagation constant. For propagation in rectangular coordinates and the assumption of zero field propagation in x and y directions, equation (1) simplifies to a second order ordinary differential equation of the form:

$$\frac{\partial^2}{\partial z^2} \tilde{E} = -K_0^2 \tilde{E} \quad (2)$$

which has a set of solutions in the following form:

$$E(z, t) = Re\{E_{01} e^{j(\omega t + z)} + E_{02} e^{j(\omega t - K_0 z)}\} \quad (3)$$

Therefore, with arbitrary choice of direction (left propagating or right propagating) the incident EM wave is described as in the following:

$$E(z, t) = Re\{E_{02} e^{j(\omega t - K_0 z)}\} = E_{02} \cos(\omega t - K_0 z) \quad (4)$$

Equation (4) however shows a real-valued wavenumber which corresponds to a lossless propagation of the plane EM waves [41], [42]. The interaction of the plane EM wave and detector results in a complex wavenumber, for which the real component corresponds to the preserved portion of the wave's energy and the complex component describes the

portion absorbed by the detector [11], [41], [42]. The wavenumber in equation (4) therefore becomes of the following form:

$$\begin{aligned}\tilde{K} &= K_0\sqrt{\varepsilon_c\mu} \\ \varepsilon_c &= \varepsilon' - j\varepsilon''\end{aligned}\tag{5}$$

The absorbed wave energy results in an exciton (electron-hole pair) generation that forms the photocurrent in a photoelectric medium or amplification of the molecular vibrational modes that lead to generation of heat in a lossy and isotropic thermoelectric medium [41], [42]. In the equation above \tilde{K} is the complex wavenumber, μ is the medium's permeability, ε_c is the complex permittivity, \tilde{E} is the phasor transform of the wave's electric field, ω is the angular frequency of the propagating wave and σ is the medium's conductivity. The wave-matter interaction can be described through the following expression [41]:

$$E(z, t) = Re\{E_{0_2}e^{j(\omega t - bz)}\} = E_{0_2}\cos(\omega t - bz)e^{-az}\tag{6}$$

where a and b are the attenuation and the propagation constants respectively. The interaction as described by equation (6) is schematically shown in figure below (Figure 2-1).

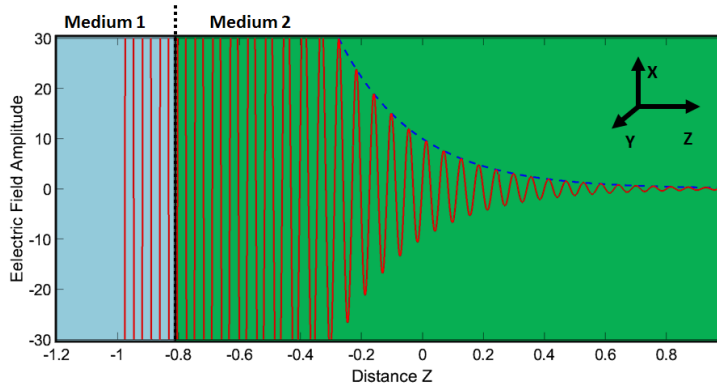


Figure 2- 1 Electromagnetic field decay as a result of wave-matter interaction

2.2. Black Body Radiation and Radiometric Models

An infrared source is generally modeled as a black body radiator that emits infrared photons. The radiation of a black body is a non-linear function of the wavelength and temperature (figure 2-2) where according to Rayleigh law for radiative modes with Planck's modifications has the formalism presented as [13], [15], [42], [43]:

$$u(\lambda) = \frac{8\pi c}{\left(e^{\frac{hc}{\lambda k_B T}} - 1\right) \lambda^5} \quad (7)$$

where, $u(\lambda)$ is the radiation profile, c is the speed of light in vacuum, λ is the emitted wavelength, h is the Planck's constant, k_B is the Boltzmann constant and T is the absolute temperature of the radiating body in degrees Kelvin. The black body radiation assumption is a practical assumption, if the majority of the incident EM radiation on the IR source is absorbed ($\varepsilon_{source} \approx 0.99$) in other words in order to be a good emitter the material used as an IR source must be a good absorber at a given wavelength [9], [11], [13]. Taking into account the Kirchhoff's law of thermal radiation and the conservation of energy principle, at a given wavelength, the following statement can be made regarding an IR source [13], [14]:

$$\varepsilon(\lambda) + \rho(\lambda) + \tau(\lambda) = \varepsilon(\lambda) \equiv A(\lambda) \quad (8)$$

where $\varepsilon(\lambda)$ is the material's emissivity (or $A(\lambda)$, material's absorbance), $\rho(\lambda)$ is the material's reflection and $\tau(\lambda)$ is the material's transmittance. The majority of actual IR sources are opaque material hence have very small (close to zero) transmittance. Ergo equation (8) simplifies to the following form:

$$\varepsilon(\lambda) + \rho(\lambda) = \varepsilon(\lambda) \equiv A(\lambda) \quad (9)$$

Although most IR sources emit less than predicted by Planck's thermal radiation law (there is no $\varepsilon=1$), the calculated spectral response of a black body radiator from Planck's formalism gives an accurate measure of the peak wavelength that is emitted from the IR source. This allows for choice of the sensing material and mechanisms that are tuned to possess peak sensitivity at the predicted peak wavelength for IR detection systems [13], [21], [42].

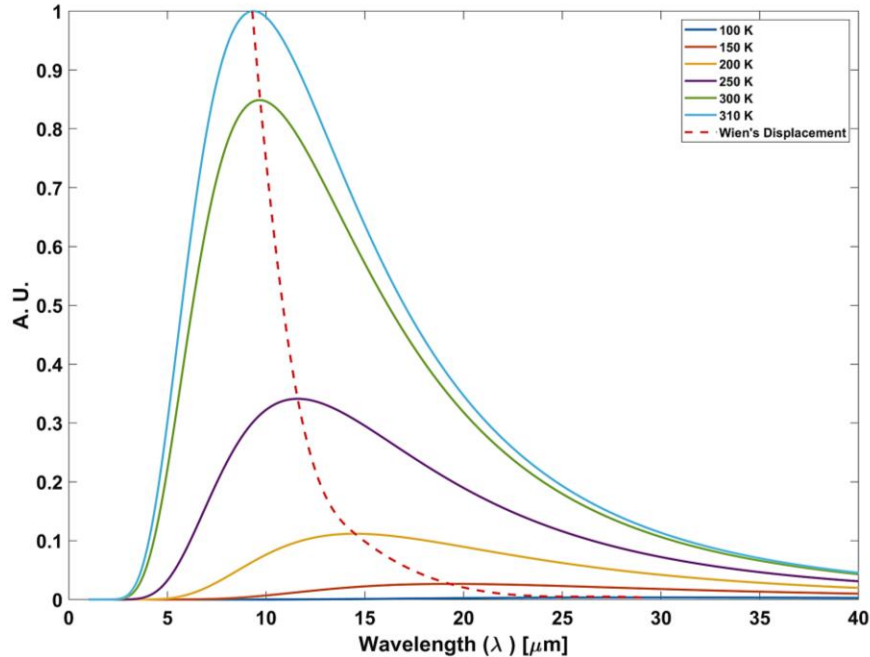


Figure 2- 2 Planck's Spectral Power Distribution of a Black Body Radiator for bodies 100, 150, 200, 250 and 300 K. The red dashed line signifies the peak wavelength occurrence according to Wien's displacement law.

2.3. Infrared sensing

Infrared sources emit infrared radiation as a result of their temperature (black body radiation) [13], [15], [21], [44]. Thermal radiation has a non-uniform distribution across the electromagnetic spectrum with a peak wavelength that is correlated to the temperature of the source that is emitting infrared photons. The main challenges associated with infrared detection are directly related to the low energy of the infrared photons. The low frequency of infrared photons allows for their interaction with many materials regardless of their phase. Atmospheric attenuation of infrared radiation is high compared to the near infrared and visible portions of the spectrum. As a result, infrared detection systems are not practical for use with distances longer than a few hundred meters. However, the existence of spectral windows wherein the atmosphere is transparent to the IR radiation has made it possible for the optical coupling of the incident IR photon with the detector's material over larger distances within a certain group of spectral bands (Figure 2-3). Detection efficiency within these spectral bands to a large extent depends on the geographical characteristics and meteorological conditions under which the detector setup operates [9], [13], [14].

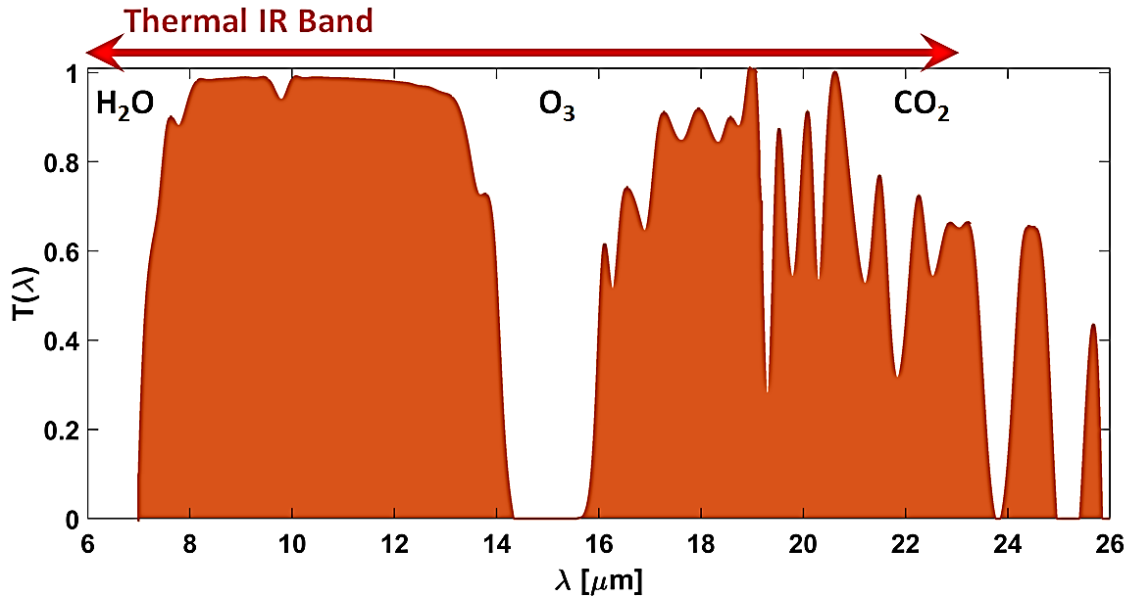


Figure 2- 3 Transmitted thermal IR spectral bands of the atmospheric window and the corresponding absorbing atmospheric molecules in the far infrared region of the EM spectrum

2.3.1. Types of Infrared Detectors

Based on their detection mechanism which is indicative of the detector's interaction with IR radiation and the generated response, IR detectors are categorized under two main groups: 1) Photon Detectors and 2) Thermal Detectors

Photon Detectors

Photon detectors rely on the electrical properties of semiconductor material. The use of this class of optical detectors, similar to the advent of semiconductor age is more recent than thermal detectors. The signal amplitude in photon detectors is proportional to the photon flux perceived by the detector. Depending on different mechanisms of operation, photon detectors can be classified into four different categories: 1) Photochemical detectors, 2) External photoemission detectors, 3) Avalanche photodiode detectors and 4) Semiconductor photoelectric detectors. In the first group, the incident photon causes an ionization of the sensing material and the resulting ions are reduced and solidify to register a physical change in the sensing material [13], [14]. This mechanism is often used in imagery and photographic systems. The second group implements a high voltage between two electrodes kept in vacuum, where one (the cathode) is subject to photonic interaction. As a result of photon absorption, electrons are ejected and accelerated towards the anode under the influence of the potential difference (figure 2-4). This way

the higher the photon flux, the more electron ejection and the higher the induced photocurrent. Avalanche photodiode detectors use a particular threshold for the breakdown of the pn junction in reverse bias mode, whereby, a photon with enough energy to push the junction into breakdown mode induces a sudden current surge in the system. The mechanism for this group of photon detectors implies that the photon's energy and wavelength to be above a certain threshold and that of the amount needed to break down the junction barrier [13], [14], [21]. It is therefore limited by a relatively high frequency or short detection wavelength. This imposes a high performance barrier on this class of detectors since the majority of metals and semiconductors have high work functions that translate into cut-off wavelengths in the order of 250 nm to 350 nm which are closer to blue end of the spectrum rather than red. Finally, the fourth group is the state of the art pn junction where in, the photon-matter interaction generates excess charge carriers that induce a photocurrent in the biased detector material. In this group, the interaction between the incident IR photon and the material's electronic structure triggers an excitonic event where electrons are promoted from the material's valence band into the conduction band hence a photocurrent is generated which is proportional to the photon flux density that is interacting with the material. Given that the IR photon's energy must surpass the material's bandgap, in order for the photocurrent generation, the larger the bandgap of the sensing material, the higher the energy of the photon that can be detected by the material or the shorter its wavelength. Some of the most frequently used semiconductor materials in IR detection are silicon and germanium with the detection wavelength cut-offs at 1.11 μm and 1.8 μm respectively [13], [15], [21]. These wavelengths only cover a limited range of the IR portion of the spectrum, hence, in order to extend the spectral responsivity of semiconductor based IR detectors, multi-component semiconducting materials have been made to create narrow energy states in the otherwise forbidden bandgap of pure semiconductors such as silicon and germanium [13], [45], [46]. Some common examples of such material are binary compounds such as indium antimonide (InSb) and ternary mixtures such as cadmium mercury telluride (CdHgTe) for which the responsivity cut-off is at 7.7 μm and 14 μm respectively. Although photonic detectors have a much faster response time along with much higher energy conversion efficiency, there are manufacturing difficulties associated with them. As the material's complexity increases, the tuning of the different elements involved becomes stricter in such way that in order to get optimum response, material parameters such as the purity of the base semiconductor phase and the uniformity of the additives must be near to excellent for the device to be

functional [2], [13], [46], [47]. The latter requires advanced processing which adds up to both the detector's fabrication time and overall costs.

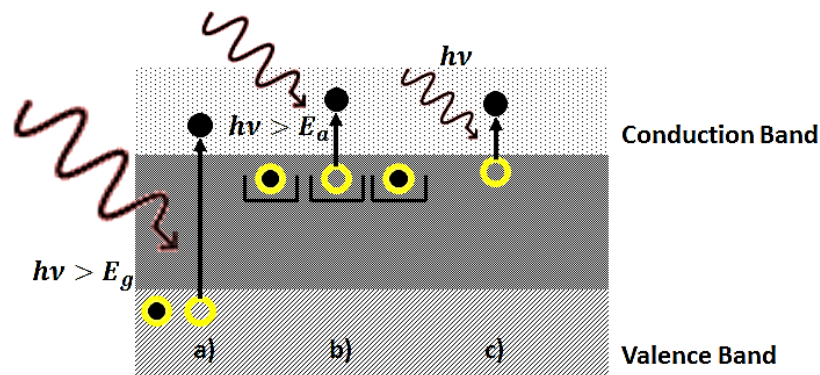


Figure 2- 4 Principle of operation of a photon detector where the incident photon induces a) intrinsic absorption b) extrinsic absorption and c) free carrier absorption

Thermal Detectors

Thermal detectors are sensitive to the energy that is carried by the incident IR radiation. The absorption of IR photons, induces changes in the detector material's properties such as expansion, electromotive force induction as well as electrical resistance and charge polarization [11], [13], [14]. Thermal detectors are cheap and easy to make and were the first type of IR detectors that were made. The main limitation associated with this class of detectors is the response time as to the fact the underlying mechanisms of change do not offer efficient energy transformation between the incident photon and the sensing material.

On the other hand, due to their large spectral response, room temperature operation, material stability in higher temperatures, high signal to noise ratio and finally lower fabrication costs compared to photonic devices, thermal IR detectors have gained a wide range of application. Given that all different forms of thermal detectors rely on the conversion of the incident IR radiation to heat, the fundamental governing principle of a thermal detector is modeled with heat flow equation to describe the temperature increase as a result of the incident radiation [11], [13], [44]. Although there are three main mechanisms by which the induced heat can flow across the target material (radiation, convection and conduction), conduction is the main design consideration made in the structure of a thermoelectric IR detector. Since the flow of heat from the sensitive area to the surrounding thermal elements can reduce the degree of the induced change in the

sensor, IR sensitive structures are designed in a way to minimize the conduction pathways for the generated heat away from the surface of the IR sensitive material (figure 2-5) [13].

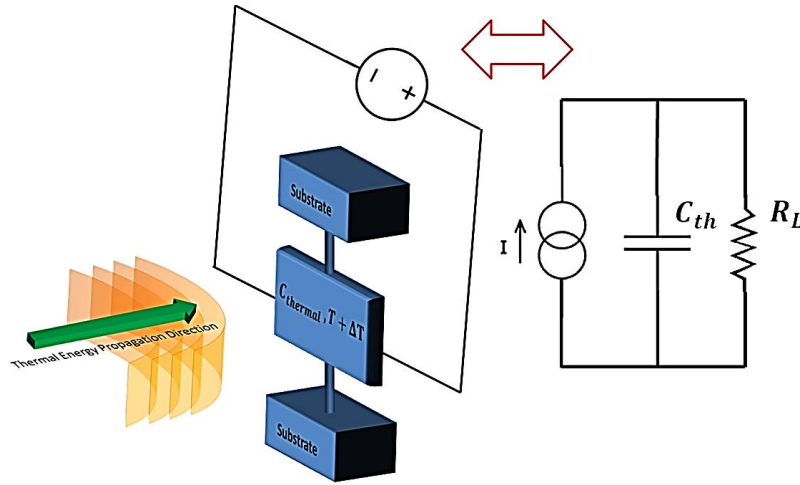


Figure 2- 5 Principle of operation of a thermal IR detector and its equivalent circuit (simplified)

A simple way to model thermal IR detectors is through the definition of the two quantities thermal (heat) capacity of the thermo-sensitive material and the overall thermal conductance of the physical contact between the material and the rest of the supporting structures. For a material with a defined thermal capacity C_{th} and the overall thermal conductance that exists between the material and the rest of the device G the first order heat conduction equation is of the form [11], [13], [14]:

$$C \frac{\partial(\Delta T)}{\partial t} + G(\Delta T) = \eta P_0 e^{j\omega t} \quad (10)$$

where P_0 , η and ΔT are the amplitude of the incident IR radiation on the thermoelectric material, the absorbed portion of the incident radiation and induced change of temperature as a result of absorption of the incident IR radiation by the material respectively. The solution to the above differential equation in the case when the frequency of incident IR modulation (the $e^{j\omega t}$ term in equation 10) is low or non-existent ($\omega t \ll 1$) simplifies to the following form, where the induced temperature change ΔT , becomes linearly correlated to the absorbed infrared radiative power and reciprocally correlated with the thermal conductance between the sensing material (region or area) and the rest of the sensing structure [13], [15]:

$$\Delta T = \frac{\eta P_0}{G} \quad (11)$$

The thermal response time of the system is also defined as the ratio between the thermal capacity of the thermoelectric material and the total thermal conductance:

$$\tau = \frac{C_{th}}{G} \quad (12)$$

Based on the energy conversion mechanism, thermal IR detectors are classified into two main groups: 1) Thermocouples and Thermopiles and 2) Thermo-electric Detectors. Thermocouples make use of thermal electro-mechanical effects such as the Thomson Effect, the Peltier Effect and the Seebeck effect. In such system, in the absence of Joule's heating, the potential difference across the circuit interface will solely depend on the temperature difference in which the circuit is placed and the type of the materials that comprise the circuit. Thermopiles (thermocouples put in series) employ this mechanism to detect minor changes in a medium's temperature via adding a heat probe to the Seebeck measurement system [11], [13], [48]. Thermopile IR detectors therefore comprise of an absorber layer that is thermally insulated from the rest of the sensor's structure whereby the different metals with different Peltier coefficients form a junction on the surface of the absorbing layer, where they detect the changes in the medium's temperature as a result of the incident IR radiation absorption. The thermoelectric signal for such a system is defined as in the following expression [13], [48]:

$$V_S = N(S_1 - S_2)\Delta T \quad (13)$$

where V_S is the generated potential as a result of the detector's heating, S_1 and S_2 are the Seebeck coefficients of the two metals that form the junction and N is the number of thermocouple elements put in series to form the thermopile (figure 2-6).

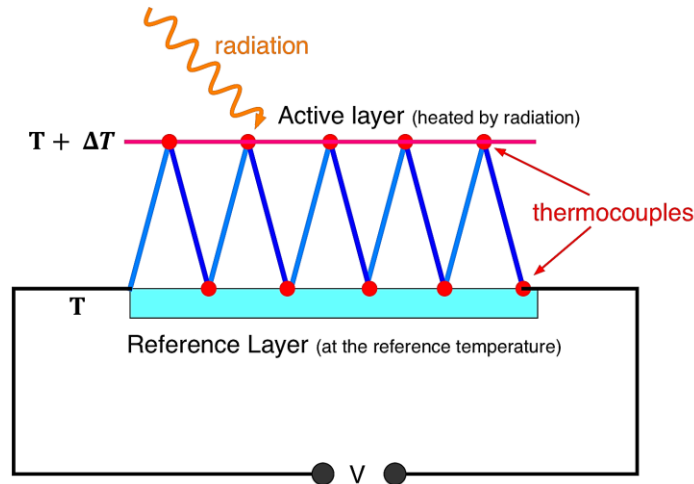


Figure 2- 6 Schematic of a thermopile comprised of thermocouple elements in series

Given the diversity of thermal IR sensing industry there are other implemented techniques which, depending on the response time of the material in use, the type of interaction between the incident IR radiation and the sensing material as well as the detectable spectrum offer comparable or selective advantages over thermo-couple and thermo-pile IR detectors. Some of these techniques are introduced below.

Tunneling Thermal Infrared Detectors

The incident IR radiation in these detectors is converted to heat by an absorber layer and then conducted to a thermometer where it can be read and interpreted. In this setup the sensitivity is dependent upon the absorbing layer's efficiency in absorbing the incident IR and the resolution at which the thermometer can detect changes in the materials temperature. In recent years there has been a wide body of industrial research focused on miniaturization of the thermometer unit in order to manufacture chip sized, high accuracy tunneling IR detectors [13], [14], [48]. Modern tunneling IR detectors use other physical changes other than solid state thermal effects to increase the resolution of the thermometer component such as thermal expansion of gases that allow induced changes as large as 0.3% / K of the heated target gas when coming in contact with the conducted heat that comes from the absorber layer. The designated range for tunneling thermal IR detectors covers the mid to far infrared (3 μm to 100 μm). These detectors suffer from noise sources common to all thermal IR detectors such as Johnson-Nyquist thermal noise and signal amplification noise for small signals in the system, as well as fluctuations in the absorption process by the absorber layer and in the temperature of the gas. Overall,

tunneling heat thermal IR detectors show good scalability and miniaturization yet offer little noise equivalent power compared to other devices [48].

Micro-resonating Thermal IR Detectors

Although many of the manufactured quartz resonators are used in traditional electronics applications such as oscillators and analog filters, their precision in frequency control makes them a choice for thermal IR detection applications as well. While offering high signal to noise ratios, quartz resonators' fundamental resonance mode frequencies have multiple temperature dependent factors such as in-bound propagated wave velocity, resonator thickness, resonator modulus of elasticity and resonator density. [48]. The mechanism by which these detectors detect IR radiation is similar to other thermal IR detectors in that the incident radiation induces a change in the resonating material's temperature. However, unlike the previous examples, the correlated parameter of change is the micro-resonator's fractional frequency, or its deviation from its nominal mode which is known to vary monotonically with the material's temperature (Figure 2-7). Typically, quartz fractional frequency changes monotonically with a slope of 10^{-4} /K and hence such devices can resolve changes in the temperature in orders of nK [48], [49]. However the specific performance depends on the particular sensor design and is typically determined parameters such as the temperature coefficient of frequency, the micro-resonator's spectral noise level, the thermal conductance between the resonator and the support structure, and the resonating material's IR absorbance and resonator's cut direction with respect to its crystalline structure. Although accurate, micro-resonating thermal IR detectors have challenges associated with both the fabrication's precision and IR absorbance of the quartz which is generally above 50% in the long wavelength IR portion of the spectrum (9 μm – 26 μm).

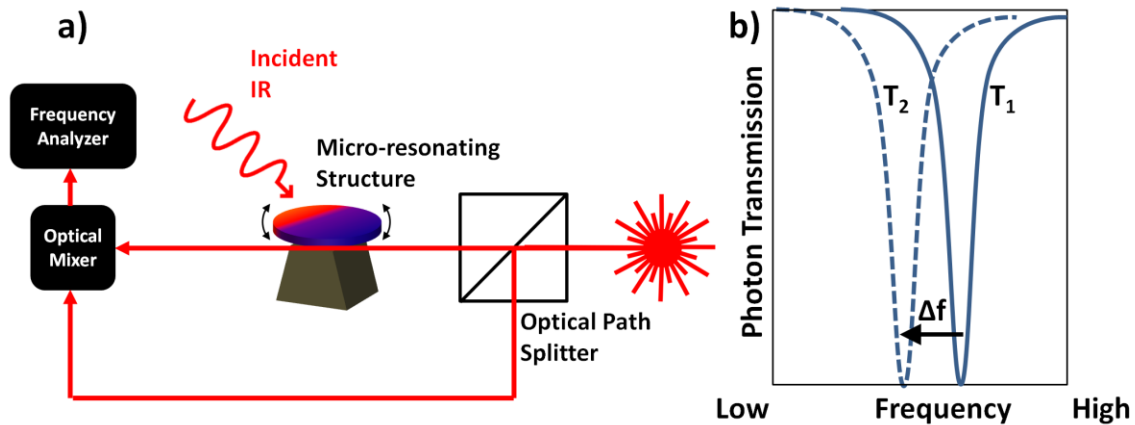


Figure 2- 7 Schematic depiction of a) micro-resonator IR detector whereby b) the resonant frequency of the micro-resonator undergoes a shift as a result of heating of resonating structure due to IR absorption

Thermoelectric Detectors

Thermo-electric IR detection systems, as indicated by their name, measure the variations of the sensing material's electrical properties as a result of the absorption of the IR radiant flux by the material. The detection system can be characterized by two main parameters, namely, thermal impedance that describes the conversion of the radiative flux into heat by the system's absorber and thermal responsivity that quantifies the amount of change that is induced in the sensing material as a result of the generated heat due to the incident IR radiation. Thermal responsivity is usually considered to be the main figure of merit of a thermo-electric IR detector and is expressed in signal units per unit temperature [11], [48].

2.3.2. Thermal Infrared Detectors

As a thermodynamic system, a thermal IR sensor is subject to temperature fluctuations noise which arises from the statistical nature of heat exchange processes between the sensor and its surrounding environment. Under the assumption of uniform spectral distribution (frequency independence), the detector's accuracy is then defined via the temperature resolution or the minimum temperature difference it can resolve over the temperature fluctuations that occur as a result of the ongoing thermal exchange processes. The latter is then defined in terms of the mean thermal power exchange between the IR detector and the environment [11], [13], [48]:

$$\overline{P_{sys}^2} = 4k_B T^2 GB \quad (14)$$

where $\overline{P_{sys}^2}$ is the mean squared power exchanged between the sensor and the ambient environment as a result of the thermal fluctuations, k_B is the Boltzmann constant, G , is the detector's thermal conductance and B is the measurement bandwidth. For a noise limited system the detectivity (D^*) is of the following form:

$$D^* = \frac{\sqrt{A_{sensor}B}}{NEP} \quad (15)$$

Hence, and considering the absorbed fraction (η) of the incident radiation as the signal power and the mean power fluctuation of the system as noise power, the detectivity of a noise limited thermal IR detector takes the form of:

$$D^* = \sqrt{\frac{\eta^2 A_{sensor}}{4k_B T^2 G}} \quad (16)$$

Detectivity defines the lower limit of the detectable radiant power by the thermal detector that is the systems noise equivalent power (NEP), therefore, the minimum temperature difference that can be detected by the system or the noise equivalent temperature difference (NETD) is given by [13], [48]:

$$NETD = \frac{8F^2 T \sqrt{k_B B G}}{\eta \tau_0 A_{sensor} \left(\frac{\Delta P}{\Delta T}\right)_{\lambda_1 - \lambda_2}} \quad (17)$$

where F , τ_0 , $\left(\frac{\Delta P}{\Delta T}\right)_{\lambda_1 - \lambda_2}$ and A_{sensor} are the detectors focal ratio, the detector's transmittance, spectral change in the radiated power per unit area and detectors sensing area respectively. The above relationships determine that for constant background temperature (case when the detector and the surrounding are at thermal equilibrium), the minimum detectable temperature change as a result of IR incidence on the sensing area of a thermal IR detector is directly correlated to the thermal conductance of the IR sensing structure. Therefore as the thermal conductance increases, the systems NETD also increases hence the systems power to resolve small temperature changes decreases. Aside from the mean thermal fluctuation noise power, thermal detectors are limited by another noise mechanism known as the Johnson noise. This noise mechanism impairs the thermally generated signal especially when the preferred method of detection relies on the sensing material's electrical resistance. Johnson noise is a spectrally independent thermal noise process that arises from the motion of electrons across a resistor.

2.3.3. Pyroelectric versus Bolometric Detectors

Of all the common thermo-electric IR detectors, thermoelectric devices offer simpler sensing mechanism that allows for the detection of DC infrared radiation from the background while offering low voltage noise. There are two different classes of thermoelectric detectors which rely on the same detection mechanism for IR detection yet make use of two different types of materials. One class uses materials known as pyroelectric whereby spontaneous changes in the net charge polarization, trigger surface charge generation in the sensing material [10], [13], [50]. The magnitude of the generated surface charge is then used as the sense signal to detect IR radiation (figure 2-8).

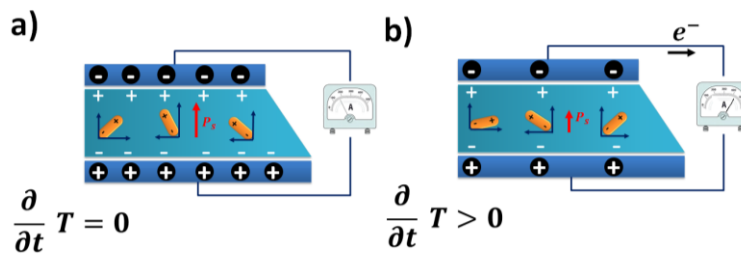


Figure 2- 8 Pyroelectric heat detection: a) No change in total dipole moment hence no current flows through the circuit b) a positive change in the temperature rearranges the surface-bound charges and an electric current flows

Pyro-electric based detectors offer a wide range of spectral responsivity as well as sensitivity to oscillating sources. Due to the mechanism of sensing which relies on a time-dependent electronic charge shift in the medium, pyro-electric detectors have no success in DC signal detection. These detectors are more complex to make and are subject to vibrational noises that impede the response of a pyro-electric device over long exposure times [51]. As a result, thermo-electric detectors are the more popular choice among thermal IR detectors. Bolometric materials are thermal resistors or thermistors that show significant variation of their electrical resistance as a function of the material's temperature change. Thermistors are described via the thermoelectric effect which is present in both conductors (metals and transition metals) and semiconductors (metal-oxides and transition metal oxides). By virtue of the intended application, bolometric materials are those with small thermal capacity and a large temperature coefficient of resistance (TCR) indicating noticeable induced changes as a result of minimal heating of the material [11], [48]. Theoretically the majority of non-magnetic crystalline solids show a temperature dependence in their electrical resistivity which mainly arises from the electron-phonon interactions [13], [51], [52]. Such interactions introduce a temperature dependent

resistivity component that attributes the temperature independent portion of the resistivity to the lattice defects and the temperature dependent portion to the charge carrier scattering due to interaction with acoustic phonons. The history of use of bolometric materials in detectors traces back to the 1800s where American astronomer P. Langley devised a bolometric detector for solar observation using blackened platinum as an absorber layer. The result was a thermal detector that was more sensitive than the state of the art thermocouples. Despite the diversity in methodology for IR thermal detection systems, bolometric devices have been among the most favored ones ever since. There are different types of bolometric materials that are being used as IR sensors [10], [13]:

1) Metallic bolometric materials: operate at room temperature and made from transition metals such as platinum and nickel or metalloids such as bismuth and antimony. Although these bolometric materials are durable and can operate in long range infrared region (this work's region of interest) they have very low TCR ($\sim 0.004\%$ K) hence low detectivity.

2) Semiconductor bolometric materials: perform optimally at sub-zero temperatures and require miniaturized dimensions for the active material due to thermal exchange minimization. They have higher TCR ($>4\%$ K⁻¹) but are prone to thermal noise more than the other two categories of bolometric materials.

3) Sintered mixes of semiconducting oxides: operate at room temperature but require post deposition processing to become somewhat crystalline in order to behave as semiconductor. They have high TCR ($\sim 2-4\%$ K⁻¹) but do not behave ohmic throughout the entire measurement span.

In metals the effect manifests itself as a positive scalar coefficient that induces a linear increase in the electrical resistance as a result of an increase in the material's temperature. The predominant factor, due to which the material's resistance to current flow arises, is the average number of collisions between the electron gas and the positive ion lattice. In general form the drift velocity is given by the following equation:

$$V_d = -\frac{e\tau}{m_e} \vec{E} \quad (18)$$

Where V_d is the electron gas drift velocity, τ is the mean time between electron ion collision, e is the electric charge of an electron, m_e is the mass of an electron and \vec{E} is the electric field acting on the metal. Therefore, as a result of an increase in temperature, an increase in the drift velocity will cause the electrons to move around faster and hence τ (the mean time between electron collisions) become smaller [13], [52]. The relationship between the metal's temperature and the mean time between collisions is as follows:

$$\tau \propto \frac{1}{\sqrt{T}} \quad (19)$$

Metal bolometers can operate at room temperature yet have very low TCR in thin film form ($\sim 0.004\% \text{ K}^{-1}$) and longer response times in the order of 10s of milliseconds which makes them unsuitable for real time applications.

Semiconductor bolometers are among the most developed types of thermal detectors in the field of sub-millimeter infrared sensing. They are mainly designed for lower incidence levels and due to the nature of the active (sensing) material, have a much faster response time compared to the metallic bolometers. Like other bolometric materials, semiconductor bolometers respond to the IR induced change of their temperature with a consequent change in their electrical resistance. Under the assumption of temperature independent charge carrier mobility, the temperature dependence of a semiconductor is defined via the following relationship [13]:

$$R = R_0 T^{-\frac{3}{2}} e^{\frac{\beta_c}{T}} \quad (20)$$

Where R is the material's electrical resistance, R_0 is the material's resistance at infinitely large temperatures, β_c is the material's temperature constant (a characteristic of the semiconductor material) and T is the material's temperature. For optimum operation, these detectors must perform in very low temperatures to reduce the amount of thermal noise associated with thermal detection systems [13], [48]. However, at very low temperatures ($< 5 \text{ K}$), the semiconductor material must be heavily doped to maintain thermal-excitation based conductivity [13]. Semiconductor bolometers are commonly put in series with larger load resistances to lower the amount of Johnson (thermal) noise in the system. Examples of cooled semiconductor IR bolometers are gallium-doped silicon detectors and germanium detectors. P-type germanium detectors have been reported to have an

optimum efficiency when their operation is insulated from background thermal radiation and yet are equally affected by thermal and photon noise [13], [52]. In the absence of current induced heating, response time of a semiconductor bolometer only depends on dissipated power and temperature coefficient of resistance calculated from equation (21):

$$\tau_E = \frac{C}{G - \alpha(T)P_I} \quad (21)$$

where τ_E , C , G , $\alpha(T)$ and P_I are the device response time, specific heat, thermal conductance, temperature coefficient of resistance of the semiconductor material and dissipated power in the system respectively. Semiconductor bolometers have shown response times in the order 400 ms which makes them more suitable a choice for real time applications.

The third and most favorable group of bolometric materials is the sintered mixed-phase semiconductor oxides. This material category is usually a mixture of poly-crystallized metal oxides that offer relatively high changes in the electrical resistance as a result of minor changes in the temperature. Their high temperature coefficients of resistance (2 – 4% K⁻¹) are dependent on the material bandgap, defect and/or impurity density, crystallinity as well as the dominant bulk conduction mechanism [13], [53]. The temperature coefficient of resistance in this category of materials is proportional to the reciprocal of the material's temperature squared. Being a large bandgap semiconductor, mixed-phase oxides have room temperature resistivity in the order of 250 to 2500 Ω cm which introduces large magnitudes of thermal noise into the detection system [13], [54]. Since sintering allows for different ratio mixtures of semiconducting oxides, it also implies potentially that the sensing material can be tuned to respond to different portions of the IR spectra via absorption of the radiation more efficiently in that region. The room temperature characteristic of the sintered semiconducting oxides allows for detector designs that require no external cooling mechanisms hence reduce the end product's bulkiness and fabrication costs. This class of bolometric materials has little thermal capacity at room temperature, hence in order to improve the device sensitivity towards the impinging IR radiation, there should be minimal thermal conduction pathways that could guide the induced heat away from the material.

2.4. Transition Metal Oxides in Infrared Sensing

Bolometric materials are generally categorized as mid-large bandgap dielectrics which possess semiconducting properties such as a negative TCR. Therefore it is crucial to gain insight into the conduction mechanisms that govern the carrier transport across such materials when implemented as IR sensing layers in a detection system. There are two major conduction mechanisms for dielectric materials: 1) electrode limited conduction and 2) bulk limited conduction whereby the first one depends on the electrical properties of the metal (electrode) and semiconductor's interface and the second one depends on the electrical properties of the dielectric itself [54], [55]. In the case of transition metal oxides with large bandgaps (2 – 5eV), the conduction mechanisms are more likely to be trap-associated whereby charge carriers travel between defect energy states via bulk-limited conduction mechanisms. There are different bulk-limited conduction mechanisms such as 1) Poole-Frenkel Emission, 2) Hopping Conduction, 3) Ohmic conduction, 4) Space-charge limited conduction, 5) Ionic conduction and 6) Grain boundary limited conduction. Of the aforementioned mechanisms, hopping conduction is considered to be the dominant transport mechanism in disordered solids such as polycrystalline thin films grown for IR sensing.

Transition metal oxides (TMOs) have played an important role in advancing fields such as microelectronics, optoelectronics, photonics and omnipurpose sensing systems [54], [56], [57]. In case of IR detectors, use of transition metals allow for creation of various oxide materials that extend the spectral responsivity range of the device into larger portions of the incident IR field [56]. Due to their partially filled d orbitals, transition metal oxides possess a variety of distinguished characteristics that are both reversible and reproducible [54]. In terms of oxidation states, transition metal oxides can form different stable oxides while traversing through a range of meta-stable phases in response to external triggers such as heat, electrical current and electromagnetic radiation [54], [56], [58]. Aside from exhibiting a range of electronic properties, transition metal oxides also demonstrate a high degree of thermal and compositional stability at room temperature and above, which makes them suitable candidates for IR sensing applications in harsh environments. TMOs also offer cost effective fabrication routes when used as the active layer in IR sensors and can be synthesized into a variety of different forms such as ceramics, thick and thin films with a reasonable degree of surface conformality. Given that

the material can be prepared under different synthesis conditions, TMOs offer competitive solutions for CMOS compatible processes [54], [56], [58].

2.4.1. Vanadium Oxide properties

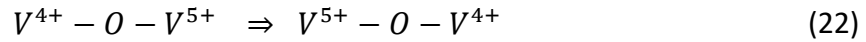
In the case of TMOs (insulating and semiconducting alike), thermal conductance is to a larger degree due to acoustic phonons travelling through the lattice structure of the material, and to a smaller degree accounted for by charge carriers [54], [56]. Since in thermal IR sensors, the smaller the thermal conductance the larger the change in the material temperature due to the incident IR, it is desirable to choose types of material that have lower degrees of thermal conduction as a result of their structural properties. At room temperature and above, phonon-induced thermal conductance becomes independent of the materials temperature and only depends on the phonon's mean free path through the material. Polycrystallinity of TMOs therefore favours the IR induced thermal sensing via hindering the thermal conductance of the IR sensing layer through introduction of larger grain boundary distribution [54], [58]. Among TMOs, vanadium demonstrates many desirable physical effects that are due to its electronic configuration in the form of $[Ar]3d^34s^2$ (providing a 3d orbital mixing in chemical bonds it forms) that leads to its multivalent characteristic [59]. As a result, formation of different ionic states of vanadium such as V^{2+} , V^{3+} , V^{4+} , and V^{5+} gives rise to a variety of vanadium oxides with different structural and electronic properties. [59]. Since occurring predominantly in one isotope (^{51}V), vanadium compounds have less isotopic disorder and offer both stable and reproducible properties [56], [58]. Although forming a large variety of oxides due to its multiple oxidation states, only a few oxides of vanadium have the necessary room temperature stability to become useful in microelectronic and sensor applications. Of these stable oxides VO_2 and V_2O_5 have been more widely studied for their metal-insulator transition (MIT) and electrochromic characteristic respectively. Classically, IR detection for wavelengths in the near infrared (up to 1 μm) and mid infrared (up to 10 μm) has been achieved via photoconduction through photonic excitation of excitonic pairs using composite semiconducting materials such indium antimonide (InSb) and mercury-cadmium telluride ($Hg_xCd_{1-x}Te$) [13], [48]. However, such detectors required cryogenic cooling (due to high intrinsic carrier concentration at RT) to avoid thermally induced noise signals. With the introduction of microbolometry, Honeywell began work that employed various materials as thermal infrared sensing layers placed on thermally insulated

structures. The advancements in silicon micromachining allowed for development of IR sensitive pixels which were thermally insulated through thin structural supports and silicon nitride protective layers. The initial trials used platinum and nickel-iron alloys as the sensing material. Despite the thermal IR sensing functionality, these materials suffered from low TCR values ($0.0018 - 0.0023 \text{ K}^{-1}$) and low resistivity. Low resistance and high $1/f$ noise hindered the noise equivalent temperature difference (NETD), a measure of signal to noise ratio, for these detectors. As a result, oxides of vanadium were then employed as the sensing layers in the microbolometer arrays [13]. Despite its higher (negative) TCR values, VO_2 could not provide reliable measurements near and about its metal-insulator (MIT) transition point, hence its employment would require thermal control to avoid undergoing MIT during IR measurements. Consequently, researchers shifted their focus to other oxidation states of vanadium such as V_2O_3 and V_2O_5 . Between the two, V_2O_5 however gained more popularity due to its chemical stability at higher temperatures and higher TCR values compared to V_2O_3 .

2.4.2. Vanadium Oxide Thin Films for Room Temperature IR Sensing

The only known crystalline form of V_2O_5 is orthorhombic with layers of in-plane VO_5 pyramids stacked in the ab crystalline plane (in the $[001]$ plane direction). The planes are held together by Van Der Waals bonds which render the material brittle in the out of plane direction. Formation of in-plane long oxygen chains that connect the VO_5 pyramids together however, makes the material quite robust along the in-plane crystalline directions. Vanadium pentoxide is considered to be a high bandgap semiconductor with an average band gap in the order of 2.3-2.4 eV [13], [60], [61]. The bandgap is considered an indirect transition from the oxygen 2p band to the vanadium 2d band. Depending on its formation mechanism, vanadium hosts two different types of cationic centers (V^{4+} and V^{3+}) when forming a crystalline lattice as a result of the ambient in which the oxidation occurs [56], [62], [63]. These cations act as oxygen vacancies or defect states in the materials band structure which allow for the thermally activated hopping conduction mechanism that governs the conduction in transition metal oxides such as vanadium pentoxide. Doubly trapped electrons normally occur in cases where the reaction leading to the formation of vanadium pentoxide are carried out under extremely reducing ambient conditions, whereas in cases where the reactions are carried out under ambient conditions (such as the hydrolysis of the alkoxide based sol into amorphous vanadium pentoxide or sputtering)

singly trapped electrons are the more likely defect state that form across the material. As a result, crystalline vanadium pentoxide is considered to contain V^{4+} as defect states whose concentration depends on the way the samples are prepared. Vanadium pentoxide is modeled as a low mobility transition metal oxide in which, conduction happens via a complex mechanism that is represented with the following formalism [64]:



Equation (22) describes the charge carrier conduction as hopping of the singly trapped electron from one V^{4+} center to the adjacent V^{5+} center and so on and so forth. Thus, in one crystalline domain of vanadium pentoxide, conductivity along any crystalline axis is strongly correlated to the V^{4+} center concentration along that axis which is roughly translated into the average separation between the vanadium cations. Given that the in-plane distances are shorter compared to the out-of-plane inter-atomic separations, there is a higher probability for the charge carriers to conduct across the in-plane directions (a and b) rather than the inter-plane one (c) (figure 2-9).

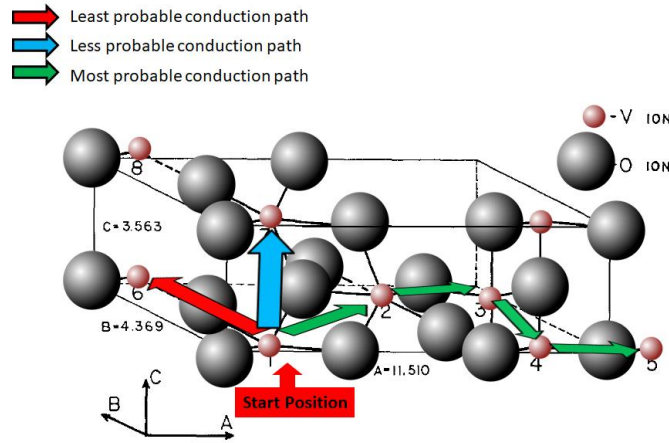


Figure 2-9 Least to most probable conduction pathways in a vanadium pentoxide unit cell for an arbitrary initiation site.

Depending on the deposition method, vanadium pentoxide thin films show different absorption spectra in the infrared regime. Prior investigations have shown that this diversity in the observed IR absorption spectra stems from the crystalline lattice orientation differences rather than structural dissimilarities that exist between the bulk mono crystalline, powder and polycrystalline vanadium pentoxide as a function of different deposition methods [65]. Amid the aforementioned diversity, vanadium pentoxide films have shown up to 15 vibrational modes in the mid and far infrared portion of the spectrum. The reported range for IR vibrational modes of vanadium pentoxide is from 10 μm all the

way to 46 μm . The shorter portion of the vibrational bands is associated with the V-O and V-O-V stretching modes while the longer portion is linked to edge-sharing 3V-O stretching mode [65]. Due to the characteristic narrow mid-far infrared absorption bands, vanadium pentoxide has been a favorable choice for the micro-detector industry [66]–[68]. Moreover and in general, oxides of vanadium have depicted suitable CMOS compatibility properties compared to other proposed bolometric material, given their low processing temperature and convenient room temperature electrical properties. Majority of designs making use of vanadium pentoxide as the infrared sensing layer, are bound to deposition limited mixed oxide phase thin films that are comprised of both vanadium pentoxide and dioxide as a function of the target material's reaction kinetics with oxygen during deposition [66], [69].

2.4.3. Vanadium Oxide Deposition techniques

There have been reports of various deposition methods for vanadium oxide thin films. Depending on the choice of deposition method's throughput and the degree of phase and surface uniformity, each of these methods offer merits that are discussed briefly herein. Of the reported deposition methods for vanadium pentoxide thin films, vacuum based techniques have predominantly been the method of choice for IR sensors. Reactive ion sputtering, pulse laser ablation, ion beam deposition, molecular beam epitaxy and chemical vapour deposition are some of the most commonly used methods for thin film vanadium pentoxide deposition. At large, these methods require use of a cleanroom environment and high precision devices such as physical vapor deposition systems to achieve nanometer thick layers of vanadium pentoxide films on silicon or other substrates [68], [70], [71]. In the case of reactive ion sputtering and ion beam deposition, both techniques yield a reasonable degree of surface uniformity and conformality yet lack the controllability over the resulting film's oxide phase composition. Occurrence of mixed oxide phases in the deposited film increases the chances of MIT transition at temperatures 30 to 40 ° C above room temperature. As earlier mentioned MIT transition can limit the infrared sensor's linear range in active measurement setups. More so, DC magnetron sputtered films have shown less densified film structure which results in lower TCR values. In DC magnetron sputtering there is a trade-off between the deposition rate and thin film conformality [72]. Pulsed laser deposition offers faster deposition rates compared to dc magnetron sputtering and ion beam deposition yet the resulting thin films require post-deposition annealing in order to decrease the percentage of Magnelli phases present in

the final composition. Finally plasma enhanced chemical vapor deposition offers thin film growth at low temperatures while maintaining a good deposition rate and structural order and preferential growth. There are other non-vacuum based deposition methods used to deposit vanadium pentoxide thin films such as spray coating and dip coating. These methods, given that in the majority of the cases do not require cleanroom environment, render the deposition process more economical than the previously mentioned vacuum based deposition techniques. However lack of desired throughput makes them less attractive for industrial applications. Dip coating and spray coating both take advantage of wet chemical synthesis methods such as sol gel synthesis whereby a hydrated gel of the target material is produced as a result of known chemical processes and then applied to the substrate via the mechanism of choice. The film quality and conformality of such methods are far more superior to vacuum deposition methods and it is possible to achieve single phase oxide thin films if the synthesis and post processing of the deposited thin films are done correctly.

Chapter 3. IR Vector Light Sensor

The following sections will describe the principles of operation, mathematical design, signal and noise modeling as well as thermal conduction simulations and related design parameters of the proposed pixel IR proximity sensor with angular target detection capability.

3.1. Device's Design and Principles of Operation

The proposed device relies on the mathematical framework that incorporates the plane wave approximation into thermal IR sensing. Given the radiation source's distance to the target and detector's dimensions, the incoming IR radiation at the detector can be modeled as a plane wave and therefore be treated as a directional or vector source of incidence. Our group has previously shown that such an approximation results in a vector treatment of the incident source for photoconductive transduction using diodic junctions on a three dimensional structure with a good degree of accuracy. As a result of such a treatment, the proposed concept in this work is dubbed the IR Vector Light Sensor (VLS) [73]. In this work we have expanded the same concept (plane wave approximation of the incident source) to thermoelectric IR sensing whereby the transduction mechanism of choice is a change in the sensing material's electrical resistance as a function of absorbed IR power. The following sections entail the mathematical modeling of the incident IR source, the proposed detector's geometry and principles of operation, as well as signal generation as a result of interaction with the incident IR.

3.1.1. Mathematical Model for the IR Source and Sense Material

Radiometric quantities associated with IR source modeling are the incident source's radiant intensity and the irradiance at the detector's surface. For a homogenous isotropic point source, the radiant intensity is defined as the radiant power of the source in a particular direction such as that of the detector per unit solid angle and is given via the following formalism [74]:

$$I_s = \frac{\Phi_s}{4\pi} \quad (23)$$

$$\phi_s = \varepsilon A_{Source} \sigma (T_{Source}^4 - T_{Room}^4) \quad (24)$$

where I_s is the source radiant intensity, ϕ_s is the source radiant power, ε is the source emissivity and σ is the Boltzmann constant. In this case, the irradiance due to the source radiation is given via the following as:

$$E_s = \frac{\partial \Phi_s}{\partial A \cdot \cos(\theta)} \quad (25)$$

where E_s is source irradiance at the surface of the detector, ∂A is the detector's unit surface area and θ is the angle between the detector's surface normal and the impinging radiation (Figure 3-1).

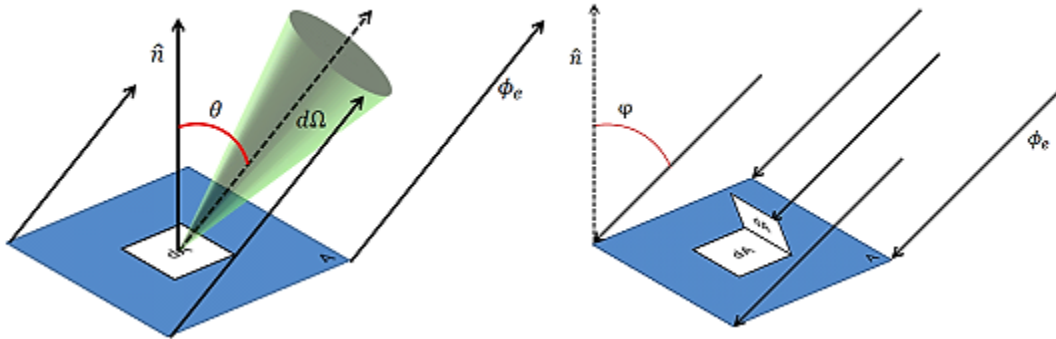


Figure 3- 1 Differential left) source emission solid angle and right) detector's perceived irradiance

As a result, the detector's response to the incoming radiation is defined as the induced change of electrical resistance that is proportional to an increase in the sensing material's temperature due to the amount of energy absorbed by the sense area at the detector's position (Figure 3-2).

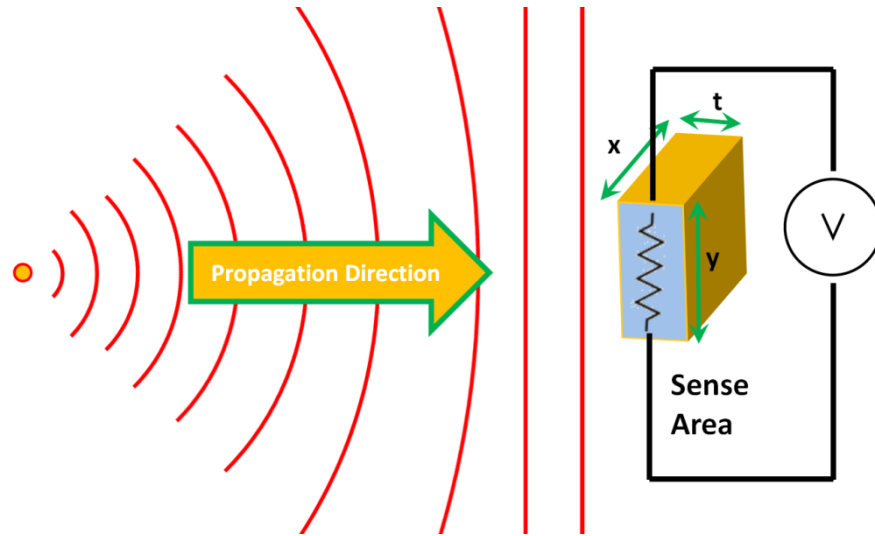


Figure 3-2 Schematic of the incidence source and the detector's material undergoing a change in the electrical resistance as a result of interacting with the incoming radiative power

A simplified model to quantify such a change in the material's electrical resistance as a result of absorption of the incident IR power can be achieved via the following expression:

$$\Delta R = \Delta T \cdot \delta_R \cdot R_o \quad (26)$$

$$\Delta T = \frac{E_S \cdot A_{sense} \cdot t_{window}}{C_p \cdot M_p} \quad (27)$$

where ΔR is the induced change in the sense material's electrical resistance, δ_R is the sense material's temperature coefficient of resistance (TCR), R_o is the sense material's room temperature (equilibrium) resistance, t_{window} is the time window of exposure, C_p is the sense material's specific heat and M_p is the sense material's mass (calculable from the sense area's volume and density). The above equation (equation (27)) assumes full absorption of the incident radiative power by the material and hence a 100% incident IR power contribution to the change in temperature and consequent change of electrical resistance during the measurement time window. This assumption is a poor one and does not incorporate the sense material's wavelength dependent absorbance nor the spectral distribution of incoming IR radiation. A modified version of the above expression taking into account the spectral dependence of the sense material's IR absorption is given by the following:

$$\Delta R = \Delta T \cdot \delta_R \cdot R_o \quad (28)$$

$$\Delta T = \frac{\eta(\lambda) \cdot E_S \cdot A_{sense} \cdot t_{window}}{C_P \cdot M_P} \quad (29)$$

where $\eta(\lambda)$ is the spectral IR power absorption fraction. Here we introduce no formal expression for the spectral absorption coefficient since this is highly material dependent. The empirical wavelength dependent absorption cross section for the sense material employed in this work (V_2O_5) is presented later in this thesis.

3.1.2. Device Design and Principles of Operation

Based on ease of fabrication and reproducibility, the device's geometry is proposed to be a flat-headed pyramid resulting from silicon micromachining through anisotropic etching [75] The principle of operation is based on the difference in the perceived radiative IR power that is impinging onto opposing inclined facets of the structure at a given incidence angle of an IR point source. The point source approximation holds true as long as the dimensions of the source of radiation are much smaller ($\sim 1/10$ th) than the distance between the source and the detector (Figure 3-3).

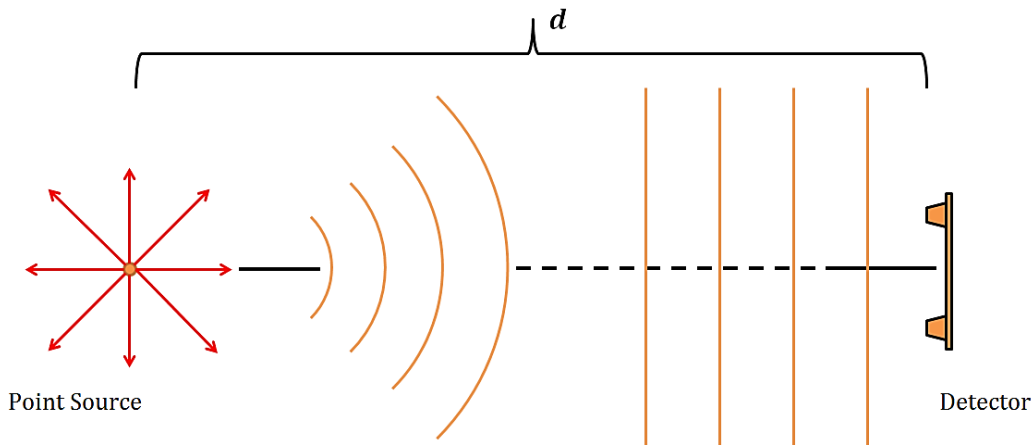


Figure 3- 3 Depiction of the radiative IR source as a point source whereby its emitted wave fronts can be approximated as plane waves at distance $d \gg$ Detector's Dimensions.

In this way, any angular deviations from the normal to the incident IR plane will result in complementary trigonometric modulation of the generated signals at each facet as a result of the absorbed radiative power (figure 3-4). Such differences can be utilized to recalculate an unknown angle of incidence had the detecting surfaces had a Lambertian cosine law

response to the incoming radiation. Since the device is a line of sight detector it relies on the ratio of the outputs on the opposing sides in order to recalculate the incidence angle. As a result, its theoretical field of view is defined as the arc confined between the opposing lines that run parallel to the inclined surfaces (silicon (111) facets). Theoretically, the device's output in one side of the device becomes zero, if the incident IR is located outside of the theoretical FOV resulting in zero or division by zero case in the recalculation process. The theoretical FOV is highlighted in the figure below (see Figure 3-4).

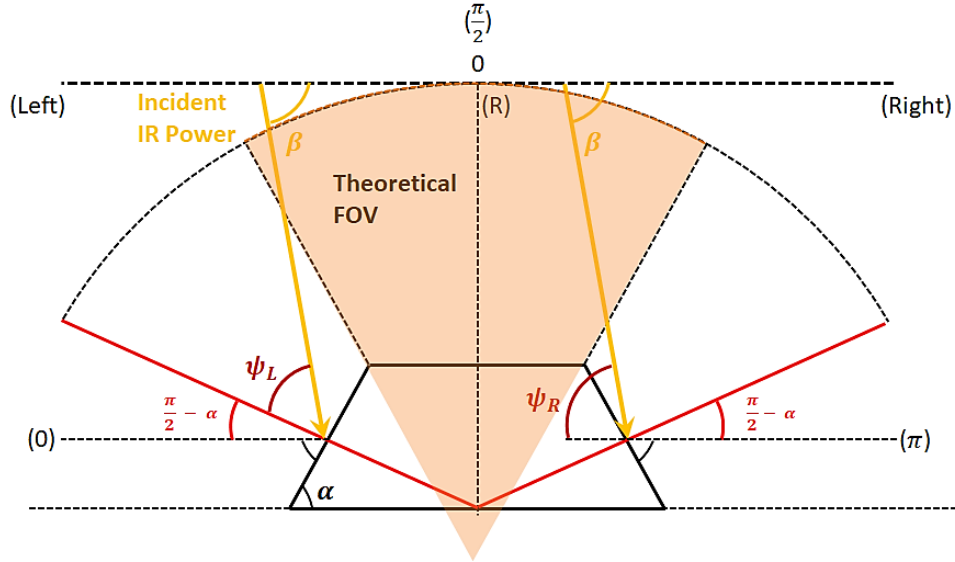


Figure 3- 4 Theoretical device's angular field of view and angular modulation of the sense facets' output as a result of changes in the angle of incidence of the incoming radiative power.

For an arbitrary case where the incident IR power is impinging onto the left side of the device the perceived power at each facet can be written as:

$$P_L = A_L \cdot I_{in} \cdot \cos(\psi_L) \quad (30)$$

$$P_R = A_R \cdot I_{in} \cdot \cos(\psi_R) \quad (31)$$

where $P_{L,R}$ are the transduced radiative power received at the left side and the right side of the device as depicted in (Figure 3-4), I_{in} is the incoming (incident) radiative power at the left and the right sides of the device, $\psi_{L,R}$ are the angular deviations between the wave vector of the incident radiative power and the normal to the left and right surfaces of the device respectively. The precursor to the incidence angle recalculation using equations

(30) and (31) is to rewrite the angular deviations ψ_L and ψ_R in terms of the silicon's (111) surface inclination angle α ($\sim 54.7^\circ$) and the incidence angle β as in the following:

$$\psi_L = \beta - \left(\frac{\pi}{2} - \alpha\right) \therefore \cos(\psi_L) = \cos\left(\beta - \left(\frac{\pi}{2} - \alpha\right)\right) \equiv \cos\left(\frac{\pi}{2} - (\beta + \alpha)\right) \equiv \sin(\beta + \alpha) \quad (32)$$

$$\psi_R = \frac{\pi}{2} - (\beta - \alpha) \therefore \cos(\psi_R) = \cos\left(\frac{\pi}{2} - (\beta - \alpha)\right) \equiv \sin(\beta - \alpha) \quad (33)$$

The second step is to form an expression that is a function of both the known angle α and the unknown angle β (the radiation incidence angle):

$$\tan\left(\frac{\pi}{2} - (\beta + \alpha)\right) = \frac{R_{LR} \cdot \cos(2\alpha) - 1}{R_{LR} \cdot \sin(2\alpha)} \quad (34)$$

$$R_{LR} = \frac{A_L \cdot I_{in} \cdot \sin(\beta + \alpha)}{A_R \cdot I_{in} \cdot \sin(\beta - \alpha)} = \frac{P_L}{P_R} \quad (35)$$

As a result, a solution for the unknown incidence angle can be found if the sense areas A_L and A_R are equal and the ratio R_{LR} is a known quantity:

$$\beta = \frac{\pi}{2} - \alpha - \tan^{-1}\left(\frac{R_{LR} \cdot \cos(2\alpha) - 1}{R_{LR} \cdot \sin(2\alpha)}\right) \quad (36)$$

Using a system of two detectors and recalculating the incidence angles β_1 and β_2 on the same side of the two adjacent structures the distance between the source and the detector's plane can also be recalculated using the following expression as shown in (Figure 3-5):

$$H = \frac{d}{\tan(\beta_1) - \tan(\beta_2)} \quad (37)$$

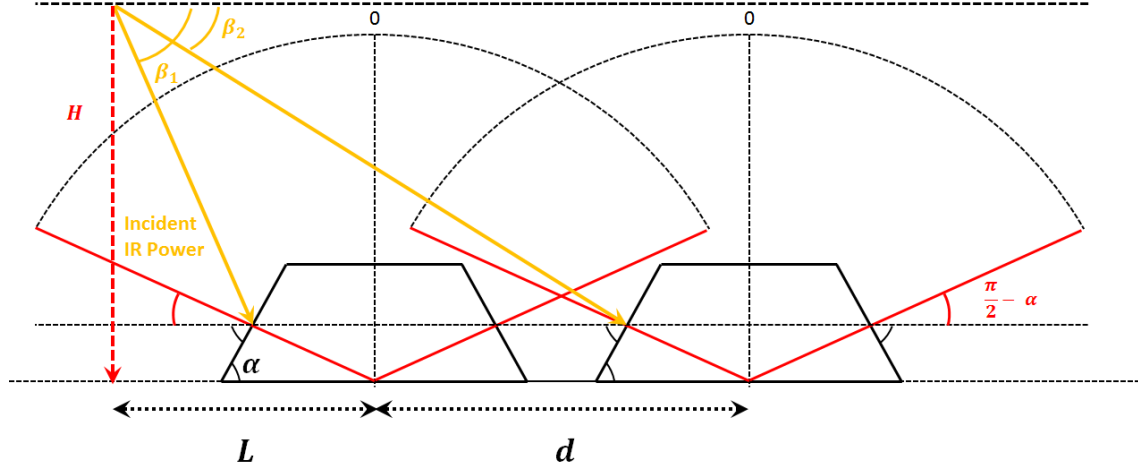


Figure 3- 5 System of two IR VLS detectors to triangulate the distance to radiation source

3.2. Thermoelectric Signal Modeling

As a bolometric system, the proposed detector's response can be characterized with 1) the device's heat (thermal) conduction equation, 2) the device's readout voltage equation and 3) the device's readout noise equation. The following sections discuss the contribution of each of these expressions to the desired output of the proposed bolometric system (signal) that is the measured change in the electrical resistance of the sense material at each facet of the proposed 3D pixel structure as depicted in Figure 3-4.

3.2.1. Device's Thermal Conduction Equation

With the assumption of constant (time-invariant) radiative power, the thermal parameters of the material and substrate can be incorporated into the general heat equation of an idealized thermal detector to form the device's thermal output expression:

$$C_s \frac{\partial}{\partial t} \theta = \frac{V_b(t)^2}{R(T)} + \varepsilon(P_i - 2A_s \sigma T^4) - G_{sub} \theta \quad (38)$$

$$\theta = T - T_{sub} \quad (39)$$

where C_s is the sense area's specific heat, V_b is the time dependent device bias voltage, R is the sense material's temperature dependent resistance, P_i is the incoming radiative power, A_s is the sensing surface area at each side of the detector, σ is the Boltzmann constant for thermal radiation, G_{sub} is the substrate thermal conductance and T_{sub} is the substrate temperature (equal to the ambient temperature). In the absence of Joule heating

of the sense material, equation (38) can be solved for an initial condition of ($T_{sub} = T_{ambient}$):

$$\theta(T, t) = T_0 e^{-\left(\frac{G_{sub}}{C_s}\right)t} + \frac{\varepsilon(P_i - 2A_s\sigma T^4)}{\sqrt{G_{sub}^2 + \omega^2 C_s^2}} \quad (40)$$

where T_0 is the detector's initial temperature and ω is the incoming radiation's angular frequency. The initial hypothesis is for the proposed detector to perform under stationary operating conditions (no thermal biasing of the sense area), as a result the transient portion of equation (40) will converge to zero for prolonged exposure times. The derivation in equation (40) is for an isolated element on the side of device. The device as described in here however has the potential to absorb radiation elsewhere as well.

3.2.2. Device's Readout Voltage Equation

The device's desired output (signal) is defined as the change in the sense material's electrical resistance as a function of the absorbed IR radiative power which is measured as the change in voltage resulting from the flow of a fixed current through the temperature dependent resistive sense material:

$$V_s(T) = I_b \Delta R \equiv I_b \cdot \Delta T \cdot \delta_R \cdot R_o \quad (41)$$

where V_s is the readout voltage, I_b is the bias current, δ_R is the sense material's temperature coefficient of resistance (TCR) and R_o is the sense material's room temperature resistance. Equation (41) indicates the changes in the resistance are a function of changes in the temperature of the material which in turn is a function of the detector's effective surface area, absorbed fraction of the incoming radiative power and the heat conductance of the device substrate. Therefore a more accurate description of the output voltage can be expressed as:

$$V_s(T) \equiv \Delta V_s = \frac{\eta(\lambda) \cdot P_i \cdot I_b \cdot \delta_R \cdot R_o}{G_{sub} \sqrt{1 + \omega^2 \tau^2}} \quad (42)$$

$$\tau = \frac{C}{G_{sub}} \quad (43)$$

where $\eta(\lambda)$ is the wavelength dependent absorption coefficient of the sense material and τ is the device's thermal time constant. At low frequencies (the case for non-modulated IR incidence) $\omega\tau \ll 1$ and hence equation (42) reduces to the following form:

$$\Delta V_s = \frac{\eta(\lambda) \cdot P_i \cdot I_b \cdot \delta_R \cdot R_o}{G_{sub}} \quad (44)$$

Finally, incorporating the sense material's mass, specific heat, and angular dependence described in equations (28) through (32), into equation (44) the device's output can be expressed in the following form:

$$\Delta V_s = \frac{I_b \cdot \delta_R \cdot R_o \cdot \eta(\lambda) \cdot P_i}{G_{sub} \cdot M_p \cdot C_p} \cdot \sin(\beta \pm \alpha) \quad (45)$$

Where β , α , M_p and C_p are the incidence angle, silicon (111) facet angle (54.7 °), sense materials mass and specific heat respectively.

3.2.3. Device's Readout Noise Equation and Parasitic Sources

As a resistive sensor the device's output is prone to three major noise sources which arise in both the material and the contacts with temperature and voltage fluctuations:

- 1) Johnson Noise
- 2) 1/f Noise
- 3) Thermal Fluctuation Noise

For a thermoelectric detector the first and last groups are inevitable whereas the second group can be avoided or made negligible given the proper choice of material for contact deposition with respect to the sense material's type and structure. The three groups of noise mentioned above are all associated with the sense material and are considered to affect the output of either of the detector's sense areas. Given the thermal nature of the IR source (IR target), there should be some consideration of noise in the incident IR radiation as well. Such noise could be important for cases where the detector's main functionality was to output an image of the target. However since the main functionality of the proposed device is to track an IR source, noise fluctuations in the incident IR source were considered negligible for this work. The white noise of the device is generally modeled as a frequency independent voltage source placed in series with the variable resistor that represents the thermoelectric sensor. The situation can be understood using an equivalent circuit model as shown Figure 3-6 [13], [76], [77].

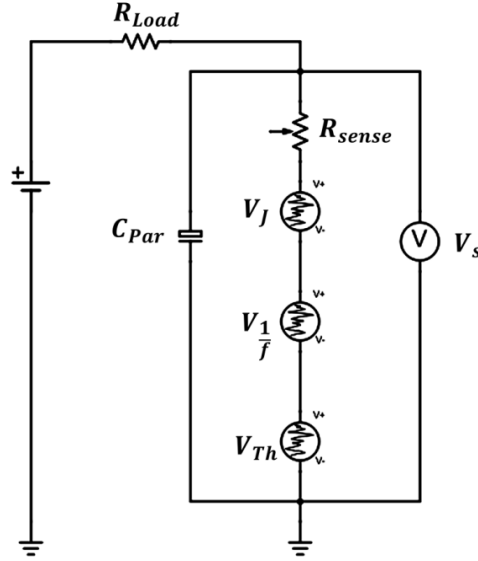


Figure 3- 6 Equivalent noise voltage sources' contribution to the output signal of the device

Johnson noise is an additive noise process with a spectrally independent power that is given by the following expression:

$$V_n^2 = 4 \cdot k_B \cdot T \cdot R \cdot \Delta f \quad (46)$$

where V_n is the noise voltage, R is the electrical resistance of the sense material and Δf is the equivalent noise measurement frequency bandwidth. The second group of noise processes is termed $1/f$ noise, which refers to a signal or process with a frequency spectrum such that the power spectral density is inversely proportional to the frequency of the signal. Therefore it has a strong presence at low frequencies e.g. DC or near DC power measurements for an IR detector. According to the literature, $1/f$ noise process for thermoelectric detectors have a strong dependence on the structural properties of the sense material that can result from different deposition techniques, the sense area size and dimensions, as well as the electrical contacts deposited across the material for electrical resistance measurement. Due to the unknown physical mechanisms that generate $1/f$ noise, there is no accurate closed form expression to model it. however, a practical approximation is given via the expression [13], [76]:

$$V_{\frac{1}{f}} = V_b \cdot \sqrt{\frac{K}{f}} \quad (47)$$

$$K = \frac{\delta_R}{n \cdot V_p} \quad (48)$$

where V_b is the detector's bias voltage, δ_R is the sense material's temperature coefficient of resistance (TCR), n is the estimated number of charge carriers and V_p is the sense material's volume. The final noise process in a thermoelectric detector is the thermal fluctuation noise voltage that arises from the fluctuations of the sense material's temperature around a given set temperature. For a thermal detector responding to an IR source with very low (close to zero) frequency the detector's thermal noise voltage can be described via the following expression [13], [48], [78]:

$$V_{th}^2 = \frac{4 \cdot k_B \cdot T^2}{G_{Sub}} \cdot \delta_R^2 \cdot \Delta f \quad (49)$$

where V_{th} is the thermal noise voltage, δ_R is the sense material TCR and Δf is the equivalent noise measurement bandwidth. Thermal fluctuation noise too is modeled as a voltage source sitting in series with the sense resistor as shown in Figure 3-6. The overall contribution of noise sources can then be represented as an additive term to the output voltage of the device as described by equation (45) in the following form:

$$\Delta V_s = \frac{I_b \cdot \delta_R \cdot R_o \cdot \eta(\lambda) \cdot P_i}{G_{Sub} \cdot M_p \cdot C_p} \cdot \sin(\beta \pm \alpha) + V_N \quad (50)$$

$$V_N = \sqrt{V_{th}^2 + V_J^2 + \frac{V_1^2}{f}} \quad (51)$$

3.3. Device Heat Conduction Modeling

The final portion of the mathematical modeling of the proposed device is a brief discussion of the effect of heat transfer across the device and substrate as a result of the incident IR radiation. This analysis will help to determine the design parameters set forth to avoid thermal contamination of the signal on one side of the device, when the other is exposed to the target IR source. In order to achieve a difference in the angular modulation of opposing (111) facets of a given device, there should, in principle, be no thermal contribution aside from that of the incident IR radiation. Such a condition is only achieved when there is enough thermal insulation between the sense material and the underlying silicon substrate to prevent inter-facet heat transfer (Figure 3-7). The following section discusses the use of finite element methods to simulate the effects of IR radiation-induced heating of one side and the subsequent transfer of thermal energy across the device. The simulations were conducted using different design parameters including the insulating layer type and thickness as well as the device's dimensions.

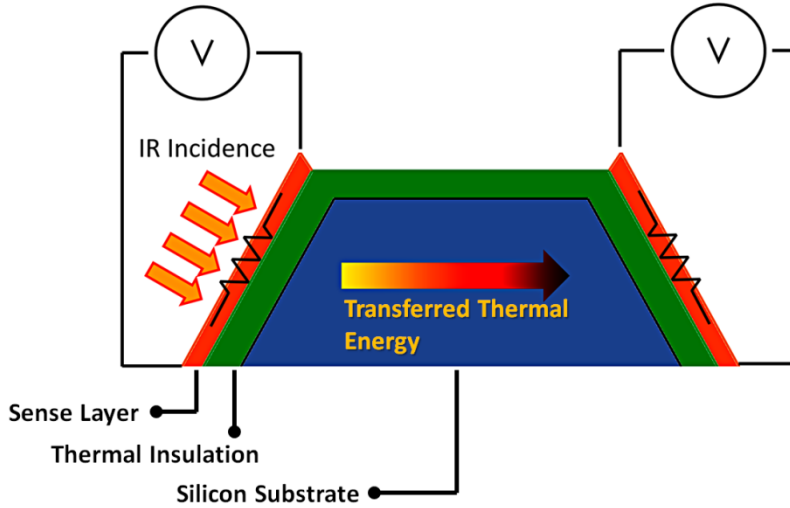


Figure 3- 7 Heat contamination of the device's output voltage (signal) as a result of inter-facet thermal conduction

Given the goal of the analysis is to investigate the transient heat conduction in a 3D system to avoid inter-facet heat contamination, reducing the problem to a 1-D setup will give an overstated estimate of the degree of transferred thermal energy and the measures that are needed to be taken to reduce the impact thereof. The general assumptions under which the simulation is conducted are

- 1- Surface temperature held constant at all times
- 2- No internal heat sources
- 3- Constant thermal conductivity of all media throughout the simulation range

MATLAB ® was used to solve the 1D heat transfer equation of the following form:

$$\frac{\partial^2 T}{\partial x^2} = \frac{1}{\alpha} \frac{\partial T}{\partial t} \quad (52)$$

$$\alpha = \frac{k}{C_p \rho} = \text{Thermal Diffusivity} \quad (53)$$

The problem was modeled as a composite 5-component system comprised of three symmetrical groups of boundaries representing the sense layer's surface, sense layer-thermal insulation interface and thermal insulation-silicon substrate interface on either end of the device structure in 1D. The boundary conditions were set such that there will be time-variant heat flow (heat pulse) at the surface at the left side of the device ($x = 0$), forward boundaries at every intermediate interface and adiabatic boundary conditions at the right side of the device ($x = L$). The initial condition was set to be at zero temperature

and the total temperature increase at the left surface was set to one degree Celsius for convenience (Figure 3-8).

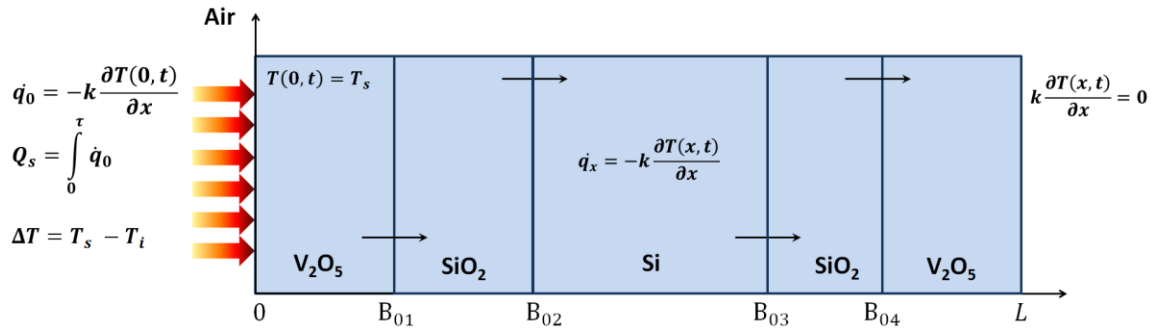


Figure 3- 8 The initial and boundary conditions of the 1D heat transfer simulation using forwarding boundary conditions at the boundaries as shown above such that the material constants before and after the boundary were those of the preceding and proceeding media.

3.3.1. Thermal Transfer Simulation Results

The simulation input was a square heat pulse with a pulse width of 100 μs and pulse amplitude of 1 K at the left surface boundary of the composite system. The sense and insulation layers were set to be comprised of vanadium pentoxide, a thermoelectric transition metal oxide with high absorption in the mid-long wavelength infrared region, and silicon dioxide, a well-known thermal insulator in microelectronics applications respectively. The induced thermal energy transfer across the multi-layered structure was simulated for the following scenarios:

- a) 100 μm wide silicon structure with following silicon dioxide thicknesses:
 - a. 0.5 μm
 - b. 2.0 μm
 - c. 4.0 μm
- b) 4500 μm wide silicon structure

The vanadium pentoxide thickness was kept constant at 0.5 μm in all the simulated scenarios. The choice of the simulated silicon structure widths were made according to the minimum and maximum allowable dimensions satisfying the design requirements for a minimum of two devices and maximum of four devices per die. The requirements were set to achieve an optimal design outcome between the number of devices per die, fabrication considerations, device dimensions and yield per every fabricated 4" wafer.

100 μm wide silicon structure

The simulation results for this scenario are presented in Figure 3-9.

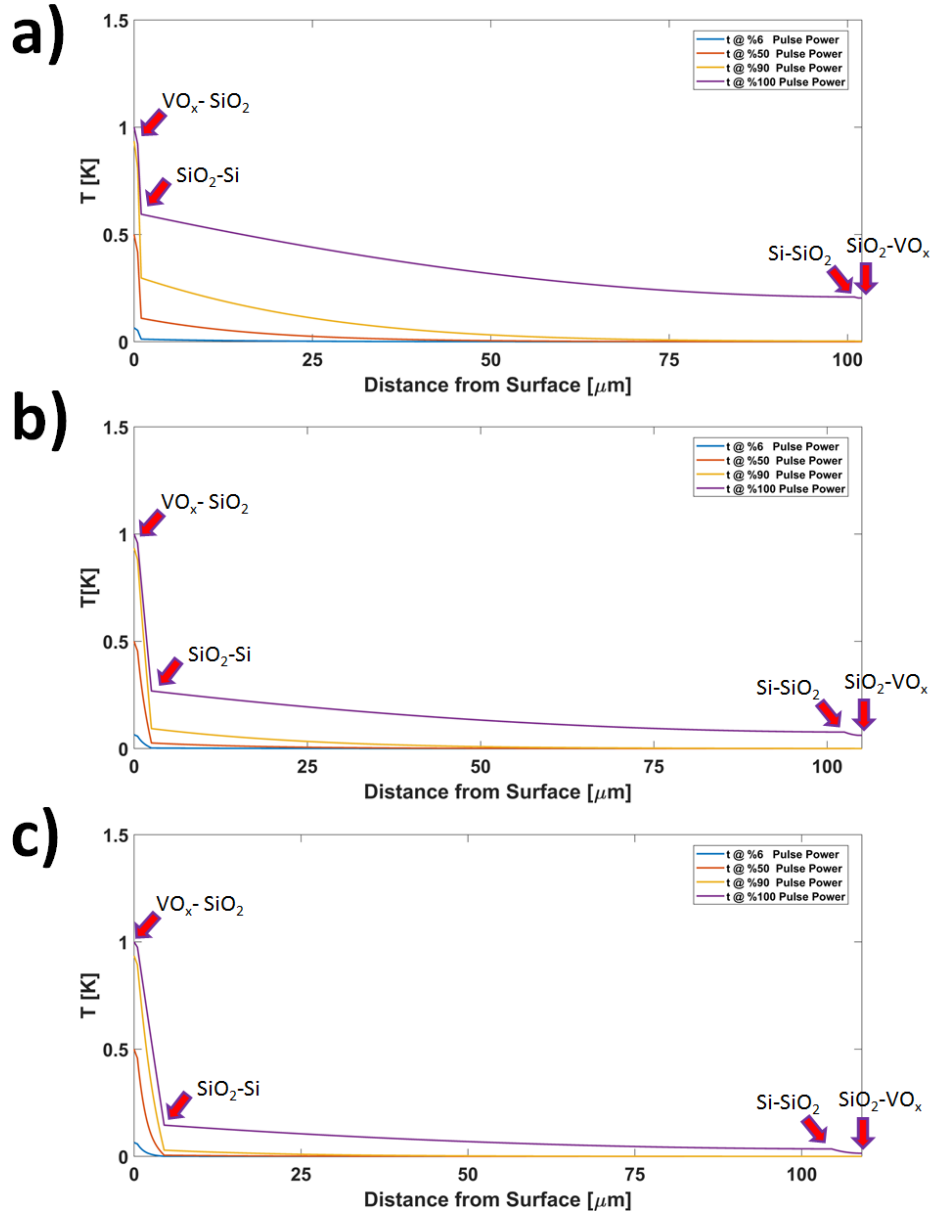


Figure 3- 9 The transient heat conduction solution as a function of distance in a 100 μm wide structure for a) 0.5 μm thick, b) 2.0 μm thick and c) 4.0 μm thick silicon dioxide as thermal insulation layer (referenced to figure 11 for the device geometry)

The heat pulse transfer time is shown through graphing the numerical solution versus time in Figure 3-10.

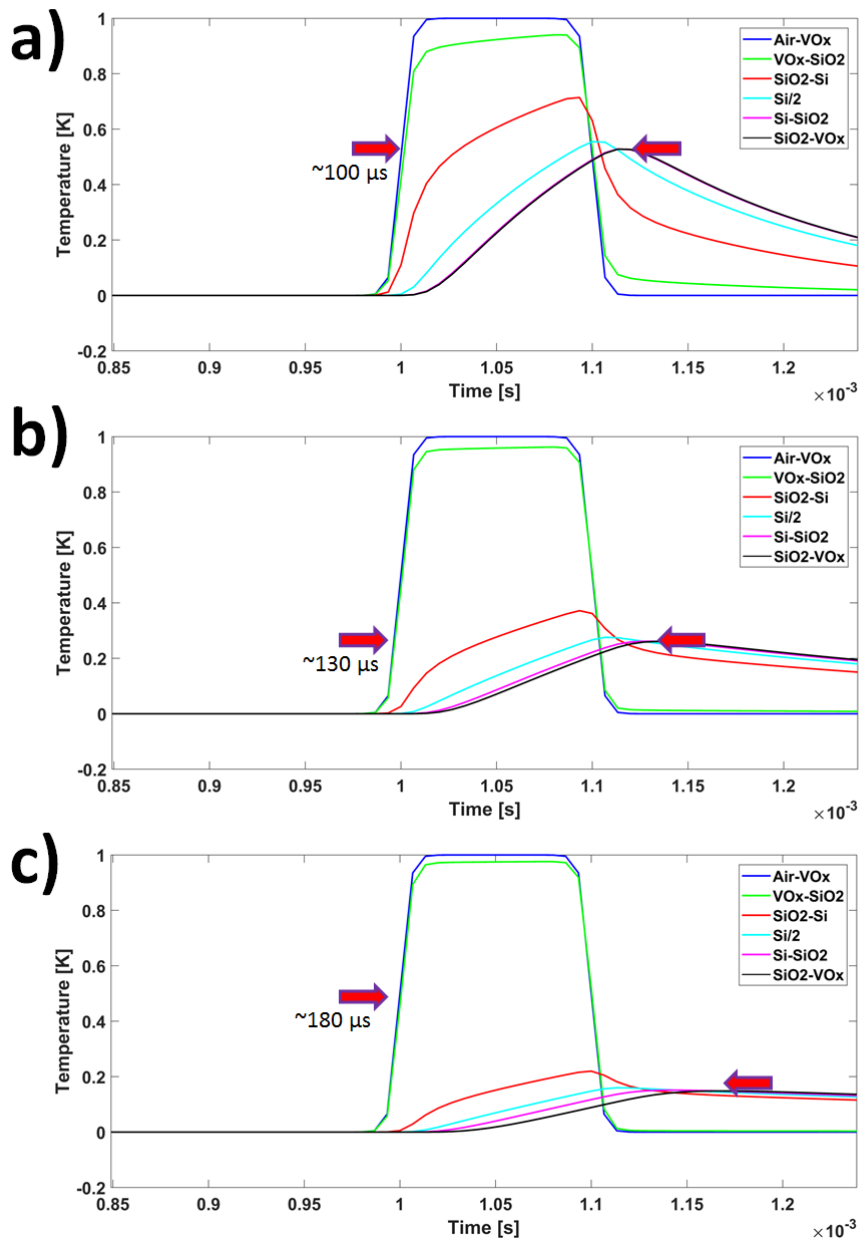


Figure 3- 10 The transient heat conduction solution as a function of time in a 100 μm wide structure for a) 0.5 μm thick, b) 2.0 μm thick and c) 4.0 μm thick silicon dioxide as thermal insulation layer (referenced to figure 11 for the device geometry)

The results show that for a 100 μm wide structure (Figures 3-9 and 3-10), 0.5 μm thick thermal insulation will retain close to %80 of the induced thermal energy within the sense layer (vanadium pentoxide) while nearly %20 of the induced heat travels across the structure and to the opposing side in time scales close to 100 μs (see Figure 3-10-a). A four-fold increase in the thermal insulation layer's thickness results in retaining of approximately %90 of the induced heat within the sense layer and %10 losses in the form

of transferred thermal energy across the device to the opposing side. The time scale for the inter-facet thermal transfer in this case increases by 30 μs . Finally, an 8 fold increase in the insulating silicon dioxide layer results in retaining of over 90% of the induced heat within the vanadium pentoxide layer while the heat energy transfer time scale is prolonged to approximately 180 μs . The simulations suggest that in order to better localize the absorbed heat in the exposed facet, the choice is between increasing the insulation layer's thickness or to decrease measurements time scales to record the device response prior to heat migration.

Given that increasing the insulation layer's thickness contributes only moderately to the retardation of heat migration across the silicon substrate and in between the device facets, another solution to decouple the two sides of the proposed device is to elongate the structure in such a way that the sense facets are placed much further apart. It is noteworthy that the 1D simulation presents a worst case scenario for heat transfer time scales and approximation of the amount of thermal energy retained as a result of the structure dimensions and the insulation layer's thickness. This is due to lack of consideration for extra dimensions of the structure through which thermal energy can also propagate.

4500 μm wide silicon structure

The final case was performed on a 40x wider silicon structure (4500 μm) to monitor the effects of a many folds increase in substrate dimension with the intent of thermal decoupling of the sense regions on reducing heat contamination between the two sides of the structure. For this case, to avoid unnecessarily prolonged simulation time and for optimal grid accuracy, given the large difference between the sense and insulation layer thicknesses and that of the silicon structure, the input thermal pulse was directly applied to the surface of the underlying silicon substrate and the sense and thermal insulation layers on both sides of the structure were neglected. The transient solution versus distance and time is depicted in Figure 3-11.

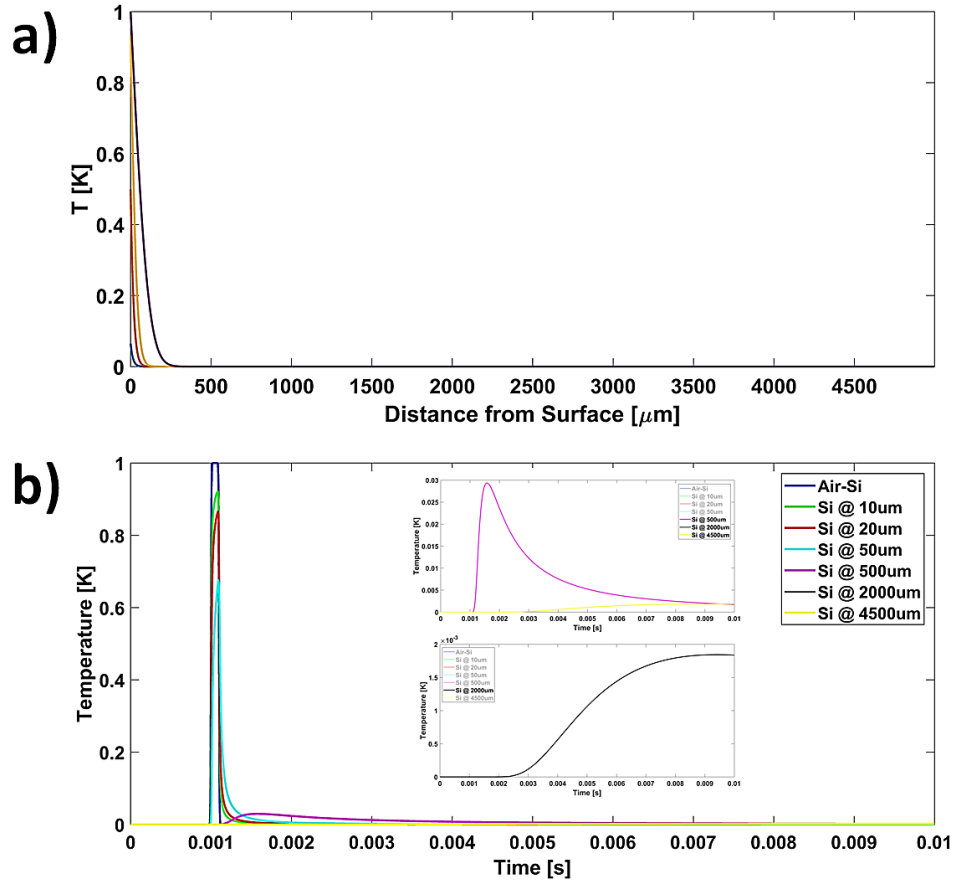


Figure 3- 11 a) Transient solution as a function of distance and b) as a function of time for 4500 μm wide silicon structure

The results shown in Figure 3-12 confirm that at such large dimensions the amount of transferred heat is minuscule (~1/1000th) and the heat travel time is extended beyond 1 ms. The above simulations were made under the assumption of one dimensional heat transfer and thermal losses occurring due to the existence of bulk silicon substrate were neglected.

2D Simulation using COMSOL Multiphysics Software

As a final checksum, the 100 μm mesa structure with 400 nm of vanadium pentoxide and 2 μm silicon dioxide layer was subject to a 100 ms heat pulse at one side as the consequent thermal transfer throughout the structure was monitored. The results show that for a 100 ms heat pulse the silicon dioxide thermal insulation layer results in minimal thermal energy transfer from one facet to the other (Figure 3-12).

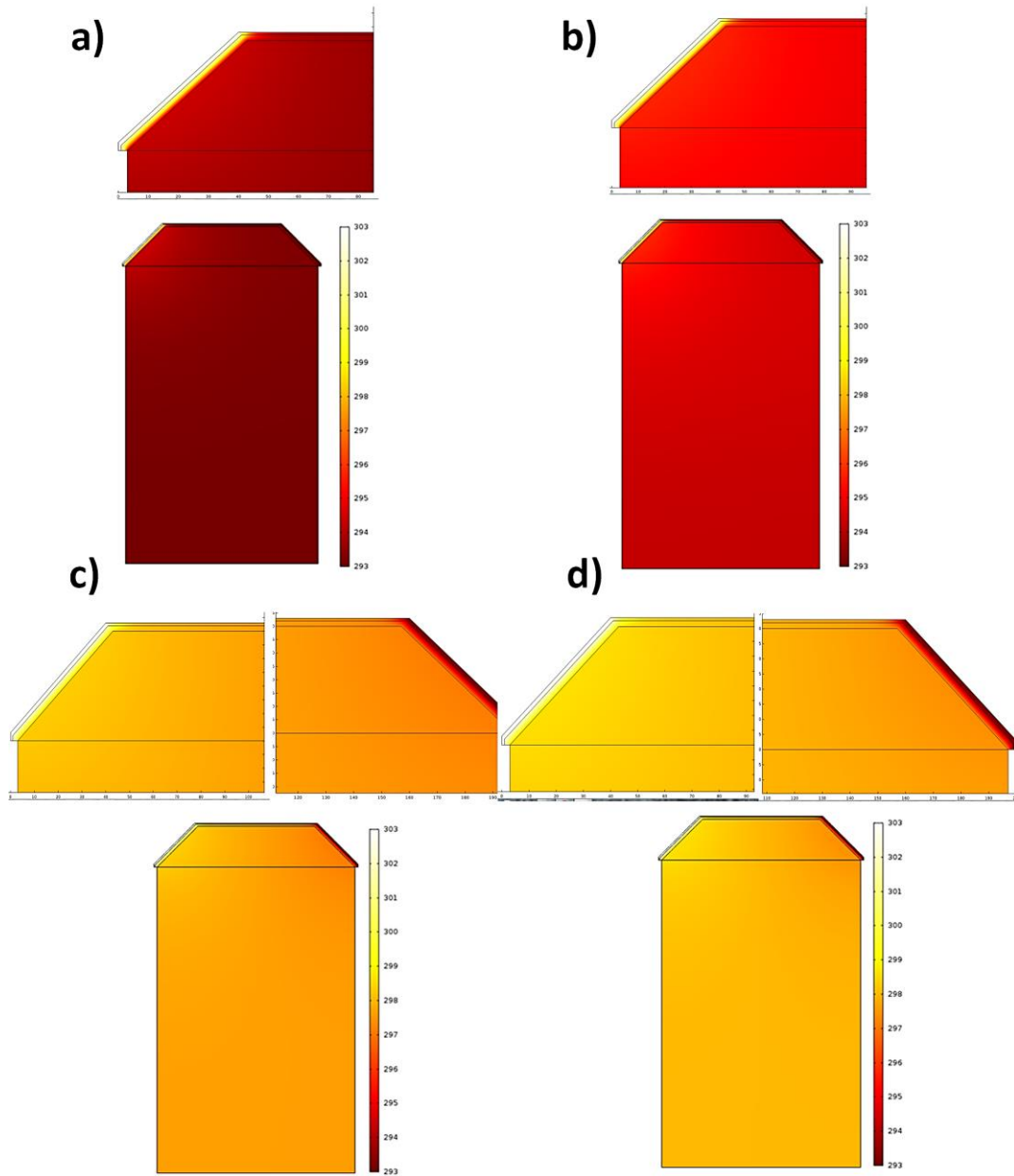


Figure 3- 12 2D heat transfer simulation of a 100 μm raised pyramid with 2 μm of oxide at a) 0.1 ms, b) 1 ms, c) 10 ms and d) 100 ms into the simulation

The main goal of this simulation was to investigate the effects of heat loss due to the underlying silicon substrate dimensions in a more realistic way. The heat pulse was set to increase the exposed side's temperature by 10 °C to visualize the propagation of the induced thermal energy across the silicon substrate in two dimensions. Results show that within 100 μs of exposure to induced thermal energy, the temperature at the surface of the vanadium pentoxide on the exposed layer increases significantly whereas the rest of the structure remains at room temperature. This is unlike the similar case for the 1D

simulation for which, within 100 μs of exposure to heat, the opposing side depicts nearly %40 increase in temperature (see Figure 3-12-a). As the exposure time to heat increases, at 1 ms into the simulation, the substrate begins to warm up as a consequence of heat propagation further away from the exposed side. Yet this increase in temperature is still minimal compared to the induced temperature increase at the exposed facet and seems to have not been affecting the opposing side of the device (see Figure 3-12-b). Finally, the observed thermal distribution at 10 ms and 100 ms indicate a uniform increase in substrate's temperature equivalent to %50 of the induced temperature increase in the exposed site, while the sense layer on the opposing side seems to be at room temperature (see Figure 3-12-c,d). The results of the 2D heat transfer simulations confirm that in a realistic scenario, the 100 μm structure can still avoid thermal contamination of the output signal in measurement time scales close to 100 ms.

Chapter 4. Device's Sense Material Preparation

4.1. Sense Material Preparation

As previously mentioned, vanadium oxides have been the focus of widespread interest in both industrial and academic applications due to their outstanding physical properties such as an insulator-to-metal phase transition observed in VO_2 [79], [80], reversible and irreversible crystalline lattice changes during thermal annealing [81], and a high temperature coefficient of resistance (TCR) [82]. The high TCR of vanadium oxide has resulted in its use in room-temperature infrared sensing applications. A broad review of the common deposition techniques distinguishes between traditional vacuum methods that require a cleanroom setup for accomplishing the task versus room temperature methods whereby the deposition occurs through chemical processes that are carried at the ambient temperature.

4.1.1. Room Temperature Methods for Sense Layer Deposition

Traditional physical deposition techniques such as reactive ion beam sputtering, RF sputtering and e-beam evaporation have yielded vanadium oxide thin films with TCR values in the range of $-2\% \text{ K}^{-1}$ to $-3\% \text{ K}^{-1}$. While the deposited thin films show high uniformity, these methods have high fabrication costs which are associated with cleanroom usage and high vacuum deposition while offering TCRs of the deposited thin films limited to this range. Vacuum deposition methods do not typically achieve stoichiometric compositions of vanadium oxide due to the existence of multiple stable phases in the vanadium-oxygen phase diagram under the prevailing deposition conditions and can result in less stable materials [83]–[87]. These techniques yield little control over the oxidation state of the deposited films and often create mixed oxide phases which can undergo physical phase transitions when heated. Physical phase transitions can introduce mechanical stress and also affect the charge transport characteristics of the resulting thin film vanadium oxide material. Of particular note is the insulator-to-metal transition in VO_2 that introduces abrupt changes in the deposited material's electrical properties over a narrow temperature range ($\sim 67^\circ\text{C}$) which can be undesirable for sensing applications above room temperature [69], [71], [88]–[92]. Researchers have also investigated room temperature deposition methods such as spray pyrolysis, spin coating,

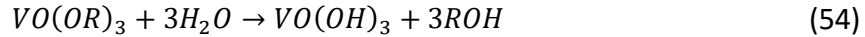
drop casting and dip coating. Due to the nature of these deposition techniques, these methods use a precursor that is synthesized prior to the thin film deposition. The TCR values for as-deposited thin films are not comparable to those from the vacuum techniques, hence high temperature annealing is needed to increase the TCR values of the deposited films. Some of the recent works in the field are reported to have TCR values of $-1.4\% \text{ K}^{-1}$ and $-2\% \text{ K}^{-1}$ for the as-deposited films [93]–[95]. Annealing increases the TCR values significantly. Of the two most studied cases, vanadium dioxide (VO_2) offers relatively higher TCR ($\sim -4\% \text{--} 6\% \text{ K}^{-1}$) yet is less stable, whereas vanadium pentoxide (V_2O_5) offers slightly lower TCR ($\sim -3.5\% \text{--} 5\% \text{ K}^{-1}$) but is physically and chemically stable [93], [96]. Vanadium pentoxide as reported by the literature has 15 experimentally observed IR active vibrational modes which cover a range between $9 \mu\text{m}$ all the way to $25 \mu\text{m}$. As a result it makes a suitable choice for IR sensing applications [97]–[99]. The sense material selected for the proposed detector is vanadium pentoxide, deposited via a low cost, room temperature method to yield thin films of high purity so as not to be hampered by the mixed oxide phase compositions characteristic of vacuum deposited methods.

4.1.2. Sol Gel Synthesis of the Sense Layer Material

Creation of metal oxides can be achieved through two general methods : 1) ceramic (solid) route whereby the reactants' interaction is governed by atomic or ionic diffusion at high temperatures and in solid state [100], [101]. However such reactions often times lead to the formation of unwanted solid compounds as well as the target ones. 2) Sol-gel (liquid) route whereby the reactions pathways are controlled at a molecular level via liquid state transformation of the precursor species into the final product. Aside from its complex underlying chemistry, the sol gel route offers a large degree of control in achieving desired oxide states via the choice of starting reactant species and control over a manifold of parameters that effect the reaction rate and product distribution such as hydrolysis and condensation rates, precursor composition, solution pH, temperature and mixing methodology. The process is comprised of four main steps: 1) homogenous solution preparation by dissolution of metal organic compounds (e.g. metal alkoxide) in an organic solvent, 2) conversion of the homogenous solution to a dispersed colloidal suspension via hydrolysis and condensation reactions of the precursor molecule to form the sol, 3) sol to gel transition occurs via cross-linking and polymerization of the metal-oxide network, and 4) Aging and consequent removal of the solvent leading to the target extended metal-

oxide material [101]. Subsequent high temperature treatment (annealing) leads to further polycondensation and enhances larger crystallite formation and mechanical properties.

Sol-gel synthesis is a low temperature process that allows the formation of stable phases of metal and transition metal oxides such as vanadium. The synthesized material is often highly porous that can be more active than the ones formed through vacuum deposition methods such as physical vapour deposition. As a result, thin films can be created through cost effective procedures such as spin casting or dip coating [84], [85], [102]. There are two main synthesis routes that, based on the molecular structure of the precursor used, can result in vanadium pentoxide sol. The inorganic route comprises of metal salts (vanadate precursors) and aqueous solutions whereas the organo-metallic route is initiated via the hydrolysis of metal alkoxides in organic solvents. The sols synthesized through quadrivalent alkoxides such as vanadium, have been reported to have optimum density and densified polymeric nature due to intermolecular bonds that form between the metal and oxygen when forming the extended oxide networks during sol condensation. The two-stage process includes the hydrolysis part which generates vanadium hydroxide [84], [103]:

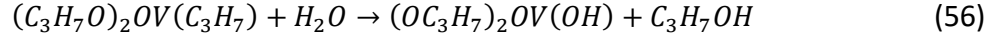


When there are sufficient vanadium hydroxide molecules present, the condensation reaction between every two vanadium hydroxide molecules produces long pentoxide chains through the solution:

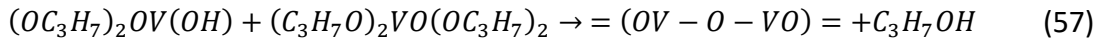


The hydrolysis ratio ($h = \frac{H_2O}{V_2O_5}$), if large enough, allows for full dissociation of alkoxy groups and therefore full hydrolysis of the precursor. For this work, vanadium pentoxide was prepared via controlled hydrolytic poly-condensation of vanadium tri-isopropoxide ($VO(OC_3H_7)_3$), purchased in liquid form from Sigma-Aldrich. The precursor was mixed with IPA to form the sol at room temperature. The prepared sol was then magnetically stirred for 30 minutes before dilution with an additional 10 ml of isopropanol (IPA). The second IPA portion was added to ensure that poly-condensation would occur more homogeneously throughout the solution. The pH of the solution was measured three times during the following 120 minutes of stirring and ranged from 3.9 to 4.7. Sample precursors were prepared with two different alkoxide concentrations. A low-concentration batch was

carried out with an alkoxide concentration of 4.00v/v% whereas the high-concentration batch was carried out with a 25.33v/v%. The thin films deposited with the low-concentration and the high-concentration batches are referred to as low-concentration and high-concentration samples throughout the rest of the text. The poly-condensation of vanadium tri-isopropoxide occurs through a series of complex chain reactions that include the occurrence of both condensation and hydrolysis concurrently. The simplified hydrolysis reaction is given through [103]:



The hydrolysis and interaction of the hydroxyl bonds with the neighbouring alkoxy groups leads into the oxide network formation [85]:



The nature of these reactions and the condensation conditions as determined by the ratio of water to alkoxide present in the solution dictates the extent to which a long and condensed oxide network forms. This ratio can be utilized as a control measure over the density and complexity of the resulting oxide network. Depending on the physical properties of the alkoxy groups involved in the synthesis (bulkiness and size of the molecules), the resulting precursor can produce monomeric or oligomeric sols. For vanadium, the literature cites tetrahedral coordination for monomeric species and square-pyramidal coordination for oligomeric species. Given the low hydrolysis ratio ($h < 3$) for the alkoxide-alcohol mixture, we expect to have oligomeric species with square-base pyramidal form. Subsequent condensation gives rise to highly branched gels resulting from the metal-oxygen-metal ($\equiv O - M - O \equiv$) bonding network [84], [94], [97], [103]. Figure 4-1 depicts the tetrahedrally shaped vanadium pentoxide ribbons in orthorhombic vanadium pentoxide gels [85], [104].

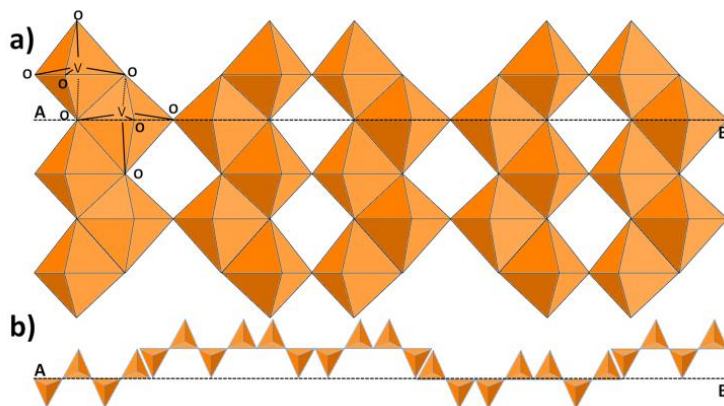


Figure 4- 1 a) 2D view of the orthorhombic α - V_2O_5 crystal lattice along the (001) direction where line AB depicts the crystal packing in the (010) direction

4.2. Sense Material Deposition

For thin film deposition, dip coating was chosen as a cost effective method to deposit thin films of V_2O_5 onto fused silica substrates for film characterization purposes. Dip coating is a simple method employed in the industry to form thin layers of material on substrates via use of semi-viscous materials. In the absence of surface active agents that can decrease the surface tension of the thin film layer, dip-coating can form a reasonably uniform layer of material across the surface of the substrate. At lower dipping rates (dipping and withdrawing speeds) one can use the Landau-Levich (L&L) model for approximating the thickness of the deposited films as a function of the substrate speed. For simplification, we assume the parameters of the precursor (viscosity μ , density ρ , and the surface tension σ) to be constant across the entire solution. The dynamic film thickness (thickness of the fluid film forming on the surface of the substrate as the dipper is being withdrawn from the precursor solution), can be calculated via the following equation:

$$H = \frac{C_N \cdot \sqrt{(\mu U_w)^3}}{1.4 \sqrt{\frac{\rho g}{\sigma}}} \quad (58)$$

with C_N being the fluid constant for Newtonian fluids, U_w is the withdrawal speed (constant rate) and g is the gravitational acceleration force. Figure 4-2 below describes the dip coating process using the L&L model [105], [106]. The average speeds at which a ~20 nm (16 nm predicted by the model) thick layer would be deposited on the substrate was

predicted to be about 2.5 mm/s which translates into 150 mm/min of dipping and pull rate (Figure 4-2)

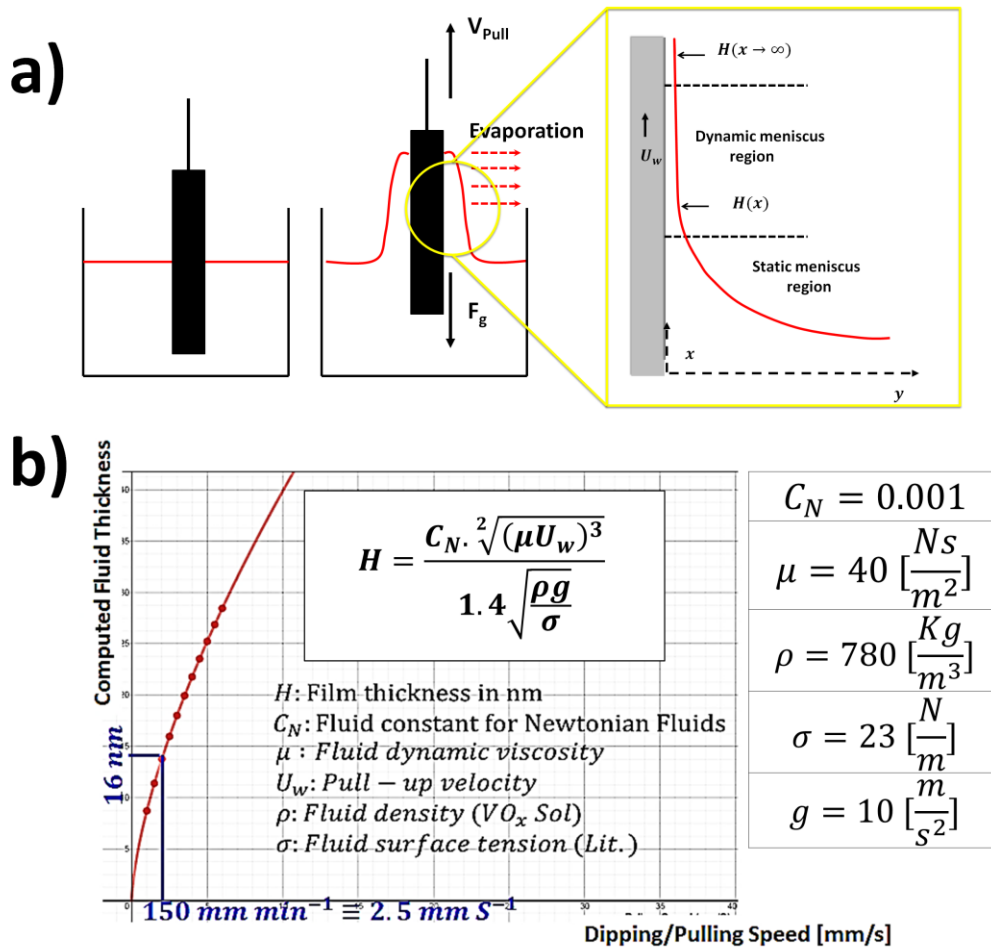


Figure 4-2 a) Landau model of a rising planar substrate from a Newtonian fluid depicting three regions for the fluid film thickness as a function of distance from the fluid bath-fluid interface b) The numerical evaluation for vanadium pentoxide sol (fluid parameters extracted from literature) and capillary constant C_N approximated for Newtonian fluids

In order to get a desired thickness of > 200 nm the dipping and pulling cycle was set to repeat 12 times at a constant speed of 150 mm/min (equivalent to 2.5 mm/s predicted by the model). Films were deposited by immersing and withdrawing the substrates into the sol with a 120 second wait time between each dip cycle, in order for the deposited layer to hydrolyze before subsequent immersion in the sol. In order to better understand the structural and conformational transitions of the vanadium oxide sol-gel films upon annealing, four samples from each concentration group were annealed at 4 different annealing temperatures (300°C, 400°C, 500°C, and 650°C) for 6½ hours in a high temperature furnace (Ney-Vulcan 3-550) while one sample from each group was kept “as-deposited” for reference.

4.3. Sense Material Characterization

All samples underwent structural characterization to investigate the effects of various degrees of thermal annealing as well as the changes in the precursor alkoxide concentration on the microstructure of the deposited thin films. Sample surface roughness and film thickness parameters were measured using a Bruker Dektak XT profilometer. Surface morphology and grain structure of the deposited films were examined using an FEI-Nova NanoSEM scanning electron microscope at $\times 10k$, $\times 30k$ and $\times 100k$ magnifications. X-Ray diffraction studies were carried out using a Bruker D-8 Advance X-Ray diffractometer equipped with a Cu K α source ($\lambda=1.5406 \text{ \AA}$) for 2θ angles between 10° and 90° at a scan rate of $0.02 \text{ }^\circ/\text{s}$ and finally Raman spectroscopy was carried out using a Renishaw Invia Raman spectrometer and microscope using 785 nm laser excitation.

4.3.1. Surface Roughness Analysis

Analysis of the average profile heights of the as-deposited and annealed films indicated a significant reduction in film thickness after the annealing step. The thickness of the as-deposited high-concentration film is approximately twice the thickness of the as-deposited low-concentration film and both groups display a significant decrease in film thickness upon annealing, suggesting that the as-deposited films are relatively porous and undergo significant densification when annealed (Figure 4-3).

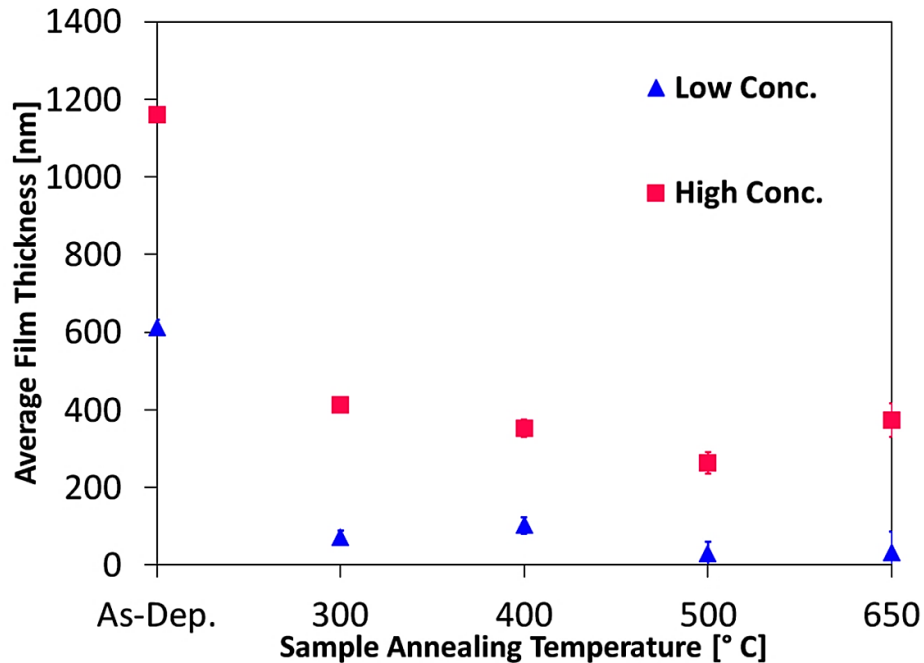


Figure 4- 3 Film thickness (derived from the average profile height in profilometry data) versus the annealing temperature of the samples.

The experimental results for 12 coatings (24 layers) indicated an approximately 50 nm film thickness per dip which was three times the value predicted by the L&L model calculated with the parameters presented in figure (4-2-b). The material specific constants used for the model such as density and surface tensions as well as the capillary number were assigned considering the bulk of the sol mixture comprised of isopropanol (IPA). The difference between the actual deposited film thickness and that predicted by the model could arise from an incorrect assignment of the mixture's viscosity. The constant two-fold increase in the deposited film thicknesses between the low and high concentration groups, across all annealing scenarios is the result of a 6.33 fold increase in the precursor concentration during the sol synthesis which can be attributed to the hydrated oxide network density as a result of the induced concentration change. Profilometry revealed that the average film thickness of the high and low-concentration films were approximately 400nm and 50nm after annealing, respectively.

4.3.2. Structural Characterization

The structural differences of the as-deposited and annealed thin films from both the low and high concentration groups were investigated using electron microscopy. Figure 4-4 shows top-view scanning electron micrographs of the low and high-concentration films subjected to different annealing conditions. The as-deposited morphologies in both groups were characterized by smooth and continuous films with no obvious appearance of crystalline structure. Both groups showed a similar progression with increasing annealing temperature, from morphologies containing many small crystallites toward few larger crystallites with well-defined grain boundaries and orientations. At annealing temperatures 400°C and higher, the grain structures became prominent.

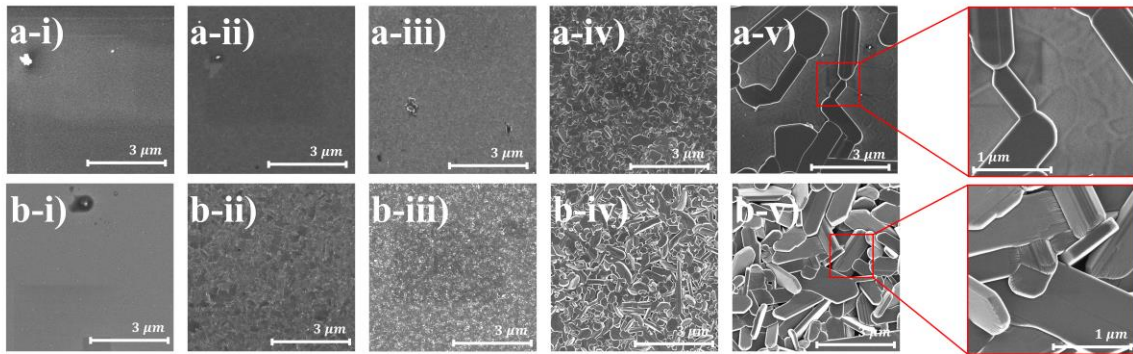


Figure 4-4 The SEM images of a-(i-v) Low concentration samples and b-(i-v) High concentration samples, annealed at 300°C, 400°C, 500°C and 650°C, respectively. The blown-up sections in either group depict the sheet structural differences between the low and high concentration.

Despite the similarities in structure growth between the two groups, the 650°C annealed samples from the high-concentration group, show the development of more, and more well-defined crystallites with well-developed grain boundaries and a larger range of grain orientations than the low-concentration counterparts. Comparable in size and shape, the low-concentration group's 650°C annealed samples contained less densely packed crystallites which coalesced to form preferentially oriented connected networks oriented parallel to the substrate.

The long range order and crystalline character of the vanadium oxide films were investigated by X-ray diffraction. The results of these studies are shown in Figure 4-5, where the XRD patterns of the low and high concentration films are displayed as a function of annealing temperature. Also shown is a reference powder X-ray diffraction pattern of vanadium pentoxide ($\alpha - V_2O_5$). The XRD data reveals that the as-deposited films are

nominally X-ray amorphous and increase their degree of crystallinity with annealing temperature, as indicated by an increasing diffraction intensity in the XRD traces. The diffraction patterns of the high and low-concentration samples are dominated by a single (001) diffraction peak at $\sim 20.4^\circ$ in 2θ , indicating that the sol-gel deposition and annealing protocol leads to the deposition of single phase $\alpha - V_2O_5$ material that is highly oriented.

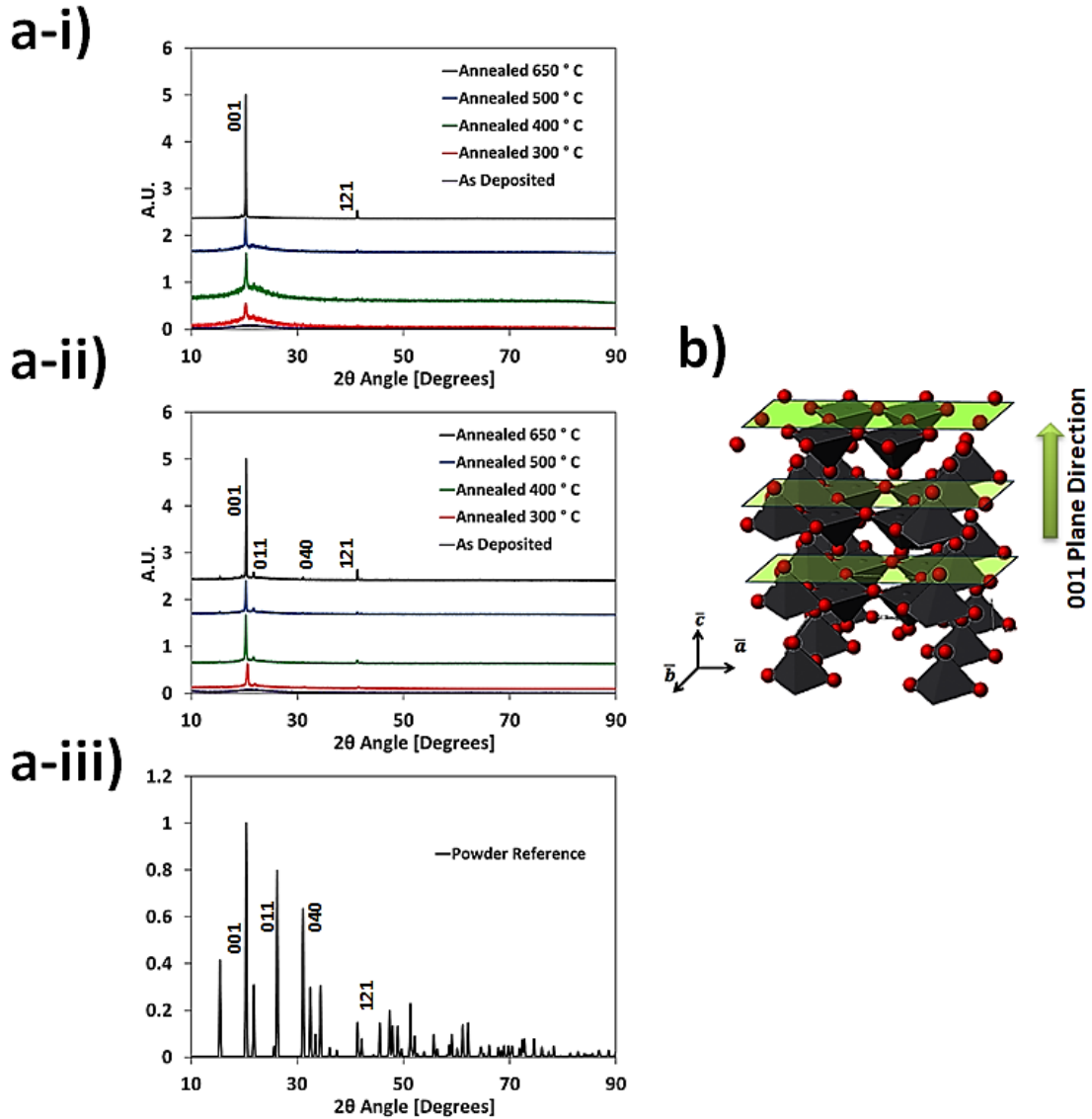


Figure 4- 5 a-i-iii) The comparison between the XRD traces of low and high concentration samples (a-i and a-ii, respectively) annealed at different temperatures against powder reference of $\alpha - V_2O_5$ (a-iii).; b) the layered structure of $\alpha - V_2O_5$

The similarity in the XRD data for all films demonstrate no significant structural differences between the low and high concentration groups nor any indication of formation of other

structural forms or oxidation states of vanadium. The strong intensity in the (001) diffraction peak is an indicator of highly oriented (ab) plane growth parallel to the substrate (Figure 4-5-b). However, the appearance of additional low-intensity diffraction peaks in the XRD pattern of the high-concentration samples which are not observable in the low-concentration group indicates morphology differences between the low and high concentration film groups. These low-intensity peaks appear more prominent in samples annealed at 650°C than those annealed at lower temperatures but are nevertheless present in all high-concentration samples. The presence of a dominant (001) diffraction peak and, albeit weak, $\alpha - V_2O_5$ diffraction peaks in the high-concentration samples indicate that the resulting films, while having a layered, oriented structure, are not quite as well oriented as the low-concentration films. Consistent with the observations from the scanning electron microscopy studies, the XRD data reaffirms that the high-concentration samples possess a larger range of crystallite orientations than do the low-concentration samples which are otherwise similar in crystallite composition. Film characterization was also carried out using Raman spectroscopy. Raman spectroscopy is a form of inelastic light scattering that provides information about a material's frequency dependent polarizability, and in this case, its dependence on the vibrational (phonon) modes of the vanadium oxide crystallites. Raman methods can provide evidence of phase purity and crystallinity and complement the SEM and XRD film characterization already described. The results of these studies are presented in Figure 4-6, where the Raman spectra of the low and high concentration films are displayed for the as-deposited and annealed films. Consistent with the SEM and XRD studies, Raman spectra from the as-deposited films show no structure, consistent with an amorphous character, without well-developed collective vibrational motion. Spectra of the annealed samples show well-defined Raman vibrational features that begin to appear and grow in intensity for films annealed at higher temperatures, consistent with the formation of larger crystallites and well-developed phonon character. In agreement with the XRD and SEM observations, the high-concentration sample group shows stronger Raman signals than the corresponding low-concentration films but do not differ in other respects, indicating that the alkoxide precursor concentration has no obvious effect on the resulting sol-gel chemistry or bonding structure in the final vanadium oxide films, but only results in an effective thickness or concentration effect on the final annealed films. The Raman modes appearing at 144, 196, (283, 303), 404, (480, 525), 699, and 993 wavenumbers, are consistent with previous observations of the lattice phonon mode structure of $\alpha - V_2O_5$ [81], [98] and support the contention that

the sol gel deposition and annealing method employed here leads to high purity, single-phase V_2O_5 . This is in contrast with the results reported for other fabrication methods such as physical vapour deposition (PVD) or pulsed laser deposition where other stable oxides of vanadium such as VO_2 and V_2O_3 form upon annealing.

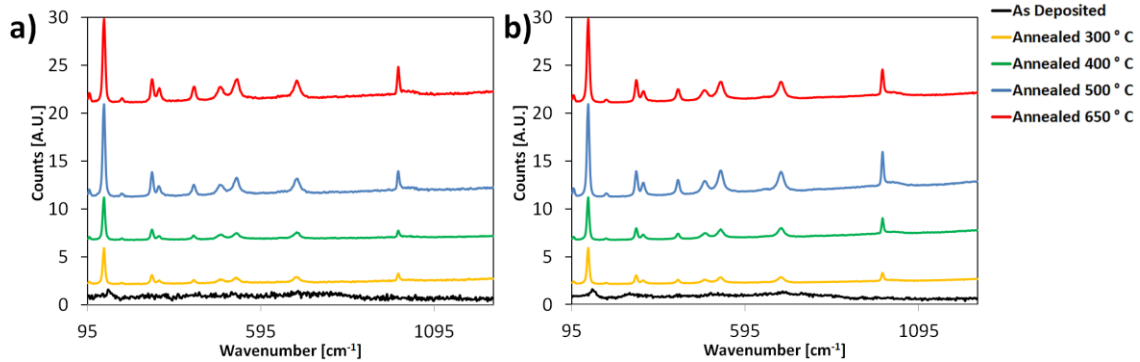


Figure 4- 6 Raman spectra of a) low-concentration and b) high-concentration samples show identical characteristics with a nearly three-fold increase in the peak amplitudes associated with α - V_2O_5 of the high-concentration group compared to the low-concentration ones

4.3.3. Thermoelectric Characterization

For the purpose of electrical characterization of the deposited thin films in response to thermal excitation, inter-digitated comb electrodes (5nm chromium + 150nm gold) were deposited on the vanadium pentoxide films using a shadow mask and physical vapour deposition (figure 4-7). Each structure had 14 digits with 100 μ m width/gap connected alternatively to two contact pads. The electrical resistance of the samples was measured as a function of temperature using a vacuum probe station with a heated chuck (Janis Research model RT-475K-4), a precise temperature controller (Scientific Instruments model 9700), and a source meter (Keithley model 2400) (see Figure 4-8). Sample electrical resistance measurements were carried out over the temperature range of 310K to 345K with a 0.5K/min temperature ramp. The wait time was ca. 10 minutes between every set temperature for the sample to reach thermal equilibrium with the underlying chuck.

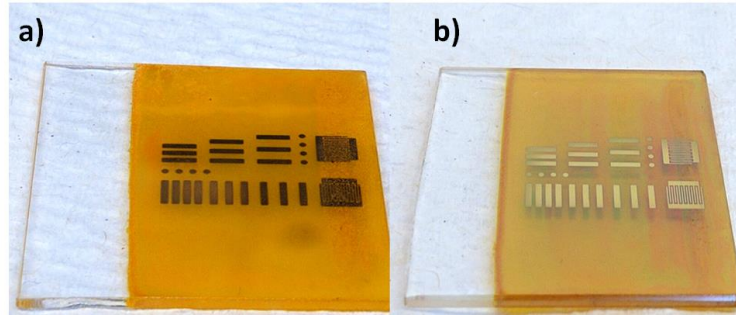


Figure 4- 7 a) 650 ° C annealed and b) as-deposited high concentration V_2O_5 samples undergone thermoelectric characterization

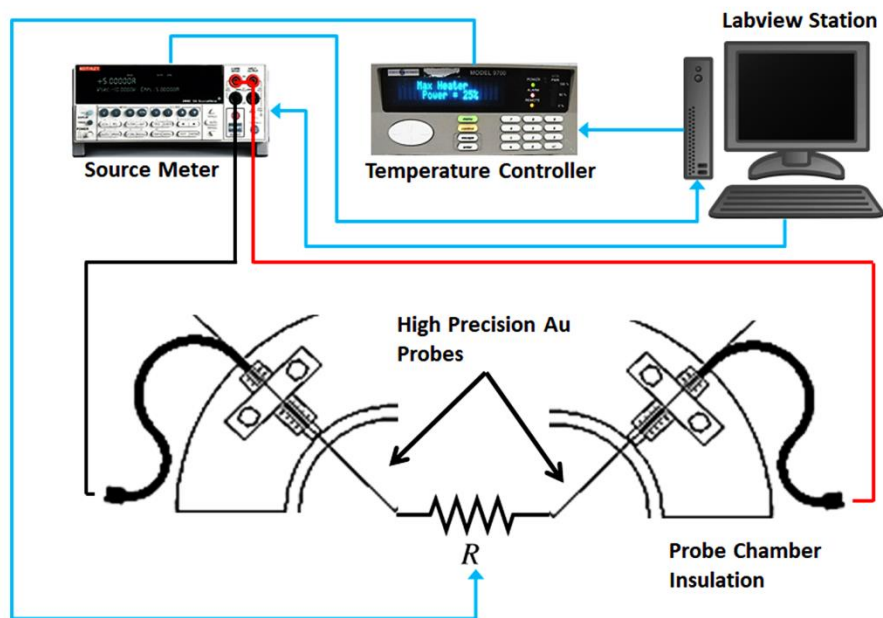


Figure 4- 8 The schematic of the measurement setup that was used to characterize the electrical resistance of the samples as a function of temperature

Figure 4-9 summarizes the sheet resistance of the deposited thin films as a function of annealing temperature. The measurements were carried out at 320 K as described in order to allow the samples to reach thermal equilibrium with the heating chuck and hence minimize the readout resistance variations. Data for the room temperature sheet resistances is added for comparison's sake. The as-deposited low and high-concentration samples display sheet resistance values of $95\text{k}\Omega/\square$ and $75\text{k}\Omega/\square$, respectively. Annealing the films led to an increase in sheet resistance except for the low-concentration 650°C -annealed sample which exhibited a significant drop to a sheet resistance of $53\text{k}\Omega/\square$.

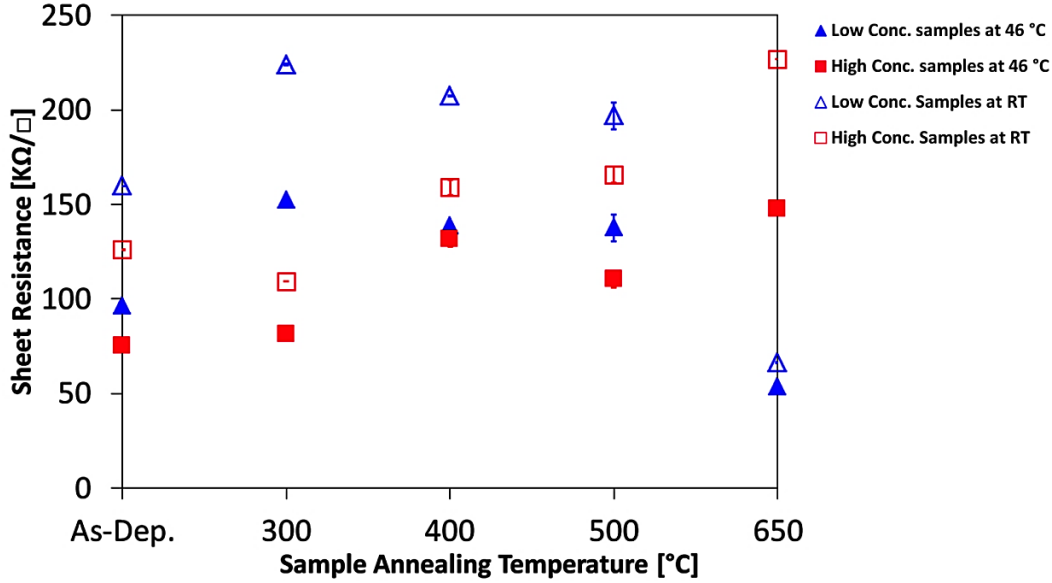


Figure 4-9 Sheet resistance of low concentration and high concentration samples at 320 K as a function of the annealing temperature. The high concentration samples follow a general increasing trend whereas the low concentration samples electrical resistance drops as a function of the annealing temperature. Room temperature (RT=295K) values are included for reference.

TCR Calculation and Sense Layer Fabrication Recipe

The resistivity of semiconducting transition metal oxides obeys a thermally activated hopping mechanism characterized by the following relationship:

$$\rho(T) = \rho_0 e^{\left(\frac{E_a}{k_B T}\right)} \quad (59)$$

where ρ is the temperature dependent resistivity, ρ_0 is the resistivity at infinite temperature, E_a is the charge carrier's activation energy, k_B is the Boltzmann constant, and T is the temperature. Consequently, the temperature coefficient of resistance (TCR) of a resistor made from such a material, α , is calculated from [62], [83], [97]:

$$\alpha = \frac{1}{R_0} \frac{\partial}{\partial T} R(T) = -\frac{E_a}{k_B} \cdot \frac{1}{T^2} \quad (60)$$

where R_0 is the resistance at infinite temperature. The TCR values for all the samples (annealed and as-deposited) in both low-concentration and high-concentration groups were calculated via fitting an exponential curve to the resistance measurements across a temperature range of 310-350K with R^2 values of better than 0.99 for all fitted curves (see Figure 4-10). The results consistently demonstrated TCR values between $-3\%K^{-1}$ and $-4\%K^{-1}$ which indicates a higher value compared to the typically reported ($\sim -2.5\%K^{-1}$) for traditional deposition methods such as DC magnetron sputtering or pulsed laser deposition. Evident from the measured electrical resistances (Figure 4-9) and the

calculated TCR values (Figure 4-11), the low and high-concentration samples followed different trends in value as the annealing temperature of the samples increased from 300°C to 650°C. With an annealing temperature of 300°C, low-concentration samples exhibited higher electrical resistance than the high-concentration ones and their electrical resistance dropped significantly as the annealing temperature was increased to 650°C. For high-concentration samples, however, the electrical resistance was lower for the samples annealed at 300°C against those annealed at 650°C. A similar trend is observed for the TCR values of the films. These trends can be explained by considering the structural differences between the two batches reflected in the development of finer and more pronounced grain boundaries in the high-concentration samples as opposed to less well-defined grain boundaries in the low-concentration group (see Figure 4-4). Since V_2O_5 samples were developed in ambient conditions, they are sub-stoichiometric which indicates they contain oxygen vacancies that serve as defect states for the proposed thermally activated hopping conduction within a given crystalline domain. In the absence of other barriers to charge migration, the formation of larger crystallites should favor increased conductivity and lower sheet resistance. However, the formation of grain boundaries introduces inter-grain activation energy to the charge migration process. Such activation energy is usually larger than the in-grain electron hopping barrier [107] and can therefore impair charge carrier conduction across the sample and through the crystalline domains. As the samples from both groups become more poly-crystallized due to the annealing process, the competing effects of grain size and grain boundary development favor the higher sheet resistance in the high concentration group and higher conductivity in the low concentration group. An exception was the case of 650 °C-annealed low concentration samples which depicted highly orientated crystalline plane growth that led to larger, coalesced grains with exceptionally lower sheet resistance.

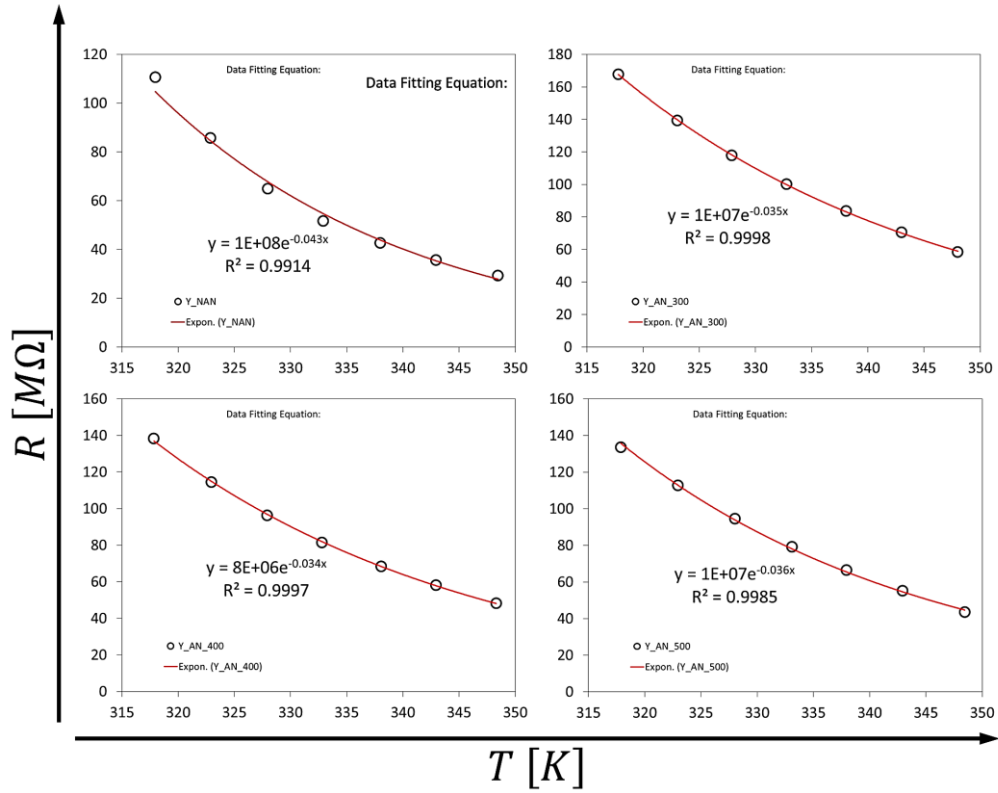


Figure 4- 10 Exponential fit to the measured temperature dependent resistance for low concentration samples a) as-deposited, and annealed at b) 300 °C, c) 400 °C and d) 500 °C.

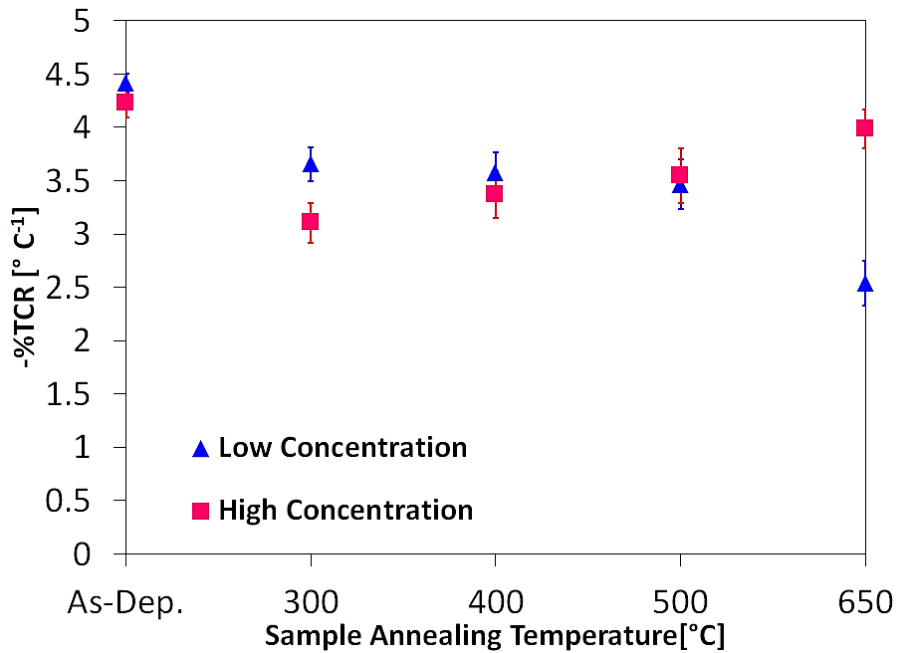


Figure 4- 11 The TCR of the low-concentration and high-concentration samples at 37 °C as a function of the sample's annealing temperature. The inset shows the exponential fit to the measurements for one of the low concentration samples annealed at 500°C. The uncertainty is calculated from the fluctuations of the electrical resistance across the measurement time at a given temperature.

The thin film characterization results for both the low and high concentration samples show opposing trends in the sheet resistance and TCR values as a function of the annealing temperature. As a consequence, an optimum point where the lowest resistivity meets the maximum TCR value defines a suitable recipe for the sense layer deposition for the proposed detector.

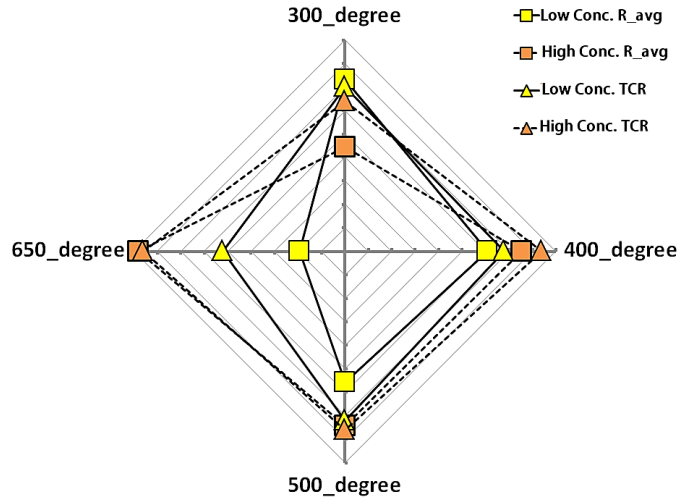


Figure 4- 12 Radar chart for the average sheet resistance and TCR as function of annealing temperature for the characterized samples

The radar chart above (figure 4-12) depicts the trends in resistivity and TCR values for both low and high concentration samples across the annealing processes. As apparent from the trends the high concentration group offers the highest TCR values across all the annealing scenarios. The sweet spot for this group can be found between the 400 °C and 500 °C where the sheet resistance is at a minimum relative to that of 300 °C and 650 °C cases.

4.3.4. Opto-Electronic Characterization

Given that V_2O_5 is a thermo-resistive material, its opto-electronic characteristics entail a quantification of the absorption spectra where the peak IR absorption regions can be identified. These absorption features are expected to be the primary means of human radiation absorption and lead directly to local heat generation and associated resistance decreases in the sense layer. As discussed earlier in Section 2.4.2, vanadium-oxygen bond stretching modes are expected to give rise to mid and far infrared vibrational absorption features. These absorption features can be seen as resonant transmission

decreases in the IR transmission spectrum (Figure 4-13). . The spectra display resonant absorption bands at 1250 cm^{-1} , 1000 cm^{-1} , 750 cm^{-1} , and 600 cm^{-1} , in agreement with previous studies of $\alpha - \text{V}_2\text{O}_5$ [108], whereby the shorter wavelength peaks (1250 cm^{-1} – 900 cm^{-1}) are associated with the vanadyl oxygen – vanadium bond stretching mode and the longer wavelength peaks (750 cm^{-1} – 650 cm^{-1}) are associated with the bridging oxygen – vanadium bond stretching mode [70], [108].

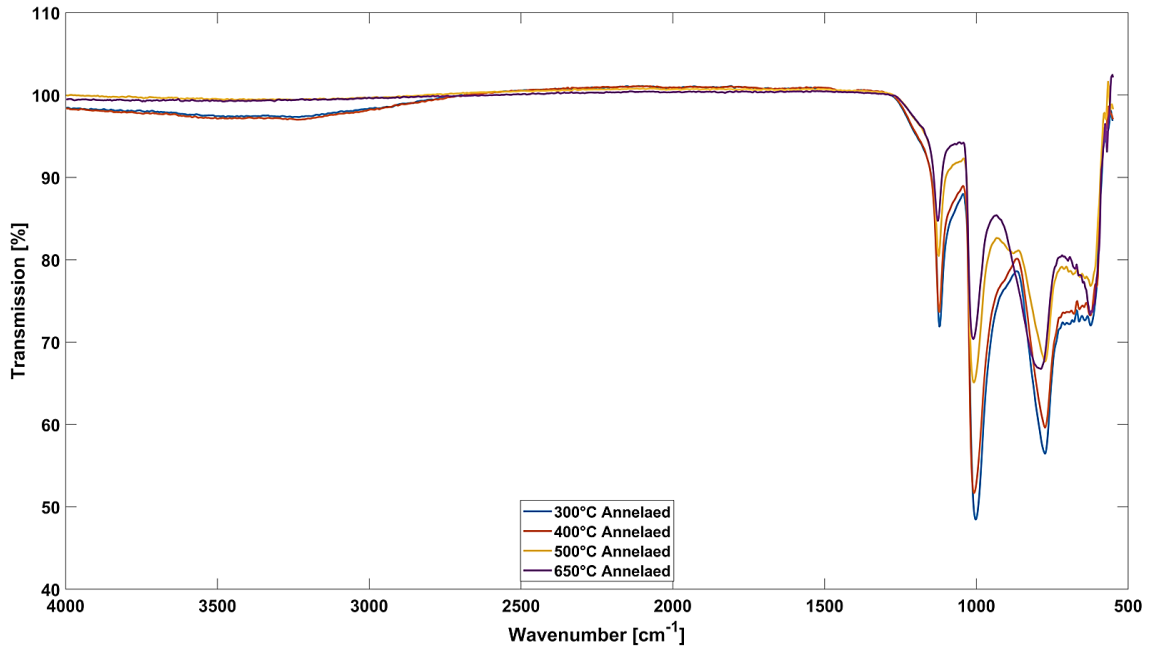


Figure 4- 13 Fourier-Transform Infrared (FTIR) spectra of V_2O_5 samples annealed at various temperatures showing all the samples begin absorption in longer portion of the infrared spectrum where the peak absorption occurring at around $10 \mu\text{m}$ ($\sim 1000 \text{ cm}^{-1}$)

Chapter 5. Vector Light Detector's Fabrication and Processes

5.1. Vector Light Sensor Fabrication Mask Design

This section presents the mask design and fabrication process flow of the proposed devices and further discusses the routes and microfabrication techniques that were involved in the realization of the originally proposed and modified-design devices. The design processes were performed using CoventorWare® Designer software application. The initial device lay out was made through incorporation of the chosen silicon structure width and the insulating oxide thickness estimates presented in Chapter 3, where the optimum combination for a single device was set to be 100 μm and [500-2] μm respectively. These design parameters along with the device per die guideline (minimum of two and maximum of four) imposed a symmetrical square die area for the proposed device mask (Figure 5-1).

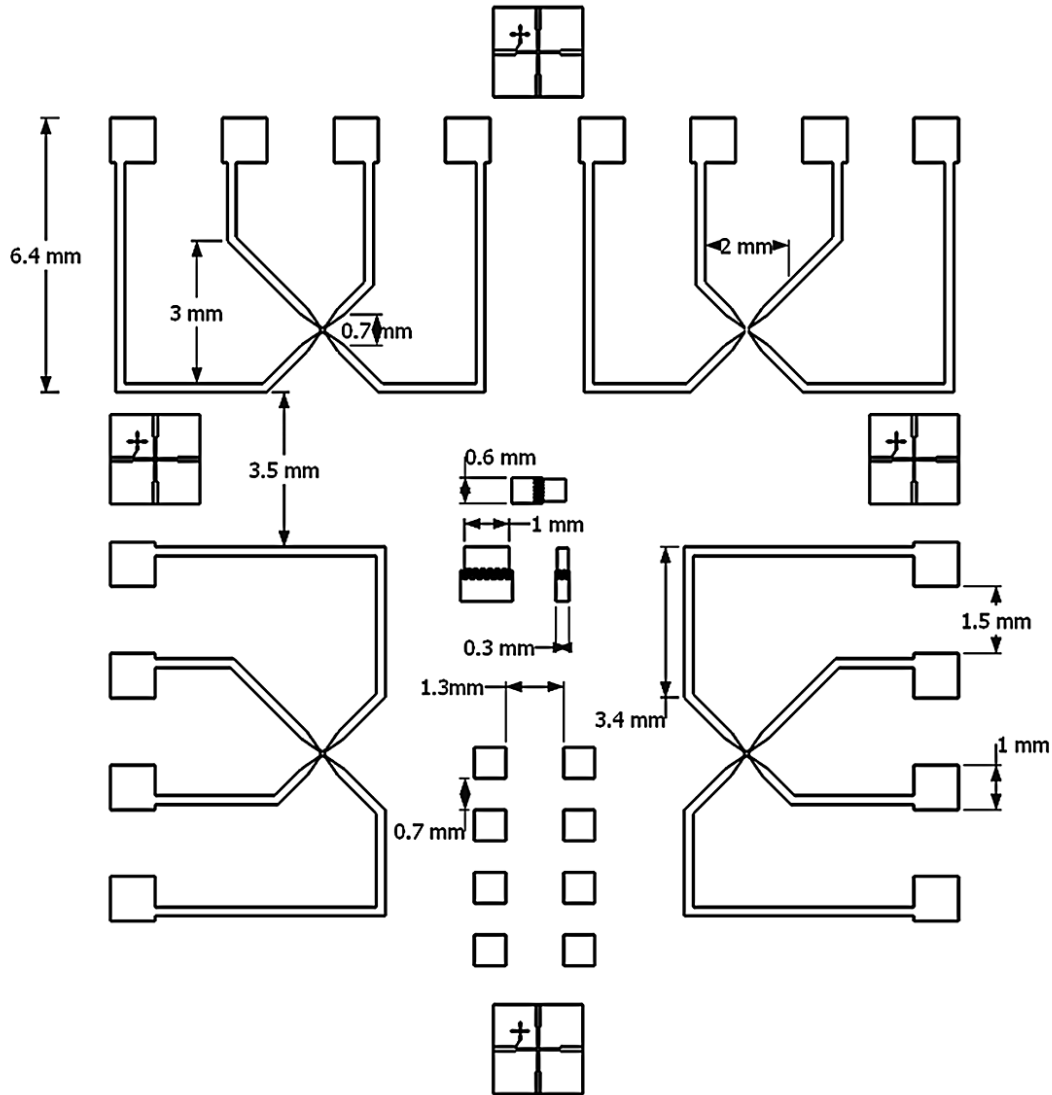


Figure 5- 1 The device floor plan including substrate and metallization masks with dimensions

Due to the resistive nature of the sense areas, in order to increase the contributions of the sense regions on the sides (silicon (111) facets) of the device, to the overall signal readout, the electrodes were designed such that they extend along the sense regions on the side of the three dimensional structure as shown in (figure 5-2) and diverge away when running across the parasitic regions. to maximize the measured contribution of the sense region via forming a minimum length stretch of resistive material between the electrodes at the sense region proximity and maximum length stretch of resistive material between the electrodes elsewhere on the device.

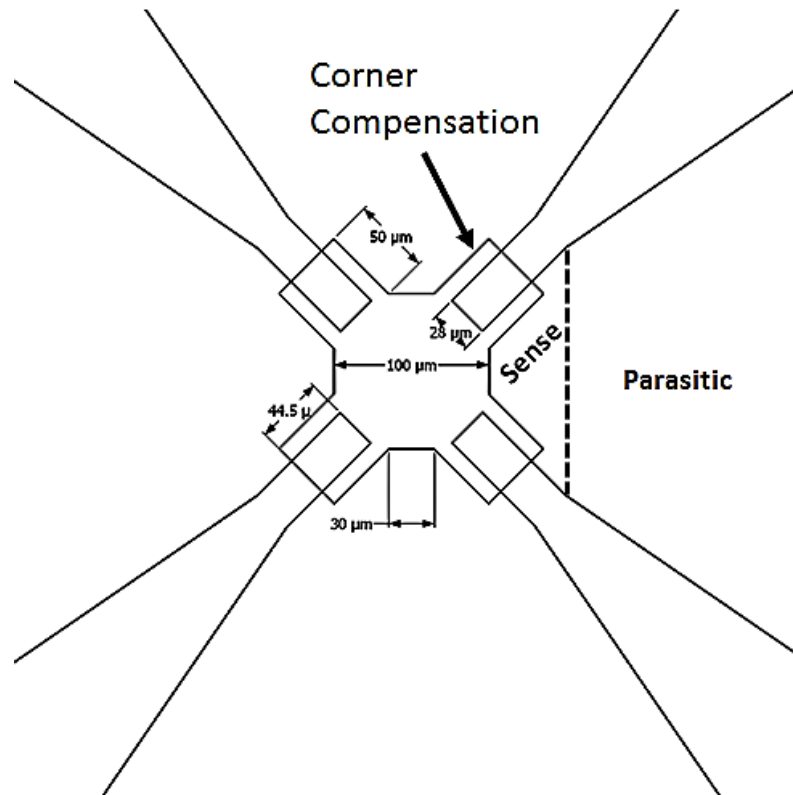


Figure 5-2 Substrate mask design and corner compensation design with dimensions

The mask design for the device as shown in (figure 5-2) contains laterally extended structures termed as “corner compensation” which are in place to counter the corner undercutting effect of silicon anisotropic etching on the pyramidal structure that forms the basis of the proposed device [109], [110]. Prior studies describe the effect that the emergence of high index crystallographic planes with fast etch rates have on the etching process. The higher etch rates of such high index planes relative to the (111) planes triggers a mismatch in the direction and magnitude of etched silicon at the vertices of the (111) planes, and hence results in rounded corners as shown in Figure 5-3 [109], [111].

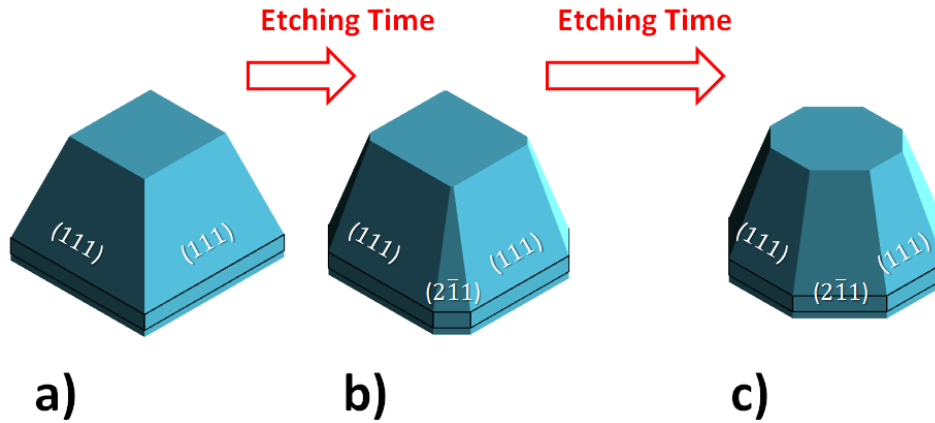


Figure 5-3 An example of emergence of high index fast etching crystalline planes at a) short, b) moderate and c) long exposures of the bulk silicon to an isotropic etchant

The compensatory extensions are therefore added to the original mask to preserve corners from the undercut via over estimating the amount of silicon to etch during the designated etch time. The shape and dimension of corner compensation structures are best defined through empirical models that take into account the type of the etchant e.g potassium hydroxide (KOH), tetra methyl ammonium hydroxide (TMAH) or ethylene diamine pyrocatechol (EDP) and the intended etch depth. Given the choice of etchant for the micromachining process (TMAH), a simple design guideline was used to estimate the shape and dimensions of the corner compensation structures (figure 5-4) [110], [111].

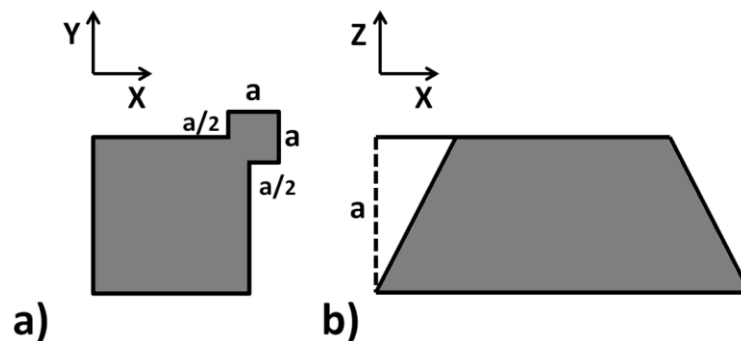


Figure 5-4 The design guidelines for the corner compensation structures with a) surface lengths and b) etch depth

A three level mask process was employed to achieve a 12 die wafer with four devices per die (Figure 5-1). Test electrodes including 4-wire measurement probe pads and interdigitated comb electrodes were included to allow for device level material sheet

resistance and TCR measurements. A second variation of the device was designed with inverted pyramidal cavities within the wafer as shown in Figure 5-5.

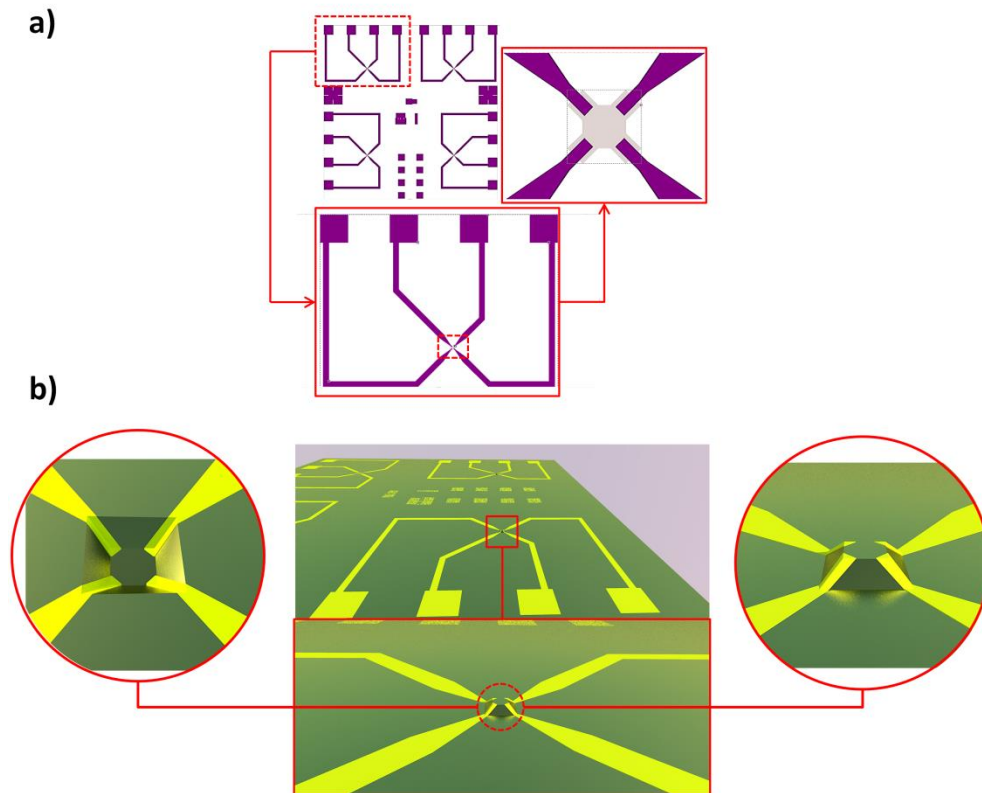


Figure 5- 5 a) 2D and b) 3D rendering of the device floor plan with both upright (mesa) and inverted pyramids in the final form

5.2. Silicon micromachining and basic structure Fabrication

Silicon micromachining has been one of the fundamental processes of modern microelectronics. The technique relies on forming the silicon substrate into particular geometries via introduction of organic/inorganic compounds capable of dissociating the silicon atom bonds, hence etching away the bulk silicon. There are two general types of etching mechanisms employed in silicon micromachining: 1) wet etching and 2) dry etching. In the first category (category of interest in this work), the silicon wafer is immersed in solution phase etchant whereby the material removal occurs through a four step process as in i) etchant molecule diffusion to the silicon surface, ii) etchant molecule adsorption onto the silicon surface, iii) chemical reaction between the etchant molecule and the silicon surface and iv) desorption and dissolution of the chemical reaction products

back into the bulk etchant. Depending on the homogeneity of etch rates across all of the crystalline planes, the process is further categorized into isotropic (homogeneous etch rates) and anisotropic (inhomogeneous or selective) etching. The majority of anisotropic silicon etchants are alkaline solutions that have higher etch rates along the (110) and (100) planes compared to the (111) crystalline planes. This mismatch results in different geometrical shapes depending on parameters such as the wafer orientation, etchant and etches duration. Given the pyramidal design of the substrate, wet anisotropic etching on silicon (100) was chosen as the method to create the basic structures. Of the available choices of anisotropic etchants KOH and TMAH, TMAH was chosen due to better etch selectivity between silicon dioxide and silicon. The other advantage of TMAH is CMOS compatibility. Use of KOH in silicon bulk etching could result in ionic contamination of the silicon surface which can impede microelectronic device functions [75]. The bulk silicon etching was performed in the cleanroom environment and the wafers underwent standard RCA I-II cleaning processes before being placed in the oxide tube furnace for a 45 minute duration thermally grown oxide mask layer. The resulting 510 nm oxide mask layer was then coated with a positive photoresist (AZ-MIR 703) that was spin coated at 3200 rpm to create a 1.3 μm thick photoresist (PR) layer. A UV mask aligner (OAI-MBA 800 with $\lambda = [245 - 364 \text{ nm}]$) was used to transfer the sub-mask pattern onto the wafer. Finally, the exposed regions of the PR were removed by the PR developer. The remaining PR was used as a masking layer to pattern the oxide layer via a buffered oxide etches (BOE) solution at room temperature (See Figure 5-6).

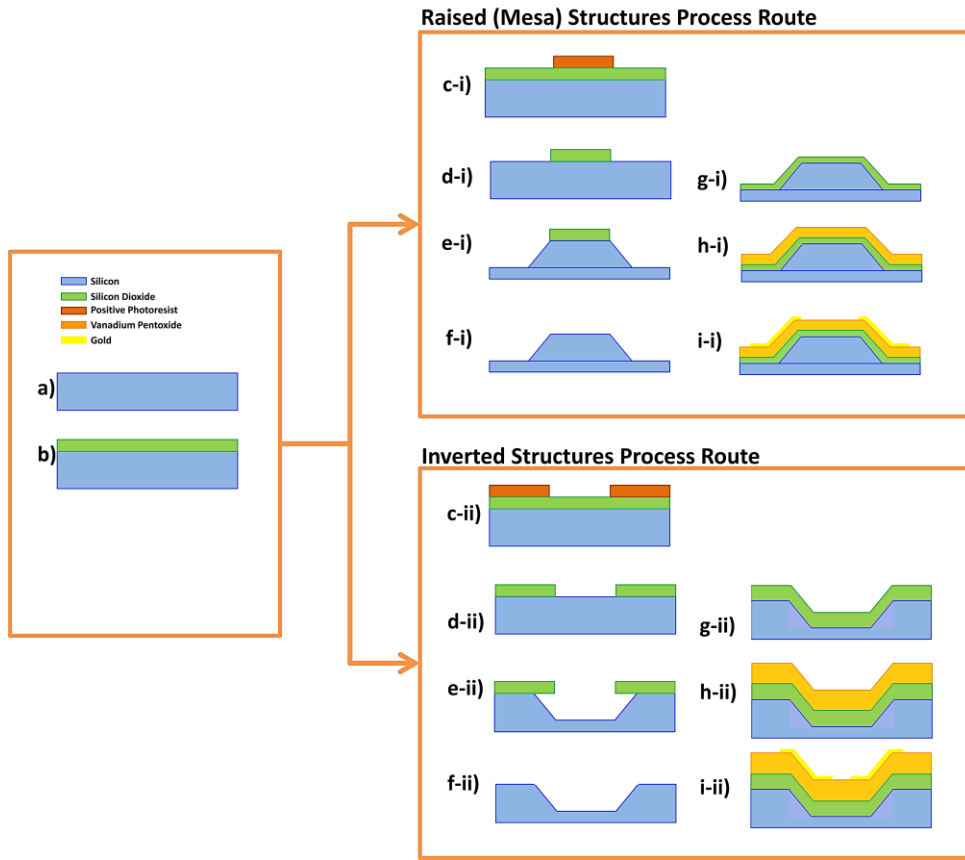


Figure 5- 6 a)-i) The device fabrication process flow with d-i) to i-i) depicting the mesa and d-ii) to i-ii) the inverted structures

The resulting oxide pattern was further used to etch the silicon substrate in TMAH solution at 90 °C. In order to achieve better surface roughness characteristics, 5 wt% isopropanol (IPA) was added into the mix during the etch time of 45 minutes at every 12 minutes for constant etching conditions. The mixture was stirred magnetically at a constant 35 rpm rate to maintain homogeneity across the etchant solution (Figure 5-7).

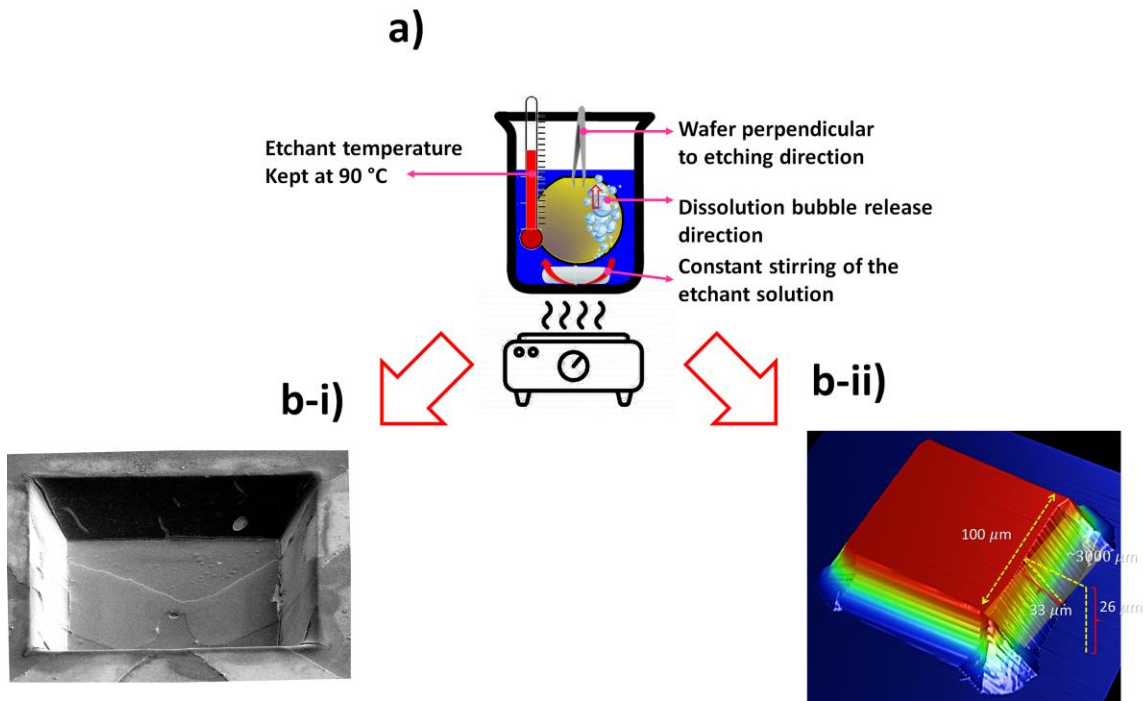


Figure 5-7 a) Silicon etching in TMAH. The wafer was oriented perpendicular to the etching direction to achieve optimum surface uniformity, b-i) the inverted pyramid structure and b-ii) the mesa pyramid structure.

After TMAH etching, the wafers were placed in an oxidation furnace for 55 minutes to achieve 560 nm of silicon dioxide as an electrical and thermal insulation layer between the substrate and the sense layer. This description of your process is unclear. You need to lay this out step by step.

5.3. Photoresist Spray Coating on 3D Structures

Figure 5-7 illustrates the typical quality of pattern transfer and fabrication resulting from the described processes. The mesa structures are depicted by the three dimensional profilometry of the micromachined silicon substrate, while the inverted pyramid structure is imaged with a tilt-view scanning electron micrograph. The images indicate acceptable agreement between the desired and fabricated device depth, width and overall quality for both structures. The next step in the device fabrication process flow was the sense material and electrode deposition. Given that the lithography process needed to be carried out on non-planar surfaces, attempts to use traditional spin coating methods proved problematic and did not yield uniform photoresist deposition that would realize the electrode and contact patterns as designed. As a consequence, it was necessary to develop a process to create a uniform resist coating of the three dimensional structures

for subsequent lithographic patterning. However, for optimum pattern transfer during photolithography on a non-planar surface, the thickness uniformity and coating surface roughness becomes an important issue due to non-uniform PR exposure. For use in contact lithography, resist thickness non-uniformities result in uneven exposure dosages that lead to variable post exposure development times. The latter has a detrimental impact on the deposited contact quality and overall metallization process. Between the two proposed coating methods, drop casting offers less control over the thickness when the structure topography varies significantly across the target surface area. The use of electro deposition and spray coating methods have been previously employed for non-planar surface coating processes [112], [113] whereby both techniques offer a good degree of corner coverage and conformality. However electrodeposition requires liquid photoresist and customized deposition setup to achieve the desired coating. As a result, spray coating was selected for the work described in this thesis. This took advantage of an available ultrasonic spray deposition system (Sono-Tek model Exacta-Coat) to deposit PR for the 3D lithography process associated with the metallization portion of the device. Since there is no readily optimized process flow for uniform PR deposition over 3D surfaces, a process-recipe was developed to assure reproducible and uniform thickness PR film deposition across the structured silicon surface. The recipe provides optimum parameters for the spray coating system such as spray nozzle sonication power, distance to surface, patterning speed, patterning inter-line width, fluid flow rate and idle power. Additionally matters such as the photoresist dilution ratio, number of coatings, inter-coating wait time and coating direction were also determined experimentally to yield the desirable coating for the ensuing 3D lithography process. The optimum parameters mentioned above are summarized in Table 5-1 supplemented by Figure 5-8.

Table 5- 1 Optimum spray coating parameters for conformal photoresist deposition

Pump Flow Rate [ml/min]	Nozzle Idle Power [Watts]	Nozzle Run Power [Watts]	Spray Path Width [mm]	Spray Path Speed [mm/min]	Spray Air Shaping [U.U]	Resist Dilution Ratio [PR:Diluent]	Distance To Sample [mm]
0.15	1.3	3.5	3	75	0.72	3:1	11

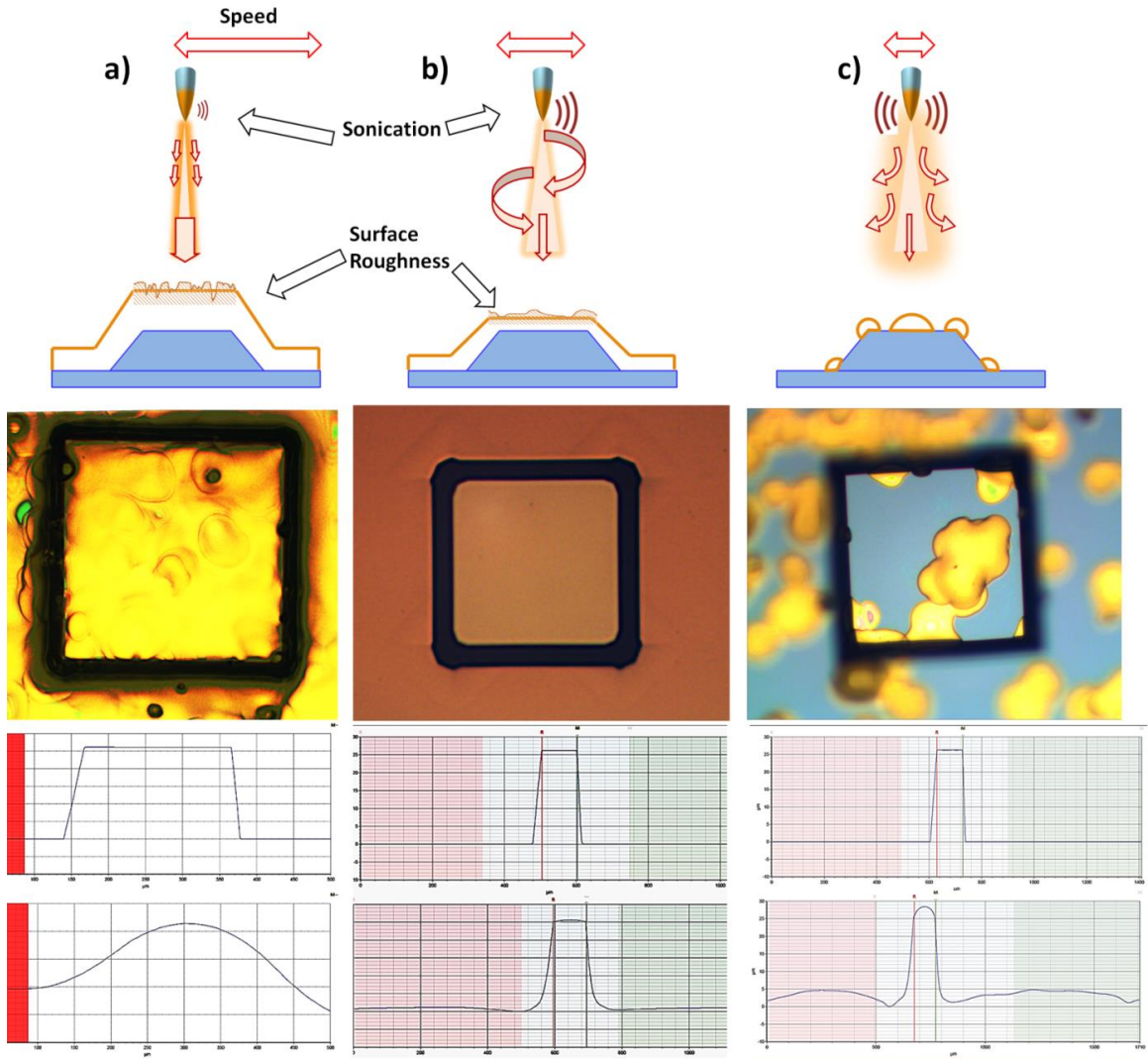


Figure 5- 8 Different parameters affecting the spray coating process on a 3D surface. The process optimization is designed to avoid a) cavity planarization as a result of excess resist deposition and c) granulized resist formation due to overly powdered resist flow as a result of high sonication power. The uniform layer is achieved in middle ground between the two extremes with high enough sonication power and low enough speed as depicted in b).

5.4. Vanadium Pentoxide Preparation and Deposition

The recipe for vanadium pentoxide sol-gel deposition was chosen based on the synthesis parameters from Chapter 4 to yield the highest TCR value and lowest possible sheet resistance. The synthesis parameters are presented in Table 5-2. An automated dip coater was used to dip the samples with constant dipping and pulling rates with appropriate wait time (how long?) for each layer in order to enable precursor hydrolysis. To choose the best dip coating recipe, the bulk micromachined silicon wafer was diced into 12 one inch square dies. Four different dies were chosen to investigate the effects of dipping frequency and orientation on the deposited thin film uniformity and integrity before coating the remainder of the devices with vanadium pentoxide. The four dipping procedures were used to investigate the effect of increase in the number of coated layers on the resulting film uniformity and coating conformality. The dipping and pulling rates (dip rate 100 mm/min, pull rate 75 mm/min) were held constant for all the four samples and were chosen based on the characterization results from Chapter 4. The number of coated layers were 4, 6, 8 and 12 respectively with the 12 layer coated sample rotated at every four coating to investigate the effects of the dipping orientation on the overall film quality and uniformity (Figure 5-9).

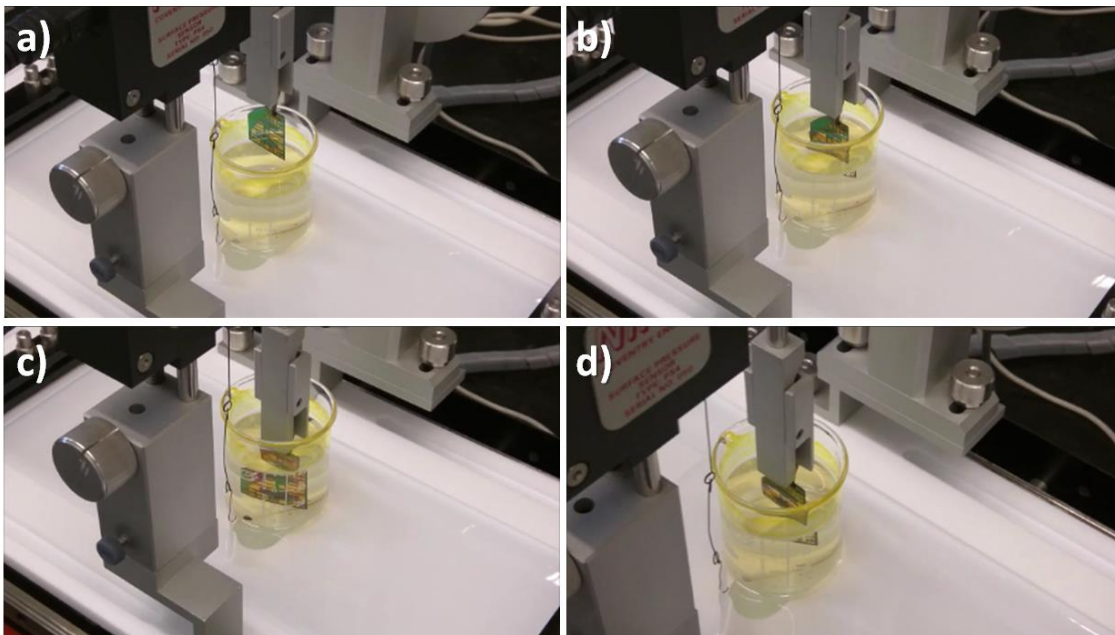


Figure 5- 9 The automated dip coating setup used to deposit vanadium pentoxide sol onto the samples. The figures a) through d) depict a full dipping cycle whereby the sample is completely submerged into the solution to avoid non-uniformities induced by dip lines as a result of multiple coatings

Further analysis of the dip coated test devices was performed using the optical microscope and profilometer. Figure 5-12 shows the optical microscope images of the four dip coating protocols. From a visual standpoint, the 4-layer and 6-layer coated devices showed no significant differences in the overall surface texture of the deposited vanadium pentoxide except for the formation of slightly larger crystallites following the annealing process in the thicker coated sample (see below). The 8-layer coated sample showed good coverage across the edges of the inverted device. The annealing process resulted in the appearance of larger crystalline domains across the coated surface while the surface integrity of the coated film remained intact. The 12-layer device showed cracked material surfaces as a result of the thick film hydrolysis. Annealing of the 12-layer sample resulted in the occurrence of many cracks in the domains as the material crystallized. The cracked morphology was attributed to both excess layer thickness and the overlapping of dipping lines, which introduces an uneven distribution of material due to gravity pull as the substrate exits the solution (Figure 5-10).

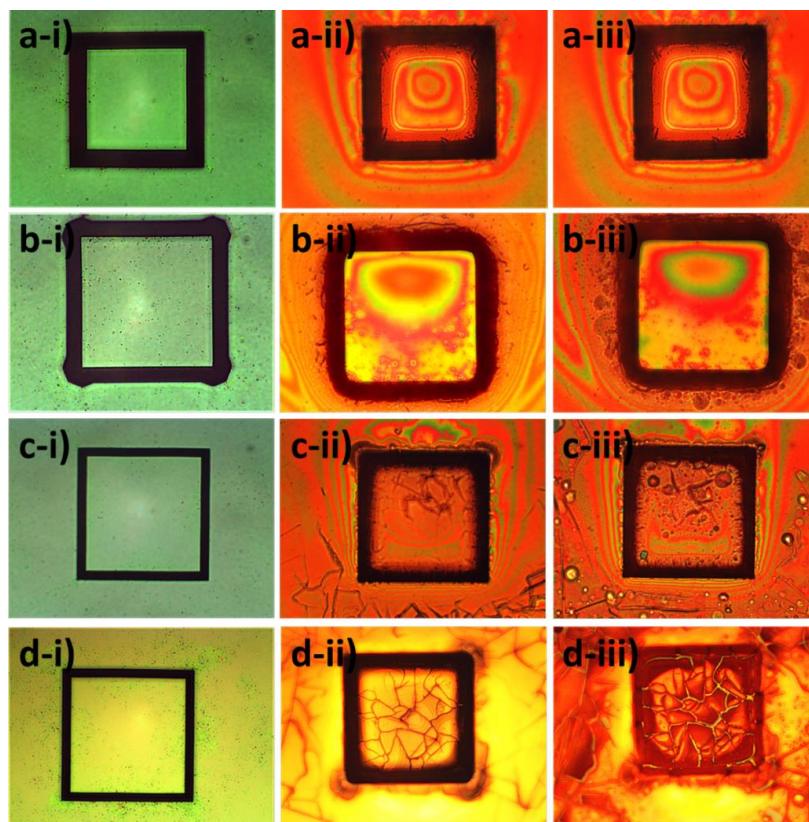


Figure 5- 10 The V_2O_5 dip coating routines one mesa and three inverted sample structures with a-i) – d-i) depicting the bare, a-ii) – d-ii) the pre-annealed and a-iii) – d-iii) the post annealed samples for 4, 6, 8 and 12 coated layers.

Table 5-2 The synthesis and annealing parameters of the deposited V_2O_5 layers

Precursor Name	Precursor Chemical Formula	Precursor Concentration [ml]	Solvent and Buffer Solution	Stirring Time [min]	Hydrolysis Temperature [$^{\circ}$ C]	Annealing Condition
Vanadium Tri-isopropoxide	$OV(OCH(CH_3)_2)_3$	7.6	Isopropanol (IPA)	120	25	480 $^{\circ}$ in Air

The analysis of the profilometry data showed similar degrees of surface integrity and coating uniformity for the pre- and post-annealing for 4-, 6- and 8-layer thick samples, however the step coverage on both of the 4- and 6-layer coated annealed samples was slightly slanted due to material flow. Given that the design goal was to have a relatively uniform coverage of the silicon substrate's (111) surfaces with vanadium pentoxide acting as the sense material, more pronounced step coverage was needed. The 8-layer coated inverted sample showed a desirable degree of step coverage and acceptably small surface roughness (Figure 5-11), and was consequently chosen for further device work. The deposition and annealing conditions for this and subsequent device fabrication are described in Table 5-2.

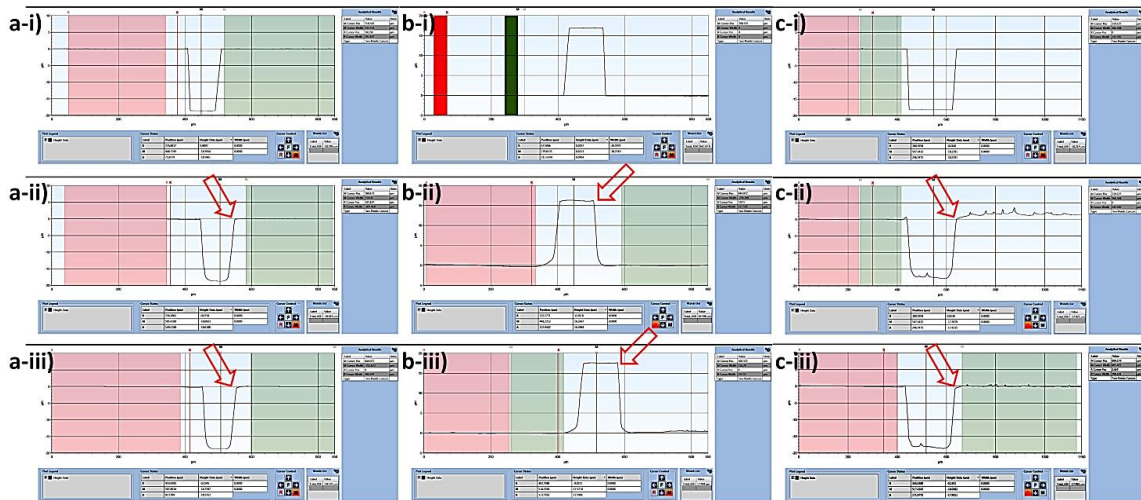


Figure 5-11 The pre deposition, post deposition and post annealing profiles of one mesa and two inverted structures undergone V_2O_5 dip coating for a-i) to a-iii) 4, b-i) to b-iii) 6 and c-i) to c-iii) 8 coatings using the synthesis parameters presented in table 2 and dipping and pulling rate of 50 mm/min

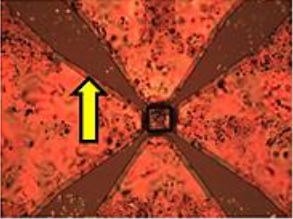
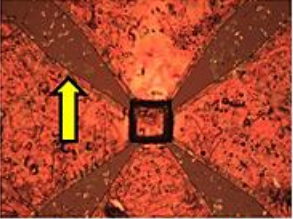
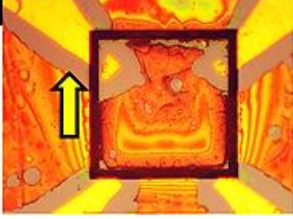
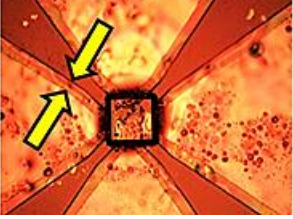
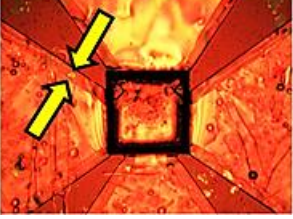
5.5. 3D Lithography and Electrical Contact Deposition

The electrode deposition and patterning on the 3D surfaces was performed through three investigative processes before achieving an acceptable final procedure. Given the introduction of vanadium pentoxide as a sense layer to the otherwise standard microfabrication process flow, material compatibility challenges arose due to its reactivity with the acidic or alkaline development solutions typically implemented in silicon processing technology. As a result, different V_2O_5 patterning processes were investigated and are briefly discussed below.

5.5.1. Process 01: Gold (Au)-Over- V_2O_5 Lift-off

The target process flow (shown in figure 5-6) was intended to transfer the desired electrode pattern onto the devices coated with the sense layer. For this process, the chosen device sample dies were dip coated with the parameters presented in table 2 to achieve a uniform and conformal layer of vanadium pentoxide across the sample. Post the annealing process, and using the optimized spray coating recipe from table 1, the die surface was coated with positive photoresist (AZ MIR 703) and exposed to UV light for three different exposure times: 1) 5 s 2) 15 s and 3) 55 s. The first two exposure times were based on the recommended amount by the PR manufacturer's manual and the third exposure was meant to investigate the effects of bleaching the thick resist layer. Results are presented in table 5-3.

Table 5- 3 The post resist development and lift-off process results for different exposure times using the process flow from figure 47. The yellow arrows mark the isotropic removal of the underlying V_2O_5 layer as a result of interaction with the photoresist developer.

Sample Name	INV_200_b_Prcs_01	MES_100_c_Prcs_01	INV_200_b_Prcs_01
Structure Type	Inverted Pyramid	Mesa (Upright) Pyramid	Inverted Pyramid
Exposure Time	5 [s]	15 [s]	55 [s]
Image 5x			
Image 10x			

For this process and using thermal evaporation technique, Chromium-Gold (Cr-Au) (10 nm-200 nm) was deposited over the annealed vanadium pentoxide layer. As depicted in table 5-3 the 5 second exposure resulted in partial electrode pattern transfer while removing the sense material along with the exposed photoresist from underneath the deposited Au layer. The lift off process was unsuccessful for the longer exposure times and resulted in complete removal of the vanadium pentoxide along with the overlying Cr-Au layer. The 10x resolution microscope images presented in table 3 show the isotropic removal of the underlying V_2O_5 layer as a result of resist development process.

5.5.2. Process 02: Gold (Au)-Over- V_2O_5 Lift-off-Chromium-Mask

Further investigation into the issue made aware of the susceptibility of the vanadium pentoxide film to the active component in the developer under use (AZ MIF 300) which is diluted tetra methyl ammonium hydroxide (TMAH). As a result an extra stage was added to the overall process flow depicted in figure 5-6, which provided a thin layer of chromium mask underneath the deposited Au. The goal of this added step was to prevent the sense material's interaction with the resist developer during the lift-off process. The process would however require use of chromium etchant in order to remove the excess chromium

from the sense area and finalize the electrode patterning stage. The variation of the process flow is depicted in figure 5-12.

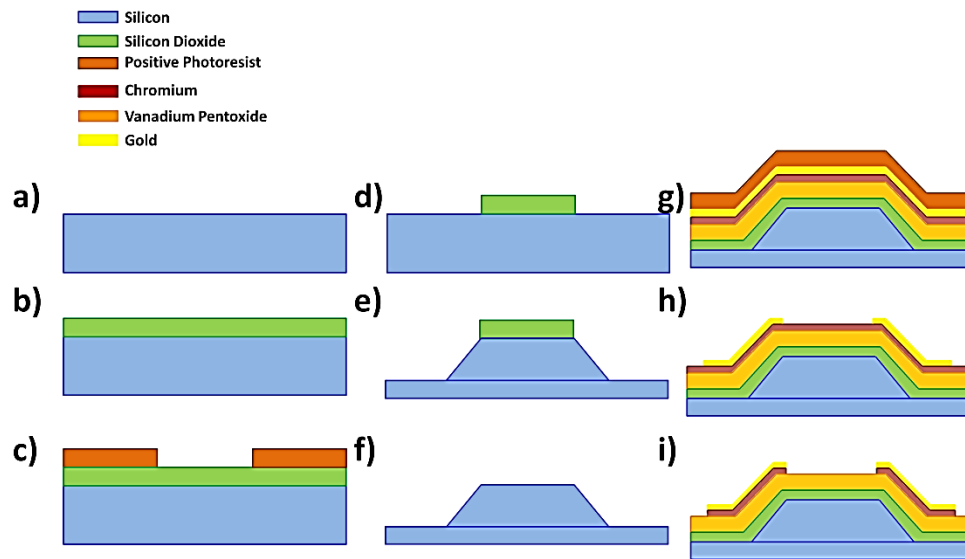


Figure 5- 12 The variation to intended process flow whereby the lift-off process happens through a layer of chromium aimed to protect the underlying vanadium pentoxide from direct interaction with photoresist developer.

For this variation and in order to verify the effects of chromium etchant on the sense layer a trial process was run having a conformal layer of chromium mask (70 nm) sputtered across a sample die. An inverted photo-mask was used to successfully transfer the target electrode pattern onto the chromium (figure 5-13), however the ensuing chromium removal using the designated etchant (CEP 200) resulted in removal of the underlying vanadium pentoxide along with the chromium.

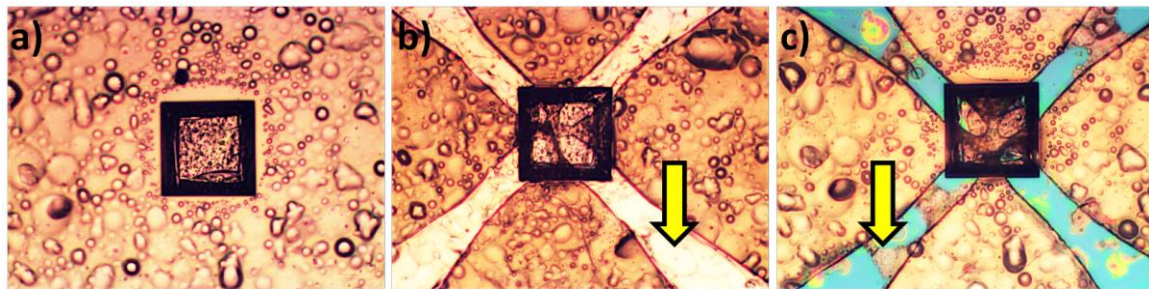


Figure 5- 13 The inverted structure undergone the trial lift-off process depicted at a) post chromium deposition, b) post PR deposition and patterning and c) post chromium etching. The result of this trial rendered the proposed process obsolete due to the removal of the underlying V_2O_5 layer due to the chromium etchant CEP 200.

5.5.3. Process 03: (Gold)-Under- V_2O_5 Lift-off-Small-Pads

As a result of unsuccessful pattern transfer trials using the main proposed process flow and the variation thereof, and taking into consideration the isotropic etching effects induced by the applied photoresist developer (AZ MIF 300) a new process flow was developed to achieve the desired electrode pattern while maintaining the deposited vanadium pentoxide integrity. Given the volatility of V_2O_5 when coming in contact with developers and etchants, prior to V_2O_5 coating of the dies, the Au electrode pattern was transferred onto the silicon dioxide insulation layer. The samples were then coated with a V_2O_5 thin film such that the electrodes were placed underneath the coated film. Given high thermal durability of Cr/Au, the annealing routine was similar to the previous process flows (480 °C – 6 ½ hours) to further hydrolyze and cure the deposited hydrated vanadium pentoxide gel. A forth mask was designed to create via-like openings over the contact pads of the already deposited Cr/Au electrode pattern. The goal of such design was to take advantage of the isotropic nature of V_2O_5 removal when placed inside AZ MIF 300 photoresist developer. Figure 5-14 shows the result of the new process flow dubbed “small-pad lift-off” due to the use of the fourth mask and small vias through to the electrode pads passed the V_2O_5 layer.

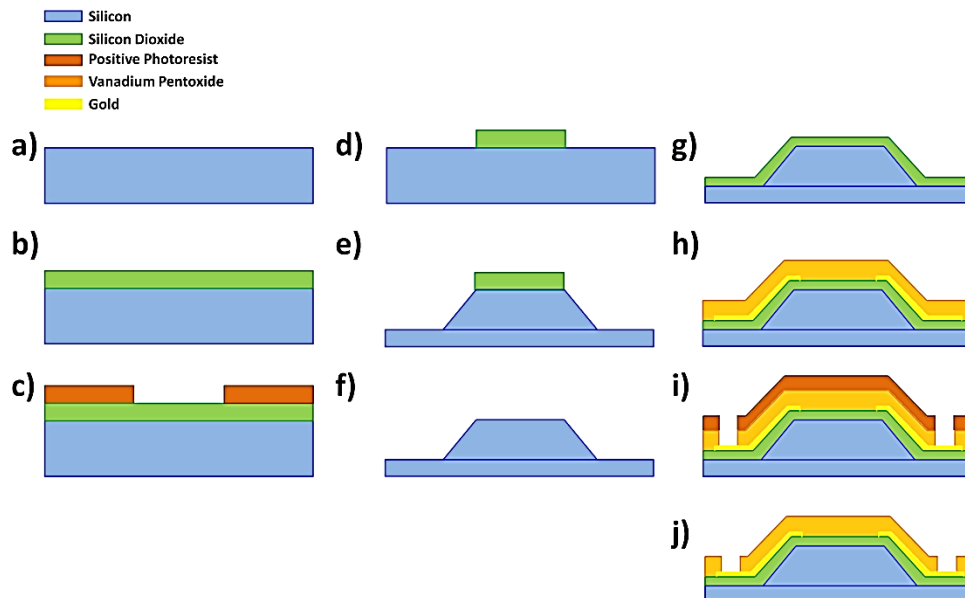


Figure 5- 14 The third and final process flow resulting in a successful deposition and lift-off of the designated electrode pattern underneath the sense material.

Figure below (figure 5-15) depicts a schematic of the position of the via-like openings on top of the Cr/Au electrode pads underneath the annealed vanadium pentoxide layer.

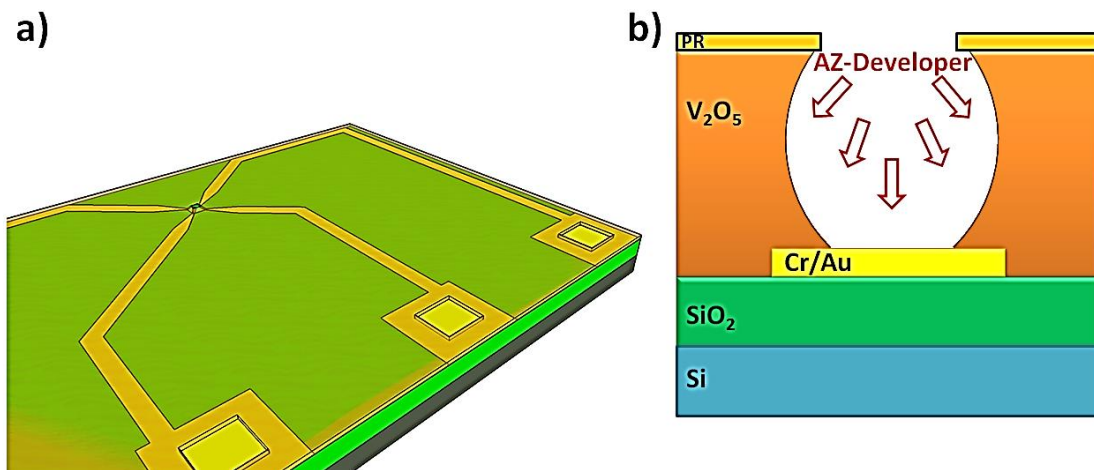


Figure 5- 15 a) 3D rendering of the device using the "Au-under-V₂O₅-SmallPad" process flow; b) a 2D cross-section of the mechanism by means of which the electrode pads were accessed through the sense material.

As a result of the last process flow, both upright (mesa) and inverted versions of the pyramid device were finalized with a good degree of vanadium pentoxide uniformity and integrity as well as via openings to the contact pads for wire-bonding and further device level characterization. Final device images are presented in the following figure 5-16.

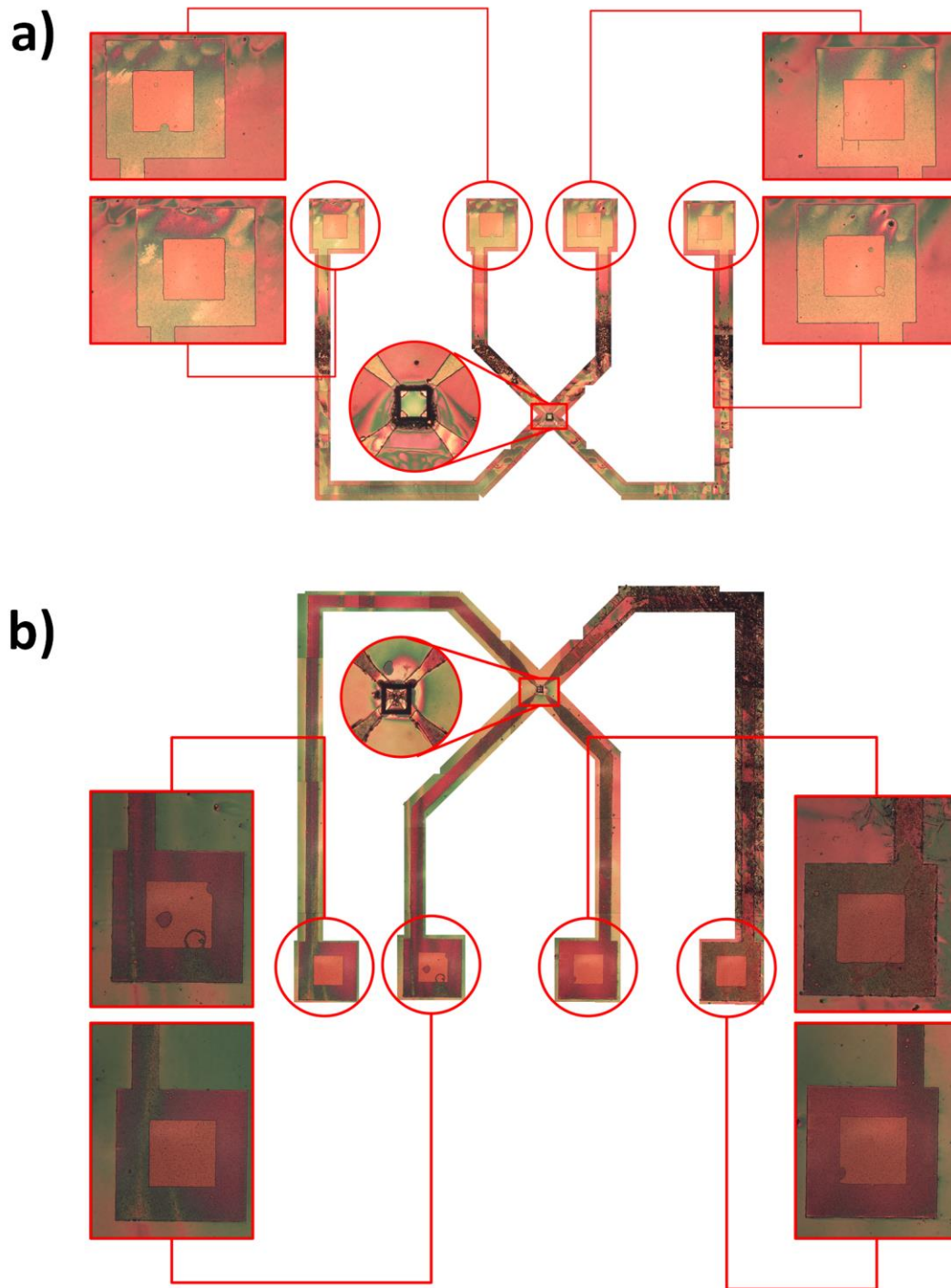


Figure 5- 16 A collage of the actual a) mesa and b) inverted pyramid structures fabricated with the final process flow. The figures show the electrode configuration on the device body as well as the contact openings providing access to the Au electrode pads through the dip coated V_2O_5 layer.

Chapter 6. Experimental Results and Discussion

6.1. Device Level Characterization

This chapter focuses on the fabricated device's electrical characteristics as well as the experimental results used to verify the accuracy and functionality of the fabrication process flows presented in the previous chapter. Further, the IR response characteristics of the fabricated devices such as responsivity, sensitivity to human induced radiation, and response time are discussed in more detail.

6.1.1. Raised (Mesa) Device IV Characteristics

I-V characterisation tests were performed on the devices in order to verify the quality of the electrical contacts and to measure the sheet resistance across the dip-coated and annealed thin films on two finished samples, one raised (mesa) pyramidal device and one inverted. The tests were performed in a class 100 cleanroom environment using a probe station. The measurements were run across two of the three test comb electrodes available on each device die as shown in Figure 6-1 below. The comb electrodes dubbed as large and medium were designed with a constant digit-to-electrode length ratio and were scaled with $\frac{1}{2}$ of size difference whereby the large electrode's single digit dimension was $40\ \mu\text{m} \times 190\ \mu\text{m}$ and the medium electrode digit dimension was $20\ \mu\text{m} \times 190\ \mu\text{m}$.

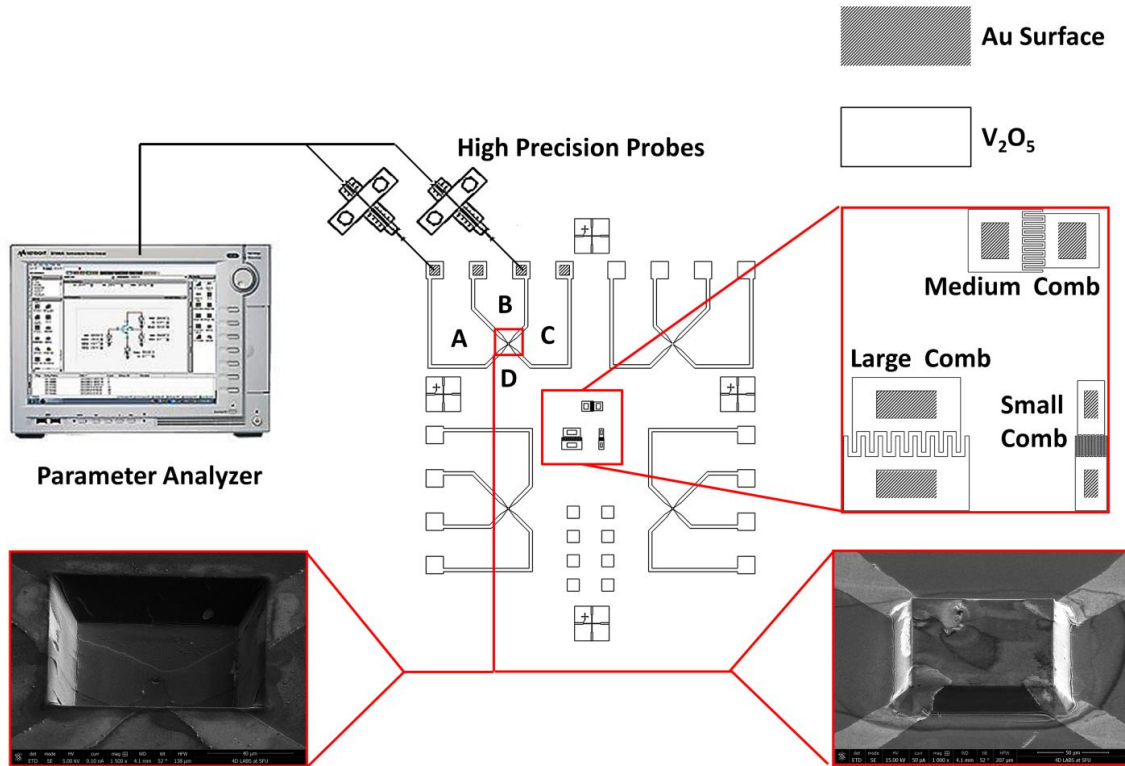


Figure 6- 1 The schematic of the experimental setup used to measure the sheet resistance of the sense material across the sample devices

The average sheet resistance from each comb electrode is calculated via a rough approximation depicted in Figure 6-2 below such that the total measured electrical resistance is equated to the parallel contribution of larger resistive stretches confined between the digits while ignoring the smaller inter-digit regions on each electrode. The overall contribution of the parallel resistances can then be used to recalculate the sheet resistance as in the following:

$$R_S = \left(\frac{N_{digit}}{N_{\square}} \right) \cdot R_{Measured} \quad (61)$$

$$R_{Measured} = \frac{1}{N_{digit}} \cdot R_{digit} \quad (62)$$

$$R_{digit} = R_S \cdot N_{\square} \quad (63)$$

Figure 6-3 and 6-5 shows the characteristic I-V curves for each of the device types. Since IV characteristics of a semiconductor material such as vanadium pentoxide is likely to be of a non-linear form, the linear and quasi-linear I-V responses of the raised (mesa) and

inverted devices suggest an ohmic contact and the successful removal of V_2O_5 from the surface of the gold (Au).

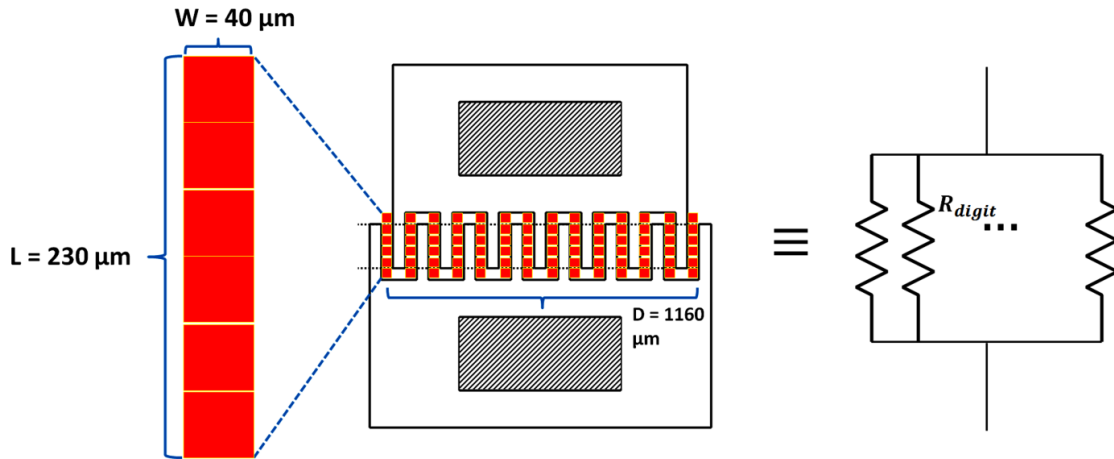


Figure 6- 2 Approximaton approach in order to evaluatre the sheet resistance of the sense layer using the comb electrode structures which resulted in $98 \text{ k}\Omega/\square$ for mesa and $91 \text{ k}\Omega/\square$ for the inverted device sample

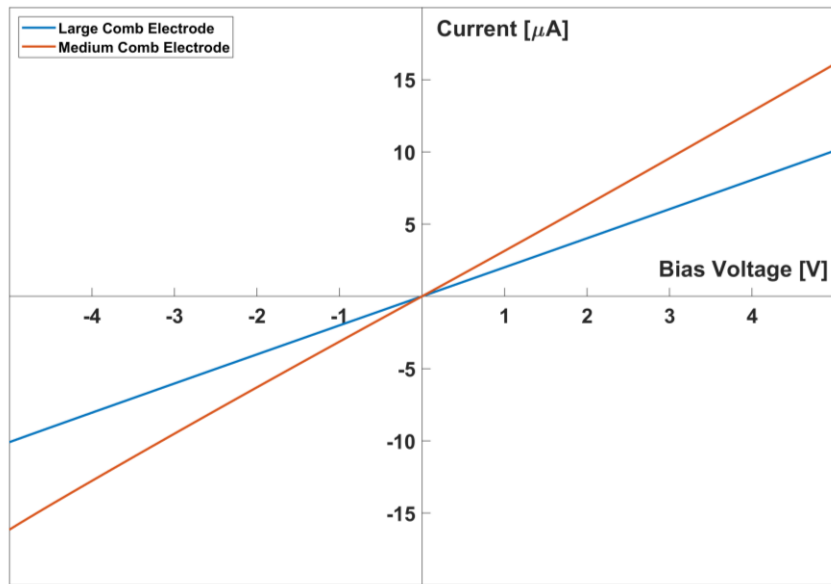


Figure 6- 3 I-V traces measured across the large and medium sized comb structures.

The response of the electrodes encompassing regions A, B and C as depicted in Figure 6-1 is presented in Figure 6.4. The linear IV characteristic curves from the readout terminal pads also indicate the effectiveness of the fabrication process flow in terms of V_2O_5 removal from the surface of the Au electrodes.

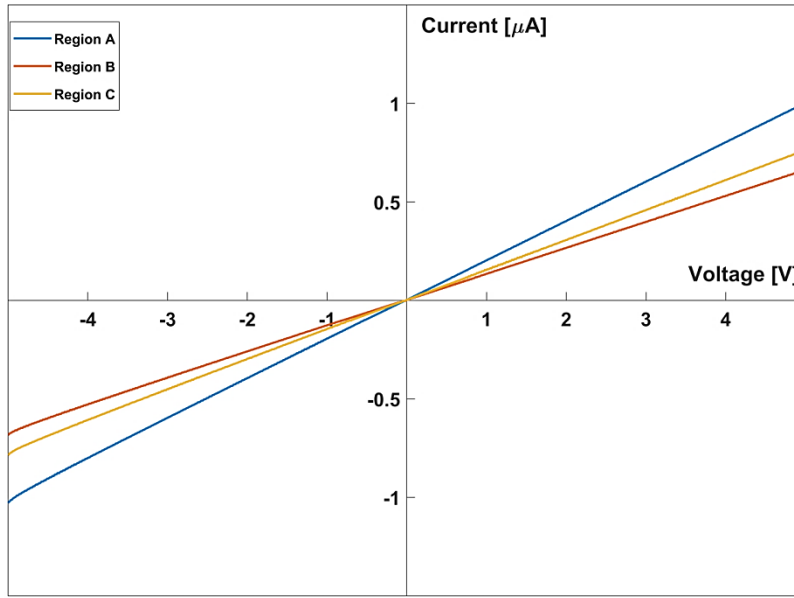


Figure 6- 4 I-V curves measured across the output terminals of different regions of the raised (mesa) device as labeled in figure 1; the slight differences in the slope of the traces from each of the regions points out the potential material thickness and/or area mismatches.

6.1.2. Inverted Device IV Characteristics

The inverted device structures were also characterized. The set up was similar to the one depicted in Figure 6-1 and the curves are shown in Figures 6-5 and 6-6 below. Similar to the raised devices, the linear I-V characteristics from the large and medium size comb electrodes indicate removal of the deposited V_2O_5 from the designated surfaces across the Au electrodes as described in Section 5.5.3.

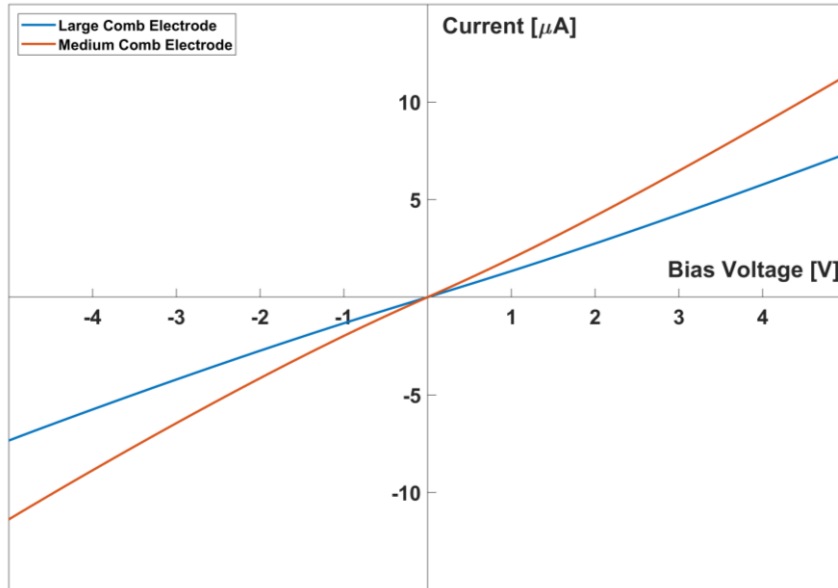


Figure 6- 5 I-V responses of the inverted device sample recorded from large and medium size comb electrodes; The traces from each size scale corrected for difference in structure dimensions show similar slopes.

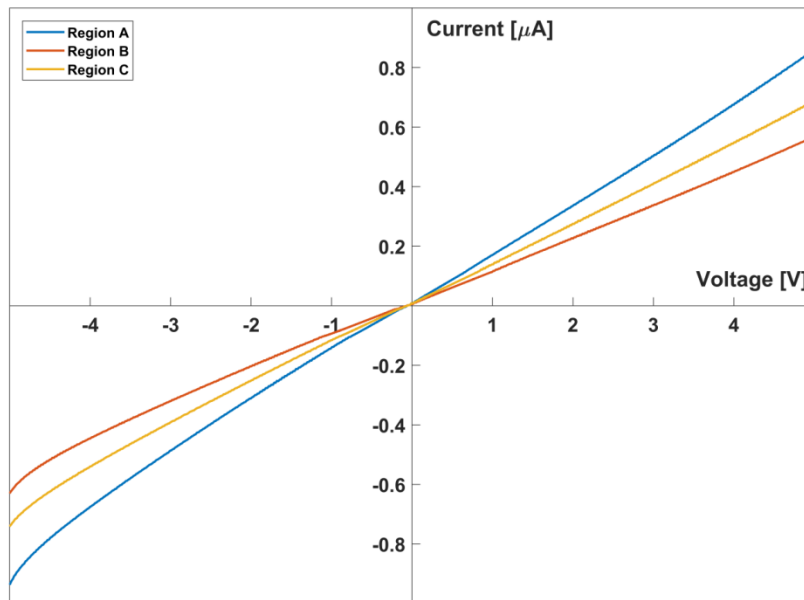


Figure 6- 6 IV curves measured across the output terminals of different regions of the inverted device as labeled in Figure 6-1; the slight differences in the slope of the traces from each of the regions points out a larger degree of potential material thickness mismatch and or area across different sense regions.

6.2. Device Level (1st Design Generation) IR Response

This section discusses the characteristic behavior of the fabricated devices using the process flow discussed earlier in Chapter 5. The characterization of the fabricated device was done to assess the device's response to IR radiation as well as its ability to track an IR source in an angular field of view and further recalculation of the incidence angle.

6.2.1. Device Level (1st Design Generation) Signal Acquisition and IR Response (Pre-FIB)

Since the die proportions of the 1st generation devices were larger than the available standard packaging, and to avoid optical reflection due to the die-to-package Au bonding, a prototyping board was used to transfer the signal from the readout terminals into standard SMA ports. For better signal acquisition and creation of good electrical contact between the device's readout terminal and the prototyping board, silver epoxy resin was used to map the output terminals into the proper connections and further into the SMA connector outlets (see Figure 6-7).

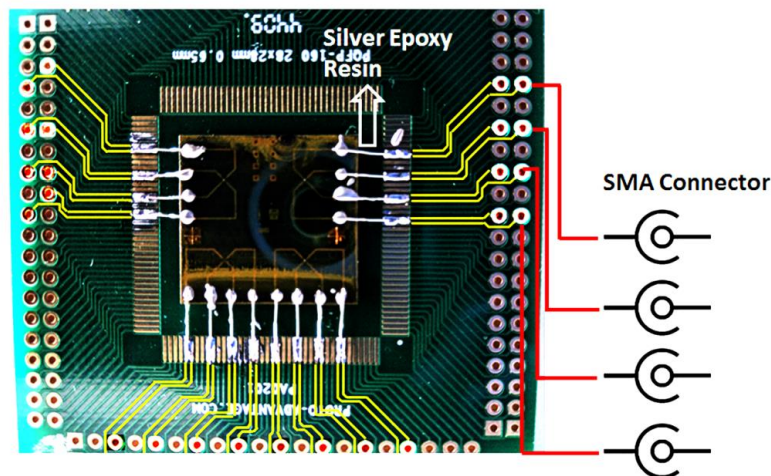


Figure 6- 7 Output routing of the sample test device wire-bonded to a prototyping board using silver epoxy resin

To measure the angular response of the devices, two opposing regions (regions A and C) were chosen. The contact to the terminal pads on each of the chosen regions was made such that to enable characterization on each side independently (See Figure 6-8).

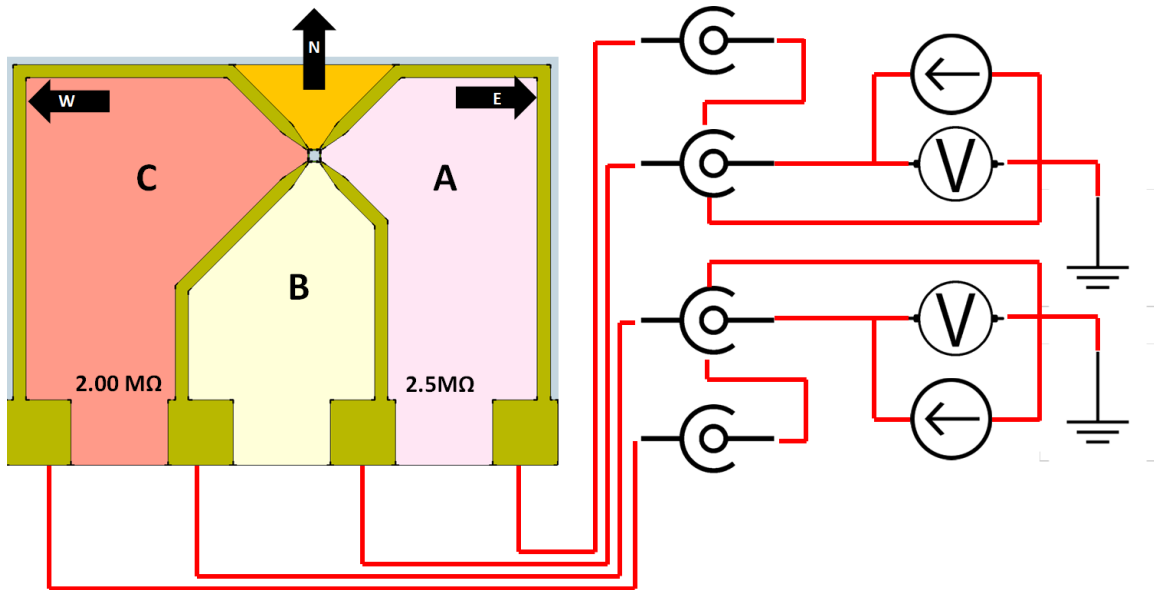


Figure 6- 8 Device's output terminal mapping as prepared for testing device's electrical resistance across each sense region. The difference in room temperature resistances across the two terminals could be a result of different surface area and/or material thickness variations on the two sides.

The I-R responsivity of the 1st design generation of the devices were tested using a proto-board-mounted raised (mesa) type device and a broadband light source (Thorlabs SLS203L Globar 500nm – 9000nm). The reason for this choice of light source was the broad spectral distribution which covered a wide range of infrared wavelengths. In order to reduce the number of unknown parameters affecting the device IR responsivity measurements, an optical test setup was put together such that the globar's output beam was spatially filtered with an iris, and focused onto a quasi-circular region encompassing the device under test (DUT). An optical rotary stage was used to enable precise angular changes of the DUT for IR angular measurements (Figure 6-9). The received power at the detector was measured using a power meter to be ~25 mW.

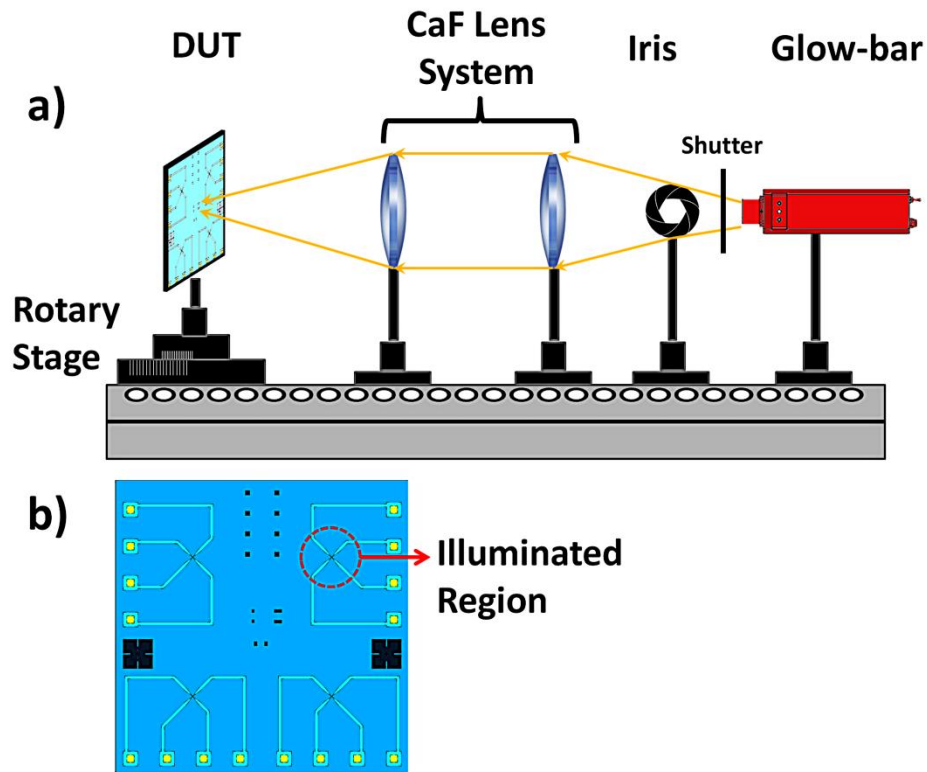


Figure 6- 9 a) Schematic of the optical test setup used for IR measurements; The calcium-fluoride (CaF_2) lenses were used to allow for focusing of the incident IR radiation onto the designated test area. b) The spotsizes of the focused IR onto the DUT sense area

An automated data capture setup was put together using two Keithley 2400 source meters and NI LabView ® software such that the source meters were linked through GPIB-USB interface to the data acquisition system. The first part of the experiment was performed using a manual optical shutter and exposure times long enough for the device signal to stabilize (~ 60 s) (Figure 6-10).

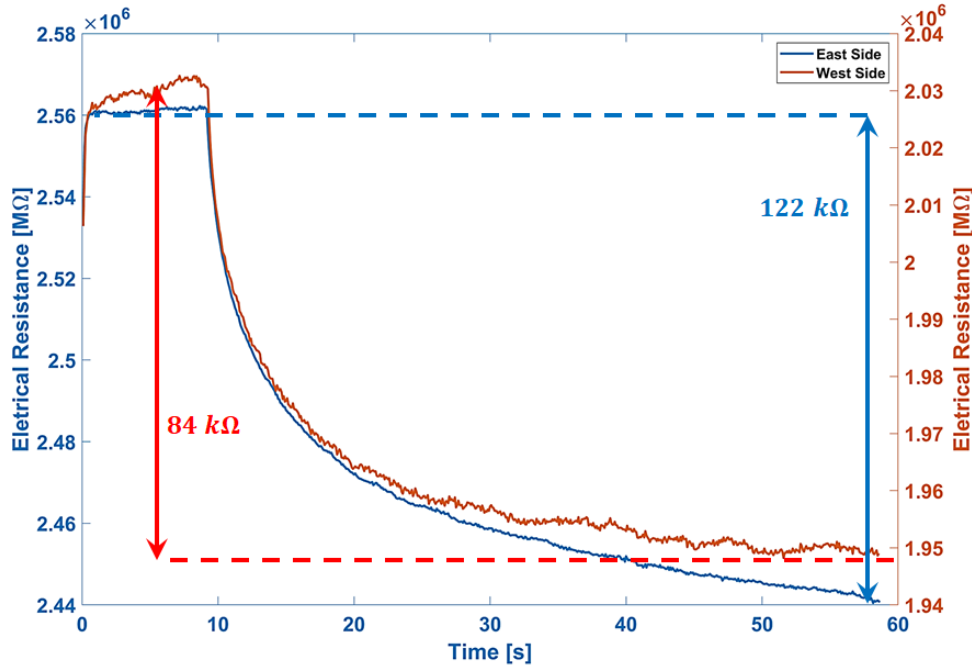


Figure 6- 10 The IR induced change in the electrical resistance of the DUT. The exposure time was set long enough for the signal to stabilize as a result of the incident radiation

The traces show the electrical resistance drop of the two opposing sides of the DUT (regions A and C in figure 6-8) as a result of being exposed to the radiative power of the global source. The regions A and C are labelled as east (left) and west (right) side of the device based on the DUT orientation with respect to the radiation source. It is evident from the traces that the two sides have different room temperature resistances yet show relatively similar IR induced resistance changes with $\Delta R_{East} \approx 122 \text{ k}\Omega$ and $\Delta R_{West} \approx 84 \text{ k}\Omega$, corresponding to 4.7% and 4.1% decreases in the room temperature resistance of the respective sides of the DUT. The device’s response to human IR emission was also tested using a similar optical setup without the iris and the converging optics (Figure 6-11). The measurements were performed on a proto-board-mounted raised (mesa) type device. The respective changes of the electrical resistances across the opposing sides of the device labelled as east and west (referenced to Figure 6-8) show minor but distinguishable trends in response to in-plane human hand motion. Given the low incident power density of the human induced IR radiation at a distance of 75 cm, the signal changes in the east and west side are minor but evident. The exposure resulted in an approximate 0.07% change in the electrical resistance of the sense material indicating sensitivity to human induced IR emission. The results and the respective trends as a function of human hand exposure to the device are presented in Figure 6-12.

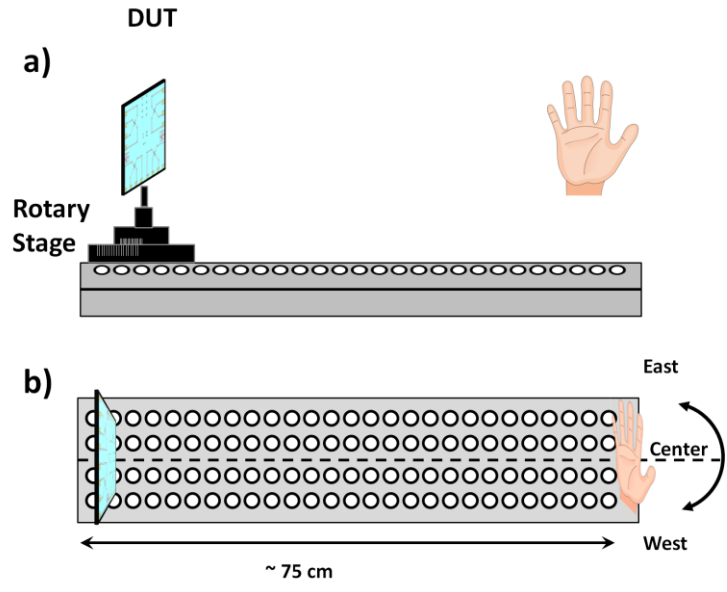


Figure 6- 11 a) out of plane and b) in plane schematic depiction of the human hand induced IR response test setup

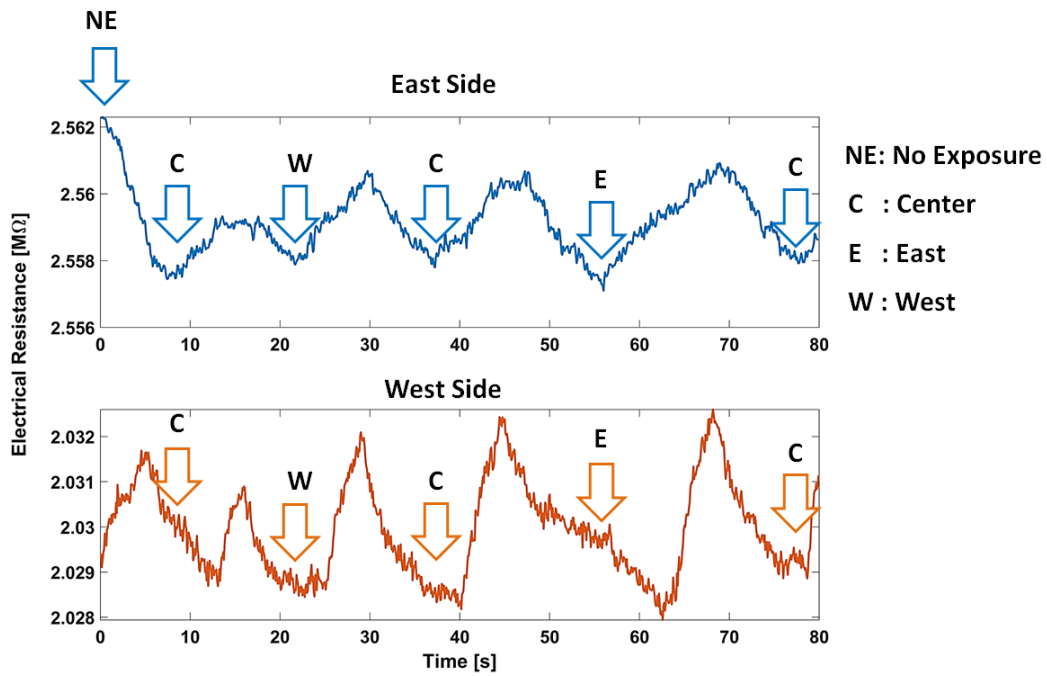


Figure 6- 12 Changes in the electrical resistance of east (top) and west (bottom) side of the device as a result of human hand exposure at 75 cm. The markers indicate slight opposing changes in the resistance as a result of in-plane angular hand motion

6.2.2. Device (1st Design Generation) IR Incidence Measurement (Pre FIB)

The angular response measurements of the devices were carried out using the test setup depicted in Figure 6-9-a by rotating the DUT with respect to the fixed incident light direction. However, a software controlled shutter was used instead of the previously used manual one to allow for consistent data acquisitions with different exposure times. In order to measure the angular modulation of the IR induced electrical resistance change, the IR source was kept at a fixed position and the device was rotated within the angular area confined between the normal to surface on either of opposing facets as shown in Figure 6-13-b.

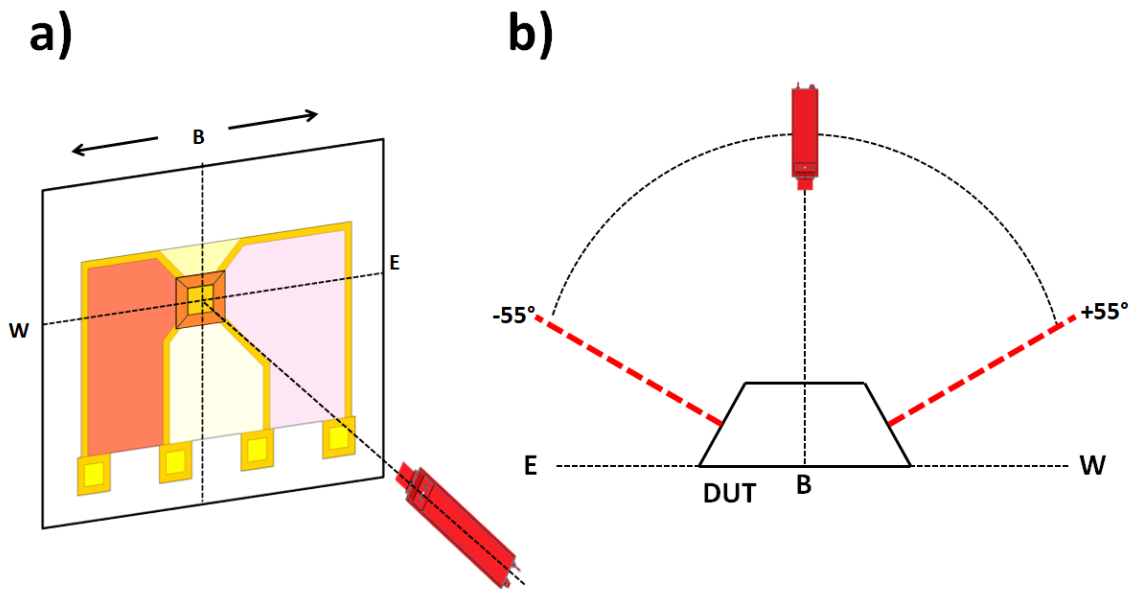


Figure 6- 13 a) 3D and b) 2D depiction of the IR source position with respect to the detector. The arc between the facet normals depicts angular path of the source to generate different incidence angles

Prior to testing the device's angular response, it was taken into account that the two sides of the DUT demonstrated different room temperature resistances yet similar responsivity to the incident IR. Since the angularly modulated response model presented in Section 3.1.2 requires similar room temperature resistances on the opposing sides of the device to quantify the IR induced changes and the incidence angle recalculation, the $\Delta R/R$ measurements were normalized. The aforementioned was accomplished via an intensity dependent responsivity test that was run using standard optical neutral density filters. The exposure was made at normal incidence to the top facet of the square pyramidal structure.

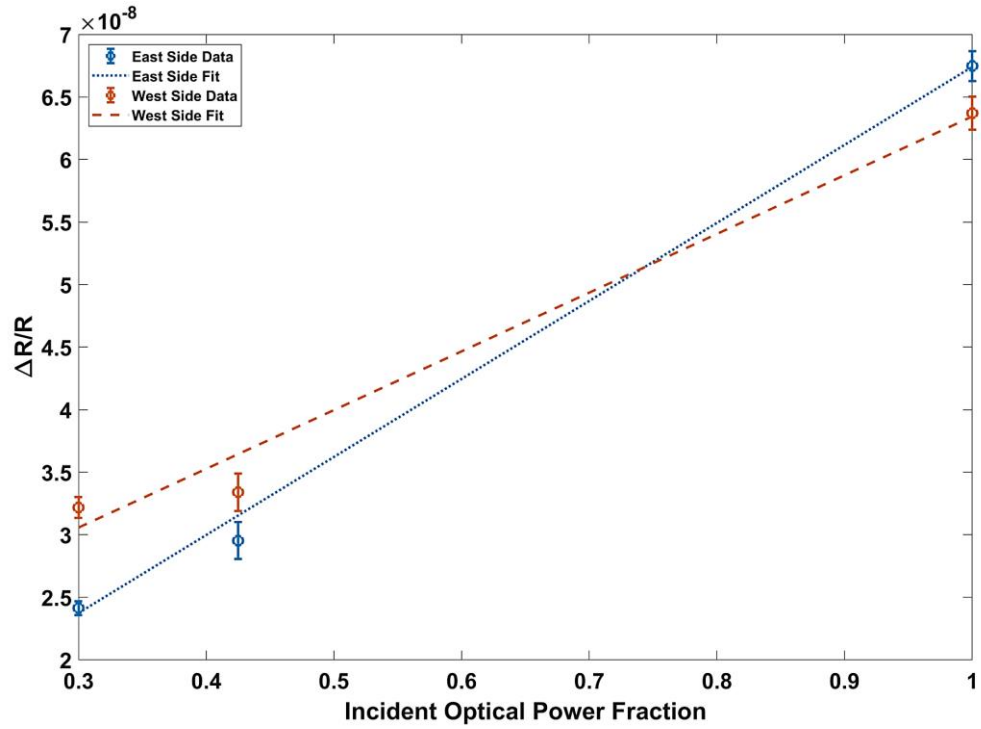


Figure 6- 14 Device's output response to fractioned incident optical power using optical neutral density filters. The mismatch in the slope of the linear fits indicates different responsivity of the two sides and the uncertainty arises from the electrical resistance fluctuations of the device prior to exposure to IR source for each fraction of the incident power.

The trends in figure 6-14 confirm the device's change in the electrical resistance on the two sides was proportional to the incident optical power fraction. The difference in the slope of the linear fits to the device response at the two sides indicates different responsivities to the incident IR. The ratio of the different slopes is therefore used to further normalize the device's angular response of one side to the other in the following sections.

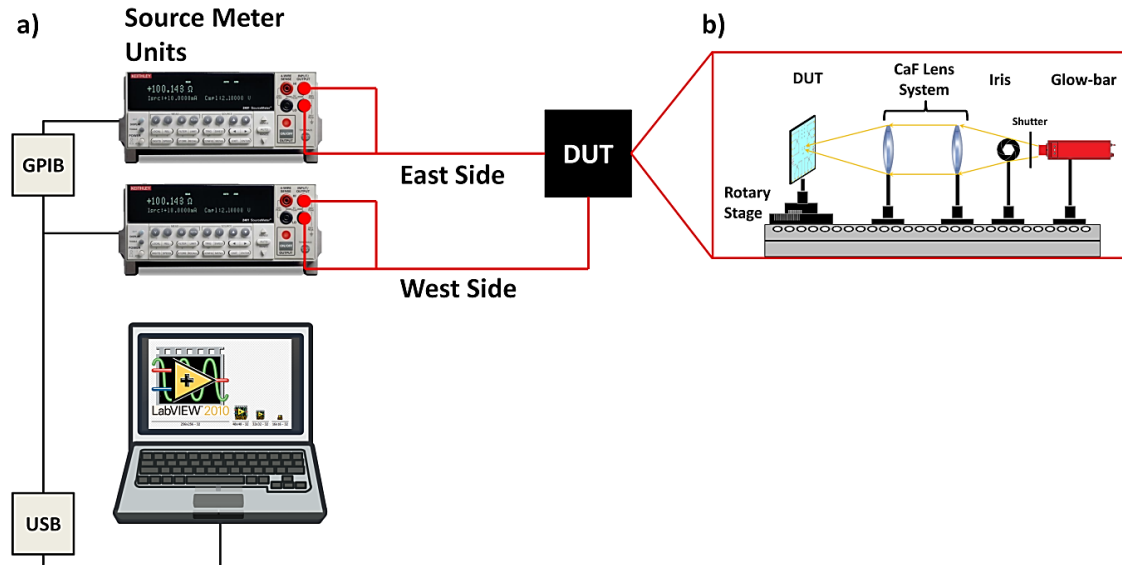


Figure 6- 15 Schematic of the optical test setup used for measuring the DUT's IR angular response

The measurements were carried out at 15 degree increments starting at -55° and ending at $+55^\circ$ (Figure 6-13-b) using an automated data capture setup (see Figure 6-15). The NI LabView[®] controlled shutter was set to an exposure time equal to 10 s and measurements were recorded at each incident angle. Due to the mismatch in responsivity, the device's absolute response to the incident IR on each side was calculated as the measured drop in the electrical resistance over the recorded value of the electrical resistance prior to the exposure of the device to the incident IR. The proportionality factor calculated from the responsivity test was used to normalize the west side resistance changes to that of the east. The acquired trend for the first generation of devices (see Figure 6-16) depicted a similar parabolic change in response to angular exposure to the IR source. This was unlike the opposing trends as predicted by equation (30) and (31) presented in chapter 3. Since the theoretical trends are the outcome of a change in the electrical resistance of the opposing sides of the device as a result of different but complementary angular exposure to the incoming radiation, similar trends indicated the existence of potential contribution of IR sensitive regions outside the designated sense areas on the (111) facets of the proposed detector. Due to the fact that this contribution would distort the device's proposed capability to recalculate the incoming IR's incidence angle, from this point on, these resistive regions are referred to as "parasitic resistive regions".

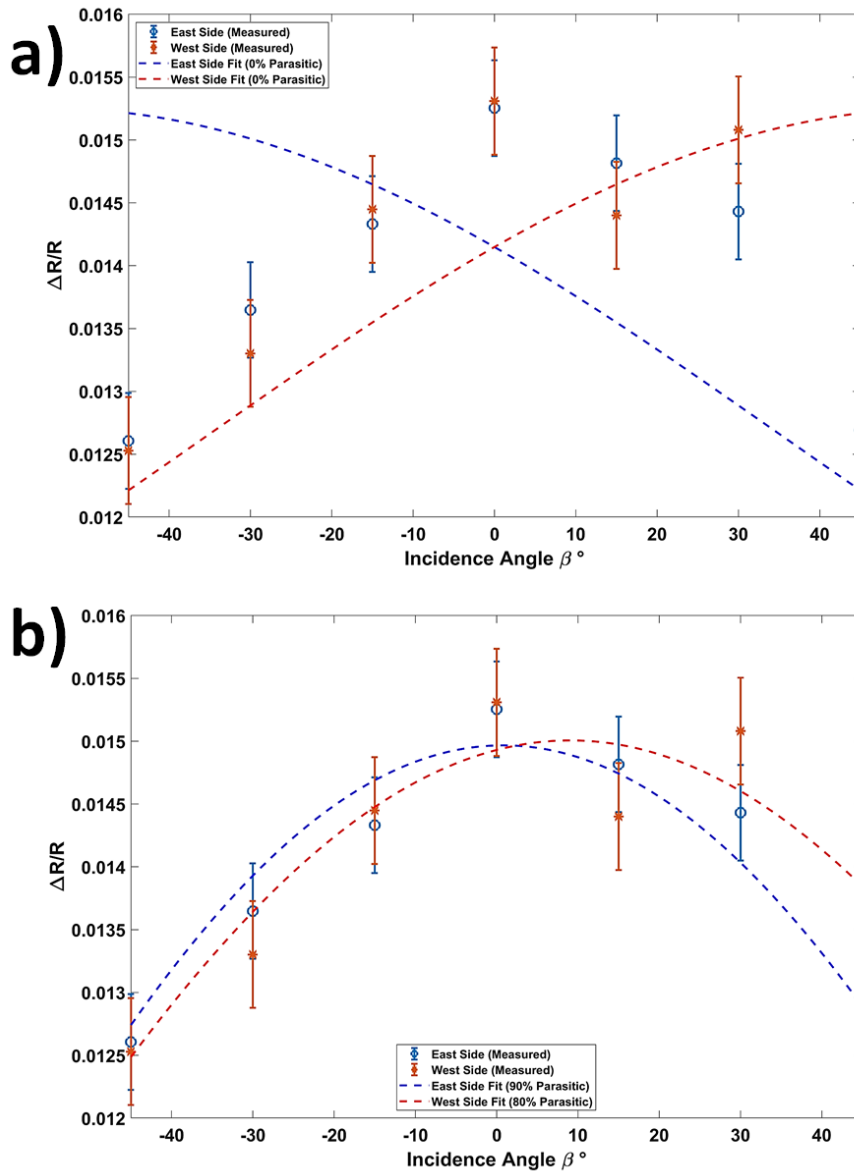


Figure 6- 16 DUT's angular $\Delta R/R$ response along with the theoretical or expected trends for a) ideal case (no parasitic resistance region contribution) and b) recalculated theoretical trends with 90% parasitic contribution to the east side and 80% parasitic contribution to the west side. The measurement uncertainty is calculated as the temperature induced fluctuations of the electrical resistance experienced over the entire duration of experiment. Statistical inference of the fitted model is provided in Appendix D.

In order to evaluate the contributions of the parasitic resistive regions and their impact on the expected trends based on the mathematical model presented in section 3.2.3, the expected trends were calculated both with and without the existence of the parasitic contributions (see Figure 6-16-b). Figure 6-17 below depicts the effect of 30%, 50%, 70%, 80%, 90% and 100% parasitic contribution on the IR trends using the proposed mathematical model by equation (36) in section 3.1.2, chapter 3.

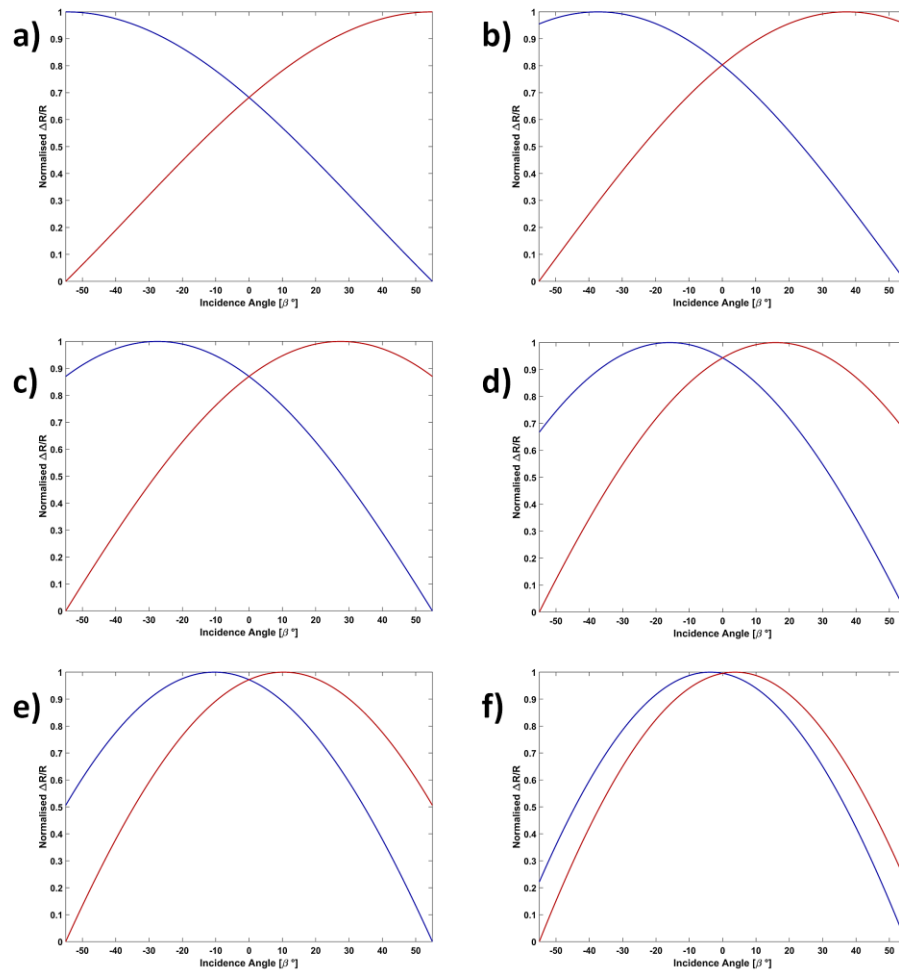


Figure 6- 17 The effect of a) 0%, b) 30%, c) 50%, d) 70%, e) 80% and f) 90% parasitic resistive contribution to the theoretical $\Delta R/R$ trends as a result of exposure to IR.

Approximation of Parasitic Resistive Regions Contribution to the Device's Performance

In this section a detailed discussion on the contribution of the parasitic regions is presented. Initially and during the design stage of the proposed detector, it was hypothesized that the overall measured electrical resistance across the readout electrodes of the device will be dominated by the charge carrier transfer through the sense vanadium pentoxide that lies on the inclined sides of the device. This was thought to be due to the lower resistive path that forms in between the electrodes on the sides in opposed to the larger surface area elsewhere across the device. The observation of the similar trends in the 1st design generation of the devices proved the case to be otherwise.

Referenced to equation (35) the angular responsivity of the proposed detector relies on the modulation of the sense areas that reside on opposing (111) facets of the silicon substrate. In the current device, deposition of the sense material across large areas such as the flat regions atop the structure and at the foot of the silicon (111) facets (Figure 6-18) would result in the formation of parasitic resistive regions that contribute to the overall measured resistance during IR exposure. The contribution of these flat areas can be modeled as a mathematical term present in the signal and that can be incorporated into the device's angular responsivity expression.

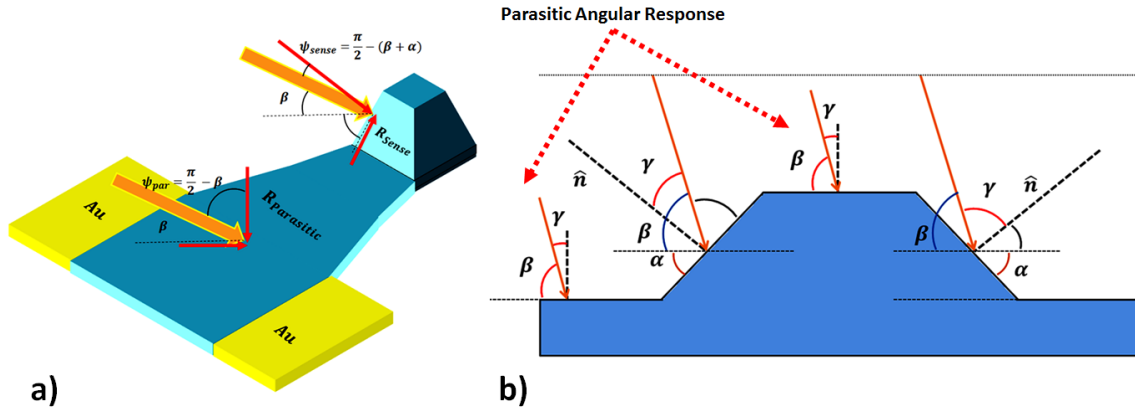


Figure 6-18 a) 3D depiction and b) cross-sectional depiction of incoming radiation angular interaction with sense and parasitic regions on the device

To evaluate the effect of parasitic regions that form on the flat surfaces, we chose a simplified symmetrical design for the electrodes which can be applied to distinguish between sense and parasitic surfaces of a single device (Figure 6-19). The equivalent electrical resistance associated with these regions can be written as in the following:

$$R_{total} = \left(\frac{1}{R_{sense}} + \dots + \frac{1}{R_{par}} \right)^{-1} \quad (64)$$

where R_{total} is the overall measured electrical resistance between the electrodes, R_{sense} is the electrical resistance of the sense region depicted in green in Figure 6-19-a and R_{par} is the resistance of the trapezoidal and rectangular parasitic regions depicted by the orange color.

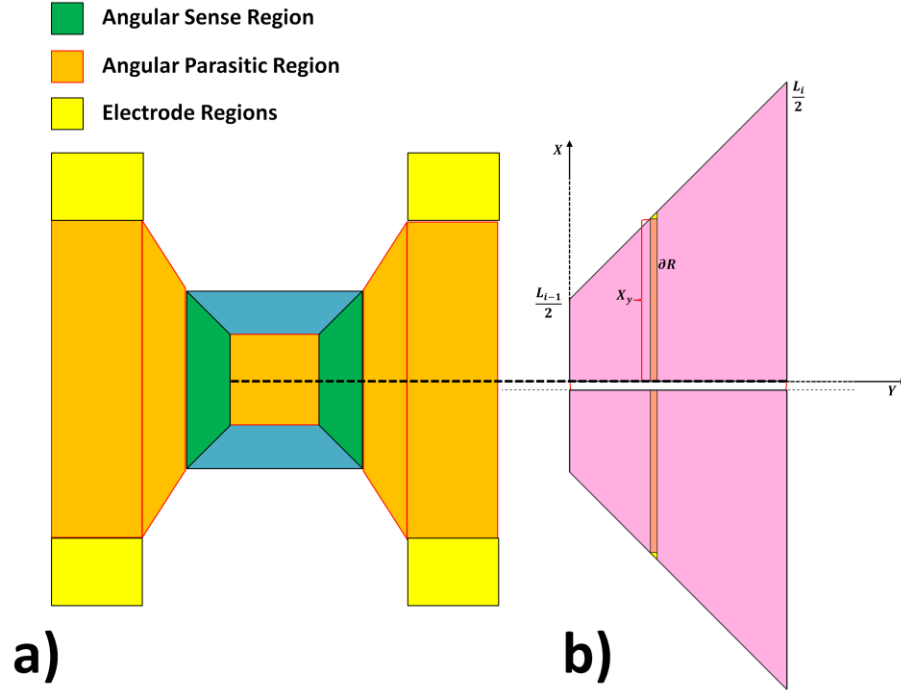


Figure 6- 19 a) Sense and parasitic regions in a single device using a symmetrical electrode design and b) division of the sense and parasitic regions along the structure symmetry line to generate rectangular and trapezoidal resistive regions

Based on equation (64), the total measured electrical resistance will inversely depend on the reciprocal of each region's contribution given their parallel arrangement. As a result, to evaluate the contribution of the sense area versus the parasitic areas, we need to find the integral of the finite resistive surfaces for every geometric division described in the figure above. The dashed line that divides the surface area between the electrodes along its symmetry axis further simplifies the calculations (Figure 6-19-b). The simple electrode geometry implemented for this calculation divides the total surface area between the two electrodes into one trapezoidal sense area (on the (111) facet of the device) and one trapezoidal and one rectangular parasitic areas atop and at the foot of the device's (111) facet (Figure 6-19). For any of the trapezoidal resistive half-regions, we can use the coordinate systems shown in Figure 6-20, where the origin of the system lies at the beginning of the region and the height and the length, along the X and Y coordinates, respectively. In this way, the resistance can be integrated along Y and across the area subtended by a straight line in the XY plane:

$$m_i = \frac{\frac{1}{2}(L_{i+1} - L_i)}{L_{y_i}} \quad (65)$$

where m is the slope along X direction, L_i is the i_{th} interface of the half-region approximation ensemble and L_{y_i} is the i_{th} trapezoidal resistive region length based on the diagram given in the figure below. As a result, the resistive element ∂R can be calculated using the standard definition of electrical resistance as in the following:

$$\partial R_i = \rho_{sense} \frac{l}{A} \equiv \rho_{sense} \frac{dY}{X_y t_{VOx}} \quad (66)$$

where ∂Y is the length of the resistive element, X_y is the height of the resistive element at any arbitrary point across the Y axis, between 0 and L_{y_i} and ρ_{sense} and t_{VOx} are the resistivity and thickness of the sense material layer that forms the resistive region.

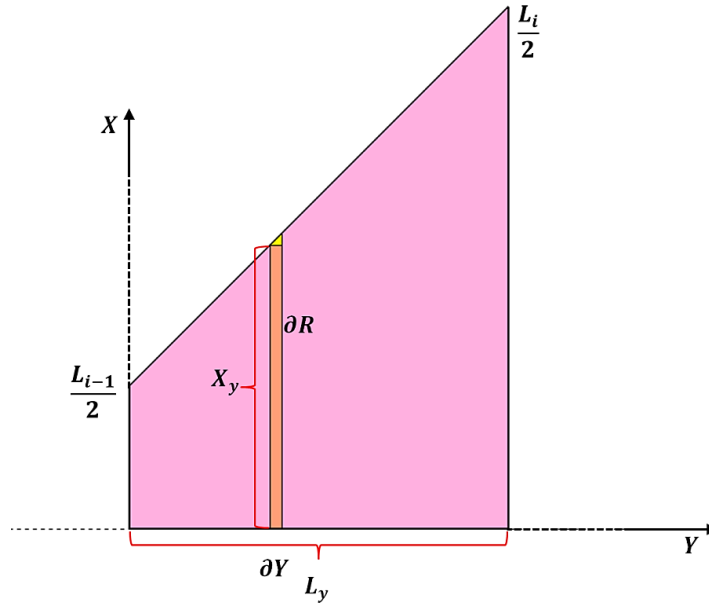


Figure 6- 20 Coordinate system used to calculate the integral resistance of an arbitrary half trapezoidal resistive region

Using equations (65) and (66) the total electrical resistance of both the sense and the parasitic group can be calculated as in the following analytical expressions:

$$R_{total} = \left(\frac{1}{R_{total,sense}} + \frac{1}{R_{total,parasitic}} \right)^{-1} \quad (67)$$

$$R_{total} = \left(\sum_{i=1}^{n_{tpz}} \left[\frac{\rho_{VOx}}{t_{VOx}} \int_0^{L_{y_i}} \left(\frac{\partial y}{m_i y + b_i} \right) \right]^{-1} + \sum_{i=1}^{n_{rec}} \left[\frac{\rho_{VOx} L_{y_i,pq}}{t_{VOx} L_{i,pq}} \right]^{-1} \right)^{-1} \quad (68)$$

$$b_i = L_i \quad (69)$$

Where n_{tpz}, n_{rec} are the number of trapezoidal and rectangular resistive regions respectively, $L_{y_i, pq}$ and $L_{x_i, pq}$ are the rectangular resistive region's dimensions along the Y and X axes respectively (see Figure 6-20). Solving the indefinite integral in equation (68) will result in the contribution of each of the sense and parasitic regions to the overall measured output of the device. The solution to equation (68) indicates that the suggested electrode geometry will result in a 30% - 70% overall contribution for sense and parasitic regions, given the sense material uniformity and homogeneity across both sense and parasitic surfaces. Such large difference indicates the necessity of the sense region's electrical isolation from the parasitic region to ensure the desirable angular modulation of the output signal. Furthermore, it is necessary to evaluate the effect of the parasitic area contribution when recalculating the unknown angle of incidence based on the proposed mathematical framework given earlier. The equivalent circuit of an ideal sense region will result in the angle of incidence recalculation based on equations (34) through (36). Incorporating the parasitic resistive regions into the model will result in the addition of the parallel component into the equivalent circuit as depicted in Figure (6-21-b). The mathematical description of the equivalent circuit with the presence of the parasitic resistance can be written in the following form:

$$R_T - R_o = \left(\frac{1}{R_S - \Delta R_S} + \frac{1}{R_P - \Delta R_P} \right)^{-1} - \left(\frac{1}{R_S} + \frac{1}{R_P} \right)^{-1} \quad (70)$$

Where R_T, R_o are the total measured electrical resistances at a given temperature T and at room temperature (including sense and parasitic components) and $R_S, \Delta R_S, R_P$ and ΔR_P are the sense area's pre and post exposure resistances and parasitic area's pre and post exposure resistances, respectively. Expansion of equation (70) results in a non-linear expression from which extraction of the parasitic term is very cumbersome. Further simplification can be made (see Appendix A) by assuming that the total change in the electrical resistance of either of the sense regions is dominated by the sum of the change of the electrical resistance in the sense and parasitic areas. As a result (70) can be represented as in the following form:

$$\Delta R_T \approx \Delta R_S + \Delta R_P \equiv \underbrace{(\eta(\lambda) \cdot I_{in} \cdot A_S \cdot \delta_R)}_a \cdot \sin(\beta \pm \alpha) + \underbrace{(\eta(\lambda) \cdot I_{in} \cdot A_P \cdot \delta_R)}_b \cdot \sin(\beta) + c \quad (71)$$

where R_T is the totaled measured electrical resistance, I_{in} , A_S , A_p , δ_R , c are the incident radiative power, sense and parasitic regions surface area, the material's temperature TCR and a constant offsetting factor. The two scaling coefficients a and b are simplified approximations of the effect of wavelength dependent absorption of the incident radiative power, across the designated sense and non-designated parasitic regions in the device.

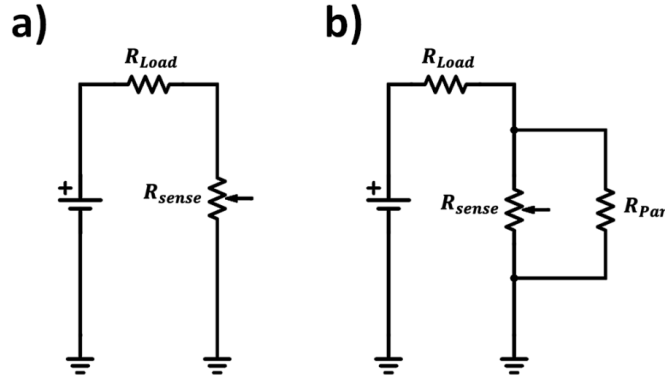


Figure 6-21 Device's equivalent circuit a) without the parasitic resistive elements and b) with the parasitic resistive elements

This effectively assumes that the absolute room temperature magnitude of the sense and parasitic resistances is large relative to their respective changes (See Appendix A). Under the simplifying assumptions, the power ratio in equation (35) can be re-written in the following form to account for the inclusion of the parasitic components contribution:

$$\frac{P_L}{P_R} = \frac{(\Delta R_{S,L} \parallel \Delta R_{P,L})}{(\Delta R_{S,R} \parallel \Delta R_{P,R})} = \hat{N} \cdot R_{L,R} \quad (72)$$

$$\beta = \frac{\pi}{2} - \alpha - \tan^{-1} \left(\frac{\hat{N} \cdot R_{L,R} \cdot \cos(2\alpha) - 1}{\hat{N} \cdot R_{L,R} \cdot \sin(2\alpha)} \right) \quad (73)$$

$$\hat{N} = \frac{\hat{C} \cdot \sin(\beta) - \cos(\beta)}{\hat{C} \cdot \sin(\beta) + \cos(\beta)} \quad (74)$$

$$\hat{C} = \frac{K_{PS} + \cos(\alpha)}{\sin(\alpha)} \quad (75)$$

where \hat{N} , \hat{C} and K_{PS} are nested symbolic coefficients representing the parasitic term in equation (71), and are related to the mass and surface area of sense and parasitic regions at the left and right side of the device as well as the sense material's properties such as specific heat and mass.

6.2.3. Device (1st Design Generation) IR Incidence Angle Recalculation (Pre FIB)

In the previous section, an attempt was made to incorporate the contribution of the parasitic regions to the device's angular recalculation expression as presented in equation (72) and (73). It can be shown that as the contribution of the parasitic regions increases the accuracy of the recalculated angle by the device diminishes. The following figure depicts a comparison between the theoretical recalculated incidence angles for an ideal device and cases with 30%, 50%, 70%, 80%, 90% and 100% parasitic contribution to the overall electrical resistance measured across the device's opposing sides (see Figure 6-22).

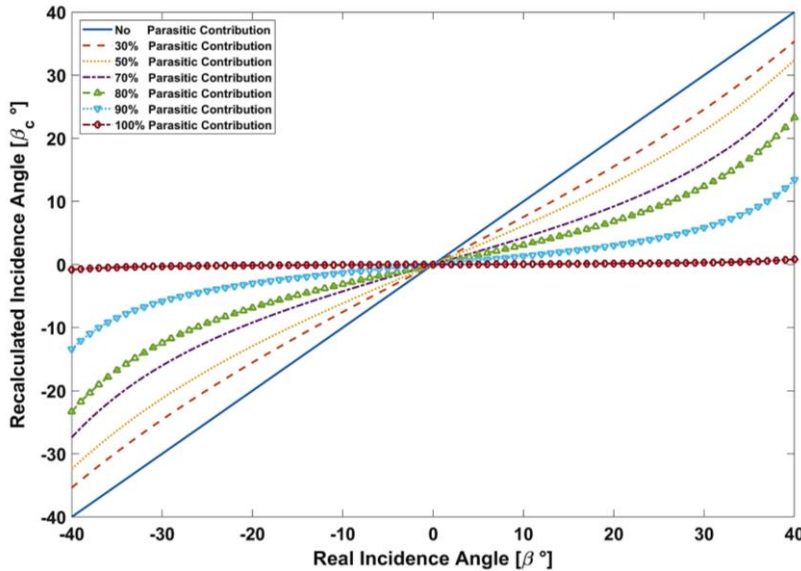


Figure 6-22 The effect of the percentage parasitic contribution on the accuracy of the recalculated angle by the device.

Evident from the figure, as the percentage contribution of the parasitic to the overall resistance increases, the device's capability to recalculate the incidence angle using the ratio of the resistance change on the opposing sides becomes more and more impeded. By the same token, the reliability of the device's output decreases near the edges of its theoretical FOV. The aforementioned is due to the fact that the output ratio is only meaningful when the incoming IR radiation is absorbed by both (opposing) sides of the device. Given that the angular dependence of the parasitic regions is similar on either sides of the device, the existence of large percentage parasitic contributions in the device's output from east and west side results in the divergence of the measured data from the expected trends into similar parabolic forms as shown in figure 6-16-b for which

the theoretical trends were calculated with 90% parasitic contribution for the east side and 80% parasitic contribution for the west side. Figure 6-23-a compares the device's practical limit in recalculating the incidence angle using the fitted curves with 90% and 80% parasitic for the east and west side responses respectively. The model predicts that for a device with 90% parasitic contribution the recalculated angles are contained within a 10 ° angular FOV in opposed to the ideal 70 °. Figure 6-23-b depicts the recalculated angles from the device output that show a general agreement with the predicted trends however the resulting FOV is much more impeded compared to the predicted recalculatation limit.

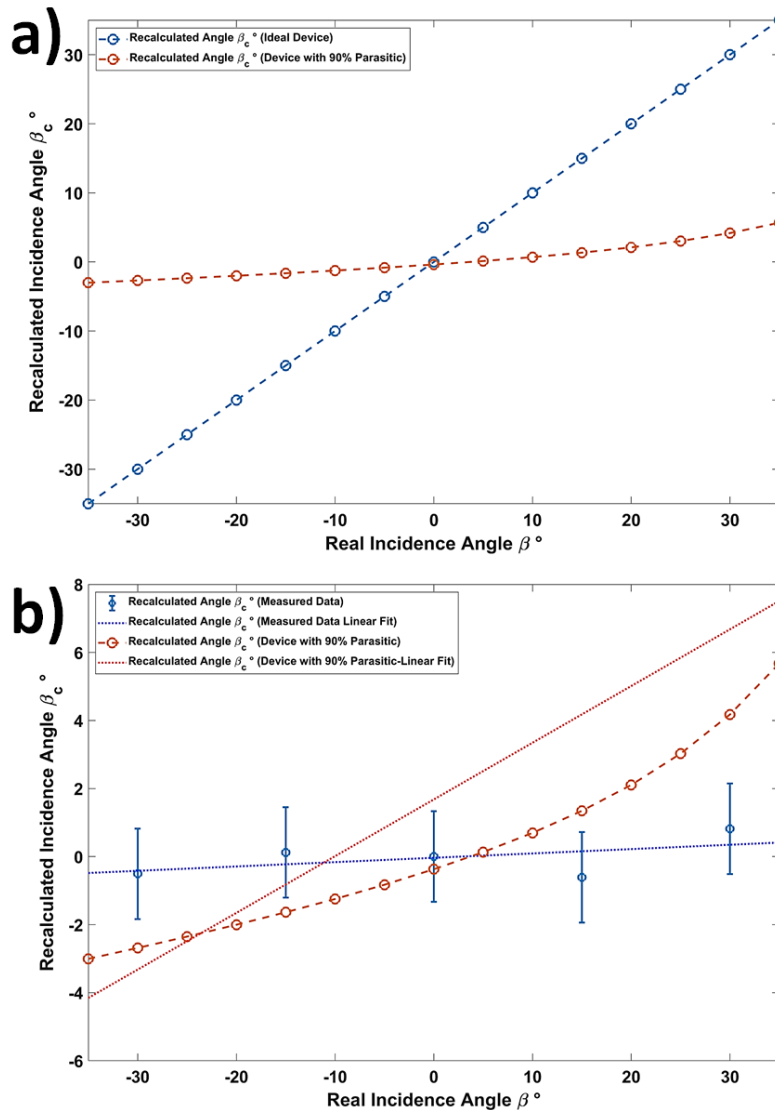


Figure 6- 23 The predicted angular recalculatation using a device output with 90% parasitic contribution compared to a) ideal device and b) recalculated angles from the measured device responses. The error bars reflect the uncertainty in the room temperature resistance of the device under test across the duration of the measurement. Statistical inference of the fitted trend lines are provided in appendix D.

6.2.4. Device (1st Design Generation) Signal Acquisition and IR Response (Post FIB)

The calculations presented earlier predicted the contribution of parasitic resistive regions to the overall readout signal that can impair the angular resolution functionality of the device as proposed. As a result, focused ion beam milling was used to physically disconnect the device readout terminals via removal of the V_2O_5 layer in designated areas depicted in Figure 6-24.

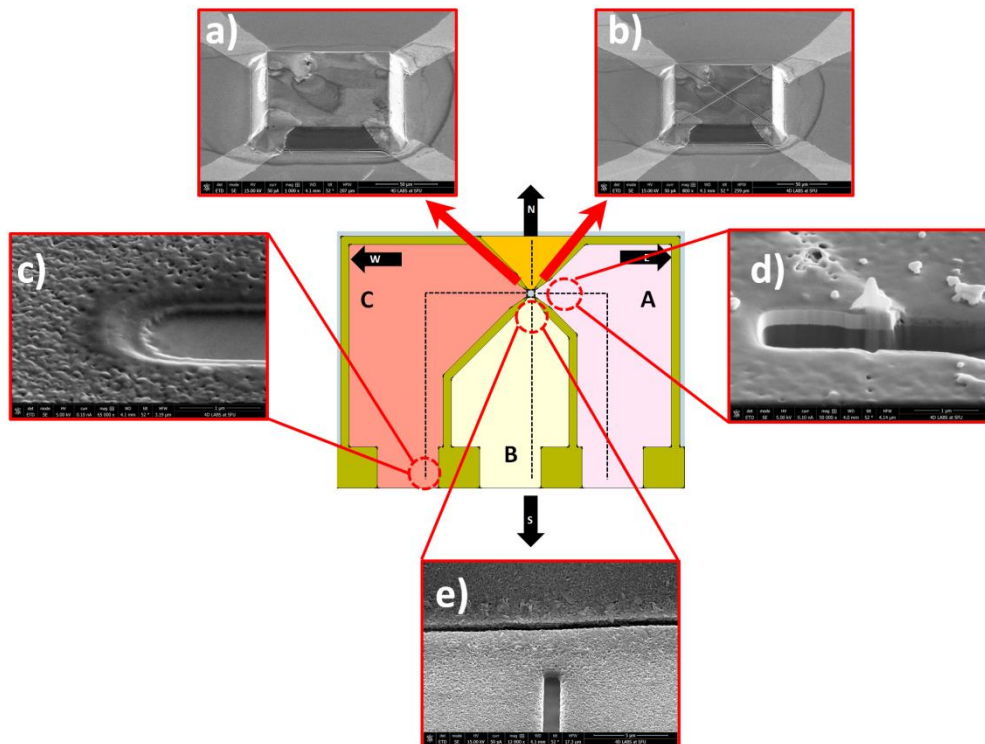


Figure 6- 24 The device die after partial removal of the sense material in order to reduce the effects of the parasitic resistance via focused ion beam milling. a) and b) depict the top of the DUT pixel before and after FIB, c), d) and e) are electron micrograms of FIB tracks across regions C, A and B.

Similar to the pre-FIB case, after the FIB process the sample device underwent a long exposure test using a similar test setup as that of Figure 6-15 throughout a 20 s exposure to the globar. Material removal via the electrical insulation of the resistive regions had impacted the pre-exposure (room temperature) initial resistance of the device as well as its IR induced resistance change on the east and west side of the device. The respective IR induced responses with $\Delta R_{East} \approx 65 k\Omega$, $\Delta R_{West} \approx 45k\Omega$ which correspond to 1.2% and 1.3% changes from the room temperature resistance show a consistent drop of roughly 3% as a result of FIB process. (see Figure 6-25).

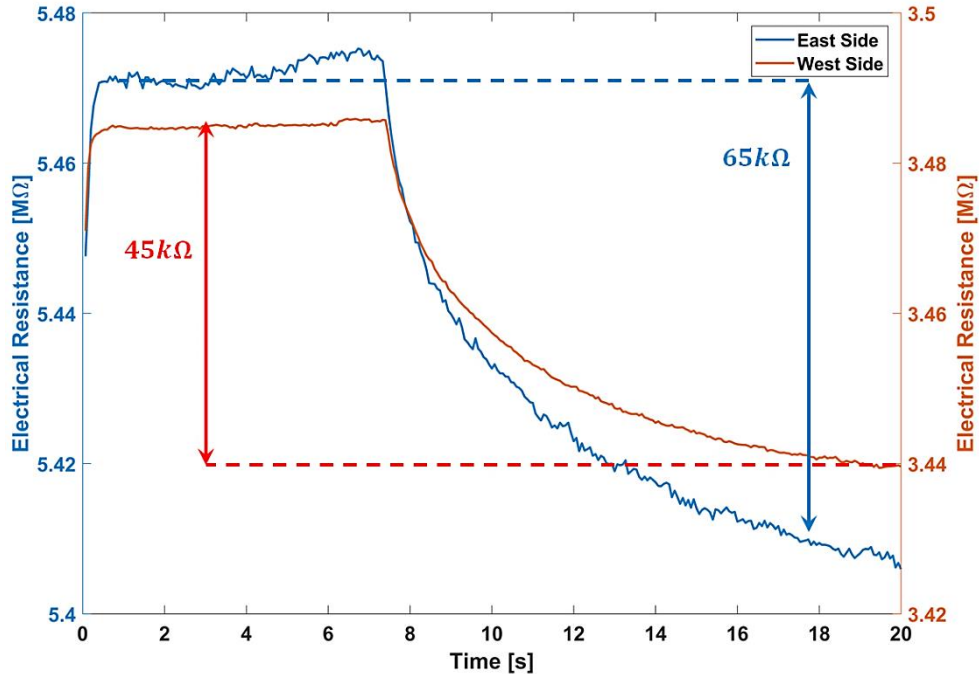


Figure 6-25 Device responsivity test at the two opposing side after FIB process

6.2.5. Device (1st Design Generation) IR Incidence Measurement and Incidence Angle Recalculation (Post FIB)

Similar experimental routines (using the setup presented in figure 6-15) to what was done prior to FIB milling process, were carried out on the same device after removal of the undesired V_2O_5 . The results are presented in Figure 6-26. As expected, the removal of IR sensitive resistive material via FIB milling led to the emergence of more pronounced opposing trends in the device's output on the east and west side. The latter is more consistent with the predictions made by the mathematical model presented in section 3.1.2. Nevertheless the discrepancy between the observed and ideal cases indicates that material removal did not entirely eliminate the effects of parasitic resistance. Figure 6-26-b shows that there is still a noticeable deviation between the theoretical trends with no parasitic contribution and the recorded data. Recalculation of the theoretical trends with 80% and 70% parasitic contribution for the east and west side respectively resulted in a closer agreement between the trends and the observed angle-dependent response from the FIB milled device. The results show that the expected trend in the recalculated angle improves by an extra 10° (see Figure 6-27-a). A comparison to the recalculated angles using the recorded data shows a general agreement to the predicted trends (see Figure 6-27-b) and a 7 fold improvement in the measured angular FOV of the device compared

to the trends prior to FIB milling process. The deviation for the recorded data at zero degree can be attributed to the uncertainties that arise from the fluctuation in the recorded room temperature resistance during measurements at that incidence angle.

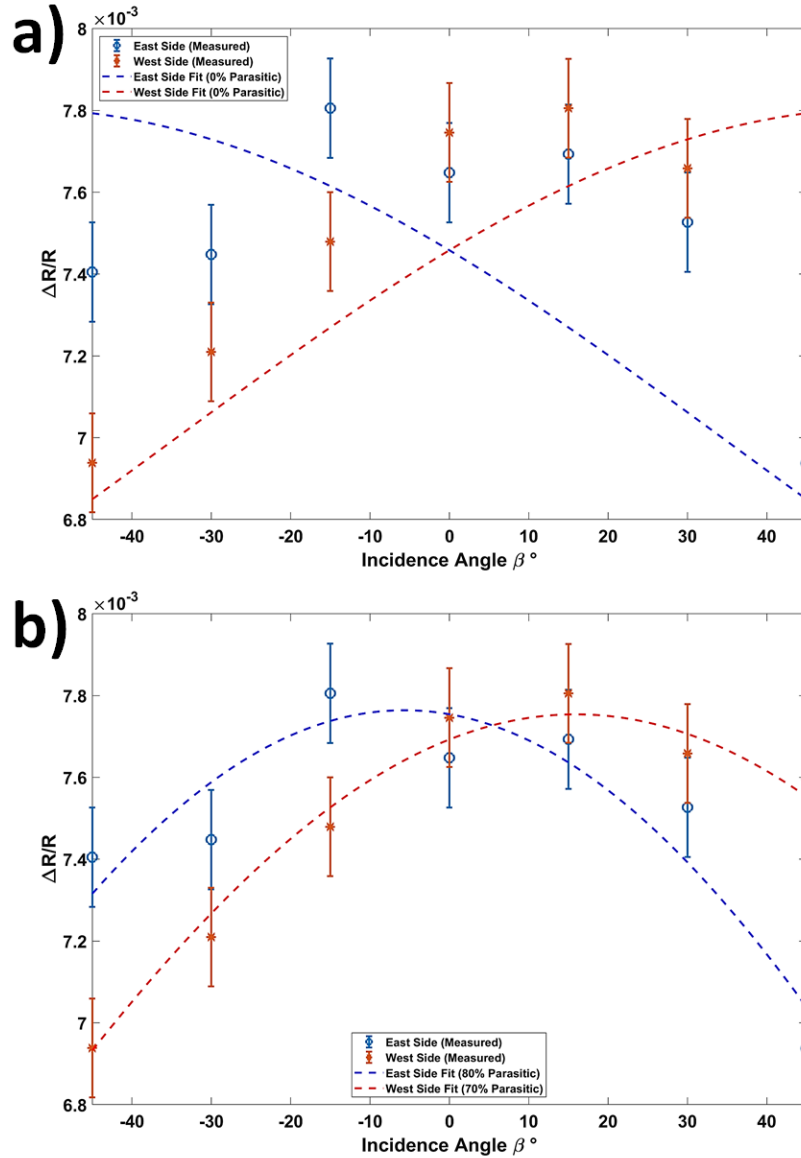


Figure 6- 26 DUT's angular $\Delta R/R$ response along with the theoretical or expected trends for a)ideal case (no parasitic region contribution) and b) recalculated theoretical trends with 80% parasitic contribution to the east side and 70% parasitic contribution to the west side. Statistical inference of the fitted model is provided in Appendix D.

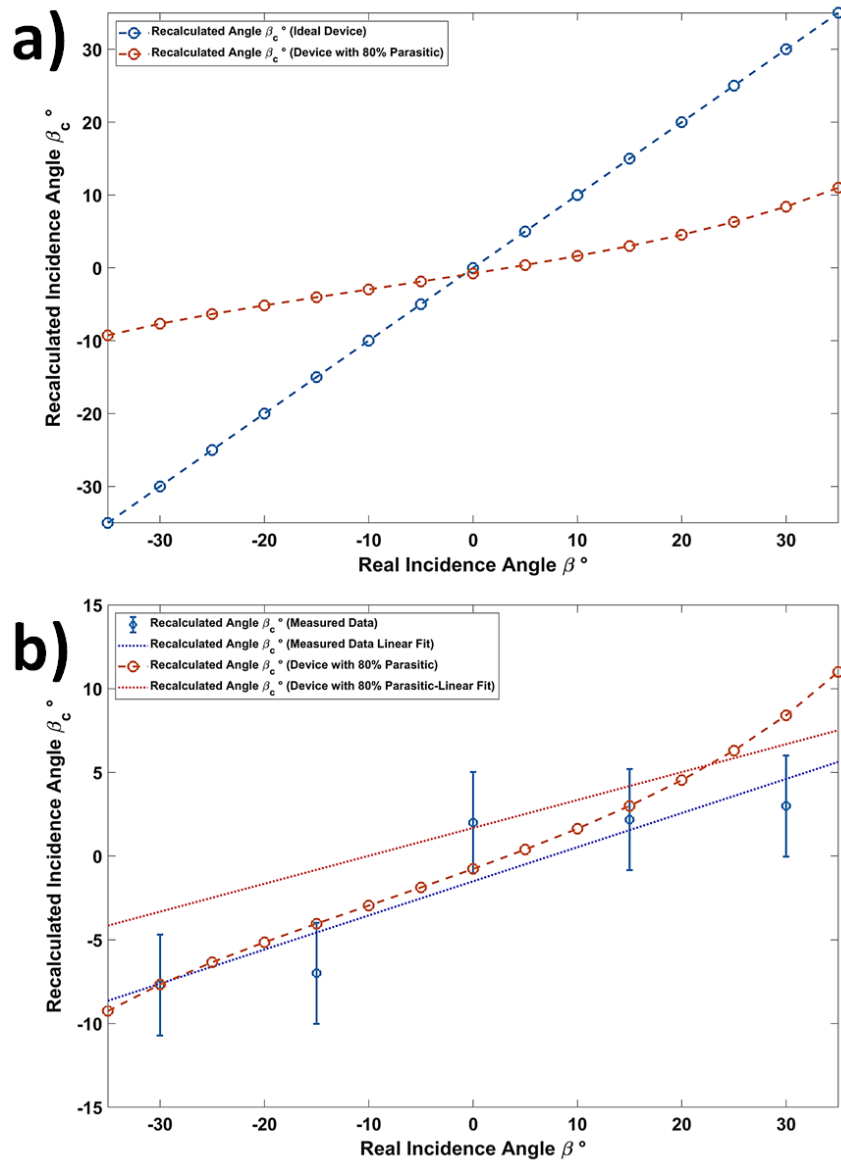


Figure 6- 27 The predicted angular recalibration using a device output with 80% parasitic contribution compared to a) ideal device and b) recalculated angles from the measured device responses post FIB milling. Statistical inference of the fitted trend lines are provided in appendix D.

While the device appears to show improvement in its angle-dependent response to an IR source post FIB milling process, the data presented in Figure 6-28-b shows weak correlation between the measurements and the expected angular response. The latter indicates that despite the FIB milling and removal of suspected parasitic regions, there is still limited ability to accurately identify the direction of an IR source on the basis of the angle dependent $\Delta R/R$ changes. This is consistent with the expectations of a device with large parasitic contributions as indicated by figure 6-22. Removal of some of the parasitic regions between the device terminals indicates that the angular resolution of the device is

strongly improved however, the range of the outputted recalculated angles are still far from the desired limits. Earlier on, the effects of the parasitic contribution to the device's angle recalculation process were modeled through equations (72-74) in 6.2.2 (repeated here for reference):

$$\beta = \frac{\pi}{2} - \alpha - \tan^{-1} \left(\frac{\hat{N} \cdot R_{LR} \cdot \cos(2\alpha) - 1}{\hat{N} \cdot R_{LR} \cdot \sin(2\alpha)} \right) \quad (76)$$

$$\hat{N} = \frac{\hat{C} \cdot \sin(\beta) + \cos(\beta)}{\hat{C} \cdot \sin(\beta) - \cos(\beta)} \quad (77)$$

where \hat{N} is the parasitic contribution to the ratio of the induced change in the electrical resistance on the east and west side of the device, \hat{C} is a scalar proportional to the magnitude of the parasitic and sense regions as well as the material related constants of the sense material across the sense and parasitic regions and β is the IR incidence angle. The effect of incorporation of \hat{N} is depicted in the following figure (figure 6-28) wherein the ratio between the $\Delta R/R$ values for east and west side of the device is calculated for an ideal case with no parasitic, for cases with 90% and 100% parasitic contribution and for cases with 90% and 100% parasitic contribution corrected via being multiplied by \hat{N} at each angle. The applied value for \hat{C} is found empirically for this work and is equal to 0.9967. Figure 6-29 shows the theoretical device responses with 90% and 100% parasitic contribution with and without use of \hat{N} . Similarly, figure 6-30 depicts the effect of correcting for the parasitic effect via use of \hat{N} for the recalculated angles using the measured $\Delta R/R$ ratio of east to west side from the 1st design generation of the device for before and after the FIB milling process. As predicted by the model the accuracy of the recalculated angles significantly improves when the effect of the parasitic contribution is accounted for via implementing the parasitic parameter \hat{N} .

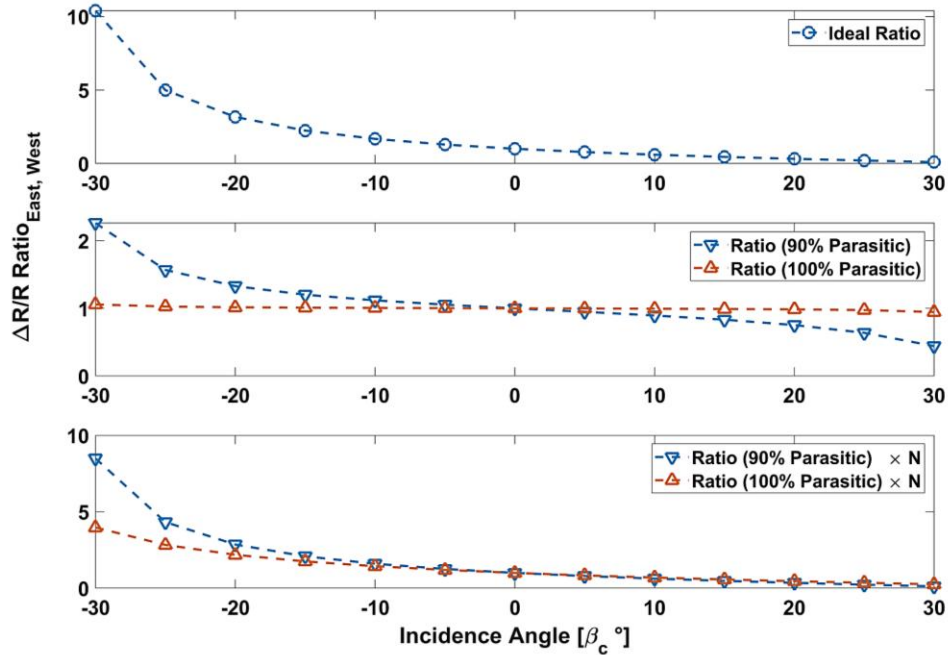


Figure 6- 28 The $\Delta R/R$ ratio for east and west side for top) ideal device, b) device with 90% and 100% parasitic contribution and bottom) device with 90% and 100% parasitic contribution corrected via multiplying the ratio with \hat{N} at each incidence angle.

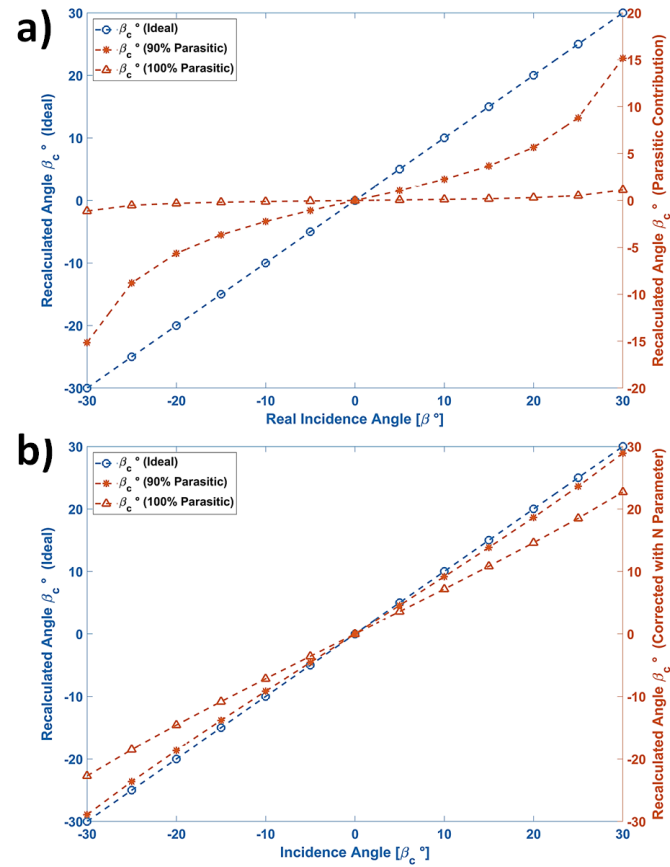


Figure 6- 29 Theoretical curves for a) devices with 90% and 100% parasitic contribution and b) corrections thereof using \hat{N} .

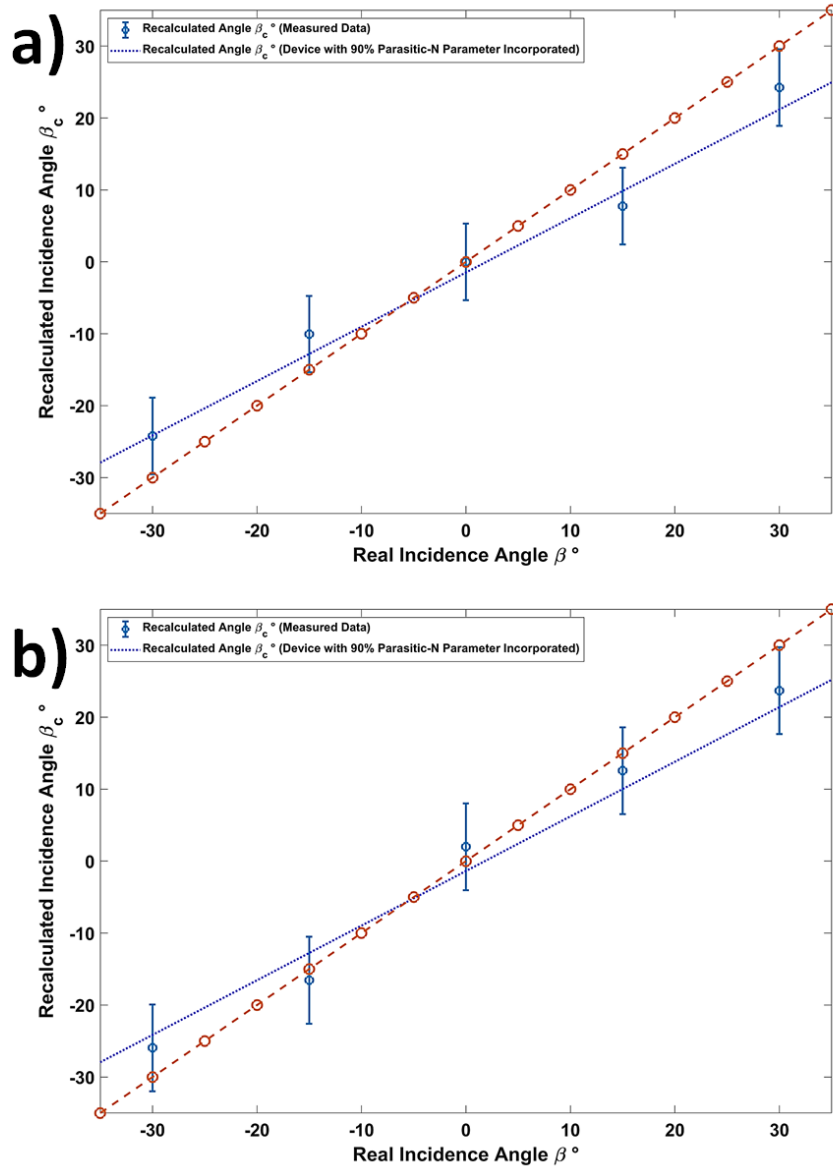


Figure 6- 30 Recalculated angles through use of \hat{N} from the measured $\Delta R/R$ for a) 1st design generation device before FIB milling and b) after FIB milling process. As predicted by the theoretical trends in figure 6-30 the range of the recalculated angles improves drastically when compensated for the effects of the parasitic. Statistical inference of the fitted trend lines are provided in appendix D.

Since the FIB milling process seemed to have had little effect in removal of the previously discussed parasitic regions, a second generation of the devices were designed and fabricated in order to improve upon the existence of the parasitic contribution via localizing the sense material deposition on the (111) facets of the devices as well as decoupling the sense regions thermally to avoid any potential signal contamination as a result of thermal energy transfer between the two sides.

6.3. Device Level (2nd Design Generation) IR Response

The second generation of the proposed devices was designed with the specific goal of isolating the sense regions from the parasitic contributions that were shown to impair the recalculation of the incidence angle of an incoming IR source. The design parameters were derived in order to maximize the angular modulation of the device's output as a function of the incoming IR radiation's angle of incidence via localizing the IR sensitive material to the silicon (111) facets while placing the sense areas further apart to avoid inter-facet thermal contamination. The device's thermal insulation layer's thickness was also quadrupled to avoid signal degradation due to thermal loss into the silicon substrate. Figure 6-31 depicts the 2D mask layout and its 3D rendering.

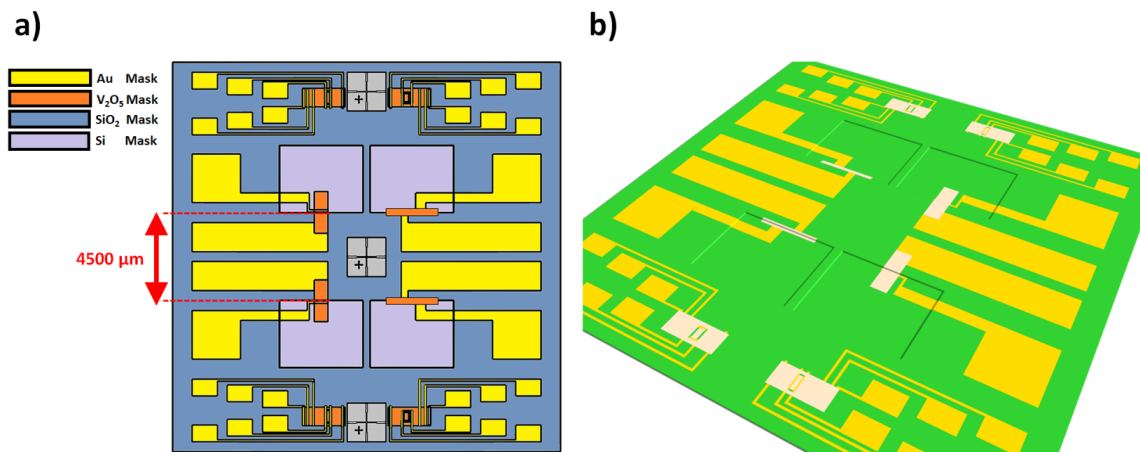


Figure 6- 31 a) 2D and b) 3D rendering of the 2nd generation device design focusing on reducing the effects of the parasitic resistive regions

6.3.1. Device (2nd Design Generation) Signal Acquisition and Conditioning

As depicted in the Figure 6-27, large area silicon anisotropic etching was preferred over smaller and more localized patterning to enable larger etch depth and active region separation via distancing the silicon substrate's (111) facets further apart compared to the previous generation. The layout for the second generation was done such that the electrode pads for both the test and sense terminals offer larger surface area for board or package bonding. The main challenge associated with the new design was the forecasted large area isotropic removal of the V₂O₅ sense layer to create localized sense regions on the (111) facet of the underlying silicon substrate exclusively. Given the very small surface

area of the silicon (111) facets, in order to ensure the integrity and precision of the patterned sense material, the sense area dimensions surpassed that of the facets. The boundaries of the sense regions were then defined via the electrodes electrically shorting the excess sense material covered areas as shown in Figure 6-32.

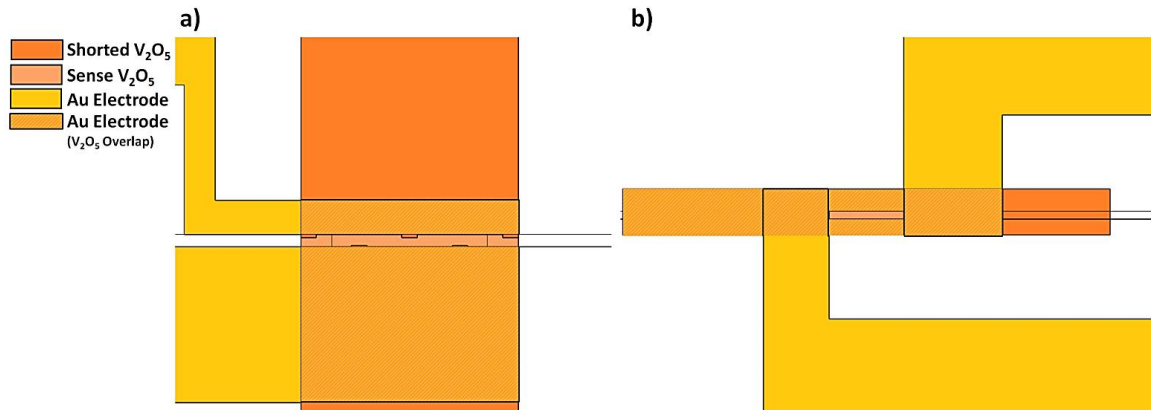


Figure 6- 32 a) Upright and b) lateral sense region patterns employed in the 2nd generation device design whereby the resistive sense regions are confined to the inclined facets of the (111) silicon.

Similar to the 1st design generation devices, the 2nd design device prototypes were mounted on prototyping board using silver epoxy resin wire bonding and their IR induced response was measured on either side in the test setup described in Figure 6-15. Due to the significantly smaller dimensions of the sense regions, the room temperature resistance of the devices is much higher than that of the previous design. The device responsivity test was performed at an exposure time equal to five seconds. Given the high sheet resistance, the device's electrical resistance drop resulting from the five second exposure was much more prominent compared to the previous generation. Figure 6-33 shows the resistance drop of the two active facets of the device.

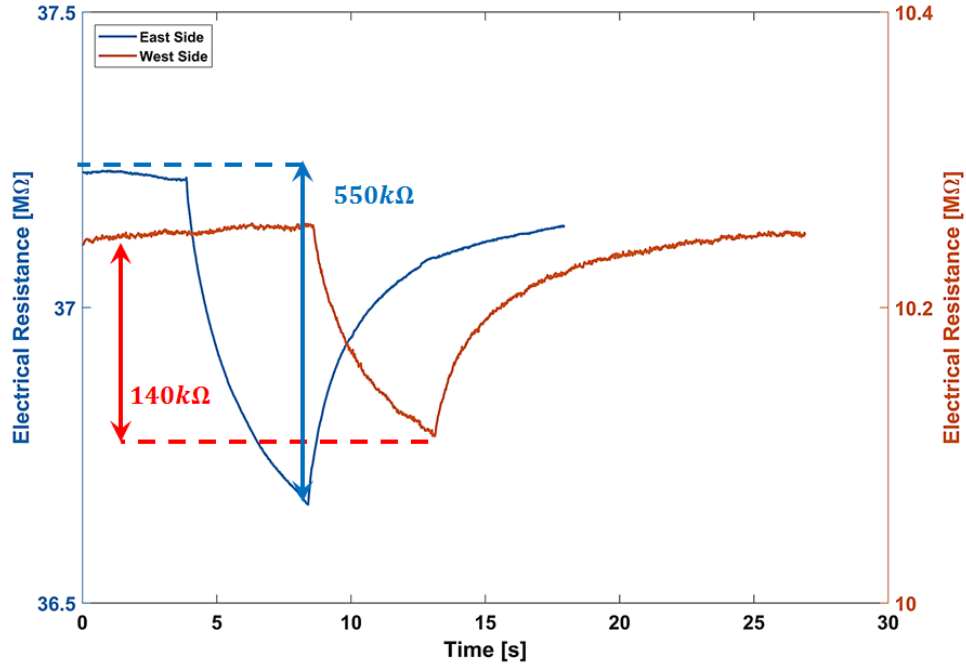


Figure 6- 33 Gen 02 device responsivity to IR radiation on the opposing east and west side

The overall device responsivity was measured to be 1.5% and 1.4% for the east and west side respectively. Despite the desirable change in the electrical resistance due to IR exposure, the high sheet resistance was deemed as a potential concern for signal amplification in an embedded setup. The 2nd generation devices were subject to an optical responsivity test similar to the 1st device designs types. The intensity dependent $\Delta R/R$ responses of the two facets were obtained in the same manner as described previously for 1st generation devices and is shown in Figure 6-34.

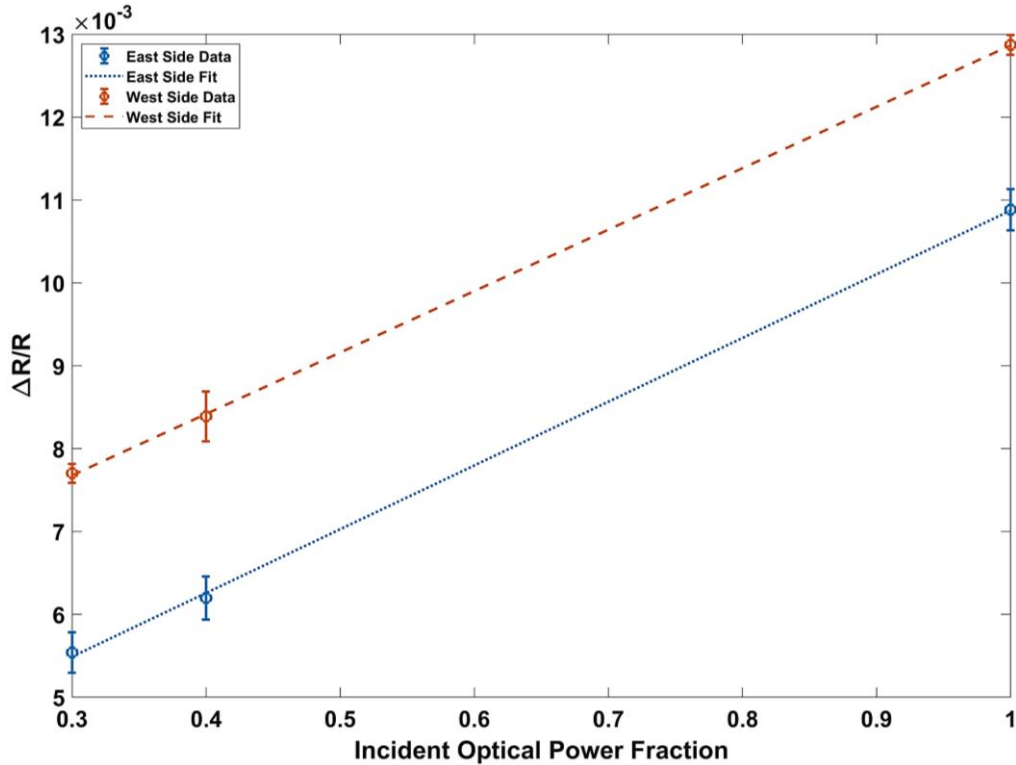


Figure 6- 34 Responsivity fits on the two sides of the 2nd device design obtained by their incident power dependence. The similar slopes of the fit lines indicate less mismatch between the sense regions on either side as result of of IR radiation. The observed offset is an indicator material induced change in room temperature resistivity which is used to normalise each side's response to the other.

The responsivity fits showed an offset between the two sides of the DUT yet the new sense region design proved to generate a more symmetrical response compared to that of the previous one.

6.3.2. Device (2nd Design Generation) Inter-Facet Thermal Insulation Control Experiment

Previous simulations (Chapter 3 section 3.3.1, figure 3-12) have shown that for a 100 ms heat pulse, the 2 μm oxide layer provides a reasonable thermal insulation barrier and limits inter-facet thermal transfer to a minimal level. Since the 2nd design generation prototypes were compensated with a 2 μm minimum desired thermal insulation layer (SiO₂) suggested by the numerical thermal simulations, a control experiment was performed to see the effectiveness of the new design parameters implemented in these device prototypes. To investigate the thermal contamination effects on the output signals of the opposing sides of the device, it was necessary to induce a localized response on a given side while measuring the effects on the other. The un-collimated nature of the globar

source's output made it difficult to create a localized spot on the 100-micron size scale of the sense region facets of the device under test. Also, given the peak spectral absorption of the sense material (Figure 4-13, Section 4.3.4) was in the long IR wavelength region, the absence of an available light source operating in this spectral range led to an alternative approach to quantify the degree of thermal contamination. A 670 nm diode laser (Coherent Optics Model SDL 7630) was used to generate a localized response in the vicinity of the device's sense region. The laser output was directed toward the DUT and focused to a nominal spot size of diameter 25 μm onto one side of the DUT. An optical chopper was mounted into the beam path and before the automated shutter such that the light incident on the DUT was modulated at a known frequency, while the electrical responses of the two facets of the device were connected to independent DMM readout units. The schematic of the test setup is provided in Figure 6-35-a.

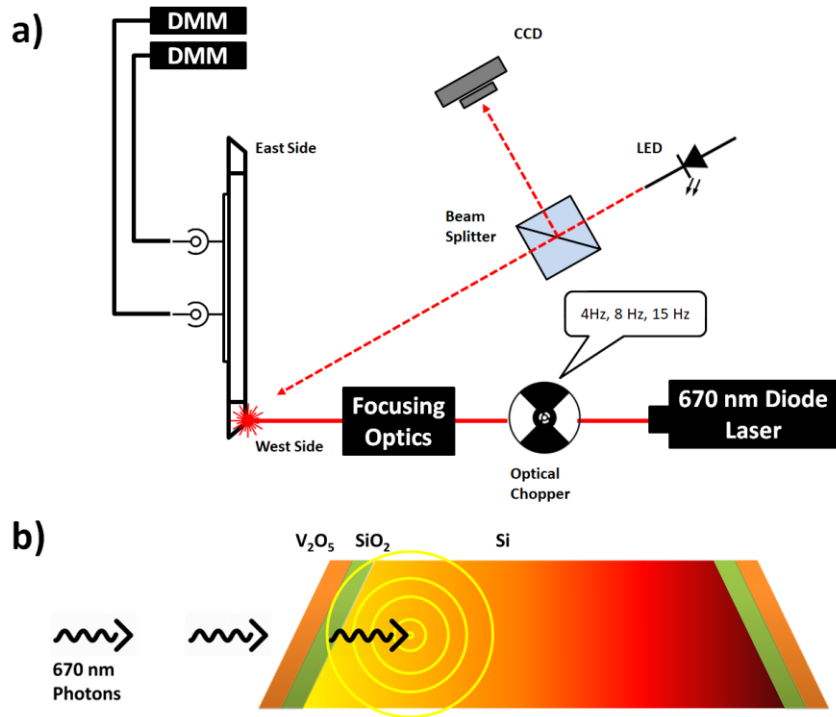


Figure 6- 35 a) Schematic of the inter-facet heat diffusion control experiment setup whereby the diode laser's spot-size on the DUT sense region was visually monitored by means of a CCD camera and a solid state LED. b) The 670 nm photons generated by the diode laser bypassing the V₂O₅ and SiO₂ layers depositing energy into the underlying silicon substrate.

The implementation of a CCD camera along with a beam splitter and solid state LED allowed for a visual confirmation that the laser spot size was confined to a single sense region of the DUT. Data acquisition was performed for optical chopper frequencies of 4 and 8 Hz. Use of 670 nm photons was expected to allow for indirect sense material heating

through energy deposition into the silicon substrate. Given that 670 nm wavelength is below the bandgap energies of both vanadium oxide and silicon dioxide, the incident photons were expected to pass these layers largely unaffected by their presence. The results of the experiment using the optical chopper at 4Hz is shown in figure 6-36 a) and b), where the modulated device output on the exposed facet shows a large response to the modulated incident radiation, whereas the opposing (unexposed) facet response demonstrates little-to-no corresponding modulation. Instead, the unexposed facet shows only a gradual decay in the electrical resistance consistent with overall device heating. The fast resistance drop (red trend) as a function of the optical chopper induced exposure times indicates the device's response at the exposed sense region whereas the slow decay (blue trend) corresponds to the gradual increase in the opposing side's temperature due to heat migration between the two facets. Figure 6-36-b gives a better visual of the measured change in the electrical resistance at the two sides of the device within one optical chopper's cycle. The relative changes in the red and blue trend during an exposure time close to 125 ms show an 18% resistance drop on the exposed side versus no change on the unexposed facet. The latter is consistent with the 2D heat transfer simulation that was presented in chapter 3 (figure 3-12). Given that the simulation was done on the 1st device design with smaller dimensions compared to the 2nd generation, the observed relative changes in figure 6-36-b indicate that the 2nd design generation of the devices, do not experience inter-facet heat transfer during exposure periods as short as 125 ms. The measured material response time as a function of localized heating was on the average 130 ms which is significantly smaller than device's thermal response time (~20 s) by two orders of magnitude. As a result, the proposed device can be suitable for on-chip (real-time) applications when integrated with bridge and/or amplifying circuits.

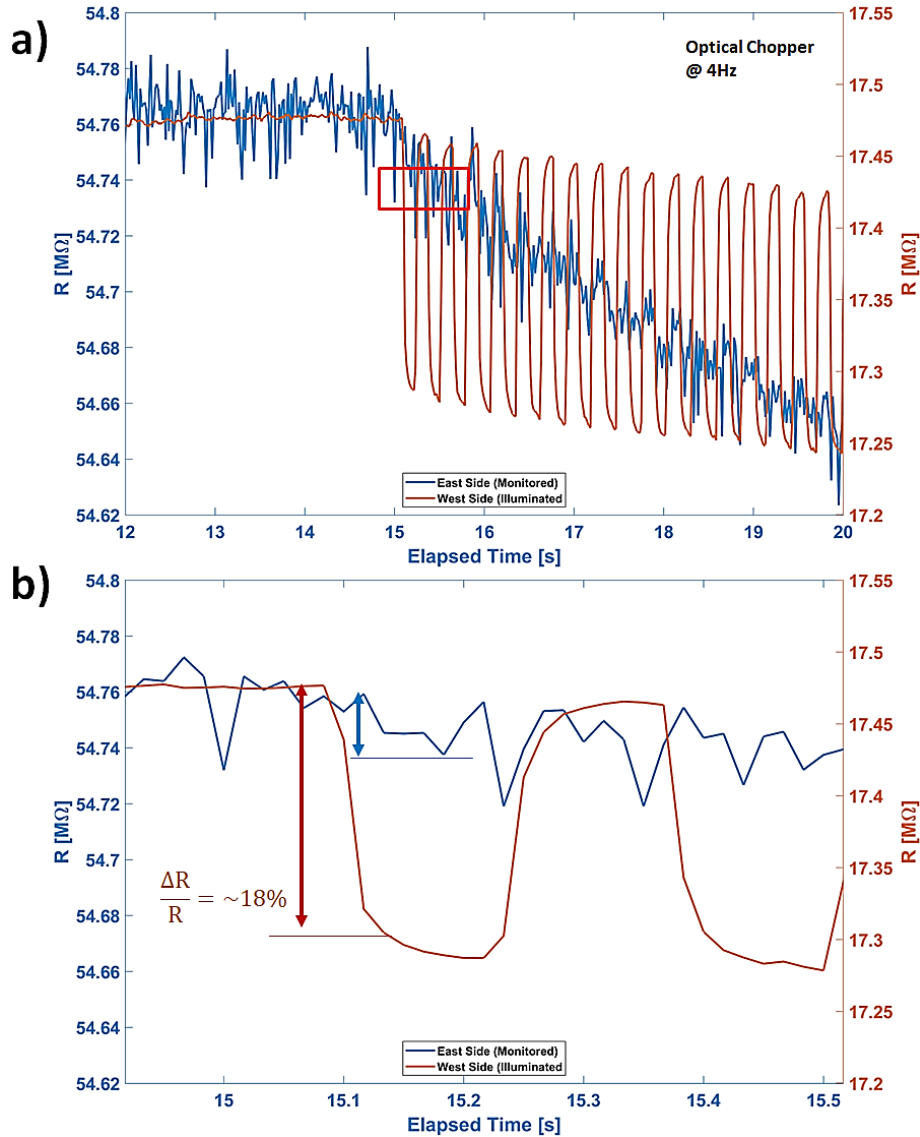


Figure 6- 36 a) The modulated device response at the exposed side (west side) in opposed to the non-exposed side's gradual drop (east side) at optical chopping frequency of 4 Hz. b) The blowup of the marked region depicting the amount of induced ΔR across one optical

6.3.3. Device (2nd Design Generation) Incidence IR Measurement and Recalculation

Figure 6-37 shows the device's angular response as a function of 15° changes in the incidence angle. The results show better general agreement with the trends as predicted by the analytical model compared to 1st generation design devices. However, similar to 1st generation devices, their angular response shows the appearance of effects that are similar to the parasitic signatures. This observation was deviated from the expected results given the large area removal of V_2O_5 in order to minimize parasitic contributions.

The persistence of this observation may indicate incomplete material removal or remaining residues. Alternatively, it may also indicate unwanted thermal contributions from background radiation sources that are captured along the source direction (See Appendix B). Figure 6-37-b shows that incorporation of a 30% contribution akin to the parasitic contributions characteristic of 1st design generation types improves the fits of the 2nd generation devices as well.

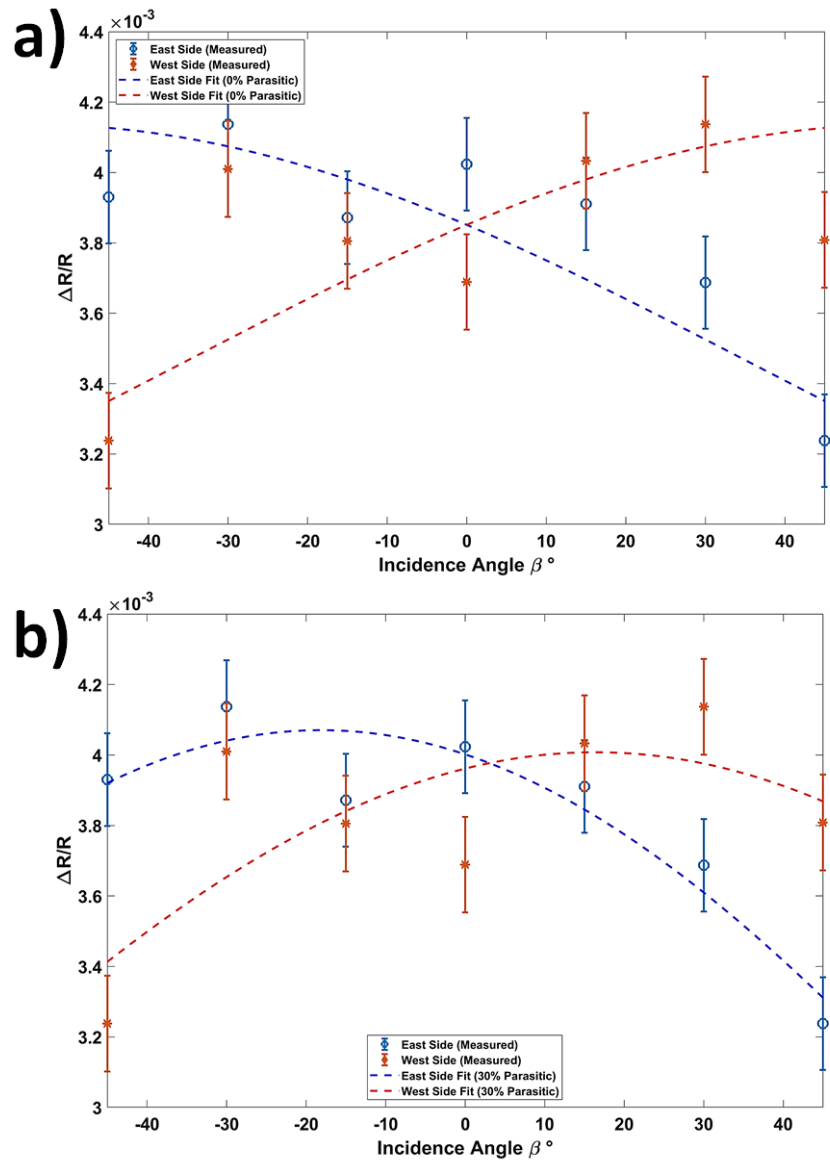


Figure 6- 37 Angular $\Delta R/R$ responses of gen 02 devices in 15° increments to IR radiation fitted with a) 0% parasitic and b) 30% parasitic contribution. Errorbars were calculated from the uncertainties in the room temperature resistance across the duration of the measurements. Statistical inference of the fitted model is provided in Appendix D.

The recalculated angles using the fits with 30% parasitic contribution improves the theoretical angular FOV by a total 10 ° (see Figure 6-38-a). The recalculated incidence angles from the recorded data as well, show two folds improvement in the device FOV. The deviation observed in the recorded value for zero degree incidence can be attributed to the fluctuations of the device’s pre-exposure electrical resistance as a result of variations in room temperature during the measurements (see Figure 6-38-b).

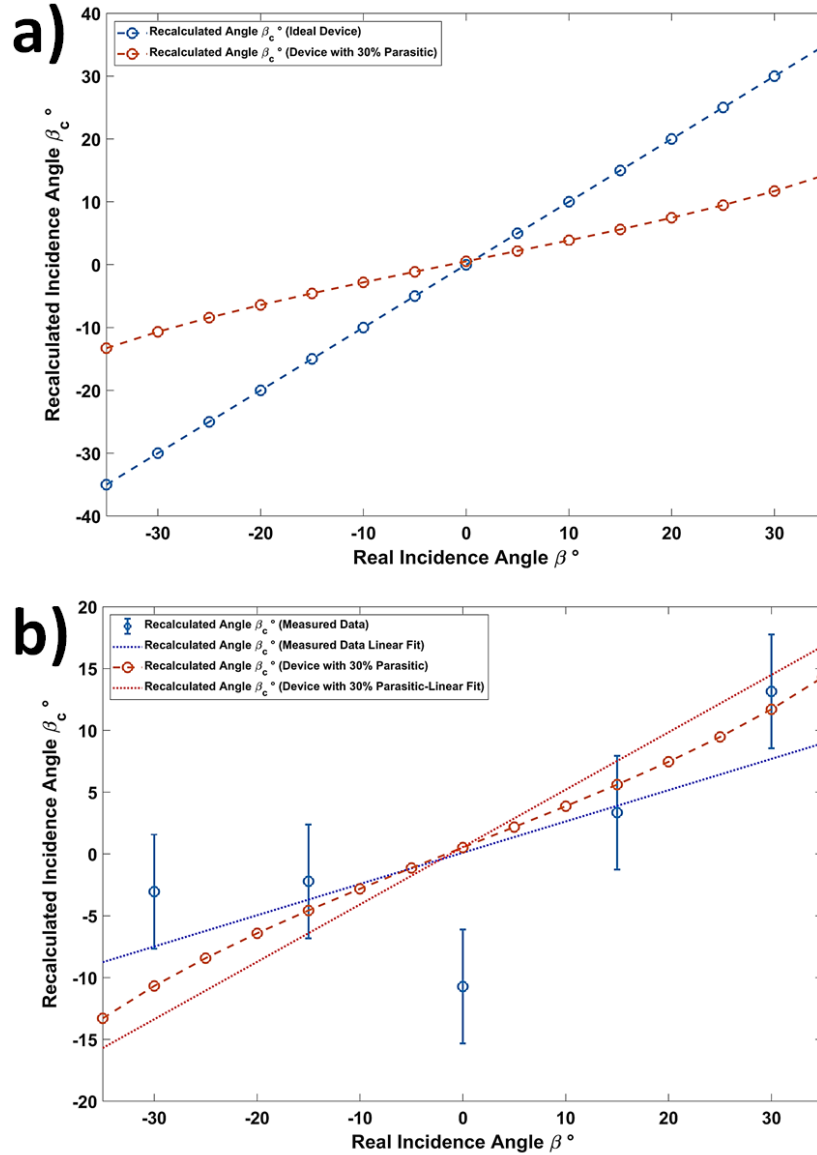


Figure 6- 38 The predicted angular recalculation using a device output with 30% parasitic contribution compared to a) ideal device and b) recalculated angles from the measured angular $\Delta R/R$ trends for 2nd design generation device. Statistical inference of the fitted trend lines are provided in appendix D.

6.3.4. Device (2nd Generation) Model Refinement to Account for Optical Power Losses

The expected and measured angular response behaviours of the devices have thus far incorporated only incident angle “line-of-site” arguments and materials properties (resistance effects) to account for the angle dependent observations. Further model development includes incorporation of the wavelength dependent, angle dependent polarization effects of the incident radiation. In general terms, the “polarization” of a photon refers to the direction of its electric field vector with respect to its plane of incidence (the plane containing the incident and reflected wave vectors as well as the normal to the surface, the photon is incident upon). The two basic polarizations are referred to as perpendicular (\perp) or S (Senkrecht) and parallel (\parallel) or P wherein the electric field is perpendicular to the incidence plane in S polarized photons and parallel to the incidence plane in P polarized photons (see Figure 6-39-a and b). The interaction of S and P polarized photons with a surface possessing a refractive index different than the incidence medium results in different degrees of the reflected optical power (see Figure 6-39-c). Since the photons from an unpolarized source can be decomposed into their respective P and S components, an unpolarized source is modeled to output 50% of each of the polarization at any given time. The aforementioned losses can be incorporated into the model in conjunction with the wavelength dependent refractive index of air and the sense material. The model described in Section 3.2.1 was revisited to account for the effect of incidence angle and the sense material refractive properties. Using Fresnel reflective power loss equations, the mathematical expression describing the output of the system was re-written to take into account such losses:

$$\Delta R_S = K_{th} \cdot K_R \cdot A_S \cdot \eta(\lambda) \cdot \left(\mathfrak{S}_P(n_{air}, n_{V_2O_5}, \beta) + \mathfrak{S}_S(n_{air}, n_{V_2O_5}, \beta) \right) \cdot P_i \cdot \sin(\beta \pm \alpha) + V_N \quad (78)$$

$$K_R = \delta_R \cdot R_o \quad (79)$$

$$K_{th} = \frac{1}{G_{sub} \cdot M_p \cdot C_p} \quad (80)$$

where ΔR_S is the sense region’s IR induced change in the measured electrical resistance, δ_R is the sense materia’s TCR, R_o is the sense material’s room temperature electrical resistance, K_{th} is the thermal sink coefficient as described by equation (80), \mathfrak{S}_S and \mathfrak{S}_P

are the angle dependent Fresnel coefficients for S (\perp) and P (\parallel) polarized transmitted incident IR. As mentioned earlier, in the case of an unpolarized electromagnetic source such as the IR source used for the described experimental setup, it is assumed that it produces equal fractions of S- and P-polarized photons. Hence, the Fresnel equations governing the angle dependent optical power losses can be presented as follows [114]:

$$\mathfrak{T}_S(n_{air}, n_{V_2O_5}, \beta) = 1 - \left(\frac{n_{Air} \cdot \cos(\beta) - n_{V_2O_5} \cdot \sqrt{\left(1 - \left(\frac{n_{Air}}{n_{V_2O_5}}\right) \cdot \sin(\beta)\right)^2}}{n_{Air} \cdot \cos(\beta) + n_{V_2O_5} \cdot \sqrt{\left(1 - \left(\frac{n_{Air}}{n_{V_2O_5}}\right) \cdot \sin(\beta)\right)^2}} \right)^2 \quad (81)$$

$$\mathfrak{T}_P(n_{air}, n_{V_2O_5}, \beta) = 1 - \left(\frac{n_{Air} \cdot \sqrt{1 - \left(\left(\frac{n_{Air}}{n_{V_2O_5}}\right) \cdot \sin(\beta)\right)^2} - n_{V_2O_5} \cdot \cos(\beta)}{n_{Air} \cdot \sqrt{1 - \left(\left(\frac{n_{Air}}{n_{V_2O_5}}\right) \cdot \sin(\beta)\right)^2} + n_{V_2O_5} \cdot \cos(\beta)} \right)^2 \quad (82)$$

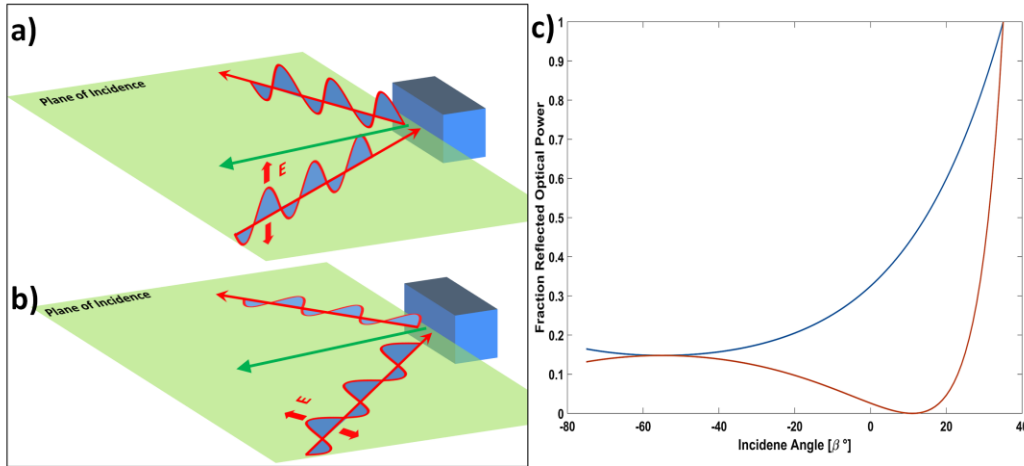


Figure 6- 39 Schematic depiction of a) S and b) P polarized photons. The graph in c) shows the fraction of the transmitted optical power as a function of the incidence angle from normal to the surface and refractive indices of air and V_2O_5 .

To verify the mathematical models presented above, the test setup under the discussion was used with a higher degree of control over the incidence parameters such that using a bandpass optical filter with a cut-off frequency at around 800 nm, the visible portion of the global spectral power distribution was eliminated to limit the device response to that of the IR photons. The rotary stage was then moved in 10° increments measuring the device's IR induced angular response with higher resolution hence generate higher chances of observing incidence angle induced reflection losses for comparison with the derived

mathematical model. The results were fitted to the theoretical trend with 30% parasitic contribution where the effect of polarization dependent reflective power losses for an even distribution of P and S polarized photons was incorporated into the model for comparison. Figure 6-40-a and b depicts the angle dependent $\Delta R/R$ trends for the east and west side separately to compare the theoretical trend with 30% parasitic contribution with and without the reflective loss, to the fitted trends to the data. As evident from the presented data, the output trends on the east and west side of the device show a better agreement with the theoretical trends corrected for reflective power losses with the east side agreeing with the corrected model to a larger degree compared to the west side. The recalculated angles from 2nd design generation samples with 10° increments are presented in the following set of graphs in Figure 6-41. The results depict that the new design improves in resolving in the unknown incidence angles with a better range compared to the first generation of the device proposed initially. Despite the significant increase in the range of the recalculated angles from the measured trends, the device output is still far from ideal in terms of accuracy of the values. Incorporation of the parasitic parameter \hat{N} to the recalculated angles for the 10° increment angular exposure test, results in a mild improvement in terms of accuracy. The latter could indicate that the impairment of the device's output is not, for the large part, due to the effect of the parasitic regions and may have to do with other factors such as that of the optical reflection induced losses. Such optical power losses arising from the polarization dependent reflectance can impair the magnitude of the difference in the $\Delta R/R$ trends from which the incidence angles are recalculated. Another hypothesized reason for deviation from the expected degree of accuracy in angular recalculation despite formidable changes in the device structure in the new design, is the susceptibility of thermal IR sensors to background radiation resulting from black body radiators other than the target, surrounding the structure during a measurement. The effect of such issue is simulated theoretically for two black body radiators one (the target) radiating at 37 °C and the other (the background) radiating at 15 °C (Appendix B).

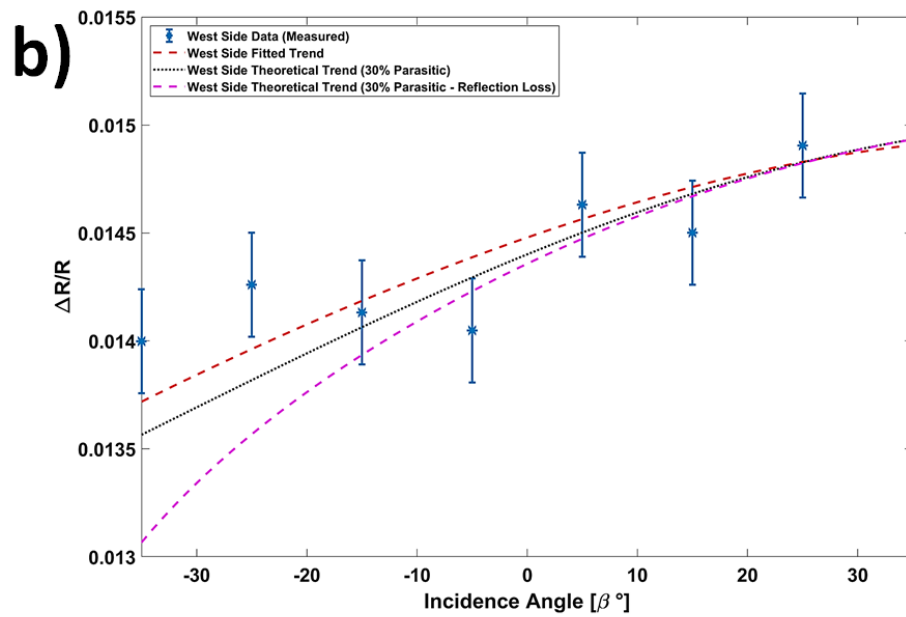
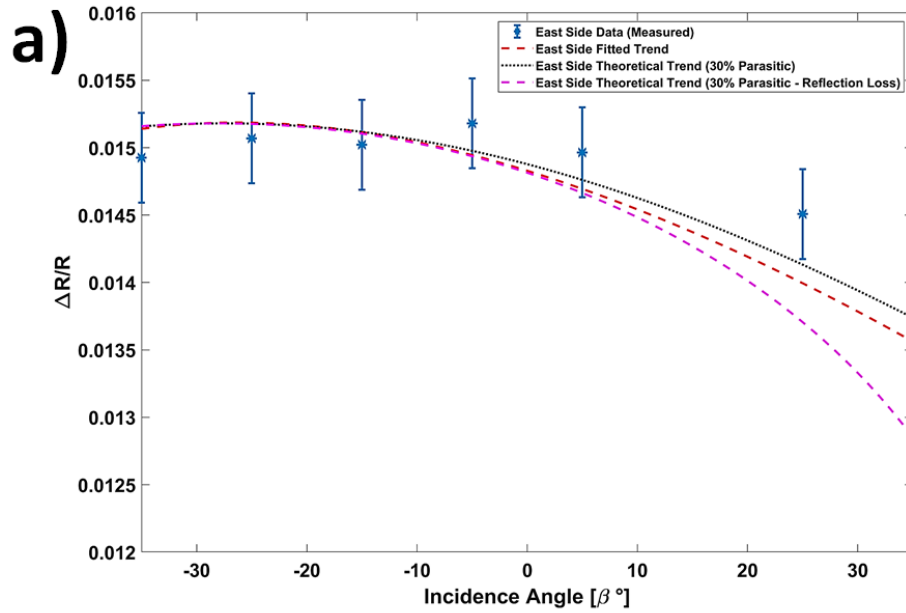


Figure 6- 40 Device output on the east and west side for 10 ° increment angular exposure being fitted to theoretical model with 30% parasitic contribution with and without accounting for the reflective losses for a) east side and b) west side of the 2nd design generation device. Statistical inference of the fitted model is provided in Appendix D.

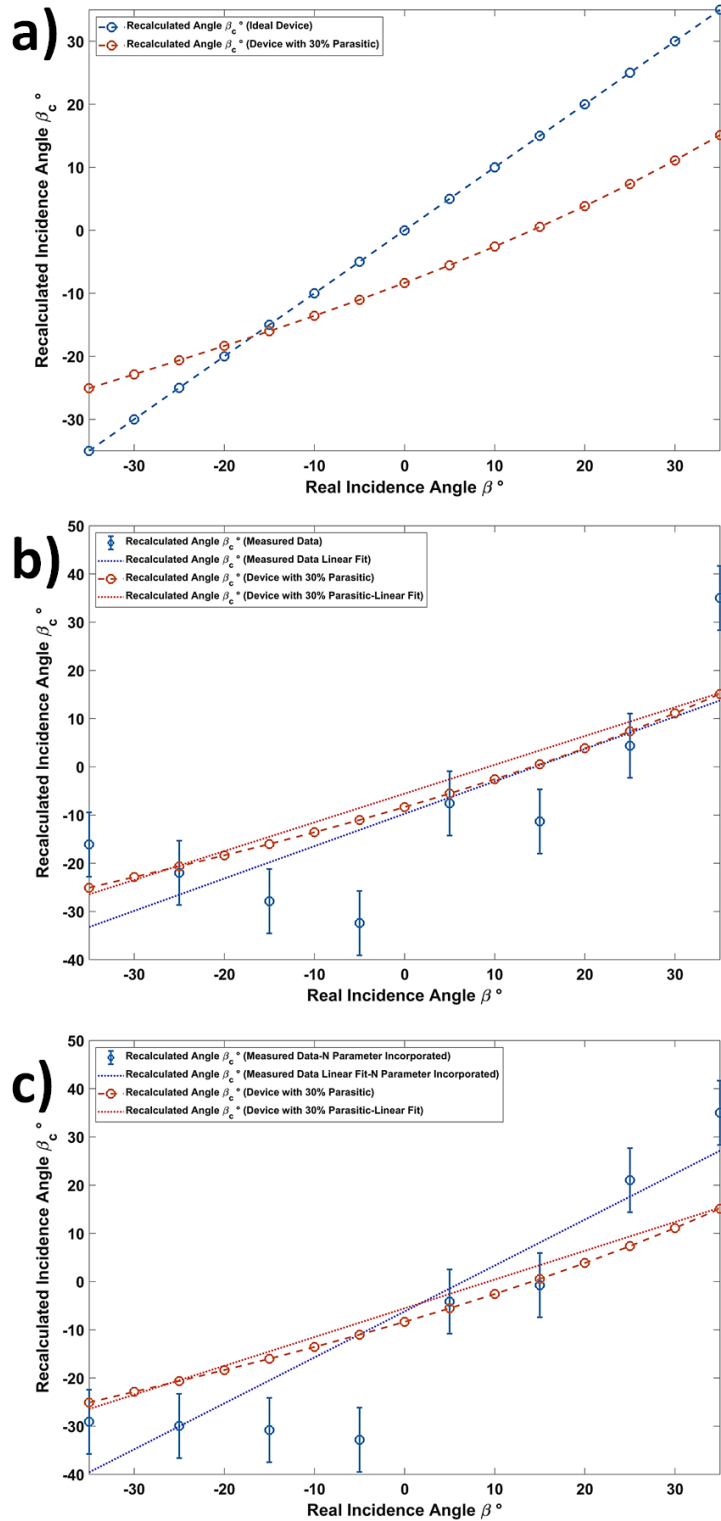


Figure 6- 41 The predicted angular recalibration using a device model output with 30% parasitic contribution and reflection induced optical power losses compared to a) ideal device and b) recalculated angles from the measured angular $\Delta R/R$ trends for 2nd design generation with linear trend lines fitted to the expected and measured data. c) Incorporation of parasitic parameter N does not improve the recalculated trends from measured data. Statistical inference of the fitted trend lines are provided in appendix D.

6.3.5. Device (2nd Design Generation) Angular Response Control Experiment

Previous experiments demonstrated that in its current form, the proposed directional IR pixel detector can track the angular path of an incident IR source using the ratio of the thermally generated $\Delta R/R$ at the two sides of the device. However in presence of loss factors discussed earlier, the difference in the measured electrical resistance change may deviate from the ideal values hence decrease the degree of accuracy with which the device can output the recalculated incidence angles. To investigate the 2nd design generation device's capability in recalculating the unknown incidence angle in the absence of the aforementioned losses, angular proximity measurements were performed using a similar test setup as described in figure 6-35-a. In the absence of an IR laser in the desired wavelength, use of the 670 nm diode laser as a collimated source of incidence allowed for an indirect excitation of the sense areas in a localized and accurate fashion. The latter eliminated the angular dispersion resulting from a none-collimated radiation source. To avoid heating the structure entirely, the laser was focused onto the sense regions as each side's response was recorded separately.

Similar to the previous control experiment use of proper optics along with the CCD camera allowed for visual confirmation of the diode laser's focused spot size on the sense region of the DUT. A NI LabView® controlled shutter was put in place of the optical chopper that allowed exposure times close to 66 ms. Figure 6-42 below captures a snapshot of the device under test, the optical test setup used for the measurements as well as the position of the laser during the measurements along with CCD image of the exposed area.

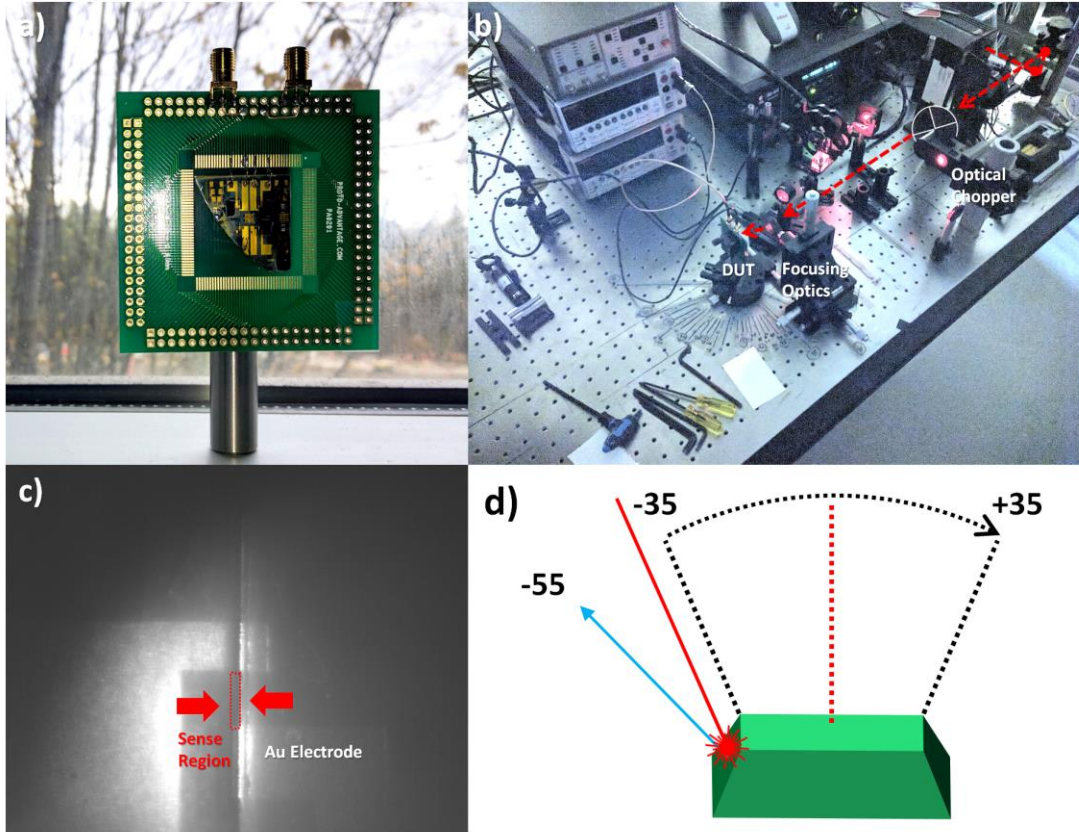


Figure 6- 42 a) A 2nd design generation device mounted on the prototyping board, b) The optical test setup used for inter-facet heat contamination; the dotted line shows the laser beam's path from the laser cavity all the way to DUT sense region, c) CCD image of the sense region; the red square shows the surface area the beam was focused onto and d) the angular path through which the DUT was exposed by the diode laser

The measurements were performed such that at each designated incidence angle the diode laser's spot was adjusted to lie directly on the sense region as depicted in Figure 6-42-c. The recorded $\Delta R/R$ trends in Figure 6-43-a display a better agreement to the predicted behavior by the mathematical model used to describe the device's output. This could be due to the elimination of the angular dispersion resulting from an extended source of incidence. When excited with a collimated source of incidence in a localized fashion, the device also shows a dramatic improvement in both range and the accuracy of the recalculated angles. The reason can be attributed to the bypassing of different processes that contributed to the loss of the perceived power ratio when the device was subject to none-collimated sources of radiation. Figure 6-43-a depicts a slight mismatch between the east and west side $\Delta R/R$ trends as a function of the incidence angle which can be a result of optical alignment mismatches arising from the focusing optics that converge the laser beam onto the sense regions of the device.

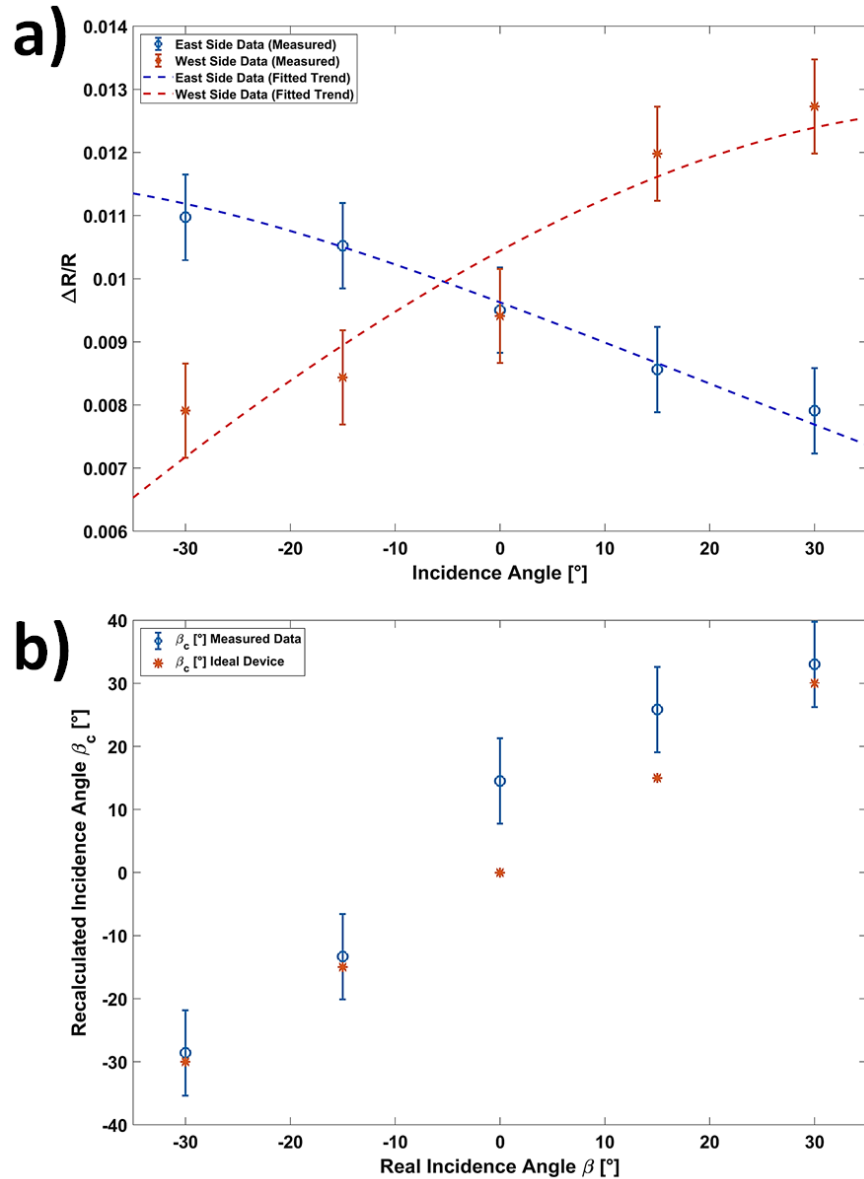


Figure 6- 43 a) The $\Delta R/R$ trends measured on the east and west sides of the 2nd generation device using the optical test setup described in Figure 6-42-a; b) the recalculated incidence angle using the ratio of the east and west side's $\Delta R/R$ trends in a). The recalculated angles show a dramatic improvement in both range and accuracy of the outputted values relative to the ideal case.

The associated uncertainty in results presented in figure 6-43, is calculated as the overall temperature induced fluctuations of the electrical resistance experienced over the entire duration of experiment at each measured angle. The presented deviation is before removing the drift due to the heating of the structure over the experiment duration that causes a large error. Shorter measurements should therefore be less susceptible to this.

6.3.6. Device (2nd Design Generation) Incidence Angle Recalculation Considerations

The control experiments revealed that in its current form, the 2nd design generation devices provide a reasonable degree of thermal insulation between the two sides of the device within shorter exposure times. As demonstrated (see Figure 6-36) within 125 ms of exposure to radiation, the exposed side's electrical resistance underwent a dramatic change in opposed to the unexposed side which showed little to no response. This however was despite the gradual heating and consequent gradual drop of the electrical resistance of the unexposed side as a result of thermal transfer through the underlying silicon substrate. The latter indicated that although in the current design the opposing sides of the device are thermally decoupled during shorter exposure times, if the measurements were to occur within greater time scales (~ 20 s), the unexposed side of the DUT begins to heat up and contribute to the otherwise independent readings that form the desired $\Delta R/R$ trends. Hence, to avoid inter-facet thermal energy transfer and localizing the measured response to that of a designated sense region, readout instances must be in time scales shorter than the time required for the opposing facet to fully heat up and contaminate the device output response. Despite the design considerations made, there were some resemblances between the 2nd generation device's angular output and 1st generation device models with 30% parasitic contribution which could be attributed to partial removal of the sense material (V_2O_5) across the surface of the device and in areas other the designated sense regions. In conclusion, in its current form the design offers novel capability to track the angular path of an incident IR source via thermoelectric sensing mechanism, however the degree of accuracy of the device's recalculated angles is poor when subject to none-collimated radiation sources. The theoretical model in chapter 3 (section 3.1.2) predicts the device's output to increase and decrease as a function of the target source of radiation hence the opposing sides generate a complementary response due to the incident thermal radiation absorption by the sense material. In practice, the opposing sides may heat up as a result of background sources of radiation and due to the absorption of radiative heat at different areas of the structure other than the sense regions and/or suffer from inevitable optical power losses arising from the radiation source's polarization. Hence, the following chapter offers some discussion on future avenues to improve the device's performance as a directional long wavelength infrared sensor.

Chapter 7. Conclusion and Future Work

7.1. Conclusion

In this chapter some final thoughts regarding the design considerations and means by which the proposed functionality of the device can be improved are laid out. Conclusions drawn as a result of the control experiments made aware of the challenges associated with free-space coupling of the incoming photons with the device's proposed three dimensional geometry. These challenges entail the optical power losses due to the polarisation dependent interaction of the incoming photon with that of the sense material surface. Such losses impose signal amplitude deterioration which in turns impacts the differential signal's range or ratio such that the recalculated value for the incidence angle is offsetted from the desired (true) value. Other issues associated with the free-space coupling of the incoming photons are related to the angular dispersion of an incoherent radiation source. The latter introduces a range of incidence angles instead of a single one and due to the differences in the incident's photon's wavelength and/or the source's radiation pattern due to its geometry. Such angular dispersion was seen to impose undesirable fluctuations in the device's angular response and distort the incidence angle recalculation. At the end amid the technical issues mentioned, the project resulted in design and fabrication of two different flavours of a novel three dimensional room temperature IR sensors for directional sensing. The fabricated devices were capable of directional sensing of human induced IR radiation at a distance close to 1 m and were capable of tracking an IR source with a good degree of accuracy. Given the natural complexities regarding signal and noise generation in thermal IR sensors and in the absence of optimised signal readout circuitry, the devices depicted a reasonable degree of compliance to the predicted functionality they were initially proposed for.

7.1.1. Contributions

In this PhD project, use of thermoelectric material for room temperature directional IR sensing was investigated for the first time. Prior to the present work, there have been no reports on pixel detectors capable of not only sensing the IR source using thermoelectric sensing mechanism, but also recalculating the incidence angle using the ratio of the induced changes in the electrical resistance at opposite output terminals of the device. Traditionally IR sensitive thermoelectric materials are used in planar pixel arrays to record a thermal image of the target IR source. The proposed pixel detector offers new IR sensing capabilities at room temperature which can be well suited in applications such as robotic and autonomous vehicles. The angular field of view (FOV) of the proposed device provides an extra array of information that would enhance the autonomous vehicle or robot's interaction with its surrounding environment hence create a much safer interaction between human and robotic workforce.

In the course of this PhD project, contributions were made in three main areas of scientific research: 1) IR material synthesis and characterisation, 2) device level analytical modeling and 3) device level fabrication process flow development. The room temperature IR sensitive material employed by the project was thoroughly researched and characterised while investigating alternative material deposition methods for the fabrication of the proposed device. A thorough analytical model was initiated, improved upon and verified in order to form a mathematical understanding of signal, parasitic and noise portions of the device's output. Some aspects of the device designs were also numerically simulated to give a better fabrication guideline for the device process flow. Given the unorthodox route chosen for synthesis and deposition of the IR sensitive material, a precise fabrication process flow was developed to enable repeatable prototyping of the device. Amid the initial design, optimisation processes were employed both in the process flow and the design of the proposed devices in order to yield results closer to what was forecasted based on the analytical models. Finally, and through rigorous scientific control experimentation, design flaws and/or physical limitations of the proposed devices were investigated to set the path for future work. The project has resulted in four peer reviewed journal and conference publications as listed below:

- 1) Grayli, Siamack V., et al. "Room temperature deposition of highly sensitive vanadium oxide films for infrared light sensing applications." *2015 IEEE SENSORS*. IEEE, 2015.

- 2) Ferrone, A., et al. "Flexible near infrared photoresistors based on recrystallized amorphous germanium thin films." *2016 IEEE SENSORS*. IEEE, 2016.
- 3) Grayli, S. V., et al. "Infrared photo-resistors based on recrystallized amorphous germanium films on flexible substrates." *Sensors and Actuators A: Physical* 263 (2017): 341-348.
- 4) Grayli, Siamack V., Gary W. Leach, and Behraad Bahreyni. "Sol-gel deposition and characterization of vanadium pentoxide thin films with high TCR." *Sensors and Actuators A: Physical* 279 (2018): 630-637.

7.1.2. Future Work

The control experiments performed on the two generation of the devices revealed a series of challenges associated with the proposed mechanism of IR sensing. Based on the nature of the challenges as were described in 6.4.3 and the ramifications thereof can be resolved via expanding the future work in three main directions which will be discussed briefly in the following sections.

Device Field of View Limitation Improvement

According to the proposed model for a line of sight detector, the current devices (with sense regions at the sides) are bound to a geometrical FOV limitation that arises from the known angle of silicon (111) facets. Given that the known value of this quantity is one of the key elements in the mathematical model that relates the otherwise unknown angle of incidence to the ratio of the perceived power by the two sides of the device, a few techniques are proposed to improve the FOV.

- 1) Use of facets with narrower inclination silicon anisotropic etching results in formation of slanted facets that form different angles with horizontal plane. Use of these facets as an alternative to the proposed (111) facet by this work can increase the device FOV by a total of 30 ° via pushing the reliable detection area to -45 °: 45 ° instead of the -35 °: 35 ° for the proposed devices (See figure).

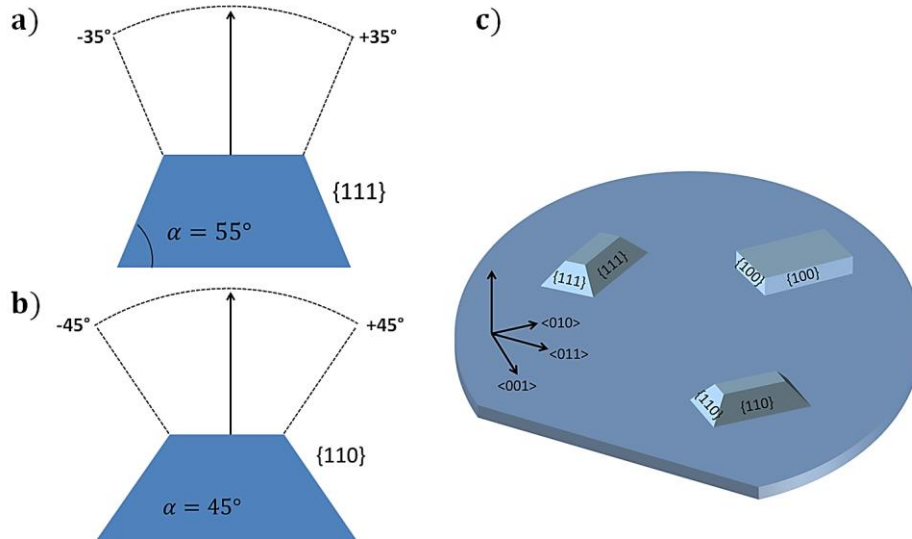


Figure 7- 1 2D Schematic of different micromachined silicon facets with the inclined surface to be on a) $\{111\}$ facet and b) $\{110\}$ facet of the silicon substrate and their effects on the device FOV. c) 3D depiction of such structures on a $\langle 001 \rangle$ wafer

- 2) Use of a reference sense region on the top of the pyramidal structure another way of rectifying the facet angle induced limitation is to employ a reference region whose perceived power never becomes zero. Existence of such reference facet allows for evaluation of the incidence angle at larger angular FOV and through evaluation of both facets with respect to the reference (See figure).

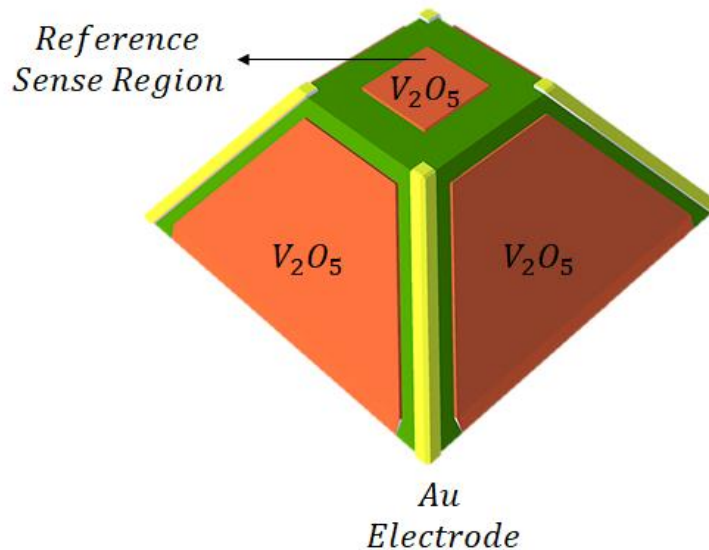


Figure 7-2 Schematic of a device design with reference sense region on the top surface

Device Thermal Conduction Improvement

Given the thermal nature of the detector, there are challenges associated with differentiating between the target radiation source and other thermally radiating sources in the background. An example calculation in appendix B discusses the case of the device in the presence of thermally radiating sources with comparable temperature, and the effects of such interference on accurate angle recalculation capability of the device. To mitigate such issue and make the devices more selective a few routes can be taken which are discussed briefly in this section.

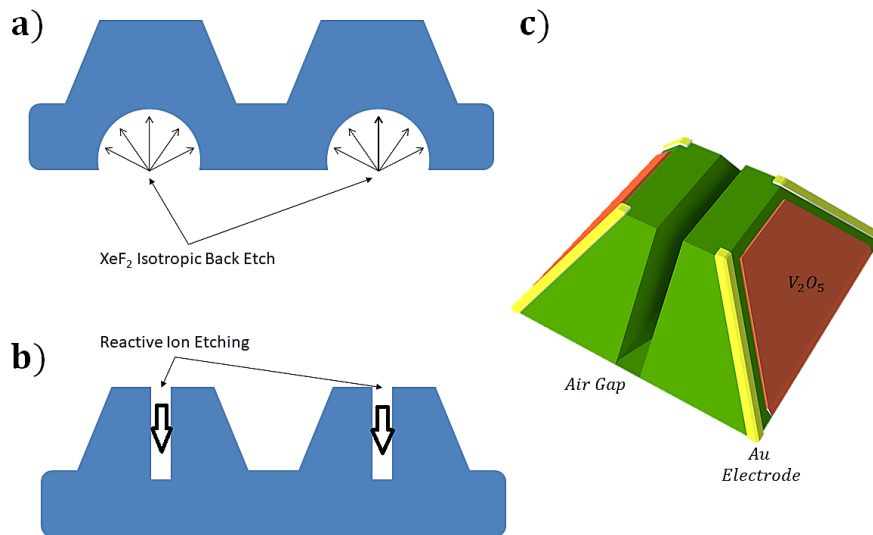


Figure 7- 3 Device thermal contamination reduction for a) reducing the bulk silicon heat sink effect and b) 2D and c) 3D depiction of air gap introduction between the device sense facets to reduce inter facet heat transfer

Device Thermal Response Selectivity Improvement

Tuning of the Sense Material's Absorption Peak

Given that thermal radiation peak emission wavelengths are different for radiation sources at different temperatures, the sense material can be tuned to have peak absorption at the difference between the peak wavelengths for the desired target and the background. Such tuning can be done through varying different synthesis parameters of the sense material's sol and prior to its deposition onto the sense regions of the device. Figure below shows the peak absorption for differentiating between a target IR source such as human at 37 °C and a source at room temperature (~ 25 °C).

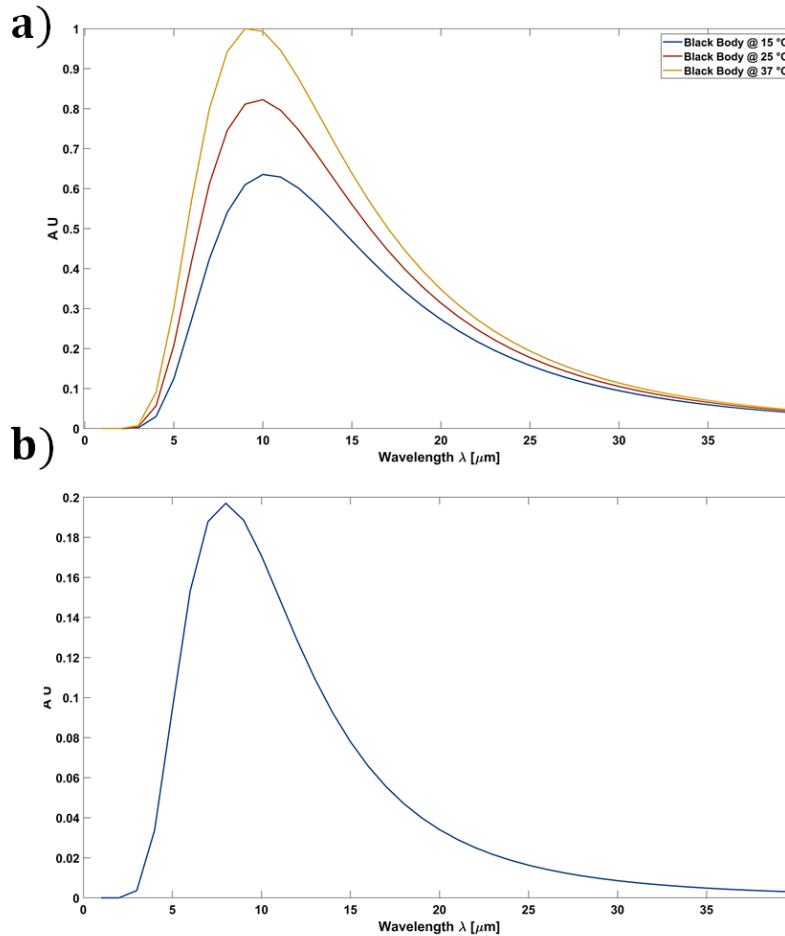


Figure 7- 4 a) Radiation spectra of blackbodies emitting at (from lowest intensity to the highest intensity) at 15 °C, 25 °C and 37 °C. b) the difference between the peak emission spectra of a target at 37 °C and room temperature object at 25 °C.

Use of Selective Optical Coupling Techniques

Aside from the material's peak absorption, the device's selectivity towards a specific spectral band can also be tuned via employment of spectrally selective coupling processes wherein the designated sense area resonantly responds to an incoming photon of a specific wavelength the optical structures are tuned to. The selectivity in this case arises from generation of localized heat as a result of photon's interaction with the optical structure hence the device's response becomes much more pronounced when exposed to a specific spectral band. An example of such process is plasmonic coupling of the incident wavelength to the sense region of the device. Plasmons are the quantization of the bulk plasma oscillations in metallic solids. At a metal-dielectric interface this quantization describes a coherent electron cloud (plasma) oscillation referred to as the surface plasmon. Specifically designed optical structures on such interfaces allow for

spectrally selective interaction and coupling of an incoming photon's electric field with the surface plasmons which results in photothermal decay, inducing a thermoelectric response in the sense material at the vicinity of optical structures. Depending on the wavelength of choice, the size and dimensions of these optical structures vary. Employment of such coupling mechanism however would introduce challenges regarding the fabrication of the optical structures onto the designated sense region as well as compatibility between the metallic solid used as a plasmonic material. However, if implemented, plasmonic coupling shows a strong spectral dependence hence would diminish the device's response to background radiation in favor of the desired (target) wavelength (see Figure).

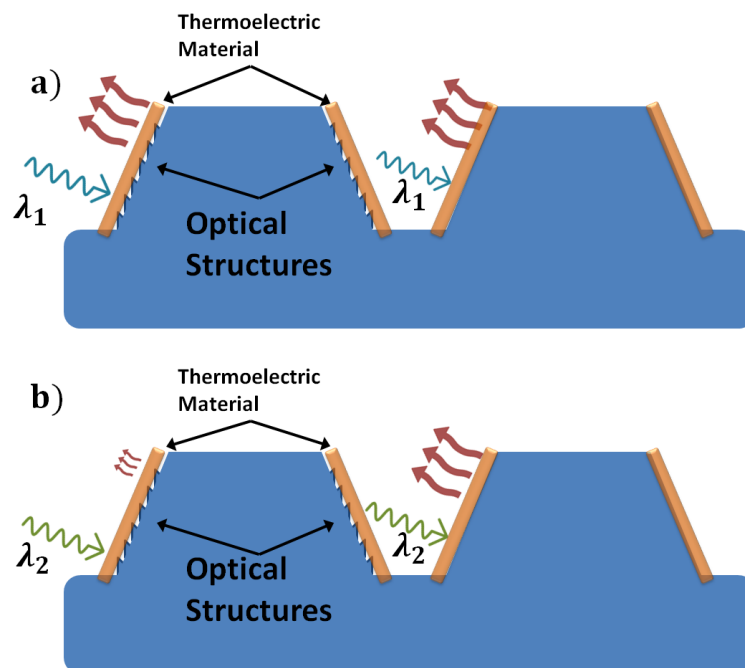


Figure 7- 5 Schematic of spectrally selective devices vs current design for a) incidence of a photon at the desired wavelength (λ_1) and b) undesired wavelength (λ_2). The heat symbol's size indicates the magnitude of the thermal response due to absorbed photon.

References

- [1] D. Zhang, *Advanced Mechatronics and MEMS Devices*. Springer Science & Business Media, 2012.
- [2] G. Rieke, *Detection of Light: From the Ultraviolet to the Submillimeter*. Cambridge, UNITED KINGDOM: Cambridge University Press, 2002.
- [3] H. Baltes, O. Brand, G. K. Fedder, C. Hierold, J. G. Korvink, and O. Tabata, *CMOS-MEMS: Advanced Micro and Nanosystems*. John Wiley & Sons, 2008.
- [4] K. Takahata, *Advances in Micro/Nano Electromechanical Systems and Fabrication Technologies*. BoD – Books on Demand, 2013.
- [5] S. Nihtianov and A. Luque, *Smart Sensors and MEMS: Intelligent Sensing Devices and Microsystems for Industrial Applications*. Woodhead Publishing, 2018.
- [6] S. Park, A. Lay-Ekuakille, O. Postolache, and P. M. B. da S. Girão, *Intelligent Sensing Technologies for Nondestructive Evaluation*. MDPI, 2018.
- [7] *Intelligent Sensor Networks*. .
- [8] H. Yamasaki, *Intelligent Sensors*. Elsevier, 1996.
- [9] J. L. Miller, *Principles of Infrared Technology: A Practical Guide to the State of the Art*. Springer Science & Business Media, 2012.
- [10] A. Rogalski, *Infrared and Terahertz Detectors, Third Edition*. CRC Press, 2019.
- [11] H. Budzier and G. Gerlach, *Thermal Infrared Sensors: Theory, Optimisation and Practice*. John Wiley & Sons, 2011.
- [12] K. Chrzanowski and A. Rogalski, "Infrared devices and techniques," in *Handbook of Optoelectronics (Two-Volume Set)*, Taylor & Francis, 2006, pp. 653–692.
- [13] A. Rogalski, *Infrared Detectors*. CRC Press, 2010.
- [14] M. Henini and M. Razeghi, *Handbook of Infrared Detection Technologies*. Elsevier, 2002.
- [15] J. Caniou, *Passive Infrared Detection: Theory and Applications*. Springer Science & Business Media, 2013.
- [16] H. Kaplan, *Practical Applications of Infrared Thermal Sensing and Imaging Equipment*. SPIE Press, 2007.
- [17] K. R. Kozlowski, *Robot Motion and Control 2007*. Springer Science & Business Media, 2007.
- [18] T. Bräunl, *Embedded Robotics: Mobile Robot Design and Applications with Embedded Systems*. Springer Science & Business Media, 2013.
- [19] G. Benet, F. Blanes, J. E. Simó, and P. Pérez, "Using infrared sensors for distance measurement in mobile robots," *Robotics and Autonomous Systems*, vol. 40, no. 4, pp. 255–266, Sep. 2002.
- [20] H. R. Everett, *Sensors for Mobile Robots*. CRC Press, 1995.
- [21] P. Capper and C. T. Elliott, *Infrared Detectors and Emitters: Materials and Devices*. Springer Science & Business Media, 2013.
- [22] K. Matoy *et al.*, "A comparative micro-cantilever study of the mechanical behavior of silicon based passivation films," *Thin Solid Films*, vol. 518, no. 1, pp. 247–256, Nov. 2009.
- [23] V. A. Sethuraman, M. J. Chon, M. Shimshak, V. Srinivasan, and P. R. Guduru, "In situ measurements of stress evolution in silicon thin films during electrochemical lithiation and delithiation," *Journal of Power Sources*, vol. 195, no. 15, pp. 5062–5066, Aug. 2010.
- [24] X. Wu, J. Yu, T. Ren, and L. Liu, "Micro-Raman spectroscopy measurement of stress in silicon," *Microelectronics Journal*, vol. 38, no. 1, pp. 87–90, Jan. 2007.

- [25] A. Gupta, J. P. Denton, H. McNally, and R. Bashir, "Novel fabrication method for surface micromachined thin single-crystal silicon cantilever beams," *Journal of Microelectromechanical Systems*, vol. 12, no. 2, pp. 185–192, Apr. 2003.
- [26] J. Beyerer, F. P. León, and C. Frese, *Machine Vision: Automated Visual Inspection: Theory, Practice and Applications*. Springer, 2015.
- [27] L. Salgado-Conrado, "A review on sun position sensors used in solar applications," *Renewable and Sustainable Energy Reviews*, vol. 82, pp. 2128–2146, 2018.
- [28] T. D. Drysdale, "Plasmonic angle sensitive pixel for digital imagers," in *2016 IEEE 6th International Conference on Photonics (ICP)*, 2016, pp. 1–3.
- [29] V. Varghese and S. Chen, "Polarization-based angle sensitive pixels for light field image sensors with high spatio-angular resolution," *IEEE Sensors Journal*, vol. 16, no. 13, pp. 5183–5194, 2016.
- [30] D. A. Hoang, T. T. Tung, C. M. Nguyen, and K. P. Nguyen, "Rotating Sensor for Multi-Direction Light Intensity Measurement," in *2019 International Conference on System Science and Engineering (ICSSE)*, 2019, pp. 462–467.
- [31] M. Levoy, R. Ng, A. Adams, M. Footer, and M. Horowitz, "Light field microscopy," *ACM Transactions on Graphics (TOG)*, vol. 25, no. 3, pp. 924–934, 2006.
- [32] R. Ng, M. Levoy, M. Brédif, G. Duval, M. Horowitz, and P. Hanrahan, "Light field photography with a hand-held plenoptic camera," *Computer Science Technical Report CSTR*, vol. 2, no. 11, pp. 1–11, 2005.
- [33] M. Levoy, "Light fields and computational imaging," *Computer*, no. 8, pp. 46–55, 2006.
- [34] A. Lumsdaine and T. Georgiev, "The focused plenoptic camera," in *2009 IEEE International Conference on Computational Photography (ICCP)*, 2009, pp. 1–8.
- [35] A. Trebi-Ollennu, T. Huntsberger, Y. Cheng, E. T. Baumgartner, B. Kennedy, and P. Schenker, "Design and analysis of a sun sensor for planetary rover absolute heading detection," *IEEE Transactions on Robotics and Automation*, vol. 17, no. 6, pp. 939–947, 2001.
- [36] Y. Away and M. Ikhsan, "Dual-axis sun tracker sensor based on tetrahedron geometry," *Automation in Construction*, vol. 73, pp. 175–183, 2017.
- [37] C. Perra, "Lossless plenoptic image compression using adaptive block differential prediction," in *2015 IEEE International Conference on Acoustics, Speech and Signal Processing (ICASSP)*, 2015, pp. 1231–1234.
- [38] C. C. Liebe and S. Mobasser, "MEMS based sun sensor," in *2001 IEEE Aerospace Conference Proceedings (Cat. No. 01TH8542)*, 2001, vol. 3, pp. 3–1565.
- [39] V. Varghese and S. Chen, "Polarization-based angle sensitive pixels for light field image sensors with high spatio-angular resolution," *IEEE Sensors Journal*, vol. 16, no. 13, pp. 5183–5194, 2016.
- [40] Z. Zivkovic and C. C. Tak, "Integrated sensor chip package with directional light sensor, apparatus including such a package and method of manufacturing such an integrated sensor chip package," May-2017.
- [41] U. S. Inan, *Engineering Electromagnetics*. Addison Wesley Longman, 1998.
- [42] P. A. Tipler, *Modern Physics*. Worth Publishers, 1978.
- [43] S. Soloman, *Sensors Handbook*. Mcgraw-hill, 2009.
- [44] C. Kuenzer and S. Dech, *Thermal Infrared Remote Sensing: Sensors, Methods, Applications*. Springer Science & Business Media, 2013.
- [45] A. Rogalski, K. Adamiec, and J. Rutkowski, *Narrow-gap Semiconductor Photodiodes*. SPIE Press, 2000.
- [46] M. A. Kinch, *Fundamentals of Infrared Detector Materials*. SPIE Press, 2007.
- [47] A. Rogalski, *New Ternary Alloy Systems for Infrared Detectors*. SPIE Press, 1994.

- [48] P. W. Kruse, *Uncooled Thermal Imaging: Arrays, Systems, and Applications*. SPIE Press, 2001.
- [49] H. Bhugra and G. Piazza, *Piezoelectric MEMS Resonators*. Springer, 2017.
- [50] A. Rogalski, "Optical detectors for focal plane arrays," *Optoelectronics review*, vol. 12, no. 2, pp. 221–246, 2004.
- [51] P. Guggilla, A. K. Batra, J. R. Currie, M. D. Aggarwal, M. A. Alim, and R. B. Lal, "Pyroelectric ceramics for infrared detection applications," *Materials Letters*, vol. 60, no. 16, pp. 1937–1942, 2006.
- [52] A. Rogalski, "Recent progress in infrared detector technologies," *Infrared Physics & Technology*, vol. 54, no. 3, pp. 136–154, 2011.
- [53] *Proceedings of the International Conference on Smart Materials, Structures and Systems: In Conjunction with the Ninth National Seminar on Aerospace Structures, 7-10 July, 1999, Bangalore*. Allied Publishers, 1999.
- [54] P. A. Cox, *Transition Metal Oxides: An Introduction to Their Electronic Structure and Properties*. Oxford University Press, 2010.
- [55] F.-C. Chiu, "A Review on Conduction Mechanisms in Dielectric Films," *Advances in Materials Science and Engineering*, 2014. [Online]. Available: <https://www.hindawi.com/journals/amse/2014/578168/abs/>. [Accessed: 28-May-2019].
- [56] I. B. Bersuker, *Electronic Structure and Properties of Transition Metal Compounds: Introduction to the Theory*. John Wiley & Sons, 2010.
- [57] R. R. Heikes and W. D. Johnston, "Mechanism of Conduction in Li-Substituted Transition Metal Oxides," *The Journal of Chemical Physics*, vol. 26, no. 3, pp. 582–587, 1957.
- [58] S. Walia *et al.*, "Transition metal oxides – Thermoelectric properties," *Progress in Materials Science*, vol. 58, no. 8, pp. 1443–1489, Oct. 2013.
- [59] R. B. Darling and S. Iwanaga, "Structure, properties, and MEMS and microelectronic applications of vanadium oxides," *Sadhana*, vol. 34, no. 4, p. 531, Oct. 2009.
- [60] S. Lany, "Semiconducting transition metal oxides," *J. Phys.: Condens. Matter*, vol. 27, no. 28, p. 283203, Jun. 2015.
- [61] N. Fieldhouse, S. M. Pursel, M. W. Horn, and S. S. N. Bharadwaja, "Electrical properties of vanadium oxide thin films for bolometer applications: processed by pulse dc sputtering," *Journal of Physics D: Applied Physics*, vol. 42, no. 5, p. 055408, 2009.
- [62] B. D. Gauntt, E. C. Dickey, and M. W. Horn, "Stoichiometry and microstructural effects on electrical conduction in pulsed dc sputtered vanadium oxide thin films," *Journal of materials Research*, vol. 24, no. 4, pp. 1590–1599, 2009.
- [63] G. M. Gouda and C. L. Nagendra, "Structural and electrical properties of mixed oxides of manganese and vanadium: a new semiconductor oxide thermistor material," *Sensors and Actuators A: Physical*, vol. 155, no. 2, pp. 263–271, 2009.
- [64] T. Allersma, R. Hakim, T. N. Kennedy, and J. D. Mackenzie, "Structure and Physical Properties of Solid and Liquid Vanadium Pentoxide," *J. Chem. Phys.*, vol. 46, no. 1, pp. 154–160, Jan. 1967.
- [65] A. Šurca and B. Orel, "IR spectroscopy of crystalline V2O5 films in different stages of lithiation," *Electrochimica Acta*, vol. 44, no. 18, pp. 3051–3057, May 1999.
- [66] A. Subrahmanyam, Y. B. K. Reddy, and C. L. Nagendra, "Nano-vanadium oxide thin films in mixed phase for microbolometer applications," *Journal of Physics D: Applied Physics*, vol. 41, no. 19, p. 195108, 2008.
- [67] G. M. Gouda and C. L. Nagendra, "Preparation and characterization of thin film thermistors of metal oxides of manganese and vanadium (Mn-VO)," *Sensors and Actuators A: Physical*, vol. 190, pp. 181–190, 2013.

- [68] G. M. Gouda and C. L. Nagendra, "Structural and electrical properties of mixed oxides of manganese and vanadium: a new semiconductor oxide thermistor material," *Sensors and Actuators A: Physical*, vol. 155, no. 2, pp. 263–271, 2009.
- [69] R. R. Kumar *et al.*, "Pulsed laser deposited vanadium oxide thin films for uncooled infrared detectors," *Sensors and Actuators A: Physical*, vol. 107, no. 1, pp. 62–67, 2003.
- [70] S. Guimond *et al.*, "Well-ordered V₂O₅ (001) thin films on Au (111): growth and thermal stability," *The Journal of Physical Chemistry C*, vol. 112, no. 31, pp. 11835–11846, 2008.
- [71] Y. J. Park, K. S. Ryu, N.-G. Park, Y.-S. Hong, and S. H. Chang, "RF-Sputtered Vanadium Oxide Films Effect of Film Thickness on Structural and Electrochemical Properties," *Journal of The Electrochemical Society*, vol. 149, no. 5, pp. A597–A602, 2002.
- [72] Y. J. Park, K. S. Ryu, N.-G. Park, Y.-S. Hong, and S. H. Chang, "RF-Sputtered Vanadium Oxide Films Effect of Film Thickness on Structural and Electrochemical Properties," *Journal of The Electrochemical Society*, vol. 149, no. 5, pp. A597–A602, 2002.
- [73] I. El-chami, S. Vosoogh-Grayli, D. Zhuo, and B. Bahreyni, "A vector light detector for proximity sensing applications," in *2016 IEEE SENSORS*, 2016, pp. 1–3.
- [74] M. Bukshab, *Applied Photometry, Radiometry, and Measurements of Optical Losses*. Springer Science & Business Media, 2012.
- [75] P. Pal and K. Sato, *Silicon Wet Bulk Micromachining for MEMS*. CRC Press, 2017.
- [76] N. Topaloglu, "Analysis and Modeling of Uncooled Microbolometers with Tunable Thermal Conductance," May 2009.
- [77] "report_FLIR.pdf." .
- [78] W. A. Lentz, "Characterization of noise in uncooled IR bolometer arrays," PhD Thesis, Massachusetts Institute of Technology, 1998.
- [79] C. Venkatasubramanian, O. M. Cabarcos, D. L. Allara, M. W. Horn, and S. Ashok, "Correlation of temperature response and structure of annealed VO_x thin films for IR detector applications," *Journal of Vacuum Science & Technology A: Vacuum, Surfaces, and Films*, vol. 27, no. 4, pp. 956–961, 2009.
- [80] N. Fieldhouse, S. M. Pursel, M. W. Horn, and S. S. N. Bharadwaja, "Electrical properties of vanadium oxide thin films for bolometer applications: processed by pulse dc sputtering," *Journal of Physics D: Applied Physics*, vol. 42, no. 5, p. 055408, 2009.
- [81] P. Vilanova-Martínez, J. Hernández-Velasco, A. R. Landa-Cánovas, and F. Agulló-Rueda, "Laser heating induced phase changes of VO₂ crystals in air monitored by Raman spectroscopy," *Journal of Alloys and Compounds*, vol. 661, pp. 122–125, 2016.
- [82] B. Wang, J. Lai, H. Li, H. Hu, and S. Chen, "Nanostructured vanadium oxide thin film with high TCR at room temperature for microbolometer," *Infrared Physics & Technology*, vol. 57, pp. 8–13, 2013.
- [83] T. Allersma, R. Hakim, T. N. Kennedy, and J. D. Mackenzie, "Structure and physical properties of solid and liquid vanadium pentoxide," *The Journal of Chemical Physics*, vol. 46, no. 1, pp. 154–160, 1967.
- [84] J. Livage, "Vanadium pentoxide gels," *Chem. Mater*, vol. 3, no. 4, pp. 578–593, 1991.
- [85] P. Aldebert, N. Baffier, N. Gharbi, and J. Livage, "Layered structure of vanadium pentoxide gels," *Materials Research Bulletin*, vol. 16, no. 6, pp. 669–676, 1981.
- [86] R. R. Kumar *et al.*, "Room temperature deposited vanadium oxide thin films for uncooled infrared detectors," *Materials Research Bulletin*, vol. 38, no. 7, pp. 1235–1240, 2003.

- [87] M. S. de Castro, C. L. Ferreira, and R. R. de Avillez, "Vanadium oxide thin films produced by magnetron sputtering from a V₂O₅ target at room temperature," *Infrared Physics & Technology*, vol. 60, pp. 103–107, 2013.
- [88] T. Blanquart *et al.*, "Atomic layer deposition and characterization of vanadium oxide thin films," *RSC Advances*, vol. 3, no. 4, pp. 1179–1185, 2013.
- [89] K. G. West *et al.*, "Growth and characterization of vanadium dioxide thin films prepared by reactive-biased target ion beam deposition," *Journal of Vacuum Science & Technology A: Vacuum, Surfaces, and Films*, vol. 26, no. 1, pp. 133–139, 2008.
- [90] K. R. Asmis and J. Sauer, "Mass-selective vibrational spectroscopy of vanadium oxide cluster ions," *Mass spectrometry reviews*, vol. 26, no. 4, pp. 542–562, 2007.
- [91] J. Verkelis, K. Breivé, V. Dikinis, and R. Šarmaitis, "Vanadium oxides thin films and fixed-temperature heat sensor with memory," *Sensors and Actuators A: Physical*, vol. 68, no. 1–3, pp. 338–343, 1998.
- [92] D. Barreca *et al.*, "Highly Oriented V₂O₅ Nanocrystalline Thin Films by Plasma-Enhanced Chemical Vapor Deposition," *Chem. Mater.*, vol. 12, no. 1, pp. 98–103, Jan. 2000.
- [93] Q. Shi *et al.*, "Preparation and phase transition characterization of VO₂ thin film on single crystal Si (100) substrate by sol–gel process," *Journal of sol-gel science and technology*, vol. 59, no. 3, p. 591, 2011.
- [94] L. N. Son, T. Tachiki, and T. Uchida, "Characteristics of vanadium oxide thin films prepared by metal–organic decomposition for bolometer detectors," *Japanese Journal of Applied Physics*, vol. 50, no. 2R, p. 025803, 2011.
- [95] Y. Vijayakumar *et al.*, "V₂O₅ nanofibers: Potential contestant for high performance xylene sensor," *Journal of Alloys and Compounds*, vol. 731, pp. 805–812, 2018.
- [96] A. A. Darhuber, S. M. Troian, J. M. Davis, S. M. Miller, and S. Wagner, "Selective dip-coating of chemically micropatterned surfaces," *Journal of Applied Physics*, vol. 88, no. 9, pp. 5119–5126, 2000.
- [97] L.-J. Meng, R. A. Silva, H.-N. Cui, V. Teixeira, M. P. dos Santos, and Z. Xu, "Optical and structural properties of vanadium pentoxide films prepared by d.c. reactive magnetron sputtering," *Thin Solid Films*, vol. 515, no. 1, pp. 195–200, Sep. 2006.
- [98] C. V. Ramana and O. Mahammad Hussain, "Optical absorption behaviour of vanadium pentoxide thin films," *Advanced Materials for Optics and Electronics - ADV MATER OPT ELECTRON*, vol. 7, pp. 225–231, Sep. 1997.
- [99] M. Benmoussa, E. Ibnouelghazi, A. Bennouna, and E. L. Ameziane, "Structural, electrical and optical properties of sputtered vanadium pentoxide thin films," *Thin Solid Films*, vol. 265, no. 1, pp. 22–28, Sep. 1995.
- [100] C. J. Brinker and G. W. Scherer, *Sol-Gel Science: The Physics and Chemistry of Sol-Gel Processing*. Academic Press, 2013.
- [101] S. Dervin and S. C. Pillai, "An Introduction to Sol-Gel Processing for Aerogels," in *Sol-Gel Materials for Energy, Environment and Electronic Applications*, S. C. Pillai and S. Hehir, Eds. Cham: Springer International Publishing, 2017, pp. 1–22.
- [102] A. Chakrabarti, K. Hermann, R. Druzinic, M. Witko, F. Wagner, and M. Petersen, "Geometric and electronic structure of vanadium pentoxide: A density functional bulk and surface study," *Physical Review B*, vol. 59, no. 16, p. 10583, 1999.
- [103] N. Özer, "Electrochemical properties of sol-gel deposited vanadium pentoxide films," *Thin Solid Films*, vol. 305, no. 1–2, pp. 80–87, 1997.
- [104] J. Livage, "Optical and electrical properties of vanadium oxides synthesized from alkoxides," *Coordination Chemistry Reviews*, vol. 190–192, pp. 391–403, Sep. 1999.
- [105] I. Schmidhalter, R. L. Cerro, M. D. Giavedoni, and F. A. Saita, "Liquid film drag out in the presence of molecular forces," *Physics of Fluids*, vol. 25, no. 3, p. 032105, Mar. 2013.

- [106]“The effect of film thickness and TiO₂ content on film formation from PS/TiO₂ nanocomposites prepared by dip-coating method.” [Online]. Available: <https://dl.acm.org/citation.cfm?id=2336648>. [Accessed: 28-May-2019].
- [107]T. W. Kelley and C. D. Frisbie, “Gate voltage dependent resistance of a single organic semiconductor grain boundary,” *The Journal of Physical Chemistry B*, vol. 105, no. 20, pp. 4538–4540, 2001.
- [108]Q. Su, W. Lan, Y. Y. Wang, and X. Q. Liu, “Structural characterization of β -V₂O₅ films prepared by DC reactive magnetron sputtering,” *Applied Surface Science*, vol. 255, no. 7, pp. 4177–4179, 2009.
- [109]P. Pal, K. Sato, and S. Chandra, “Fabrication techniques of convex corners in a (1\hspace0.167em0\hspace0.167em0)-silicon wafer using bulk micromachining: a review,” *J. Micromech. Microeng.*, vol. 17, no. 10, pp. R111–R133, Sep. 2007.
- [110]W. Fan and D. Zhang, “A simple approach to convex corner compensation in anisotropic KOH etching on a (1\hspace0.167em0\hspace0.167em0) silicon wafer,” *J. Micromech. Microeng.*, vol. 16, no. 10, pp. 1951–1957, Aug. 2006.
- [111]P. Pal, K. Sato, M. A. Gosalvez, and M. Shikida, “An improved anisotropic wet etching process for the fabrication of silicon mems structures using a single etching mask,” in *2008 IEEE 21st International Conference on Micro Electro Mechanical Systems*, 2008, pp. 327–330.
- [112]P. Kersten, S. Boustra, and J. W. Petersen, “Photolithography on micromachined 3D surfaces using electrodeposited photoresists,” *Sensors and Actuators A: Physical*, vol. 51, no. 1, pp. 51–54, Oct. 1995.
- [113]N. P. Pham, J. N. Burghartz, and P. M. Sarro, “Spray coating of photoresist for pattern transfer on high topography surfaces,” *J. Micromech. Microeng.*, vol. 15, no. 4, pp. 691–697, Feb. 2005.
- [114]D. Goldstein and D. H. Goldstein, *Polarized Light, Revised and Expanded*. CRC Press, 2003.
- [115]A. Feteira, “Negative Temperature Coefficient Resistance (NTCR) Ceramic Thermistors: An Industrial Perspective,” *Journal of the American Ceramic Society*, vol. 92, no. 5, pp. 967–983, 2009.
- [116]S. Jagtap, S. Rane, U. Mulik, and D. Amalnerkar, “Thick film NTC thermistor for wide range of temperature sensing,” *Microelectronics International*, Apr. 2007.

Appendix A. Derivation of the Parasitic Parameter N

In presence of parasitic resistance, the thermally induced change in the electrical resistance at a given side of the proposed device becomes of the form:

$$\Delta R_{equ} = \left(\frac{1}{\Delta R_{sj}} + \frac{1}{\Delta R_{pj}} \right)^{-1} \quad (83)$$

where ΔR_{equ} is the equivalent change in the electrical resistance at a given side of the device (j = left, right), ΔR_{sj} and ΔR_{pj} are the change in the electrical resistance in the sense and parasitic regions of the device respectively. Therefore the relationship between ΔR_{sj} (sense region resistance change at side j) and ΔR_{pj} (parasitic region resistance change at side j) can be expressed as in the following:

$$\Delta R_{pj} = K_j \cdot \Delta R_{sj} \quad (84)$$

where K_j is the ratio between the change in the electrical resistance in the sense and parasitic region of a given side (j = left, right). Plugging equation (84) into (83):

$$\Delta R_{equ} = \frac{K \cdot \Delta R_{sj}}{K + 1} \quad (85)$$

Given that the change in the electrical resistance of the sense and parasitic regions are of the form:

$$\Delta R_{sj} = K_{sj} \cdot K_{thR} \cdot I_{in} \cdot \sin(\beta \pm \alpha) \quad (86)$$

$$\Delta R_{pj} = K_{pj} \cdot K_{thR} \cdot I_{in} \cdot \sin(\beta) \quad (87)$$

where K_{sj} and K_{pj} are scalar values proportional to the sense and parasitic region's mass, surface area and specific heat at a given side (j = left, right) respectively and K_{thR} is a scalar proportional to the sense material's TCR and room temperature electrical resistance. Plugging equations (86) and (87) into (85) the ratio scalar K can be approximated:

$$K_j = \frac{K_{pj} \cdot \sin(\beta)}{K_{sj} \cdot \sin(\beta \pm \alpha)} \quad (88)$$

The ratio of the device's change in the electrical resistance at the left and right side can be rewritten to take into account the contributions of the sense and the parasitic regions in the following form:

$$\hat{\mathcal{R}}_{L/R} = \frac{K_L \cdot (K_R + 1)}{K_R \cdot (K_L + 1)} \cdot \frac{\Delta R_{SL}}{\Delta R_{SR}} \quad (89)$$

where $\hat{\mathcal{R}}_{L/R}$ is the ratio of the change in the electrical resistance between the left and right side of the device and K_L and K_R are the ratio between the parasitic and sense regions' change in the electrical resistance at the left and right side of the device respectively. Plugging in equation (88) into (89) will result in an expression of the following form:

$$\hat{\mathcal{R}}_{L/R} = \frac{K_{pL} \cdot (K_{pR} \cdot \sin(\beta) - K_{sR} \cdot \sin(\beta - \alpha))}{K_{pR} \cdot (K_{pL} \cdot \sin(\beta) + K_{sL} \cdot \sin(\beta + \alpha))} \cdot \frac{\Delta R_{SL}}{\Delta R_{SR}} \quad (90)$$

Assuming identical sense and parasitic regions on the left and right side of the device:

$$\frac{K_{pL}}{K_{sL}} = \frac{K_{pR}}{K_{sR}} = K_{PS} \quad (91)$$

Equation (90) can be simplified to the following form:

$$\hat{\mathcal{R}}_{L/R} = \frac{\left(\frac{K_{pR} \cdot \sin(\beta)}{K_{sR}} - \sin(\beta - \alpha) \right)}{\left(\frac{K_{pL} \cdot \sin(\beta)}{K_{sL}} + \sin(\beta + \alpha) \right)} \cdot \frac{\Delta R_{SL}}{\Delta R_{SR}} \quad (92)$$

This can be rewritten in a closed form as in the following expression:

$$\hat{\mathcal{R}}_{L/R} = \frac{\left(\frac{K_{PS} + \cos(\alpha)}{\sin(\alpha)} \cdot \sin(\beta) - \cos(\beta) \right)}{\left(\frac{K_{PS} + \cos(\alpha)}{\sin(\alpha)} \cdot \sin(\beta) + \cos(\beta) \right)} \cdot \frac{\Delta R_{SL}}{\Delta R_{SR}} \quad (93)$$

Equation (93) presents a mathematical approximation of the parasitic region's contribution to the overall device output ratio in the form of a multiplicative noise parameter with dependence on both sense and parasitic regions' material related parameters such as specific heat, thickness and resistivity as well as the known angle of silicon (111) facet α and the unknown incidence angle β . Since the components of the multiplicative term in equation (93) can be approximated with scalar values, the overall contribution of this term can therefore be presented in the following form:

$$\hat{\mathcal{R}}_{L/R} = \hat{N} \cdot \mathcal{R}_{L/R} \quad (94)$$

$$\hat{N} = \frac{\left(\frac{K_{PS} + \cos(\alpha)}{\sin(\alpha)} \cdot \sin(\beta) - \cos(\beta)\right)}{\left(\frac{K_{PS} + \cos(\alpha)}{\sin(\alpha)} \cdot \sin(\beta) + \cos(\beta)\right)} \quad (95)$$

Where $\mathcal{R}_{L/R}$ is the ratio of the change in the electrical resistance between the left and right side of the device in the absence of parasitic resistance contributions and \hat{N} is the approximated incidence angle dependent, sense material dependent parasitic multiplicative term affecting the ratio of the change in the electrical resistance as a function of the perceived optical power on the left and side of the device. In order to recalculate the incidence angle β from the parasitic affected electrical resistance change ratio between the left and right side of the device $\hat{\mathcal{R}}_{L/R}$, the overall contribution of the sense and parasitic resistances and their respective thermally induced change can be written in the following form:

$$R_T - R_o = \left(\frac{1}{R_S - \Delta R_S} + \frac{1}{R_P - \Delta R_P}\right)^{-1} - \left(\frac{1}{R_S} + \frac{1}{R_P}\right)^{-1} \quad (96)$$

where R_T and R_o are the room temperature (pre-exposure) and post exposure measured electrical resistance at a given side of the device and R_S , ΔR_S , R_P and ΔR_P are the sense and parasitic regions pre-exposure (room temperature) and post exposure measured electrical resistances respectively. Expansion of equation (96) into the following form:

$$R_T - R_o = \frac{(R_S - \Delta R_S) \cdot (R_P - \Delta R_P)}{(R_S - \Delta R_S) + (R_P - \Delta R_P)} - \frac{R_S \cdot R_P}{R_S + R_P} \quad (97)$$

Since the changes in the electrical resistance are nominal relative to the room temperature resistance, equation above be simplified to the following form:

$$R_T - R_o \approx \frac{(R_S - \Delta R_S) \cdot (R_P - \Delta R_P) - R_S \cdot R_P}{R_S + R_P} \quad (98)$$

Equation (98) can further be expanded into the following form:

$$R_T - R_o \approx -(\Delta R_S + \Delta R_P) + \frac{R_S \Delta R_S + R_P \Delta R_P}{R_S + R_P} \quad (99)$$

Since the left term in (99) becomes a significantly small number, therefore the absolute changes of the electrical resistances ΔR_S and ΔR_P dominate the overall thermally induced drop in the measured electrical resistance at a given side of the device as a result of exposure to IR.

Appendix B. Derivation of Exponential Valued TCR

The electrical characteristics of semiconducting oxides such as vanadium pentoxide are generally described by means of narrow-band hopping conduction where the carrier concentration is temperature independent but the carrier's mobility is temperature activated. Therefore the material resistivity can be defined using the following equation:

$$\rho(T) = \rho_o e^{\frac{E_a}{k_B T}} \quad (100)$$

where ρ is the temperature dependent resistivity, ρ_o is the temperature-independent resistivity, E_a is the charge carrier's activation energy, k_B is the Boltzmann constant, and T is the sample's temperature. For thin film samples of fixed dimension the above expression can be written in terms of the material's electrical resistance without loss of generality:

$$R(T) = R_o e^{\frac{\beta}{T}} \quad (101)$$

$$R_o = \lim_{T \rightarrow \infty} R(T) \quad (102)$$

$$\beta = \frac{E_a}{k_B} \quad (103)$$

From the theoretical expression given in equation (100) [115], [116]:

$$\frac{\partial}{\partial T} R(T) = -R_o \frac{\beta}{T^2} e^{\frac{\beta}{T}} \quad (104)$$

$$\therefore \frac{1}{R_o} \frac{\partial}{\partial T} R(T) = -\frac{\beta}{T^2} e^{\frac{\beta}{T}} \quad (105)$$

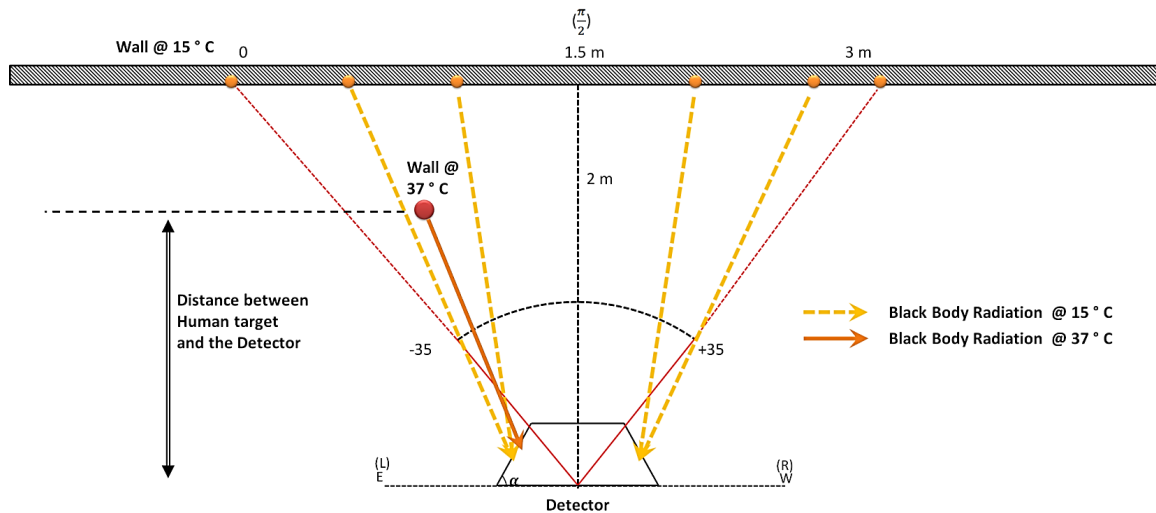
$$\therefore \frac{1}{R_o} \frac{\partial}{\partial T} R(T) = -\frac{\beta}{T^2} = \alpha \quad \text{when } T \rightarrow \infty \quad (106)$$

$$\therefore R(T) = R_o e^{\frac{\beta}{T}} \equiv R_o e^{\frac{\beta}{T^2} \cdot T} \equiv R_o e^{-\alpha T} \quad (107)$$

The data can then be fitted to a decaying exponential function such as equation (107) where the decay rate α signifies the temperature coefficient of resistance of the materials.

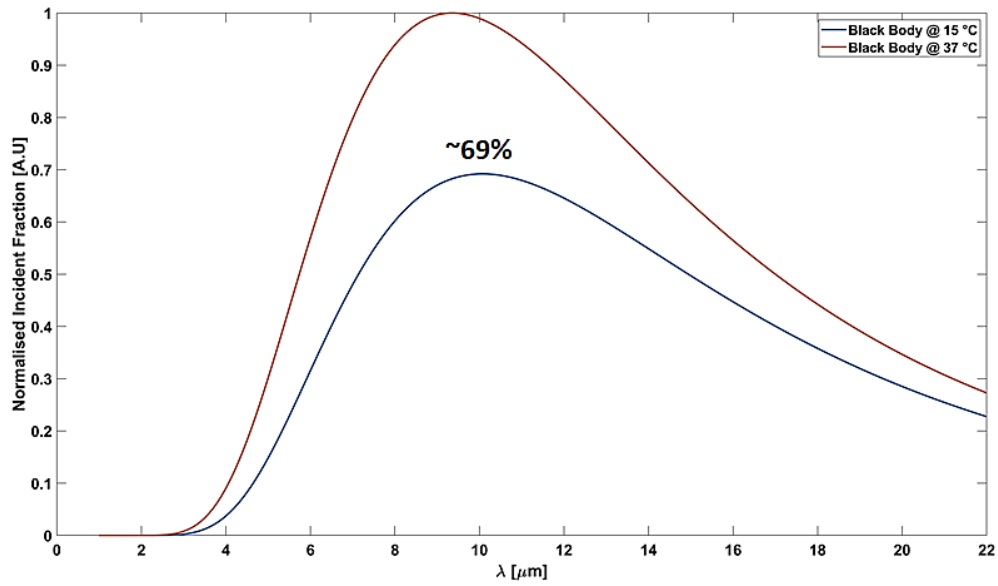
Appendix C. Effect of Background Radiation on The Detector's Angular Recalculation

The following simulation gives a measure of the proposed detector's capability to distinguish between a human target (black body radiator at 37 °C) relative to another source of IR radiation (wall at 15 °C).



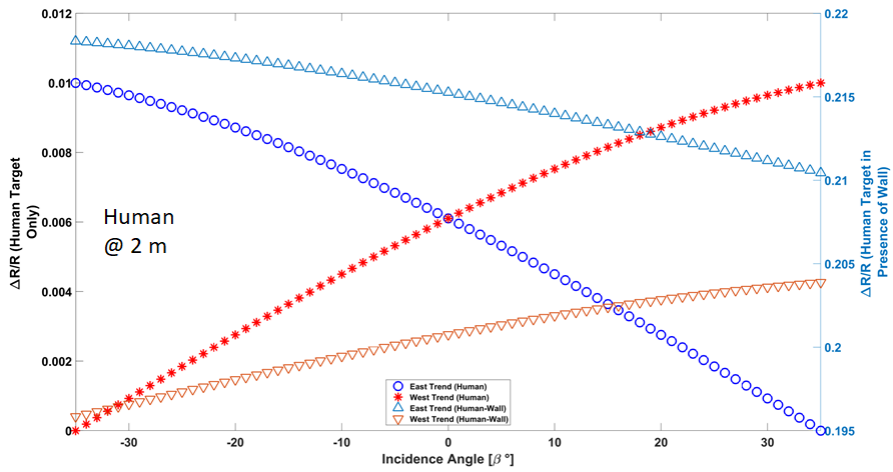
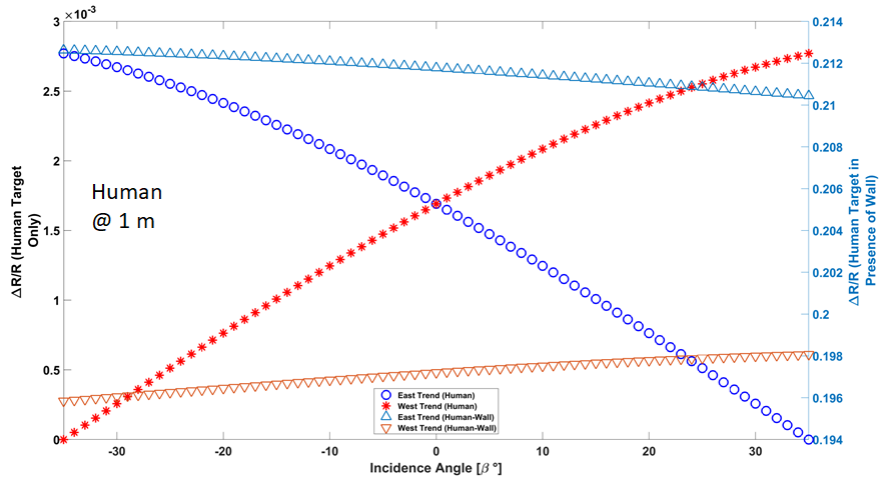
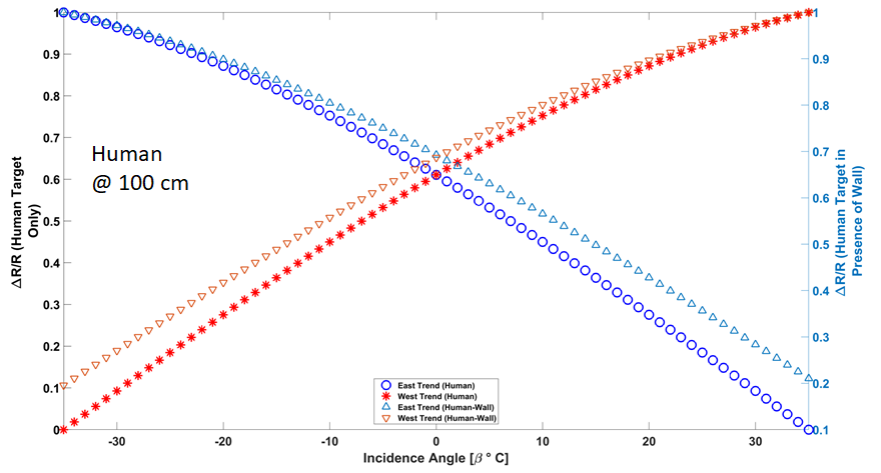
Appendix Figure- 1 Simulation schematic: the proposed detector facing a target IR point source radiating at 37 °C and a wall radiating at 15 °C

The normalised radiation curve for black bodies at 15 °C and 37 °C indicate that a black body such as a wall with an emissivity close to a white paper (~0.88) radiates at 69% of that of a human source at 37 °C:



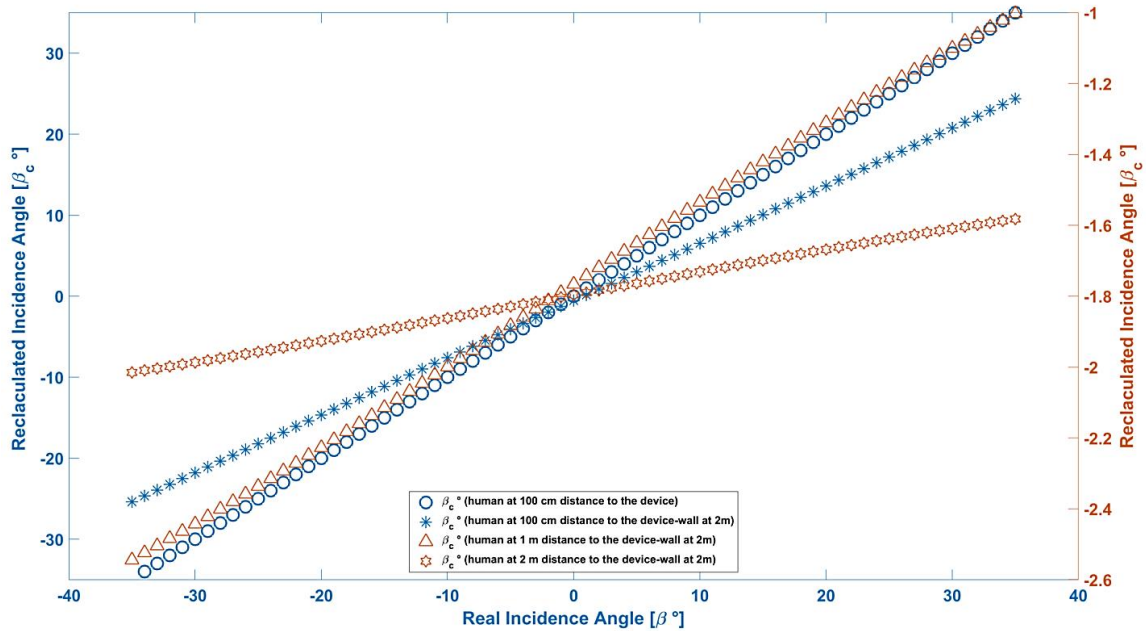
Appendix Figure- 2 Normalized radiation spectra of black body radiators at 37 °C and 15 °C

The latter indicates that if a black body at 37 °C generates a nominal figure e.g 400 mW of radiative power, the other black body at 15 °C will generate at least at least 80 mW. As a result, if the detector is placed in front of a wall at 15 °C, its ability to recalculate the incidence angle of an IR source such as a human, will be compromised due to perception of radiative power incident on the two sides of the device due to both the human target and the stationary wall. Such distortion can be observed in the detector's $\Delta R/R$ trends at either side as well as the recalculated incidence angle as shown in the following set of figures:



Appendix Figure- 3 East and west side $\Delta R/R$ trends for human vs human - wall at top) 100, middle) 1m and bottom) 2m cm human-detector distance. Wall is 2 m distance to the detector.

As a result of such distortion, the detector's accuracy in recalculating the incidence angle of the human target diminishes. As shown in the following series of figures, presence of a black body radiator such as a wall at 15 ° C will hamper the device's capability to recalculate the incidence angle within the proper range.



Appendix Figure- 4 Recalculated angle for the case of human at 1 m distance to the detector (left axis - circle maker), human at 100 cm and wall at 2m (left axis - asterisk marker), human at 1 m and wall at 2m (right axis - triangle marker) and human at 2 m and wall at 2m (right axis - hexagon marker)

Appendix D. Statistical Relevance and Goodness of the Fitted Models

ΔR/R Trend Fit Statistics

<i>Fit Parameters with 95% Confidence Bounds</i>	SSE	RSQ	a	b	c
<i>Trend(s) in Figure</i>					
Figure 6- 16 b) East Trend	6.57E-07	0.94849	0.008968001124	-0.005040070054	0.007620022931
Figure 6- 16 b) West Trend	9.83E-07	0.91704	-0.007358457229	0.005180832252	0.00890254761
Figure 6- 26 b) East Trend	7.51E-08	0.84391	0.002405605476	-0.001575571416	0.005783869614
Figure 6- 26 b) West Trend	1.75E-08	0.98431	-0.001874010186	0.00151371227	0.006157556655
Figure 6- 37 b) East Trend	6.41E-08	0.87696	0.001607786977	-0.001353259826	0.002684738092
Figure 6- 37 b) West Trend	2.63E-07	0.51108	-0.001335990648	0.001088184662	0.002867088529
Figure 6- 40 a) East Trend	9.65E-07	0.8678	0.005926583931	-0.004583926814	0.01015278286
Figure 6- 40 b) West Trend	9.33E-07	0.83242	-0.01606483375	0.01711738242	0.01346953069

Appendix_Figure- 5 ΔR/R Trend statistics for the fitted model in equation (71) to the measured data. The fitted model is of the form: $a*(\sin(\beta \pm 55)) + b*\sin(\beta) + c$.

SSE : Sum of Squared Error

RSQ: R Squared Value

$$SSE = \sum_{i=1}^n w_i (\hat{y}_i - y_i)^2$$

$$RSQ = \sum_{i=1}^n w_i (\hat{y}_i - \bar{y}_i)^2$$

<i>Fit Parameters with 95% Confidence Bounds</i>	SSE	RSQ	DFE	ADJ_RSQ	RMSE	P1	P2
<i>Device/Experiment</i>							
Figure 6-23 b) Device with 90% Parasitic Data Trend	1036.1	0.74834	108	0.74601	3.0974	5.317	1.763
Figure 6-23 b) Measured Data Trend	2.7267	0.64798	7	0.59769	0.62413	0.01276	-0.0352
Figure 6-30 a) Measured Data Trend	64.374	0.99095	7	0.98965	3.0325	0.7554	-1.476
Figure 6-27 b) Device with 80% Parasitic Data Trend	1412.1	0.91761	108	0.91685	3.616	0.3766	0.6423
Figure 6-27 b) Measured Data Trend	275.63	0.87045	6	0.84885	6.7778	0.2038	-1.508
Figure 6-30 b) Measured Data Trend	74.871	0.98569	6	0.9833	3.5325	0.7591	-1.372
Figure 6-38 b) Device with 30% Parasitic Data Trend	777.02	0.96853	108	0.96824	2.6823	0.4643	0.5602
Figure 6-38 b) Measured Data Trend	169.1	0.4599	3	0.27986	7.5077	0.253	0.1039
Figure 6-41 b) Device with 30% Parasitic Data Trend	777.2	0.9807	108	0.98052	2.6826	0.5967	-5.548
Figure 6-41 b) Measured Data Trend	1347.8	0.58411	6	0.51479	14.988	0.6713	-9.734
Figure 6-41 b) Measured Data Trend Corrected for Parasitic Parameter N	374.52	0.91001	5	0.89201	8.6547	0.9528	-6.208

Appendix_Figure- 6 Fit Statistics for the linear trend lines fitted to the recalculated incidence angles. The linear fitted model is of the form $F(\beta) = P1*\beta + P2$

SSE : Sum of Squared Error

RSQ: R Squared Value

$$SSE = \sum_{i=1}^n w_i (\hat{y}_i - y_i)^2$$

$$RSQ = \sum_{i=1}^n w_i (\hat{y}_i - \bar{y}_i)^2$$